

https://dspace.org/

Mechanisms of Heavy Ion Reactions and De-excitation in Processes Initiated by Projectiles at Intermediate Energies, Using a Gamma Detector Array

Korir, Kipkirui Arap

2007-02-28T12:06:49Z
http://hdl.handle.net/10539/2156

Downloaded from a DSpace repository. https://dspace.org/

Mechanisms of Heavy Ion Reactions and De-excitation in Processes Initiated by Projectiles at Intermediate Energies, Using a Gamma Detector Array

by

Kipkirui Arap Korir

A thesis submitted to the Faculty of Science

in fulfillment of the requirements for the degree of

Doctor of Philosophy

School of Physics

2006

I declare that this thesis is my own work. It is being submitted in fulfilment of the requirements for the degree of Doctor of Philosophy at the University of the Witwatersrand. It has not been submitted before for any degree or examination at any other university.

Kipkirui Arap Korir

Date

Abstract

The Doppler shift and the Doppler broadening of prompt gamma emissions were measured for some residues formed in the interaction of 33 A MeV ^{12}C ions with a ^{63}Cu target using the AFRODITE detector array at Faure, Cape Town. This is a potentially new technique to carry out nuclear interaction studies. Coincident gamma rays emitted by the residues are used in their identification. Detection at angles other than 90° with respect to the beam axis gives the magnitude of the mean Doppler shifts and the average linear momentum transfer. The Doppler broadening of the detected gamma lines at 90 ° with respect to the beam axis could give the residue recoil angular distribution. The precise shapes of the Doppler shifted and broadened gamma lines for each of the residues extracted, reveals the distribution, in magnitude and angle, of the momentum transferred in the interaction process. In addition, characteristic gamma energy transitions of each residue populated carry additional information on angular momentum (spin) transfer, production cross-section and nuclear excitation states. The measured residues show a unique distribution of momentum ranging from single nucleon transfer to complete damping of the projectile momentum. The measured observables are consistent with the existing data from other techniques, making the new technique viable option for studying nuclear interaction kinematics. A comparison of the experimental measurements with the predictions of the model developed in Milano [1] and GEANT4 calculations shows that the model developed in Milano model give a much better agreement compared to the GEANT4 calculations, attributed to the assumption of projectile break-up and re-emission process of some of the fragments during the first step of the nuclear interaction process.

[1] All calculations relating to this model and presented here is the work of E. Gadioli, University of Milano

Dedication

To my children **Xavier** and **Valerie**

Life is too short to make a career in physics, make it a hobby and seek a lifelong well-paying profession. That is precisely how Einstein **did it**. The training in field of financial management could potentially attract as much money in one month as the yearly pay of a physicist, yet the road to being one is *fraught with hassles* and a lot of sacrifices. There has to be a better way to gain a more meaningful and enjoyable life out there. I have lost a big junk of my productive life to the 'black hole'. A theoretical physicist could have put it better. A stitch in time saves nine.

Acknowledgements

I would like to thank the faculty, staff and students of Schonland Research Institute for creating a conducive and productive environment for research undertaking presented here.

Particularly, I would like to express my sincere thanks to S. H. Connell, E. Sideras-Haddad, J. P. F Sellschop[2] , E. Gadioli, J. J. Lawrie, S. Förtsch, G. F. Steyn and the rest of the iThemba Physics group for taking their time to read through the draft copy and making the necessary amendments. Special thanks to my supervisors for their guidance, support and assistance during the period of my research. The knowledge and the confidence they exuded were especially vital for the undertaking of what could be a very complex field of study.

E. Gadioli and his team in Milano are thanked a lot for providing some of the materials and equipment needed for the experiment and in ensuring that the experiment was done. More so for their willingness to do the calculations and allow me to reproduce them in this work. All credit goes them for putting up all the effort and for every other bit of material support presented here.

It was a pleasure to work within the iThemba-Wits-Milano Heavy Ion Research collaboration, whose contribution is rather significant to the physics community. The theoretical calculation results presented here (using the Milano university developed code) were done and provided by E. Gadioli, whose contribution is acknowledged.

I cannot miss to acknowledge the useful training skills I received from several people at the iThemba LABS, mainly J. J. Lawrie, R. Newman and J. Pilcher. More so, the co-operation I got from other members of the laboratory during the period of my stay necessitated by the data

[2] deceased (2002)

analysis process, is highly appreciated. I also cannot miss to thank G. Mabala for introducing me to the VAX computer system.

My work would not have been as productive or enjoyable, were it not for my colleagues and the staff of the accelerator building of the Schonland Research Institute. The work of the technical staff both at the Schonland and the iThemba LABS are highly appreciated for ensuring the research effort was a success.

I would like to thank my parents, Zablon and Susan Tergech, who throughout my years of existence have been a constant source of encouragement. I am grateful to my wife Rose, for all her love, support and understanding during the difficult times. My brothers, Joel, Joseph, David, Jonathan, Geoffrey and sisters, Elizabeth, Nancy, Jane, and Irene are also acknowledged for their role in my formative years. It is unfortunate that I had to take this long in pursue of further education, to make any useful contributions as per the African tradition of HARAMBEE, a process which could have taken just a few years in the first world.

On the WWW, I wish to thank the many individuals who were kind enough to guide me on the GEANT4/JQMD/EMPIREII nuclear codes and RadWare gamma analysis software problems and ready to provide the solutions promptly.

Last but not least, my greatest appreciation to all those who contributed to my Ph.D. funding, especially J. Sharpey-Schafer of iThemba LABS, for meeting my subsistence allowance and S. Connell of the Schonland Research Centre, for defraying the costs of my university fees during the 1999-2002 period and S. Connell for meeting both in the subsequent years.

The University of Nairobi is acknowledged for allowing me to take the study leave at the beginning of my two year employment contract.

The financial support provided by the NRF for this research project is highly appreciated.

Contents

Chapter

1 Introduction 1

1.1 Motivation 1

1.2 Introduction 6

2 The Physics in the Milano Developed Model 14

2.1 Nuclear Interaction Models 14

2.2 The Theory of Pre-equilibrium Emission 20

2.2.1 Particle and Cluster Emission 24

2.2.2 Photon Emission 27

2.2.3 The BME Monte Carlo Technique 28

2.2.4 BME Theory of Angular Distribution 29

2.2.5 The BME Theory of Reaction Cross Sections 30

2.3 The Coalescence Model 32

2.4 Sum Rule Model and Limitation of Complete Fusion 33

2.4.1 Alpha-like Particle Re-emission 36

2.4.2 Classical View of the Momentum Transfer Process 36

2.5 The Projectile Break-up 39

2.6 The Statistical Decay Processes 42

3 Techniques in Heavy Ion Interaction Measurements 47

3.1 Experimental Observables 50

3.1.1 Angular Momentum Measurements 50

3.1.2 Linear Momentum Measurements 51

3.1.3 Recoil Angle Measurements 54

3.1.4 Cross Sections Measurements 55

3.1.5 Charge Measurements 57

3.1.6 Reaction Time-Scale Measurements 58

3.2 Experimental Techniques 59

3.2.1 Exclusive and Inclusive Measurements 59

3.2.2 The Conventional Radiochemical Techniques 65

4 The GEANT4 Simulation Physics 75

4.1 Photon Interaction Physics 76

4.1.1 Photoelectric Effect 78

4.1.2 Photon Conversion 79

4.1.3 Compton Scattering 80

4.1.4 Multiple Scattering 81

4.1.5 Electron Ionisation 83

4.1.6 Electron Bremsstrahlung 85

4.1.7 Particle Annihilation 85

4.2 Nuclear Interaction Models 86

4.2.1 The Binary Cascade 86

4.2.2 Precompound Model 92

4.2.3 Evaporation Model 95

4.2.4 Fermi Break-up Model 101

5 Experimental Techniques and Data Reduction 103

5.1 The Multi-detector Gamma-ray Spectrometer 103

5.1.1 The Target Ladder 109

5.2 The Experimental Setup 110

5.2.1 Detector Energy Calibration 111

5.2.2 Detector FWHM Calibration 116

5.3 The Doppler Effect 118

5.3.1 Gamma Coincidence Measurements 118

5.3.2 Residue Gamma Doppler Effect 120

5.3.3 Residue Identification 126

5.3.4 Doppler Effect Extraction using the γ-γ Matrix Techniques 129

5.3.5 Doppler Effect Extraction using Offline Sorting Technique 130

5.3.6 Recoil Angle Versus Residue Velocity Simulation 132

5.4 Experimental Data Reduction 133

5.4.1 Relative Residue Production Cross Section 133

5.4.2 Residue Recoil Asymmetry and Tracking 137

5.4.3 Velocity Distribution Reproducibility 139

5.4.4 Residue Half-Lives ($T_{1/2}$) 141

5.4.5 Evidence of High Energy Photons 141

5.4.6 Residue Cross-Coincidence 143

5.4.7 Residue Velocity Reconstruction 143

5.4.8 Residue Velocity and Angle Reconstruction 145

5.5 GEANT4 Simulations 147

5.5.1 Detector Simulation 148

5.6 The BME - GEANT4 Simulations 151

6 Results and Discussion 153

6.1 Photon Interaction Processes 154

6.2 Nuclear Interaction Processes 158

6.2.1 Relative Residue Yields 158

6.2.2 Angular Momentum Transfer 160

6.2.3 The Doppler Broadening of Gamma Energy 161

6.2.4 Gamma Residue Cross Coincidence 164

6.2.5 Mean Residue Energy and Loss in the Target Foil 166

6.2.6 Average Momentum Transfer Versus the Projectile Energy 167

6.2.7 Residue Recoil Asymmetry 169

6.2.8 Relative Residue Yields 170

6.2.9 Residue Velocity Distribution 170

7 Summary and Outlook 181

Bibliography 185

Appendix

A Some Residue Observables 200

B Gamma Emission Properties 201

C Studies based on the 4π Particle Detector Arrays 213

D Nuclear Excitation Energy and the Apparent Temperature 224

E The Quantum Molecular Dynamics Model 227

Tables

Table

5.1 Some technical specifications of the AFRODITE spectrometer (Ref. [245]). . . 106

6.1 The calculation and measurement characteristics of Clover detector obtained at 1332 keV; absolute photo-peak efficiency, peak-to-total ratio (P/T) in (a) singles, total detection mode (b) any fired BGO veto and (c) adjacent BGO veto only, add-back factor F and distribution of the number of firing germanium crystal for full gamma photon energy absorption events. 155

6.2 The observed prominent residues and their corresponding observables. 163

6.3 The residue energy and the corresponding energy loss in the target foil 167

A.1 A number of the measured observables for the prominent residue gamma lines are given in table A.1. These are residue identity (A, Z) in column one, the half-life of the gamma transition energy state for the gated line and the corresponding coincident gamma cascade energies used in the identification of the residue nucleus is given in column three. 200

Figures

Figure

1.1 The isobaric yield of the residues produced in the interaction of 32 A MeV ^{12}C projectile with a ^{103}Rh target nuclei. The open and closed circles are experimental data, the solid histogram is the prediction from the model developed in Milano, the dashed histogram shows the corrected residue yield that includes the unobserved residue yields (from Ref. [1]). 4

1.2 The ratio between measured and calculated cross-sections for residue formation, as a function of the residue mass, in the interaction of 45 A MeV ^{12}C with natural copper (from Ref. [16]). 9

2.1 Schematic representation for the description of ^{12}C and intermediate mass target nuclei interactions in the comprehensive model developed in Milano. 15

2.2 The total reaction cross-section and the various contributing reaction mechanisms (cf stands for complete fusion, in stands for inelastic scattering, Be stands for incomplete fusion of a beryllium isotope, α stands for incomplete fusion of one α particle, p stands for proton transfer, n stands for neutron transfer, ^{5,6,7}Li stands for incomplete fusion of a ^{5}Li or a ^{6}Li or a ^{7}Li, ^{3,5}He represents incomplete fusion of a ^{3}He or a ^{5}He) (from Ref. [1]). 18

2.3 Upper panel: Typical model mean excitation energy (in MeV/A) of the intermediate equilibrated nucleus produced in the interaction of the ^{12}C projectile with ^{103}Rh as a function of the incident energy assuming the inelastic contribution. Lower panel: The ratio between the predicted residue linear momentum p_F and the projectile linear momentum p_{inc}. The label 'mean' stands for the average values for all the processes, while CF, Be, α, p and n labels are the values for complete fusion, ^{8}Be and α-particle incomplete fusion, proton and neutron transfer processes, respectively (from Ref. [2]). 19

2.4 The model prediction of the intermediate equilibrated nucleus excitation energy distributions in the interaction of 400 MeV ^{12}C projectile with ^{103}Rh for each of the process and their combined contribution assuming the inelastic process. The label 'tot' is the predicted distribution for the combined processes labelled by CF, Be, α, p and n, for the complete fusion, ^{8}Be and α-particle incomplete fusion, proton and neutron transfer processes, respectively (from Ref. [2]). . . . 20

2.5 Some composite system observables (from Ref. [23]). 37

3.1 A plot of the excitation energy versus angular momentum for the intermediate equilibrated nucleus produced. 49

3.2 The gamma emission multiplicity M_γ, for energy >35 MeV, as function of the residue recoil velocity to the centre of mass value, for the 37 A MeV Ar + Mo (full symbols) and the 27 A MeV Ar + Zr (open symbols) interactions. The y-axis error bars are due to statistical errors while the x-axis error bars represent the bin width (from Ref. [41]). 54

3.3 The conventional radiochemical-based catcher foils used in the technique for measuring the angular distributions of residues. 55

3.4 The differential production cross section variation with angle of some residues for 6 A MeV incident energy for the present system (from Ref. [46]). 56

3.5 Angular distributions of residues produced in the interaction of 19 A MeV ^{12}C with ^{103}Rh target nuclei. The full dots with error bars are experimental values, the full line histograms are theoretical predictions of the model developed in Milano described in chapter 2 (from Ref. [2]). 56

3.6 The reconstructed velocity V_{qp} of the quasi-projectile break-up with respect to c. The arrow indicates the projectile velocity (from Ref. [151]). 58

3.7 The spectra of ^{8}Be emitted at 9° in the interaction of ^{12}C with, respectively, ^{59}Co (full dots) and ^{197}Au (open squares) at incident energy of 33.3 A MeV (from Ref. [94]). 62

3.8 The spectra of ^{8}Be fragments observed at the indicated angles in the interaction of ^{12}C with ^{197}Au at incident energy of 33.3 A MeV, 25 A MeV and 16.7 A MeV. The open points are the experimental results, the full line histograms are the predicted break-up spectra based on the description given in section 2.5 (from Ref. [94]). 63

3.9 The fractional velocity transfer for the interaction of copper with the ^{12}C projectile at various energies (from Ref. [23, 33]). 69

3.10 The maximum induced linear momentum transfers for ^{12}C-induced interactions between 10 A MeV and 84 A MeV (from Ref. [25]). 70

3.11 The deduced residue yield distributions in the interaction of copper with different energies of the ^{12}C projectiles (from Ref. [21]). 71

3.12 The excitation functions for (a) low mass (b) intermediate mass, and (c) high-mass products of the interaction of ^{12}C with copper target nuclei (from Ref. [21]). 72

4.1 The energy dependence of photon interaction processes in Si and Ge materials. 77

5.1 The target chamber showing kapton windows, beam line, the closed circuit TV camera, two LEPS (subtended at 45° and135°) and two Clovers (subtended at 45° and135°) are visible on the upper and lower section of the photograph, respectively. 105

5.2 Typical electronics of the AFRODITE gamma detector array. 107

5.3 The target ladder. 110

5.4 The position (p) and detector number in the array during the experiment, L and C represents LEPS and Clover, respectively. 111

5.5 The Clover detector versus the LEPS detector coincidence hits. 112

5.6 The calibration fits for the Clover detector (C3) elements, the open circles and asterisks are the residuals multiplied by 500 and centred along the Y-axis for 2-parameter and 5-parameter fits, respectively. 113

5.7 The typical energy efficiency curve for the combined 90° detectors 115

5.8 The FWHM calibration curve for the combined Clover detectors. 116

5.9 Simulation of the Doppler broadening of the gamma line detected in the Clover detector, full histogram represents the experimental spectrum. 118

5.10 The coincidence measurements of two gamma lines, E^1 and E^2, produced in a cascade during the de-excitation of a nucleus. 119

5.11 The effect of intrinsic detector resolution on the velocity distribution, with (full-line) and without the correction. 125

5.12 Recoil velocity (full-line) versus recoil angle ambiguity. 126

5.13 The spectrum of the coincident gamma lines of ^{55}Fe gated at 274 keV, the lines are of energies 605 keV, 1223 keV and 1317 keV produced from three 90° matrix (top), all the seven Clovers matrix and the 90° Clovers gated on any other coincident detector in the array. 128

5.14 The effect of residue recoil angles θ_r assuming a constant velocity value. 134

5.15 Two dimensional plot of opposite detectors oriented perpendicularly to the beam axis. 138

5.16 Two opposite detectors on one plane detecting two coincident gamma rays of energies E^1 and E^2, Doppler broadening causes $E^1 > E_0^1$ and $E^2 < E_0^2$ and for $\theta_r = 0^\circ$ or $\beta_r = 0$, $E^1 = E_0^1$ and $E^2 = E_0^2$. 139

5.17 The comparison of raw velocity distributions for the different gamma transition energies of ^{55}Fe (top) and ^{54}Mn nuclei. 140

5.18 The total projection spectrum of coincidence hits within the Clover detectors. The characteristic gamma lines and X-rays observed in the spectrum are due to the excitation of the detector and surrounding elements. 142

5.19 The spectrum of the coincident energy gates of 194.4 keV and 316.4 keV logically ORed. The total energy is 511 keV reflecting the Compton scattered event across the adjacent detector crystal elements. 142

5.20 The reconstruction technique showing coincident gamma detection measurements and the obtained spectra used in the selection criteria. 144

5.21 The HPGe crystal element in the Clover detector. 149

5.22 The geometry of simulated Clover detector, the gamma-rays are produced at the target position (T) and directed randomly to the front face of the Clover detector. 150

6.1 The relative gamma energy photo-peak efficiency curves obtained from GEANT4 calculations compared to the experimental values (open boxes). 155

6.2 The percentage error estimates in the evaluation of the relative gamma intensity ratios of 212 keV, 705 keV 852 keV and 1416 keV lines for the ^{54}Mn nucleus gated on the 156 keV gamma line, and those of the 203 keV, 212 keV, 479 keV and 1019 keV lines for ^{64}Cu nucleus gated on the 159 keV line represented by the closed and open boxes, respectively. 157

6.3 The total projection spectrum corrected for photo-peak efficiency. Gamma lines are assigned to their respective emitters based on gamma-gamma coincidence identification. 159

6.4 Typical level schemes for some nuclei. 161

6.5 The Doppler broadening effect versus gamma energy for the three nuclei, ^{64}Cu (astericks), ^{55}Fe (open boxes) and ^{54}Mn (closed boxes) 162

6.6 The intermediate mass fragments extracted using the extended energy inclusive Clover matrix (section 5.4.5). The spectrum is a potential target frame ^{24}Mg residue product with the two coincident line gates ORed. 164

6.7 The Doppler broadening asymmetry due to detector angle position of the 948 keV ^{61}Ni gamma line. 165

6.8 The spectrum gated on 351 keV shows the sharp ^{62}Cu lines and the two Doppler broadened potential target-like fragments gamma lines. 166

6.9 The mean fractional momentum transfer (β/β_{cn}) versus the ^{12}C projectile energy for the ^{55}Fe nucleus. 168

6.10 Gamma-gamma coincident gates showing the recoil asymmetry of ^{54}Mn and ^{64}Cu nuclei, line drawn on the ^{54}Mn locus. The transitions are 156 and 212 keV lines $5^+ \rightarrow 4^+ \rightarrow 3^+$ for ^{54}Mn; 159 and 212 keV lines $4^+ \rightarrow 3^+$, $2^+ \rightarrow 1^+$ for ^{64}Cu. 169

6.11 The relative residue yields based on the predictions of the various theoretical calculations reported, with respect to the experimental measurement. The closed circles are the predictions of the model developed in Milano and the open circles are GEANT4 values. 171

6.12 The experiment residue velocity distribution (shaded) comparison with the model developed in Milano (dotted) and GEANT4 (line) model calculations. The experimental values have not been corrected for the intrinsic detector resolution. . 172

6.13 The residue mean relative velocity (β/β_{cn}) as predicted by the various theoretical calculations compared to the experimental values. These are the experimental values with (open boxes) and without angle correction (closed boxes), model developed in Milano (closed circles), GEANT4 pre-compound (open circles) and GEANT4 inelastic (asterisks). 173

6.14 The model developed in Milano predictions versus experiment measurements (histogram) 177

6.15 The model developed in Milano predictions versus experiment measurements (histogram) 178

6.16 The model developed in Milano predictions versus experiment measurements (histogram) 179

C.1 The contour plots "total pseudo linear momentum versus total charge" for the events detected in Ar + KCl and Xe + Sn systems at two bombarding energies. The measured quantities have been normalized to their expected values (from Ref. [146]). 214

C.2 The charged particle total multiplicity distributions for the Xe + Sn system at 39 A MeV. Full curve: all events; dashed curve: "complete events", dotted curve: "completed events" (from Ref. [146]). 215

C.3 The 'Wilczyński diagram' for complete events: The logarithmic intensity scale representing measured cross section as a function of total measured centre of mass kinetic energy (as a fraction of the available centre of mass energy) and 'flow' angle θ_f or direction of the event principal axis flow. The four zones indicated classify the complete events. For events in Zones 2 to 4 the mean value of TKE is indicated (points) for each flow bin (from Ref. [145]). 221

C.4 The fragment charge-velocity correlations for the four classes of events corresponding to the zones defined in the Wilczyński diagram (Fig C.3). The mean charge density is plotted as a function of the velocity parallel to the beam axis (thick lines) or the principal axis of each event derived from the tensor (shaded histograms) (from Ref. [145]). 222

C.5 Typical calorific curve of the nucleus (from Ref. [339]). 223

E.1 The mass and charge distribution of residues produced using the QMD calculation for the ^{12} and ^{63} collision system. 229

Chapter 1

Introduction

1.1 Motivation

Studies of ^{12}C and ^{16}O ion induced reactions at energy ranges from just above the Coulomb barrier to tens of A MeV found that a new mechanism of fast alpha-like fragment re-emission could play a significant role in the interaction processes. The implication of this is not only the increase in the cross-section of near-target residues, but of relatively lower linear momentum transfer than is the case for complete or partial fusion, pre-equilibrium emission and subsequent particle evaporation processes. Another additional mechanism, that of the contribution from the decay of the target nuclei excited in the inelastic scattering process of the incident projectile nuclei has also been incorporated, based on more recent work of the collaboration [1]. These mechanisms were incorporated into the model developed in Milano, in order for it to adequately describe the measurements of excitation functions, angular distributions and energy distribution of residues observed in the conventional radiochemical foil stack activation techniques [2]. This technique uses a stack of foils to capture the reaction residues after which radionuclide assay is performed on them. The Milano model is developed by collaborators in this work and described in chapter 2. The mass yield measurements of near-target residues were also shown to agree with the above theoretical interpretation. Independent double differential cross section measurements of alpha-particle emission supported this theoretical framework, with evidence of an energetic forward-peaked alpha component in the spectra, typical for this kind of mechanism [3]. The yield is intermediate between the break-up and pre-equilibrium

alpha emission predictions in energy. A single theoretical framework with good agreement for both the radiochemical measurements and the double differential data was used. The incorporation of fast re-emission of alpha-like fragments in the model was shown to play a vital role, especially at the higher projectile energies.

This study was proposed in order to measure the relative residue production yields and their momentum distributions using the AFRODITE gamma detector array [4]. Besides allowing for the direct determination of residue momentum, yields not accessible previously could be verified. These residues could not have been apparent in the conventional radiochemical techniques for varied reasons as elaborated in Ref. [2], and so the need to extend the study further to measure prompt gamma emissions was clear. The theoretical calculations predicted significant yields of these near-target residues with rather small recoil ranges not fully ascertained experimentally. The choice of ^{63}Cu was made because it was in the investigated mass range (59<= A <=103) and excitation function data existed (section 3.2.2), while for^{59}Co and ^{93}Nb, targets on which the collaboration did extensive measurements, excitation function data was essentially non-existent. In the theoretical model developed in Milano, a good agreement of the experimental data at that time was achieved by assuming that the dominant reaction mechanisms were: (i) the complete fusion of projectile and target, (ii) the incomplete fusion of and ^{8}Be fragments from ^{12}C break-up with the target, and (iii) single-nucleon transfers from ^{12}C to ^{103}Rh. Complete fusion and break-up-fusion processes were assumed to depend on the mean field interaction between ^{12}C and ^{103}Rh and their probabilities were determined by the critical angular momentum model. The double differential cross-section spectra of the spectator fragments were calculated using the Local Plane Wave Approximation (LPWA) (chapter 2). In the case of incomplete fusion, another process which was incorporated in the theoretical calculation, was α particle re-emission. This is the process where the fast α particles are re-emitted with most of their energy, either as single entities or as constituents of the^{8}Be fragment after the ^{12}C break-up [5]. The re-emission process may occur after a few interactions with the target nucleons. This mechanism, as well as single nucleon transfer reactions, produces slightly excited

nuclei, which emit only very few nucleons during the statistical decay process. The probability of the α particle re-emission process was fixed based on the experimental cross-section values of the nuclei for the mass slightly smaller than that of the target, mainly the heaviest observed target isotopes, (^{102}Rh and ^{101}Rh). The theoretical model calculations had shown that the near-target residues were produced with the highest production cross-sections, with the most abundant observed residue being the target nucleus. Nonetheless, neither the theoretical interpretation for this observation nor the main contribution to these near-target residue yields is mentioned in earlier studies except in work of the collaboration given in Ref. [2]. To reproduce the prominent feature of the experimental mass distribution of the residues, another mechanism that could compensate for the decrease of the near-target residue yield was sought based on the initial energy loss and the survival-probability concept [1]. This is the inelastic scattering of the projectile with the target nucleus followed by the break-up of the projectile with both fragments escaping at very forward angles. This mechanism is obtained from the inelastic scattering cross section of the best-fit to the experimental cross-section measurements.

The near-target information cannot be obtained from the existing data for the present collision system (see section 3.2.2) as natural copper material was used for the target nuclei in most instances. This problem was avoided in the present setup by using an enriched copper target (^{63}Cu). The decay modes of these expected residue yields for the ^{103}Rh target inhibited their full off-line identification in the follow-up study. Alternative techniques were sought and the study has since then been extended to measurements of residues which were previously unobserved, as shown in figure 1.1.

The theoretical prediction, on the one hand, is capable of handling whichever target nuclei is used independent of the mass and the corresponding residue yields [4]. For instance, the plot given in figure 1.1 scaled down by ~ 0.6 in the x-axis could give the approximate residue yield expected for the present mass target calculation. Given below are some of the salient features of the present experimental setup unique as compared to similar systems studied in the past:

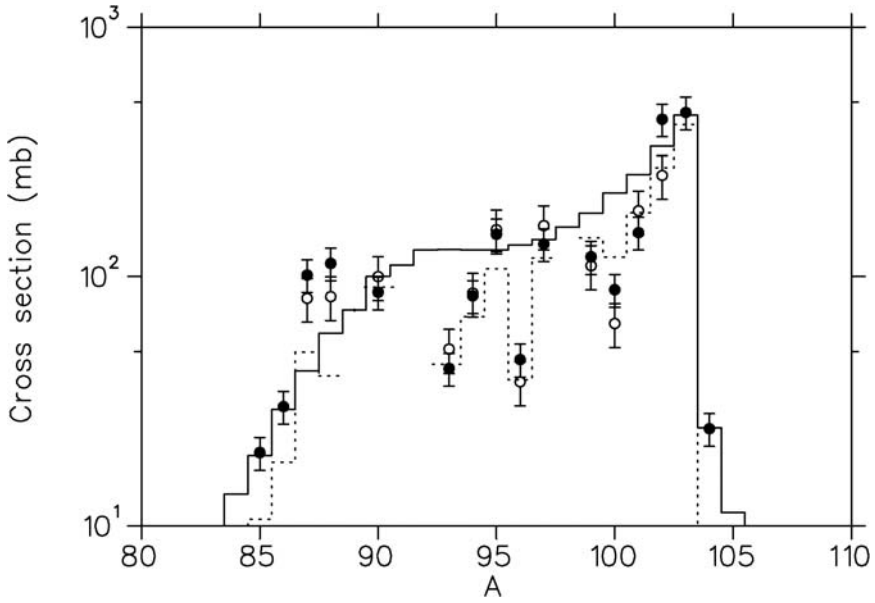


Figure 1.1: The isobaric yield of the residues produced in the interaction of 32 A MeV ^{12}C projectile with a ^{103}Rh target nuclei. The open and closed circles are experimental data, the solid histogram is the prediction from the model developed in Milano, the dashed histogram shows the corrected residue yield that includes the unobserved residue yields (from Ref. [1]).

- The measurements were taken on-line; unlike previous measurements which were all done off-line.
- The prompt gamma emissions have been measured. This extends the residue decay life times to nearly the time of production.
- An exceptionally thin target (≈17 nm.) was used in order to minimise the energy loss in the target and also the secondary interactions.
- The AFRODITE array is equipped with detectors which cover nearly 23.5% of 4π space, most of which are the low energy photon spectrometers (LEPS). Therefore the solid angle and the detection efficiency are improved significantly compared to the single detector counters.
- The excited slow moving or static residues produced, which went undetected previously because of the recoil energy thresholds limitations, are easily detected with opti-

mal efficiency in the present setup.

- The present experimental setup allows for the simultaneous measurement of residue recoil angle and momentum (velocity).
- The corrections inherent with the catcher foil and other conventional radiochemical techniques using the recoil ranges (uncertainty in heavy ion stopping powers) are avoided.
- The population of the different energy states in gamma spectroscopy provide information on the independent residue production yields and corrections due to the cumulative production common in the conventional radiochemical techniques are minimised.
- The limitation brought about by the detector dead-layer or energy loss inherent with particle detection techniques is avoided in electromagnetic radiation measurements.

The following aspects of the study were made possible with the present setup:

- The process of residues interaction identification using the concept of γ-γ coincidences is an exclusive measurement. Use of multiple coincidences of the gamma emissions eliminate ambiguities which could arise in the identification procedure of the residues.
- The relative residue cross-sections or relative population of states could be deduced [6].
- The magnitudes of the residue recoil velocity were measured using the Doppler shift effect and hence the average momentum transfer was determined.
- The residue recoil angles and their distributions were deduced through the application of Doppler broadening effect and software reconstruction algorithm relying on the gated experimental spectra of the different detector angles.
- The gamma-gamma cross-coincidence studies of the target-like and the projectile-like fragments emissions were explored.

1.2 Introduction

The experiment described in this work was performed as part of the Milano-Schonland-iThemba-Stellenbosch collaboration. The objective of this collaboration is to obtain comprehensive information on the reactions induced by ^{12}C and ^{16}O with intermediate mass target nuclei and establish a comprehensive phenomenological description. The projectile incident energy range studied is 5-45 A MeV for target mass $A \gtrapprox 60$. Large sets of experimental data have been accumulated in over a decade of research work. These measurements have shown that the de-excitation of the highly excited composite system created in the interaction process can be described by means of a model based on a cascade of nucleon-nucleon interactions, a modified and further developed form of the Boltzmann Master Equation (BME) theory [7]. The measurements have also identified the dominant reaction mechanisms leading to the production of the composite system and the subsequent de-excitation processes. This leads to the development of a comprehensive theoretical framework that reproduces the large sets of experimental measurements in great detail and with good mutual consistency.

This particular study involves Doppler shift and Doppler broadening of prompt gamma emission measurements for the interaction residues of ^{12}C projectile at 33 A MeV energy with a ^{63}Cu target using the AFRODITE detector array at iThemba LABS, Cape Town. This forms one of the many series of systematic experimental measurements done and reported elsewhere. They include

- Residue cross-sections variations (excitation functions) [8, 9, 10];
- Angular and forward recoil range measurements of target-like residues [2];
- Projectile-like fragment spectra and exit channels [3, 11];
- Light particle emission [12, 13, 14]; and
- Hard photon emission [15]

These measurements have been described with the comprehensive and consistent model based on the hypothesis that incorporates only a few interaction processes to account for the total reaction cross section [3]. These processes include complete fusion of the projectile with the target, projectile break-up into α-like fragments (two correlated α particles as ^{8}Be in the case of ^{12}C) with either of the fragments possibly fusing with the target nucleus, nucleon transfer or the inelastic scattering of the projectile. These processes have been incorporated into the MILANO code, which has been developed within the aegis of the collaboration and which is described further in chapter 2.

Chapter 2 provides an in-depth look at the physics used in the Milano model, a comprehensive theoretical description of the nuclear interaction processes code. The Boltzmann Master equation theory is utilised to predict the time evolution of the momentum distribution of the nucleons of the excited composite nucleus produced in the interaction of two energetic nuclei. In order to perform these calculates [16, 17], the nucleon's momentum space is divided into bins. The time variation of the occupational probability of the states of each bin, is evaluated considering nucleon-nucleon interactions and emission into the continuum, of one nucleon or a cluster of nucleons. Assuming azimuthal symmetry with respect to the incident projectile, then with a simple change of variables, the occupation probability n_i of the states of a given bin i, can be estimated as a function of $n_i(\epsilon, \theta, t)$, where ϵ is the nucleon energy, θ is its direction with respect to the projectile direction, t is the time. The set of quantities $n_i(\epsilon, \theta, t)$ are then calculated in a time differential manner by integrating the set of coupled Boltzmann Master equations, over only a small time interval t to $t + \Delta t$, as a function of the occupation probabilities at the initial time t=0, and the probabilities per time unit of each occurring process. This provides a way of evaluating also the double differential particle spectra emitted in the time interval Δt as well as all the particles emitted on integration over the full time scale. In order to integrate these equations, the bins' occupation probabilities are needed at the initial time t=0, depending on the interaction dynamics of the system [14, 13, 18, 12]. The time-stepped integration above could be used as input into the Monte Carlo calculations to obtain the probability

of a given sequences of events leading to say, exclusive measurements or residue production cross sections. This probability cannot be obtained by simply solving the set of equations, as this would produce quantities averaged over many exit channels. The natural reference frame in the calculation is the centre of mass of the composite system, assumed to be of infinite mass, such that, if the nucleus recoils in the course of particle emissions, the theoretical calculations cannot predict the inclusive measurements in the laboratory frame of reference. This problem is avoided if the differential multiplicity $d^3\hat{M}(\epsilon, \theta, t)$ of a given particle is assumed to be the probability of emitting it with energy ϵ and direction θ in the time interval t to $t + \Delta t$. Using these quantities, the probability of any pre-determined complex event or as a joint probability, can be evaluated [7], allowing for the proper transformation of each emission from the (decaying) composite nucleus centre of mass to the laboratory frame of reference. The model, however, assumes macroscopic properties of the nucleus such as the nucleon radial flow, nuclear density, temperature, mean field effects [7]. Figure 1.2 shows the ratio between the measured and the calculated cross-sections for residue produced in the interaction of 45 A MeV ^{12}C projectile with the natural copper target nuclei [19]. The experimental cross sections measurements are in agreement with the calculations to within a factor of two or less, independent of the residue production yields. The BME theory has been used successfully for incident energies up to 50 A MeV.

Chapter 3 describes some of the existing experimental techniques for studying nuclear interactions, starting with the experimental observables such as angular momentum (section 3.1.1), angular distribution (section 3.1.3), momentum transfer (section 3.1.2), cross section (section 3.1.4) interaction time-scales (section 3.1.6) and their determination. The nucleon interaction time-scales has not been measured directly even though it is used a lot in theoretical calculations. This is followed by the major experimental techniques for measuring the observables i.e. inclusive/exclusive measurements and the conventional radiochemical measurements typical of the present system [20, 21, 22, 23, 24, 25, 26, 27, 28, 29, 30]. These referred sections give an account of the experimental measurements of light and medium mass projectiles over

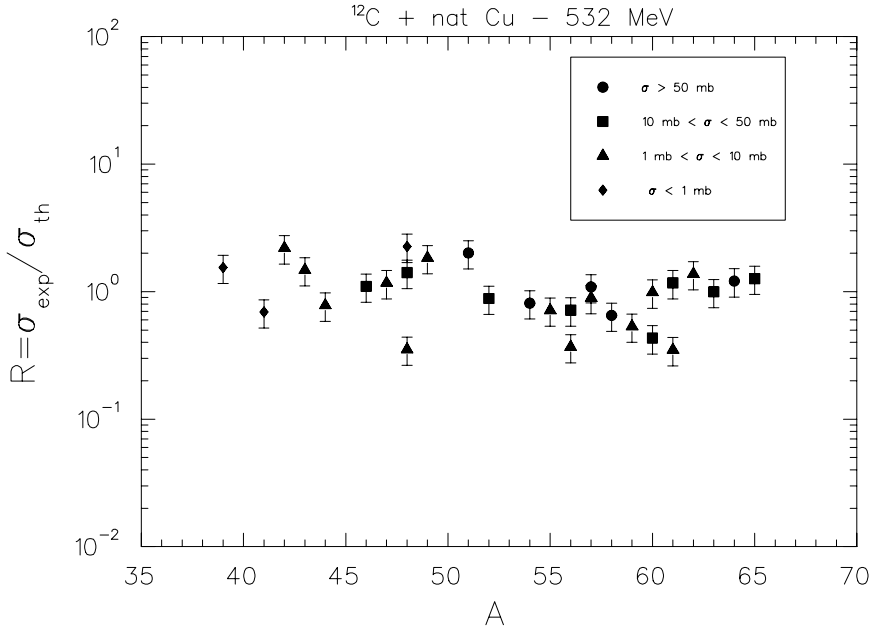


Figure 1.2: The ratio between measured and calculated cross-sections for residue formation, as a function of the residue mass, in the interaction of 45 A MeV ^{12}C with natural copper (from Ref. [16]).

the past decades. The mode of interpretation (e.g. in [31, 32]) of some of these experimental measurements are disputed by recent work done by the collaboration [2]. Despite some individual short-comings, these measurements taken as a whole provide comprehensive information on nuclear interaction mechanisms.

The following observables relating to the present collision system and projectile energy regime, based on over three decades of accumulated experimental measurements, not limited to the collaborations work, are presented in section 3.2.2. In the list of available information are isobaric yields, residue mass distribution and total reaction cross-section, as a function of the projectile mass and/or energy. The collaboration has pointed out some of the discrepancies existing within these studies and suggested alternative ways to overcome them [2]. The isobaric yield measurements were reported to remain essentially unchanged within the projectile mass range ($3 < Z < 10$) for the interactions with the copper target. The maximum in the residue distribution yields peaked at 3-6 nucleons removed from the target whereas the minimum occurred

at A ~25-30 [23], contrary to the work of the collaboration, which has recently shown that there is in fact an abundant production of undetected near-target residues yields [2]. The use of a heavier projectile (Z=10) is reported to have resulted in greater yield of intermediate mass fragments production, construed to mean that the binary fragmentation process is enhanced [33], while the lighter projectiles (Z≤3) produced no mass yield upturn in the distribution of the intermediate mass fragments on the low mass region [34]. The reported V-shaped residue yield distribution, symmetric about the target mass, which vanishes for projectile energies above 25 A MeV [33] is inconsequential, based on the collaboration findings. The average longitudinal momentum expressed as a fraction of the projectile value had been reported to vary inversely with the projectile energy, peaking at ~15-25 A MeV [25, 24, 21, 23] or ~170-220 MeV/c per incident nucleon, which is also largely over-estimated according to the collaboration's work [4]. The measurement of the total reaction cross section through the integration of the mass yield distributions was reported as ~2b, peaking at about 25 A MeV projectile energy [21], while the collaboration has system given a more realistic value of ~3.4b. The collaboration has also accounted for the missing cross section by the mechanism of fast α re-emission and coalescence, in addition to systematic errors [2].

Modern techniques in gamma spectroscopy of heavy ion interactions studies attempt to account for all the produced fragments without any assumptions made for the unobserved yields [35, 36]. This approach if used could shed light on the elusive near-target residue production. The setup needed to widen the scope of the conventional radiochemical approaches, to obtain in-depth residue observable measurements, involves a number of steps listed as:

- In-beam residue production measurements (prompt gamma emissions) for very short-lived nuclei in the nanosecond range using thin or thick targets.
- Off-beam residue production measurements (delayed gamma emissions from isomers) for short-lived nuclei in the millisecond range using thick targets.
- After-beam residue production measurements for long-lived nuclei in the second/minute

range using thick targets.

- Conventional techniques (off-line) for much longer-lived residue production measurements in the days/year range.

The first two measurements above rely on the cyclotron RF time signal for the first pulsed beam burst. The on/off state of the pulsed beam of projectile ions is used to provide the logic signal to discern the prompt from the delayed gamma emissions when taking measurements with a thick target. In the third stage, preferably using a relatively thick target so as to stop most of the residues produced, the non-pulsed is allowed on to the target for few hours only. The data acquisition then starts immediately after the beam stops and continues for up to three days compared to up to six months for the conventional techniques. However, samples are highly radioactive after irradiation and unless special handling procedures are used, time is lost before the actual data acquisition of the sorted stacked foils commence when using the conventional techniques. With a gamma detector array, it is possible to extract the independent residue yields and the relative production cross-sections measurements using a thick target [35, 36]. However, the effective incident projectile energies vary from the true value down to the Coulomb barrier energy, leading to indeterminacy of the actual beam energy. A thin target, on the other hand, gives the extra information of momentum distributions measurement in addition to the relative residue yields.

A highly efficient gamma-ray detector array is used to detect and isolate the gamma emissions from the myriad of reaction residues produced during heavy ion interaction studies. A great deal of spectroscopic information concerning many target-like and projectile-like reaction products has been obtained from this technique [36]. In some cases, the studies conducted have taken advantage of the presence of isomeric states to aid in the identification of the reaction residues. The gamma-rays from low-lying yrast states emitted from nuclei at rest are detected and although many excited nuclei with masses around the projectile and target are produced, the resulting complexity of the spectra is unravelled using gamma-gamma coincidence matrix tech-

niques if the data set has sufficiently high statistics and good energy resolution [36]. For nuclei in which gamma energy emission cascades and intensities are known, this approach is used for precise product identification and relative yield measurements [6]. In favourable situations the mutual excitation of both the target-like and projectile-like nuclei are observed directly through the cross-coincidence of their corresponding gamma emission. The observation of this cross-coincidence provides instant identification of both the outgoing nuclei and establishes the nature of their emission decay process [37]. The approach should be applicable to the experimental conditions where the projectile ions are as light as ^{12}C. However, break-up of the projectile-like fragment partners make it impossible to detect them. Besides, these very light nuclei rarely emit coincident gamma rays within the detectable energy range limited to just 2 MeV in the present experimental setup. Some cross-coincidence measurements have shown that a given target-like fragment is associated in different events with two or more projectile-like fragments in more symmetric collisions, namely the primary complementary partner or its respective daughter product from the subsequent decay through emission of one or more nucleons.

The Doppler Effect phenomena could be an alternative way to study the momentum transferred to target-like fragments via in-beam prompt gamma emission measurements. There are no known records of the application of the technique to the study of residue kinematics in the past. On the contrary, it has commonly been treated as an experimental setback. The Doppler Effect has had a wide application in several techniques for life-time measurements of excited nuclear states, [38] (and Refs. therein). The electromagnetic emission studies relating to interaction mechanisms have, however, been done. The studies covered in-beam and off-line gamma-ray spectroscopy measurement of residues, angular momentum transfer [39, 40], dependence of linear momentum on the impact parameter [41], mass and charge distribution of target-like fragments [42, 43, 44, 40] and projectile-like fragments [42], exotic nuclei [45], residue cross-sections variations (excitation functions) [39, 46, 2], gamma-gamma cross coincidence [47, 48, 49, 6, 50], gamma-particle coincidence [51, 52] and gamma multiplicity measurements [42, 50]. The list goes on, see section 3.2.1. There have been measurements also

involving high energy gamma rays or hard photons not originating from the giant dipole resonance [53, 54, 55, 56, 57, 58]. These are bremsstrahlung emissions from the nucleon-nucleon cascade in the early stage of the nuclear interaction and an ideal tag to investigate the fast-step composite system properties [59, 60]. Because this study focuses on residue kinematics to probe the reaction mechanism, it is therefore a new diagnostic tool and a first use of such a technique. The research therefore develops data analytical procedures which are novel.

The experimental techniques and principle concepts of the present study are covered in detail in chapter 5. This technique requires a 4π gamma detector array of high granularity as well as efficiency at low gamma energies. This is followed by the residue identification through the gamma-gamma coincidence technique, and Doppler broadened and shifted gamma line shape measured as a function of detector angle. An important reason for such a measurement is to gain access to additional information on residue yields, previously inaccessible via the conventional radiochemical techniques. This new technique provides information similar to the application of the high-resolution fragment mass separator combined with inverse kinematics [61, 62]. One may probe peripheral interactions and open up a new avenue of examining more closely the near-target residue yields. The two techniques just mentioned are favourable due to the fact that the momentum transfer in the interaction process could be extremely small to be registered with the conventional techniques. In the former case, one studies the near-stationery residues whereas in latter case it is the vice versa.

Chapter 2

The Physics in the Milano Developed Model

2.1 Nuclear Interaction Models

In general, theoretical models provide useful insight into the physical properties involved in the underlying nuclear interaction processes. A viable comprehensive theoretical model needs to describe all the observables, within reasonable limits and also the general trends in the observables in the simplest way possible. The development of theoretical models has, to a large extent, relied on the development of experimental techniques, which has also depended on the limitations and the availability of the right equipment or experimental setup. There are few models which have been used to describe the majority of the observables (section 3.1) either due to the lack of measurements, or model inadequacy. However, such questions as whether the relaxation of a highly excited nuclear system could ascribed be to statistical, dynamical or hybrid processes remain answered [63, 64]. The application of computer simulations therefore serves to gain useful insights into the physical properties involved in nuclear interaction processes.

This chapter is dedicated to the physics incorporated into the model developed in Milano in order to create the comprehensive theoretical model used to describe the various nuclear interaction processes (see figure 2.1). The majority of the nuclear interaction models incorporate a two-step process in the main simulation code of the de-excitation process of the composite system produced during heavy ion interactions [65, 66, 67, 68, 69], while a single step process is rare [70]. The fast step describes the initial interaction between the nucleon constituents of the target and the projectile nucleus. It occurs in the order 10^{-23} seconds. In the model

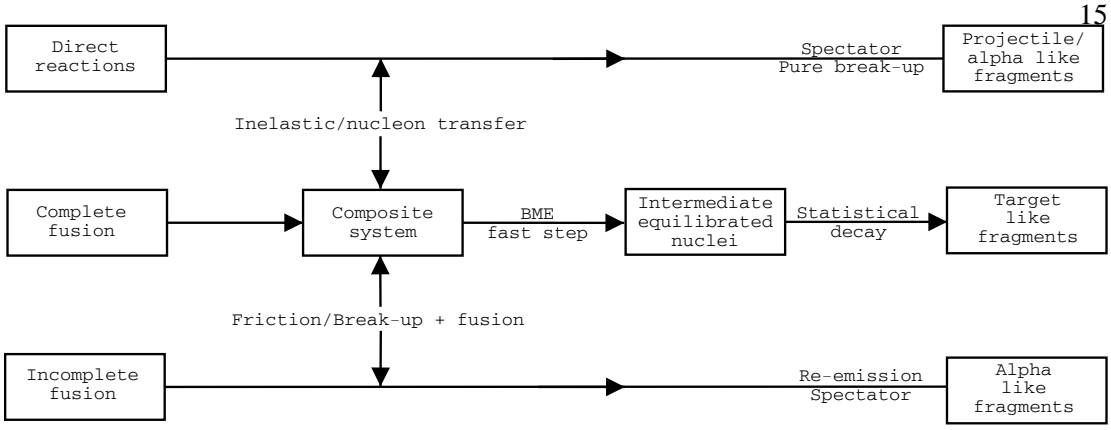


Figure 2.1: Schematic representation for the description of ^{12}C and intermediate mass target nuclei interactions in the comprehensive model developed in Milano.

developed in Milano, it is performed using the Boltzmann Master Equation (BME) approach following the description given in section 2.2. The second de-excitation step of the intermediate equilibrated nucleus produced by the fast step process occurs at time scales typically of the order 10^{-16} to 10^{-18} seconds. This step is simulated using the statistical decay process technique presented briefly in section 2.6. The composite system is produced either in the complete fusion, incomplete fusion, transfer or inelastic projectile interaction with the target. The physics used to simulate each of these interaction processes are different.

The Boltzmann Master equation provides a procedure of tracking the time-dependent characteristics of de-excitation and relaxation of the Fermi gas produced in the first step of the interaction [66, 67, 71] referred here as the composite system. As a microscopic transport model, every nucleon in the system is treated independently. The description of the nucleon collisions is based on the particle-hole principle, which requires that the more energy in the system, the more the particle-hole pairs created. The approach has been applied to interactions over very broad range of composite system excitation energies [7]. The output of each step of the time differential integration of the Boltzmann Master equations could be used as an input for Monte Carlo calculations, thus allowing the evaluation of the probability of particular sequences of events like those observed in an exclusive experiment or those which lead to the formation of

a particular residue in a reaction. This probability cannot be obtained by simply integrating the set of Boltzmann Master equations to the end, as this produces only averaged information over many reaction pathways. The original concepts of the model are first described in section 2.2. The model has since undergone tremendous development to incorporate the features mentioned below (among others) [7, 13, 18, 14]

- Particle and cluster emission, section 2.2.1
- Photon emission, section 2.2.2
- Monte Carlo techniques, section 2.2.3
- Emission angular distribution, section 2.2.4
- Reaction cross-sections, section 2.2.5

While the excitation energy is not evenly distributed among all the particle and hole pairs in the composite system, a lot of emissions into the continuum of the more energetic particles occur. After these emissions, the product formed is the intermediate equilibrated nucleus, described using the statistical decay process presented in section 2.6. The inclusion of the pre-equilibrium emissions during the de-excitation of the excited composite nucleus as described in Refs. [2, 3, 8], allows for the accurate reproduction of the measured cross-sections, the forward recoil range and angular distributions of the residues and the spectra of the copious α-particle production [72].

The model developed in Milano assumes that complete fusion, incomplete fusion, single nucleon transfer and inelastic scattering process makes up the major contribution to the total reaction cross-section for the ^{12}C and ^{16}O induced reactions on intermediate mass target nuclei. The complete fusion cross-section uses the value taken from Ref. [73]. The incomplete fusion processes are governed by the break-up fusion processes [2, 8], covered in sections 2.5 and 2.4. The optimum Q-values leads to the projectile break-up populating key specific channels, which are α-particle channels (two originate from the weakly bound ^{8}Be nucleus) for the case

of ^{12}C nucleus. Similarly, α-particle and ^{12}C or two ^{8}Be (four alphas) channels are mostly populated by the ^{16}O nucleus break-up. The incomplete fusion reactions involve the fusion of these break-up fragments with the target nuclei, with ^{8}Be and α-particle fragments common to both the projectiles, while ^{16}O nucleus has extra ^{12}C channel contribution. Other projectile break-up channels taken into account include ^{5}Li + ^{7}Li, ^{6}Li + ^{6}Li, ^{9}Be + ^{3}He and ^{7}Be + ^{5}He). Shown in figure 2.2 are the cross-sections of the processes, which contribute mainly to the total reaction cross-section in the interaction of ^{12}C with ^{103}Rh. The cross-sections were mostly obtained directly from the analysis of double differential spectra measurements of break-up fragments in the interaction of ^{12}C with ^{93}Nb through scaling [1, 74]. The reaction cross-section as a function used for the projectile incident energy is adopted from Ref. [73] to closely match the experimental value of Ref. [75]. The inelastic scattering cross-section value is obtained from the best-fitting of the experimental production cross-sections. At 33 A MeV incident energies, the value is estimated to be 60% higher than the corresponding pure inelastic scattering process. This has been extracted through extrapolation from the spectra of ^{12}C ions inelastically scattered by the ^{93}Nb nuclei from recent experiment measurements undertaken by the collaboration. For higher incident projectile energies, single nucleon transfer from the projectile to the target could play a significant role [2]. According to the critical angular momentum model description given in section 2.4, incomplete fusion processes are assumed to dominate in windows of angular momentum which increase with decreasing mass of the fusing fragment. The cross-sections corresponding to these angular momentum windows are evaluated following the description given in section 2.4. The energy and angular distribution of the spectator fragment that escapes with minor modification to their energy and the corresponding excitation energy and angular distribution of the excited composite system nucleus produced in the processes, are described as given in section 2.5. This composite system nucleus produced by all the possible fusion combinations, is initially a simple configuration but de-excites to a more complex system by means of nucleon-nucleon interactions (α-nucleon interactions for the case of incomplete fusion) and particle emissions into the continuum. A considerable amount of the initial excitation

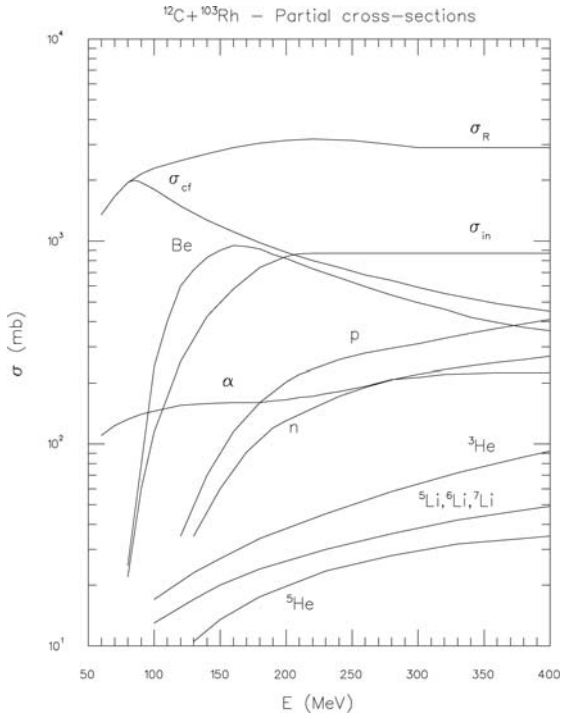


Figure 2.2: The total reaction cross-section and the various contributing reaction mechanisms (cf stands for complete fusion, in stands for inelastic scattering, Be stands for incomplete fusion of a beryllium isotope, α stands for incomplete fusion of one α particle, p stands for proton transfer, n stands for neutron transfer, ^{5,6,7}Li stands for incomplete fusion of a ^{5}Li or a ^{6}Li or a ^{7}Li, ^{3,5}He represents incomplete fusion of a ^{3}He or a ^{5}He) (from Ref. [1]).

energy is consequently lost. The procedure to evaluate the relative probabilities of intra-nucleon cascade and particle emissions follows from the description given in section 2.2. The α-particle re-emission probability in the course of α-nucleon interactions, relies heavily on the geometry of the incomplete fusion process, and is estimated from the experimental measurements [8, 76].

The predicted typical values of excitation energy for the intermediate equilibrated nucleus, for the ^{12}C projectile induced reactions on ^{103}Rh target nuclei, is shown for the combined processes above excluding the inelastic contribution, in the top panel and for each individual contribution and their overall average in the bottom panel of figure 2.3, as a function of the incident energy. The excitation energy distributions for the 33 A MeV incident energy is shown in figure 2.4, as a function of the A MeV of the equilibrated intermediate nucleus. From which

it is observed that the incomplete fusion of α-particle, based on the weighted average, causes the least excitation energy to the composite system. This is due to the fact that the fusing α-particle stands a high chance of being re-emitted with most of its energy intact. The nucleon transfer processes gives the composite system nucleus a much higher excitation energy because high energy nucleons transferred to the target are very unlikely to be re-emitted with most of their energy intact [2]. Most of the parameters used by the model are given in Refs.

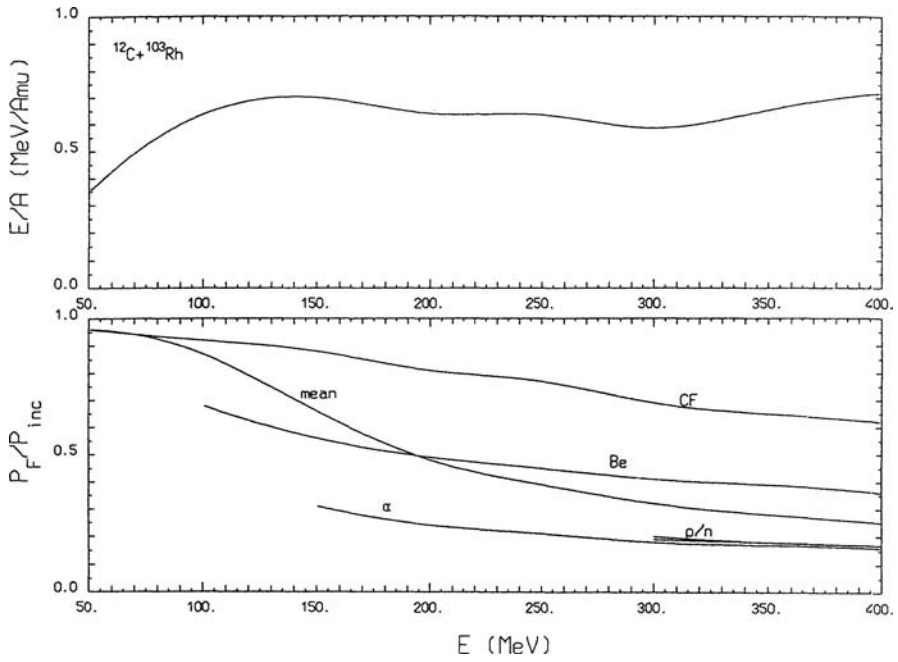


Figure 2.3: Upper panel: Typical model mean excitation energy (in MeV/A) of the intermediate equilibrated nucleus produced in the interaction of the ^{12}C projectile with ^{103}Rh as a function of the incident energy assuming the inelastic contribution. Lower panel: The ratio between the predicted residue linear momentum p_F and the projectile linear momentum p_{inc}. The label 'mean' stands for the average values for all the processes, while CF, Be, α, p and n labels are the values for complete fusion, ^{8}Be and α-particle incomplete fusion, proton and neutron transfer processes, respectively (from Ref. [2]).

[1, 74, 7, 8, 10, 18]. The parameter used for the binding energies is taken from the available experimental values. Otherwise the mass formula of Myers and Swiatecki is applied [2]. The particle inverse cross-sections uses the semi-classical expressions with parameters from optical model calculations, section 2.2.3.

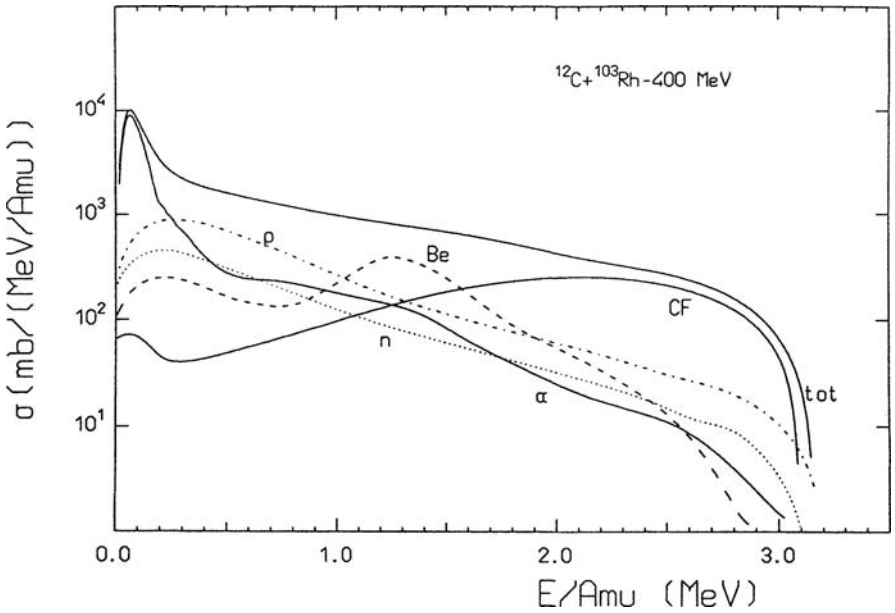


Figure 2.4: The model prediction of the intermediate equilibrated nucleus excitation energy distributions in the interaction of 400 MeV ^{12}C projectile with ^{103}Rh for each of the process and their combined contribution assuming the inelastic process. The label 'tot' is the predicted distribution for the combined processes labelled by CF, Be, α, p and n, for the complete fusion, ^{8}Be and α-particle incomplete fusion, proton and neutron transfer processes, respectively (from Ref. [2]).

2.2 The Theory of Pre-equilibrium Emission

In this theory [66], the nucleus is assumed to be made up of some volume of fermions gas. The state of the residual excited nucleus remaining after the fast cascade is described by the occupational numbers of single-particle nucleon states. The energy levels in the Fermi gas are either occupied by particles or holes. Relaxation of the single-component Fermi gas assumes that it is made up of independent fermions and that the occupational numbers for the single-particle states specify its configuration fully. The equilibrium states of the excited residual nucleus is characterised by the excitation energy and the particle numbers of the residual excited nucleus. The gas is initially confined to translational states with dimensions of the nuclear volume V, with access to the translational states of the laboratory volume Ω. The volume is then adjusted to get the Fermi energy of ϵ_F, with the maximum bound state energy of a neutron

given by $\epsilon_b = \epsilon_F + B$, where B is the binding energy and ϵ_F is the Fermi energy. The gas is assumed to equilibrate within the energy states lying $0 - 2\epsilon_b$. The particles whose energies are above the ϵ_b have access to the laboratory states. Other assumptions made include

- The states interact pair-wise within the nucleus.
- The transition probabilities connecting either two different pairs of states inside or a state inside to a state outside depend on the energy only.
- The transition probabilities vary slowly with energy over energy interval $\Delta\epsilon$.

With these assumptions, the states are characterised by energy bins such that the ϵ_i is the mean energy of the ith bin. The total number of states in the ith bin, g_i, is given by

$$g_i = \int_{\epsilon_i - \Delta\epsilon/2}^{\epsilon_i + \Delta\epsilon/2} \rho(\epsilon) d\epsilon, \qquad 0 \leq \epsilon_i \leq 2\epsilon_b \tag{2.1}$$

for

$$\rho(\epsilon) = 4\pi V (2M)^{3/2} \epsilon^{1/2} / h^3 \tag{2.2}$$

where $\rho(\epsilon)$ is the density of translational states and M is the neutron mass. On the same note, the laboratory states g_i' for the particles escaping from the nucleus, with the total number of states in the i'th bin is given by

$$g_i' = \int_{\epsilon_i' - \Delta\epsilon/2}^{\epsilon_i' + \Delta\epsilon/2} \rho'(\epsilon) d\epsilon, \qquad 0 \leq \epsilon_i' \leq \epsilon_b \tag{2.3}$$

for

$$\rho'(\epsilon) = \left[4\pi\Omega (2M)^{3/2} \epsilon^{1/2} / h^3 \right] \epsilon^{1/2} \tag{2.4}$$

where $\rho'(\epsilon)$ is the density of laboratory translational states. The two quantities, $\rho(\epsilon)$ and $\rho'(\epsilon)$ have a spin degeneracy of two for the fermions incorporated. The occupational number N_i of the ith bin is

$$N_i = n_i g_i \tag{2.5}$$

The set of coupled Master equations used to describe the relaxation of the single-component Fermi gas are given by [66]

$$\begin{aligned}\frac{d\left(n_i g_i\right)}{dt} &= \sum_{jkl} \omega_{kl\to ij} g_k n_k g_l n_l \left(1-n_i\right)\left(1-n_j\right)\left(g_i g_j/\Delta\epsilon\right) \\ &\times\delta\left(\epsilon_i+\epsilon_j-\epsilon_k-\epsilon_l\right) - \sum_{jkl} \omega_{ij\to kl} g_i n_i g_j n_j \left(1-n_k\right) \\ &\times\left(1-n_l\right)\left(g_k g_l/\Delta\epsilon\right)\delta\left(\epsilon_i+\epsilon_j-\epsilon_k-\epsilon_l\right) \\ &-n_i g_i \omega_{i\to i'} g_{i'}\delta\left(\epsilon_i-\epsilon_b-\epsilon_{i'}\right) \end{aligned} \tag{2.6}$$

for all i in the energy range $0 \le \epsilon \le 2\epsilon_b$ and

$$\frac{dN_{i'}}{dt} = n_i g_i \omega_{i\to i'} g_{i'}\delta\left(\epsilon_i-\epsilon_b-\epsilon_{i'}\right) \tag{2.7}$$

for all i' in the energy range $0 \le \epsilon_{i'} \le \epsilon_b$.

where $\omega_{i\to i'}$ is the probability per unit time that a particle in specific state of the ith bin escapes, $\omega_{i\to i'} = 0$ if $\epsilon_i \le \epsilon_b$. The $\omega_{ij\to kl}$ term is the probability per unit time that a particle in a specific one of the states in the kth bin scatters from a particle in another of the states in the lth bin so that the one particle moves to the ith bin, the other to the jth bin. The δ functions ensure that there is energy conservation in these transitions. Pure classical transition probabilities were used, given by

$$\omega_{ij\to kl} = \frac{\sigma_{nn}(\epsilon_i+\epsilon_j)\left[(2/M)(\epsilon_i+\epsilon_j)\right]^{1/2}}{V\sum_{mn}\left[(g_m g_n/\Delta\epsilon)\delta(\epsilon_i+\epsilon_j-\epsilon_m-\epsilon_n)\right]} \tag{2.8}$$

where $\sigma_{nn}(\epsilon)$ is the neutron-neutron scattering cross-section at energy ϵ, whereas, $\omega_{i\to i'}$ are given by

$$\omega_{i\to i'} = \frac{\pi r_0^2 A^{2/3}\left[(2/M)\epsilon_{i'}\right]^{1/2}}{g_i\Omega} \tag{2.9}$$

where $\pi r_0^2 A^{2/3}$ is the geometrical cross-section for the nucleus, A is the original number of nucleons in the gas and r_0 is chosen such that a Fermi gas of A particles in the volume $V = \frac{4}{3}\pi r_0^3 A$ has a Fermi energy level given by ϵ_F. The emission of nucleons before equilibrium leads to a much faster decrease in the excitation energy of the nucleus than in the case of evaporation, thus reducing the number of particles which may be emitted further thus favouring

the production of higher mass residues [77]. With this approach, such mechanisms as multi-fragmentation are inhibited by the fact that the pre-equilibrium process takes away much of the excess excitation energy of the nucleus.

When one is considering the relaxation of a two-component Fermi gas, the nucleus is treated as consisting of independent proton and neutron Fermi gases. This demands that the occupation numbers for the single-particle states of the two gases specifies the internal configuration of the system completely. Equilibration is achieved through the binary nucleon-nucleon cascade initially confined to the translational states within a volume $V = \frac{4}{3} r_0^3 A$ where r_0 = 1.5 Fm and A is the total number of nucleons in the nucleus at time t=0. The Master equations describing the relaxation of the proton Fermi gas in the system are given by [67]

$$\begin{aligned}
\frac{dn_i^P}{dt} &= \sum_{jkl} [\omega^{PP}_{kl\to ij} g_k^P g_l^P g_j^P n_k^P n_l^P (1-n_i^P)(1-n_j^P) \\
&\quad -\omega^{PP}_{ij\to kl} g_i^P g_k^P g_l^P n_i^P n_j^P (1-n_k^P)(1-n_l^P)]\delta(\epsilon_i^P + \epsilon_j^P - \epsilon_l^P - \epsilon_k^P) \\
&\quad + \sum_{jkl} [\omega^{PN}_{kl\to ij} g_k^P g_l^N g_j^N n_l^N n_k^P (1-n_i^P)(1-n_j^N)] \\
&\quad -\omega^{PN}_{ij\to kl} g_j^N g_l^N g_k^P n_i^P n_j^N (1-n_k^P)(1-n_l^N)]\delta(\epsilon_i^P + \epsilon_j^N - \epsilon_l^P - \epsilon_k^N) \\
&\quad -n_i^P \omega^P_{i\to i'} g_{i'}^P \delta(\epsilon_{i'}^P - \epsilon_i^P + \epsilon_f^P + B_P) \qquad (2.10)
\end{aligned}$$

$$\begin{aligned}
\frac{dN_{i'}^P}{dt} &= n_i^P g_i^P \omega^P_{i\to i'} g_{i'}^P \delta(\epsilon_{i'}^P - \epsilon_i^P + \epsilon_f^P + B_P), \\
&\qquad i = 1, \ldots, \epsilon_f^P + E^*, \;\; i', \ldots, E^* - B_p \qquad (2.11)
\end{aligned}$$

where $N_{i'}^P$ is the number of protons escaping with laboratory energy $\epsilon_{i'}^P$, $\omega^P_{i\to i'}$ is the probability per unit time that a proton in a particular state of the ith bin is emitted, B_p is the binding energy of the proton and E^* is the initial excitation energy in the system. With the exception of P, all other terms have the same meaning as given in equation 2.6 and 2.7. Similar, internal transitions typical of those given by equation 2.8 and 2.9 are used, i.e.,

$$\omega^{PP}_{ij\to kl} = \frac{\sigma_{PP}(\epsilon_i^P + \epsilon_j^P)\left[(2/M)(\epsilon_i^P + \epsilon_j^P)\right]^{1/2}}{V \sum'_{mn} \left[(g_m^P g_n^P \delta(\epsilon_i^P + \epsilon_j^P - \epsilon_m^P - \epsilon_n^P)\right]} \qquad (2.12)$$

where $\sigma_{PP}(\epsilon)$ is the corrected proton-proton elastic scattering cross-section at energy ϵ, the σ'_{mn} means summation over those states that are allowed in the scattering process. The only difference between $\omega^{PP}_{ij\to kl}$ and $\omega^{PN}_{ij\to kl}$ is the normalising factor, $\sum'_{mn} g^N_m g^N_n \delta(\epsilon^N_i + \epsilon^N_j - \epsilon^N_m - \epsilon^N_n)$

$$\omega^{PN}_{ij\to kl} = \frac{\sigma_{PN}(\epsilon^P_i + \epsilon^N_j)\left[(2/M)(\epsilon^P_i + \epsilon^N_j)\right]^{1/2}}{V\sum'_{mn}\left[(g^P_m g^N_n \delta(\epsilon^P_i + \epsilon^N_j - \epsilon^P_m - \epsilon^N_n)\right]} \tag{2.13}$$

where $\sigma_{PN}(\epsilon)$ is the proton-neutron scattering cross-section.

The above sets of Master equations are solved numerically using the Runga-Kutta-Gill method and the following solutions obtained for an equilibrated system ($t = \infty$) [67].

$$n^P_i(t=\infty) = \frac{1}{e^{\beta(\epsilon^P_i - \mu_P)} + 1} \tag{2.14}$$

$$n^N_i(t=\infty) = \frac{1}{e^{\beta(\epsilon^N_i - \mu_N)} + 1} \tag{2.15}$$

where $\beta = (kT)^{-1}$ and μ_N and μ_P are the chemical potentials for the neutron and proton gas, respectively, while kT have their usual meaning. These are the expectation values for $n^P_i(t=\infty)$ and $n^N_i(t=\infty)$ for the two-component Fermi gas system.

2.2.1 Particle and Cluster Emission

The model developed in Milano used in this study is an improvement of the description above, with the approximation of orthogonal nucleon collision geometry eliminated while linear momentum and energy conservation has been incorporated. The Master equations for proton gas are given by [14]

$$\begin{aligned}
\frac{d(n_i g_i)^P}{dt} \;=\; & \sum_{jkl}\Big[\omega^{PP}_{kl\to ij} g^P_k n^P_k g^P_l n^P_l (1-n^P_i)(1-n^P_j)\Big(\frac{g^P_i g^P_j}{\Delta\epsilon}\Big)\delta(\epsilon^P_i + \epsilon^P_j - \epsilon^P_k - \epsilon^P_l) \\
& -\omega^{PP}_{ij\to kl} g^P_i n^P_i g^P_j n^P_i (1-n^P_k)(1-n^P_l)\Big(\frac{g^P_k g^P_l}{\Delta\epsilon}\Big)\delta(\epsilon^P_i + \epsilon^P_j - \epsilon^P_k - \epsilon^P_l)\Big] \\
& +\sum_{jkl}\Big[\omega^{PN}_{kl\to ij} g^P_k n^P_k g^N_l n^N_l (1-n^P_i)(1-n^N_j)\Big(\frac{g^P_i g^N_j}{\Delta\epsilon}\Big)\delta(\epsilon^P_i + \epsilon^N_j - \epsilon^P_k - \epsilon^N_l) \\
& -\omega^{PN}_{ij\to kl} g^P_i n^P_i g^N_j n^N_i (1-n^P_k)(1-n^N_l)\Big(\frac{g^P_k g^N_l}{\Delta\epsilon}\Big)\delta(\epsilon^P_i + \epsilon^N_j - \epsilon^P_k - \epsilon^N_l)\Big] \\
& -n^P_i g^P_i \omega^P_{i-i'} g^P_{i'} \delta(\epsilon^P_i + \epsilon^P_F - B^P_i - \epsilon^P_{i'})
\end{aligned} \tag{2.16}$$

where P and N denotes protons and neutron gases, respectively. The emission of proton particles to the continuum are obtained from the integration of the equation

$$\frac{dN_i'^P}{dt} = n_i^P g_i^P \omega_{i-i'}^P g_{i'}^P \delta(\epsilon_i^P + \epsilon_F^P - B_i^P - \epsilon_{i'}^P) \tag{2.17}$$

where N_i' is the number of occupied states in the ith bin. The determination of the total number of particles is typical of equations 2.1 and 2.2 above, given by

$$\begin{aligned} g_i &= \int_{\epsilon_i-\Delta\epsilon/2}^{\epsilon_i+\Delta\epsilon/2} \rho^P(\epsilon) d\epsilon \\ &= \frac{Z}{\epsilon_F^{3/2}}\left[\left[\epsilon_i + \frac{\Delta\epsilon}{2}\right]^{3/2} - \left[\epsilon_i - \frac{\Delta\epsilon}{2}\right]^{3/2}\right] \end{aligned} \tag{2.18}$$

The total number of states for the particles emitted from the nucleus $g_{i'}$, are obtained by substituting the nuclear volume term V with $\rho'(\epsilon)$, equations 2.3 and 2.4. The classical transition probabilities used are typical of equation 2.8 with minor modification

$$\omega_{ij\to lm}^{NN} = \frac{\sigma_{nn}^{NN}(\epsilon_i^N + \epsilon_j^N)\nu_{ij}}{\mathrm{V}\sum_{mn}(g_m^N g_n^N/\Delta\epsilon)\delta(\epsilon_i^N + \epsilon_j^N - \epsilon_m^N - \epsilon_n^N)} \tag{2.19}$$

where $\sigma_{nn}^{NN}(\epsilon)$ is the nucleon-nucleon interaction cross-section at energy ϵ with

$$\nu_{ij} = \left[\frac{2(\epsilon_i^N + \epsilon_j^N)}{\mathrm{M}}\right]^{\frac{1}{2}} \tag{2.20}$$

These transition probabilities assign equal weight to all possible pairs of final states reached by the scattering. The particle emission decay rates are typical of equation 2.9, given by

$$\omega_{i\to i'} = \frac{\sigma_{\mathrm{inv}}\nu_{i'}}{g_i\Omega} \tag{2.21}$$

the approximation made in the calculation of the decay rates and the assumption of equiprobable between the initial and the final particle partition energies, reduces equation 2.6 to [14]

$$\begin{aligned} \frac{d(n_i g_i)^P}{dt} &= \sum_{jkl}\left[\omega_{kl\to ij}^{*,PP} g_k^P n_k^P g_l^P n_l^P (1-n_i^P)(1-n_j^P) - \omega_{ij\to kl}^{*,PP} g_i^P n_i^P g_j^P n_i^P (1-n_k^P)(1-n_l^P)\right] \\ &+ \sum_{jkl}\left[\omega_{kl\to ij}^{*,PN} g_k^P n_k^P g_l^N n_l^N (1-n_i^P)(1-n_j^N) - \omega_{ij\to kl}^{*,PN} g_i^P n_i^P g_j^N n_i^N (1-n_k^P)(1-n_l^N)\right] \\ &- n_i^P g_i^P \omega_{i-i'}^P g_{i'}^P \delta(\epsilon_i^P + \epsilon_F^P - B_i^P - \epsilon_{i'}^P) \end{aligned} \tag{2.22}$$

where, apart from the term P for the proton gas, all other terms remain as given above. The $\omega^*_{ij\to kl}$ term represents the decay rate for the scattering of particles in specific states in bins i and j to bins k and l corresponding to $\omega_{ij\to kl}g_k g_l/\Delta\epsilon$. These set of differential equations have been solved numerically using the Kutta-Merson technique, a modification of the fourth order Runge-Kutta procedure, with flexibility to the bin width energy sizes. The model developed in Milano has used this approach to show that nucleon-nucleon interaction is important in hardening of the nucleon emission spectra [14].

The concept of particle coalescence is given in section 2.3. In the new formulation used in the Milano model, the probability of coalescence of nucleons within a cluster was deduced from a joint probability of finding the nucleons with energy in the range $\epsilon_1(\bar{\epsilon_c})$ to $\epsilon_2(\bar{\epsilon_c})$ with energy distribution $\mathcal{P}(\bar{\epsilon_c}, t)$. The cluster occupation number at time t being given by [13]

$$\mathcal{N}(\bar{\epsilon_c}, t) = \left[\prod_i n_i^P(t)^{\mathcal{P}(\epsilon_i, \bar{\epsilon_c})\Delta\epsilon}\right]^{Z_c}\left[\prod_i n_i^N(t)^{\mathcal{P}(\epsilon_i, \bar{\epsilon_c})\Delta\epsilon}\right]^{N_c} \tag{2.23}$$

where the occupation numbers $n_i^{\pi(\nu}(t)$ for neutron and proton states are obtained by solving the set of Boltzmann equations 2.22, for i in the bin energy range $\epsilon_1(\bar{\epsilon_c})$ to $\epsilon_2(\bar{\epsilon_c})$. If the cluster channel emission energy is $\bar{E'_c}$, the differential decay rate for emission of the cluster c at time t is

$$\frac{d^2N_c(E'_c)}{d\bar{E'_c}t} = \mathcal{N}_c(E'_c/A_c, dt)\frac{\sigma_{\text{inv}}(\bar{E'_c})v_{\text{rel}}}{\Omega}\rho(\bar{E'_c}) \tag{2.24}$$

where $\sigma_{\text{inv}}(\bar{E'_c})$ is the inverse process cross-section, v_{rel} is the relative velocity of the cluster and

$$\rho(\bar{E'_c}) = (2i_c + 1)\frac{2^{5/2}\pi\Omega M_c^{3/2}}{h^3}\bar{E'_c}^{1/2} \tag{2.25}$$

is the cluster density of state, with i_c and $M_c \approx A_c m$ being the spin and the mass of the cluster.

The depletion term for the emission of clusters is given by

$$\frac{dD^P(\epsilon_i)}{dt} = \sum_c \sum_{i_c=i_{1c}}^{i_c=i_{2c}} \int Z_c\mathcal{P}(\epsilon_i, \bar{\epsilon_c})\Delta\epsilon\frac{d^2N_c(E_{c'})}{dE_{c'}dt}dE_{c'} \tag{2.26}$$

where Z_c is the cluster of protons gas, $\mathcal{P}(\epsilon_i, \bar{\epsilon_c})$ is the energy distribution of the cluster particles, N_c is the number of clusters emitted per unit energy E_c and t is the unit time from the principle

of detailed balance, in which

$$\frac{d^2N_c(E_{c'})}{dE_{c'}dt}dE_{c'} = \mathcal{R}_c\mathcal{N}_c(\bar{\epsilon}, t)\frac{\sigma_{\text{inv}}(E_{c'})v_{c'}}{\Omega}\rho(E_{c'}) \tag{2.27}$$

where $\mathcal{R}_c$ is the survival factor, $\mathcal{N}_c(\bar{\epsilon}, t)$ is the cluster occupation number, σ_{inv} is the inverse cross-section, $v_{c'}$ is the cluster residual nucleus velocity, Ω is an arbitrary volume and $\rho(E_{c'})$ is the density of the cluster states. The energy of the cluster outside the nucleus is given by

$$E'_c = A_c(\bar{\epsilon} - \epsilon_F + \epsilon_{c_F}) + Q_c \tag{2.28}$$

where A_c is the number of nucleons in the cluster, $\bar{\epsilon}$ is the kinetic energy per nucleon, ϵ_F is the Fermi energy and ϵ_{c_F} and Q_c are the Fermi energy and the separation energy of the cluster, respectively.

The differential decay rates is evaluated for discrete values energy E'_c varying with $A_c\Delta\epsilon$, obtain from interpolation function $d^2N_{c,\text{int}}(\bar{E'_c})/d\bar{E'_c}dt$ The decay rate for emission of a cluster c with energy in the range $\bar{E'_c} - A_c\Delta\epsilon/2$ to $\bar{E'_c} + A_c\Delta\epsilon/2$ is given by

$$\frac{dN^*_c(\bar{E'_c})}{dt} = \mathcal{R}_c\int_{\bar{E'_c}-A_c\Delta\epsilon/2}^{\bar{E'_c}+A_c\Delta\epsilon/2}\frac{d^2N_{c,\text{int}}(\bar{E'_c})}{dE'_cdt}d\bar{E'_c} \tag{2.29}$$

2.2.2 Photon Emission

In the model, a generalisation has been made in order for it to evaluate the multiplicity distribution of the photons produced in incoherent $p-n$ bremsstrahlung processes in the course of the nucleon-nucleon cascade. Photon emission is incorporated into the decay rates $\omega^*_{ij\to kl}$ given in the previous section for a proton scattering in a specific state within bin $j(i)$ with a neutron in a specific state within bin $i(j)$ to states in bins k and l followed by the emission of a photon of energy ϵ_γ leading to $\omega^*_{ij\to kl\gamma}$. The conservation of energy requirement means that

$$\epsilon_i + \epsilon_j = \epsilon_k + \epsilon_l + \epsilon_\gamma \tag{2.30}$$

because of the fact that

$$\omega^*_{ij\to kl\gamma} << \omega^*_{ij\to kl}, \omega_{i\to i'} \tag{2.31}$$

where all terms have their previous meanings. Assuming that the occupation numbers is given by equation 2.22, and that the photon multiplicities are given by [15]

$$\frac{dM(\epsilon_\gamma)}{d\epsilon_\gamma} = \int_0^\infty \sum_{i,j,k,l} \omega^*_{ij\to kl\gamma} n_i^P g_i^P n_j^N g_j^N \left(1 - n_l^P\right)\left(1 - n_m^N\right) dt \tag{2.32}$$

The photon spectra in inclusive measurements are expressed by

$$\frac{d\sigma(\epsilon_\gamma)}{d\epsilon_\gamma} = \sigma_R \frac{dM(\epsilon_\gamma)}{d\epsilon_\gamma} \tag{2.33}$$

with the reaction cross-section σ_R given by

$$\sigma_R = 2\pi \int_0^{R_p+R_T} \frac{3S(b)}{4\pi R^3} b db \tag{2.34}$$

where $R_p = r_0 A_p^{1/3}$ and $R_T = r_0 A_T^{1/3}$ are the projectile and target radii, respectively, while r_0 is the usual constant, A_p is the projectile mass, A_T is the target mass, $S(b)$ is the overlap volume and b is the impact parameter.

2.2.3 The BME Monte Carlo Technique

Integration of the sets of the coupled Master equations simply give the average emission multiplicity, the inclusive spectra of the emitted particles and photons averaged over many possible sequences of events. These include angle-integrated particle spectra and excitation functions. In order to get more detailed information, a new approach was used in the model based on the fact that in the limit of very short time intervals Δt, the multiplicity of particle emission in the time interval Δt coincides with their emission probability. Consequently, the probability of a particular sequence of events occurring in a much longer time interval could be reduced to a continuous probability calculation of a sequence of events that occur in the small time intervals using the Monte Carlo technique [18]. This is the generalized Monte Carlo - BME approach, which was shown to give good agreement with exclusive measurements [12].

The relaxation process of the two component nucleus has been presented in section 2.2, described by the Master equations for the proton gas by [7]

$$\frac{d(n_i g_i)^P}{dt} = \sum_{jlm} \Big[\omega^{PP}_{lm\to ij} g_l^P n_l^P g_m^P n_m^P (1 - n_i^P)(1 - n_j^P)$$

$$
\begin{aligned}
&-\omega^{PP}_{ij\to lm} g_i^P n_i^P g_j^P n_i^P (1-n_l^P)(1-n_m^P)\Big] \\
&+\sum_{jlm}\Big[\omega^{PN}_{lm\to ij} g_l^P n_l^P g_m^N n_m^N (1-n_i^P)(1-n_j^N) \\
&-\omega^{PN}_{ij\to lm} g_i^P n_i^P g_j^N n_i^N (1-n_l^P)(1-n_m^N)\Big] \\
&-n_i^P g_i^P \omega_{i\to i'} g_{i'}^P \delta(\epsilon_i^P - \epsilon_F^P - B_i^P - \epsilon_{i'}^P) - \frac{dD_i^P}{dt}
\end{aligned} \tag{2.35}
$$

where all symbols remain as given previously. The depletion rate dD_i^P/dt accounts for the emission of particles as nucleons or clusters. The proton multiplicity spectrum in the time interval dt from bin i is given by

$$
\frac{dn_i^C}{d\epsilon'} = -n_i^P g_i^P \omega_{i\to i'} g_{i'}^P \delta(\epsilon_i^P - \epsilon_F^P - B_i^P - \epsilon_{i'}^P) dt \tag{2.36}
$$

with the decay rates for emission of particle given by

$$
\omega_{i\to i'} = \frac{\sigma_{\text{inv}} \nu_{i'}}{g_i \Omega} \tag{2.37}
$$

where σ_{inv} is the inverse cross-section and $\nu_{i'}$ is the velocity of particle emission. The Ω term has its previous meaning which cancels an equivalent term in the $g_{i'}$ expression. The emission of neutrons and clusters uses the same expression as given in equation 2.37. The decrease in the neutron inverse cross-section with energy in the fast step process is adequately described by the expression [2]

$$
\sigma_{\text{inv}} = \frac{A}{a\sqrt{E_{\text{ch}}} + b} \tag{2.38}
$$

where E_{ch} is the neutron channel energy in MeV and the parameters A, a, b are obtained by fitting the cross-sections values of the optical model calculations.

2.2.4 BME Theory of Angular Distribution

This approach uses the nucleon momentum distribution instead of the their energy distribution in the same set of Master equations given in 2.35. The differential multiplicity of the particles emitted with energy E' in the time interval dt and angle θ is given by [12]

$$
\frac{d^3\mathcal{N}'(E',\theta,t)}{dE'd\theta dt} = R\mathcal{N}(\epsilon,\theta,t)\frac{\sigma_{\text{inv}}\nu'}{V'}\rho(E',\theta) \tag{2.39}
$$

where E' is the particle emission energy, $\mathcal{N}(\epsilon, \theta, t)$ is the occupation probability of the states inside the excited nucleus and

$$\rho(E', \theta) = \frac{\sin\theta}{2}\rho(E') \tag{2.40}$$

where $\rho(E')$ is the density of particle states. The measured multiplicities is then given by

$$\frac{d^2M}{dE'd\Omega} = \int_0^{t^*} \frac{1}{2\pi\sin\theta}\frac{d^3\mathcal{N}'(E', \theta, t)}{dE'd\theta dt}dt \tag{2.41}$$

where t^* is the time when the energetic particle emission elapses. For nucleons, $\mathcal{N}(\epsilon, \theta, t)$ gives the values of the bin occupation numbers in n_i, equation 2.35. For clusters of energy E_c and angle θ_c in the nucleus,

$$\mathcal{N}(\epsilon_c, \theta_c, t) = \prod_i (n_i^{\pi})^{P_i(E_c,\theta_c)Z_c} \cdot \prod_i (n_i^{\nu})^{P_i(E_c,\theta_c)N_c} \tag{2.42}$$

where the index i covers all bins holding the nucleons in the cluster, $P_i(E_c, \theta_c)$ is the fraction of bin i in the Fermi sphere, Z_c and N_c are the numbers of protons and neutrons in the cluster, respectively. For Q_c equal to the cluster emission and $A_c = N_c + Z_c$,

$$E'_c = E_c + Q_c - A_c(\epsilon_F - \epsilon_{Fc}) \tag{2.43}$$

where ϵ_F and ϵ_{Fc} are the nucleus and cluster Fermi energies, respectively.

The depletion term in equation 2.35 is therefore given by

$$\frac{dD_i^P}{dt} = \sum_c \int\int P_i(E_c, \theta_c)Z_c\frac{d^3\mathcal{N}'(E'_c, \theta_c, t)}{dE'_c d\theta_c dt}dE_c d\theta_c \tag{2.44}$$

where the summation covers all possible clusters while the integrals covers all possible angles and energies of the clusters containing a nucleon in bin i.

2.2.5 The BME Theory of Reaction Cross Sections

The model uses as input the partial differential multiplicities of the particles emitted in the course of nucleon-nucleon cascade using the generalised Monte Carlo technique described

in the previous section 2.2.4. By nature of the azimuthal symmetry of the nuclear collision processes, for a particle ν [7]

$$\frac{d^2\mathcal{N}'_\nu(E_\nu,\theta,t)}{dE_\nu d\theta} = \int_0^t R\mathcal{N}_\nu(\epsilon_\nu,\theta,t')\frac{\sigma_{\mathrm{inv},\nu}\nu_\nu}{V}\rho(E_\nu,\theta)dt' \tag{2.45}$$

where t is the time to emission and $\mathcal{N}_\nu(\epsilon_\nu,\theta,\mathrm{t})$ is occupation probability of the states of particle in the excited nucleus, ν_ν is the relative velocity between the particle, the rest of the terms remain unchanged.

For nucleons, $\mathcal{N}_\nu(\epsilon,\theta,t)$ is the occupation numbers $n_i(\epsilon,\theta,t)$ of momentum space intervals with volume $V_p \propto \Delta\epsilon\Delta p_z$, for given values of energy and linear momentum in the incident projectile direction. These occupation numbers are evaluated by solving the Master equations given for a proton gas by equation 2.35. The $\mathcal{N}_\nu(\epsilon_\nu,\theta,t)$ term for cluster emissions, in equation 2.45, is a function of the occupation numbers $n_i(\epsilon_\nu,\theta,t)$ of its constituents nucleons [13]. The procedure is generalised such that the probability of emission of the particle in the interval Δt about the time t_i is given by [7]

$$\frac{d^2\mathcal{N}'_\nu(E_\nu,\theta,\Delta t_i)}{dE_\nu d\theta} = \frac{d^2\mathcal{N}'_\nu(E_\nu,\theta,t_i+\Delta t_i)}{dE_\nu d\theta} - \frac{d^2\mathcal{N}'_\nu(E_\nu,\theta,t_i)}{dE_\nu d\theta} \tag{2.46}$$

The differential multiplicities given by equation 2.46 are stored at time intervals corresponding to a constant increment ΔM of the multiplicity of all the emitted particles integrated over the energy and the solid angle. The emission probability of the particle is set by the integrated multiplicity distribution. The energy and the direction of the particle emitted are selected based on the normalised double differential multiplicity and transformed into the laboratory system. The final output of a single cascade is the cross-section of all exit channels, their energy and emission angles, the residue charge, mass, velocity and its direction. The calculations of this nature allow a detailed test of the model assumptions but in practice all the processes require enormous computational resources.

2.3 The Coalescence Model

There are different perspectives of the coalescence models [78], based on the heavy ion or thermal model [79, 80, 81] and those based on the nucleon or snow-ball model [82, 83]. The approach used in the model developed in Milano is based on the former case with a new formulation which eliminates the assumption of the momentum distribution of the coalescing nucleons and the effect of emitting these clusters on the evolution of the excited composite system. In the original model, it was assumed that complex particles are formed by the coalescence of nucleons sharing the same volume element of momentum space. The radius P_0 with which coalescence occurs is the only free parameter in the expression. The probability P for getting a primary nucleon in the coalescence volume centred at a momentum per nucleon $\mathbf{P}$, is the product of this volume with the single nucleon momentum density

$$P = \frac{4\pi}{3} P_0^3 \frac{1}{\langle m \rangle} \frac{d^3N(\mathbf{P})}{m dp^3} \tag{2.47}$$

where $d^3N(\mathbf{P})/mdp^3$ is the differential nucleon multiplicity and $\langle m \rangle$ is the average nucleon multiplicity. Assuming a binomial distribution for $\langle m \rangle$ and a Poisson distribution for the multiplicities, the average value to obtain N neutrons and Z protons in the coalescence sphere is given by

$$\langle P(N,Z) \rangle = \frac{(\langle m \rangle_Z P_Z)^Z}{Z!} \frac{(\langle m \rangle_N P_N)^N}{N!} \tag{2.48}$$

assuming that the probabilities for obtaining neutrons or protons are independent. The $\langle P(N,Z) \rangle$ therefore represents the probability of forming a composite particle with momentum per nucleon given by $\mathbf{P}$. The neutron distribution is assumed to be similar to that of the proton weighted by the N/Z ratio of the composite system

$$\frac{d^3N(0,1)}{dp^3} = \frac{N_t + N_p}{Z_t + Z_p} \frac{dp^3N(1,0)}{dp^3} \tag{2.49}$$

The substitution of equations 2.47 and 2.49 in 2.48 and division by the coalescence volume, leads to the composite particle momentum distribution for relativistic energies [79].

$$\frac{d^3N(Z,N)}{dp^3} = \left(\frac{N_t + N_p}{Z_t + Z_p} \right)^N \frac{1}{N!Z!} \left(\frac{4\pi}{3} P_0^3 \right)^{A-1} \left[\frac{d^3N(0,1)}{dp^3} \right]^A \tag{2.50}$$

When the coalescence occurs in the proximity of the nuclear surface, the energy balance for the cluster of charge Z and mass A becomes

$$\frac{p_A^2}{2mA} = \frac{p_{A_0^2}}{2mA} + ZE_c \tag{2.51}$$

where E_c is the Coulomb energy per unit charge of the composite particle, p_{A_0} is the momentum at the nuclear surface, and p_A is momentum of particle in the laboratory frame. Taking equation 2.51 and 2.50 with some transformations, it is shown that the coalescence relation valid within the proximity of the nuclear Coulomb field is found to be [84, 79].

$$\frac{d^2N(Z,N,E_A)}{dE_A d\Omega} = \left(\frac{N_t + N_p}{Z_t + Z_p}\right)^N \frac{A^{-1}}{N!Z!} \left(\frac{\frac{4\pi}{3}P_0^3}{[2m^3(E-E_c)]^{1/2}}\right)^{A-1} \left[\frac{d^3N(0,1,E)}{dEd\Omega}\right]^A \tag{2.52}$$

with Ω having its usual meaning.

2.4 Sum Rule Model and Limitation of Complete Fusion

The main mechanism leading to the incomplete fusion is the break-up of the projectile followed by the transfer to the target of one or two of the α-particles or just a nucleon [2, 3, 8]. The incomplete fusion cross-sections uses the generalization of the critical distance model [44, 85, 86] with the assumption that the various transfer processes dominate in windows of angular momentum whose magnitudes increase as the fusing fragment mass decreases. According to phase-space arguments, the reaction probabilities via the partial equilibrated systems for all exit channels i are given by [86]

$$p(i) = \exp\left\{\frac{\left(Q_{\rm gs}(i) - Q_C(i)\right)}{T}\right\} \tag{2.53}$$

where T is the effective temperature, $Q_{\rm gs}$ is the ground state Q-value, and Q_C is the change in the Coulomb interaction energy due to the charge transfer process. From parameterisation,

$$Q_C = q_C\left(Z_1^f Z_2^f - Z_1^g Z_2^g\right)e^2 \tag{2.54}$$

where $Z_1^g Z_2^g$ and $Z_1^f Z_2^f$ are the atomic numbers of the constituents of the di-nuclear system before and after the transfer of charge. The entrance channel angular momentum limitations constrains

the reaction probabilities, such that for each reaction channel i, the critical angular momentum, l_{cr}, is given by

$$l_{\text{lim}}(i) = \frac{A_p}{m_{cf}} \times l_{\text{cr}}(m_{cf}) \tag{2.55}$$

where A_p is the projectile mass, m_{cf} is captured fragment mass while l_{cr} is evaluated by [87]

$$\left(l_{cr} + \frac{1}{2}\right)^2 = \frac{\mu(C_1 + C_2)^3}{\hbar^2}\left[4\pi\gamma\frac{C_1C_2}{C_1 + C_2} - \frac{Z_1Z_2e^2}{(C_1 + C_2)^2}\right] \tag{2.56}$$

for C_1 and C_2 equal to the half-density radii while γ is the surface-tension coefficient. Assuming a smooth cut-off in the distribution of the transmission coefficients then

$$T_l(i) = \left[1 + \exp\left(\frac{l - l_{\text{lim}}(i)}{\Delta_l}\right)\right]^{-1} \tag{2.57}$$

Equations 2.53 and 2.57 combines to produce the sum rule model of incomplete fusion

$$N_l \sum_i T_l(i) \exp\left(\frac{Q_g(i) - Q_C(i)}{T}\right) = 1 \tag{2.58}$$

provided i consists of all the possible exit channels. The absolute cross-sections for each channel, applying the normalisation constant N_l given by equation 2.58 result in

$$\sigma(i) = \pi\lambda\!\!\!^{-2} \sum_{l=0}^{l\text{max}} (2l + 1)N_lT_l(i) \exp\left[\frac{Q_{\text{gs}}(i) - Q_C(i)}{T}\right] \tag{2.59}$$

where l_{max} is the maximum l for which the two colliding nuclei achieve a total attractive nucleus-nucleus potential or when the distance of closest approach is smaller than the sum of the half-density radii of the two systems. For a ^{12}C projectile, if the angular momentum window of the projectile L_i falls in the ranges $L_i \leq L_{cf}$, $L_{cf} \leq L_{Be}$ and $L_{Be} \leq L_\alpha$ then complete fusion of ^{12}C, incomplete fusion of ^{8}Be and α prevails. The cross-sections corresponding to these angular momentum windows have been given by [2]

$$\sigma \approx \pi\lambda\!\!\!^{-} \sum_{L=L_i}^{L_{i+1}} (2L + 1) \approx \pi\lambda\!\!\!^{-2}(L_{i+1}^2 - L_i^2) \tag{2.60}$$

where L_i and L_{i+1} are the extreme cases of angular momentum windows for the ith channel. Typical values for the incident ^{12}C projectile nucleus are in the range of (0-50)$\hbar$ for complete

fusion, (51-71)$\hbar$ for ^{8}Be incomplete fusion, (72-113)$\hbar$ for α-particle incomplete fusion and (114-140)$\hbar$ for proton and neutron transfer processes. Similarly, for the^{16}O projectile nucleus, complete fusion dominate in the range of (0-57)$\hbar$, above which both the^{12}C and ^{8}Be incomplete fusions dominates. The fusion of ^{12}C fragment, taking into account the break-up Q-value, is assumed to be almost three times more likely than that of the^{8}Be nucleus. Above 75$\hbar$ and 106$\hbar$, respectively, ^{12}C and ^{8}Be fusion process are limited whereas incomplete fusion of α-particle occurs above 76$\hbar$ [2].

The above model when used to describe the limitations on complete fusion with the sharp cut-off approximation, the fusion cross-section is given by [88]

$$\sigma_{\text{fuse}} = \pi\lambda\!\!\!^{-2} \sum_{L=0}^{L_c} (2L+1) \approx \pi\lambda\!\!\!^{-2} L_c(E)^2 \tag{2.61}$$

where E is the centre of mass energy of the collision system and L_c is the critical angular momentum for the complete fusion. The classical cross-section for obtaining the critical distance of approach R_c is given by

$$\sigma = \pi R_c^2 \left(1 - \frac{V(R_c)}{E}\right) \tag{2.62}$$

where $V(R_c)$ is the nuclear potential. Assuming that

$$\sigma_{\text{fuse}} = \pi\lambda\!\!\!^{-2} \sum_{L=0}^{\infty} (2L+1) T_L P_L \tag{2.63}$$

where T_L is the penetration probability through the interaction barrier and P_L is the probability that fusion occur, assuming above the barrier. T_L is approximated by the penetration factor of a parabolic barrier with frequency $\hbar\omega_L$, whereas, P_L uses the sharp cut-off model i.e. $P_L = 1$ for $L \leq L_c$ and $P_L = 0$ for $L > L_c$. When the frequencies $\hbar\omega_L$ and the position of the interaction barrier R_{Bl} are approximated by constant values of $\hbar\omega$ and R_B, respectively, after which the summation is substituted in equation 2.63, followed by integration to produce

$$\sigma_{\text{fuse}} = \frac{\hbar\omega}{2} R_B^2 \frac{1}{E} \ln \frac{1 + \exp\{2\pi[E - V(R_B)]/\hbar\omega\}}{1 + \exp\left(2\pi\{E - V(R_B) - (R_c/R_B)^2[E - V(R_c)]\}/\hbar\omega\right)} \tag{2.64}$$

which is the expression for the fusion cross-section as a function of the incident projectile energy and possess both the effect of the fusion barrier and the critical distance of approach.

2.4.1 Alpha-like Particle Re-emission

For incomplete fusion, the re-emission into the continuum of the fusing α-particle, with a large fraction of its initial energy, is especially important. The evaluation of this contribution was found to be complicated by fact that the interaction tends to be highly dependent on the geometry of the incomplete fusion process, which occurs at large impact parameters. Consequently, the process involves the low density region of the target nuclei. To simulate the α-nucleon interaction in the peripheral nuclear region, the double differential cross sections of the re-emitted α using the procedure described in [89], which uses a local density approximation, reduced values of the nucleon and the α particle Fermi energy. The predicted angular distribution of the α after a nucleon interaction is given by [3]

$$\frac{d^2\sigma}{dEd\Omega} = ce^{-\theta/\Delta\theta} \tag{2.65}$$

where $\Delta\theta = 2\pi/k\Delta R$, k is the α wave number and ΔR is the thickness of the nuclear surface region where the α -nucleon collision takes place. The angular distribution of the α particle after a certain number of collisions is determined by the Monte Carlo procedure with the assumption that each collision, represented by equation 2.65, gives the angular distribution with respect to its direction prior to collision. The values use for the case of ^{12}C projectile are 0.5 and 0.8, for the ^{8}Be and α-particle incomplete fusion process, respectively. For the case of ^{16}O projectile induced reactions the probabilities of α-particle re-emission are 0.4, 0.5 and 0.95, for ^{12}C, ^{8}Be and α-particle incomplete fusion process, respectively. These values are obtained by analysing the tails of the excitation functions for reactions which incomplete fusion processes are assumed to contribute significantly and also the excitation functions for the near-target residue yields [2].

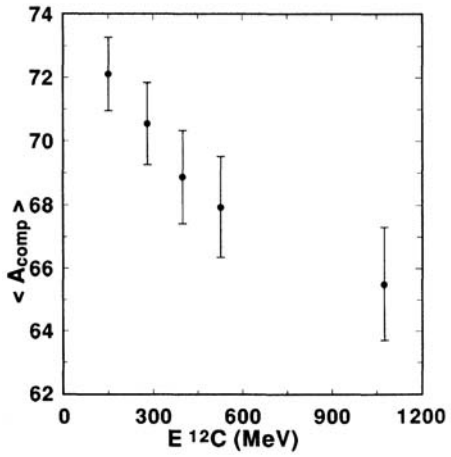
2.4.2 Classical View of the Momentum Transfer Process

In the classical view, the interpretation of the longitudinal velocity $v_{\parallel}$ may assume that the initial interaction involving incomplete fusion of incident projectile leads to the spectator

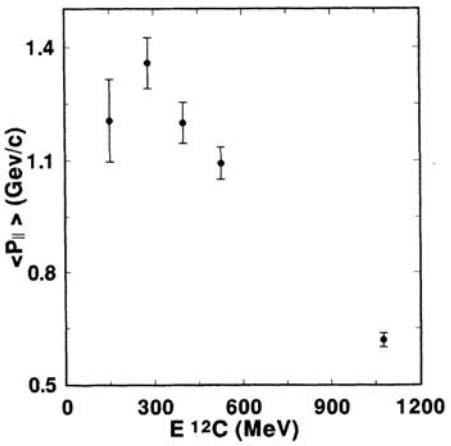
fragment of mass Δm escaping at 0°. The magnitude of Δm is estimated by [23]

$$\frac{v_{\parallel}}{v_{\mathrm{cn}}} = \frac{A_p - \Delta m}{A_p} \tag{2.66}$$

where A_p is the projectile mass. If Δm is known, the mass of the composite system A_{com} can be evaluated. The variation in $\langle A_{\mathrm{com}} \rangle$ with the incident projectile energy is shown in figure 2.5(a). At the lowest projectile energy, the average number of about 8 nucleons is transferred to the



(a) The incident energy E(MeV) ^{12}C projectile dependence of the mean mass $\langle A_{\mathrm{com}} \rangle$ of the composite system nuclei.



(b) The incident energy E(MeV) ^{12}C projectile dependence of the mean linear momentum transfer.

Figure 2.5: Some composite system observables (from Ref. [23]).

target nuclei. This number decreases linearly with increasing incident energy up to about 2 for the highest projectile energy. The drop shows the increasingly important role of the incomplete fusion process the higher the incident energy. The $v_{\parallel}$ and A_{com} product is the linear momentum transferred to the composite system by the projectile nucleus. Assuming that the mass of the emitted particles decrease proportional to the velocity, for $\Delta m = 4$ and 90% of the incident velocity for the emitted fragment, an error of about 3% in the longitudinal momentum transfer is obtained. Assuming further that the velocity spectrum of the evaporation residue is Gaussian centred about $v_{\parallel} = v_R \cos\theta$, where v_R is the velocity of the composite system and θ is the

laboratory angle of detection, then [23].

$$\frac{P_{\parallel}}{P_{\mathrm{cn}}} = \rho \frac{A_T}{A_T + (1-\rho)A_p} \tag{2.67}$$

where A_T is the mass of the target and $\rho = v_R/v_{\mathrm{cn}}$. The difference in the momentum transfer for the emitted fragment at angles θ° and 0° is evaluated using simple kinematics. For small Δm ($\approx$2), the difference is less than 1% for emission angles 10° to 45°, for ($\Delta m \approx$6) the difference goes up to 2-15% for the same angular ranges. For large masses ($\Delta m \approx$10), the difference is 2-68% for emission angles 2.5° to 20°. This shows that the calculation of momentum using the assumptions leads to underestimated values for large angle emission of large masses.

When a fraction of the projectile escapes, the momentum transfer to the composite nucleus by the fragment mass Δm causes it to recoil with the non-relativistic velocity given by

$$\beta_T \approx \left(\frac{\Delta m}{A_T + \Delta m}\right) \sqrt{\left(\frac{2E_P}{931.5A_p}\right)} \tag{2.68}$$

where β_T is the velocity in units of c, E_P is the projectile energy in MeV, A_T and A_p are the masses in atomic mass units of the target and the projectile, respectively. The energy E_T of the target-like residue is given by

$$E_T \approx 465.75 A_R \beta_T^2 \tag{2.69}$$

where A_R is the mass of the residue. The velocity of which may be different from that of the composite nucleus due to the emission of particle process. Complete transfer of momentum for the case of the present study, 400 MeV ^{12}C + ^{63}Cu, yields β_{cn} of 0.0428 while for a single nucleon transfer gives β of 0.0042. For this system, fractional momentum transfer $\beta_T/\beta_{\mathrm{cn}}$ is approximately given by $23.36\beta_T$,where β_{cn} is velocity for complete transfer of projectile momentum. Equation 2.68 assumes pure kinematics collisions, with no energy going to other degrees of freedom. By measuring the product residues β_T, the value of Δm transferred could be inferred assuming that no nucleon exchange occurs between the projectile and target.

2.5 The Projectile Break-up

It has been assumed in the model developed in Milano that before break-up, the incident projectile undergoes varying degree of energy dissipation process in the target nucleus field leading to the excitation of the target's nucleons, with possible break-up or nucleon transfer. The energy dissipation process could lead to considerable change of the projectile's properties like trajectory and momentum. To a first approximation, the trajectory of the surviving projectile nuclei is not affected even after a significant energy loss has occurred. The energy transformation is assumed to be accompanied by no mass transfer, and no loss of the incident projectile flux, except for the case of break-up and mass transfer. Other assumption made includes a constant energy loss per unit length $dE_l/dx = 1/k$, a constant break-up and mass transfer probability k' per unit length, such that the incident flux $\Phi(E_l)$ after a total energy loss of E_l, is given by [11]

$$\Phi(E_l) = \Phi_\circ \exp(-kk'E_l) \tag{2.70}$$

where $\Phi_\circ$ is the incident flux of projectile nuclei. With the assuming that the incident projectile, p, is slowed down by the Coulomb barrier of the target nucleus before its subsequent break-up, the remaining part of the of the incident energy E_p is shared by the composite system produced and the spectator fragment, according to the Serber approximation [77]

$$\frac{d^2\sigma}{dE_a d\Omega_a} \approx \frac{\sqrt{E_a E_b}}{\left(2\mu B_p + 2A_a^2 E_p/A_p + 2A_a E_a - 4\sqrt{A_a^3/A_p}\sqrt{E_p E_a \cos\theta}\right)^2} \tag{2.71}$$

where a and b denotes the spectator and fused fragment parameters, respectively. E_a is the kinetic energy, E_b is the kinetic energy, B_p is the binding energy of a and b in the projectile nucleus, μ is the reduced mass of the $a+b$ system, A_p, A_a and A_b are the masses for the projectile, a and b, respectively, while θ is the emission angle of a with respect to the projectile direction. The calculations assumes further that the projectile undergo a direct peripheral interaction before break-up, occurring for large angular momentum windows, section 2.4. The projectile probability to survive break-up or mass transfer interaction process, $P(E_l)$, is assumed to be

1 for values of energy loss $E_l < E_{l,min}$. If a constant projectile energy loss per unit length $-dE_l/dx = 1/k$ and a constant break-up and mass transfer probability k' per unit length for $E_l > E_{l,min}$ is assumed, then the projectile survival probability due to energy loss E_l is [11, 19]

$$P(E_l) \propto \exp\left[-(E_l - E_{l,min})\right] \tag{2.72}$$

A typical spectra of $^{8}\mathrm{Be}_{\mathrm{gs}}$ from the break-up of $^{12}\mathrm{C}$ is calculated by folding the local plane wave approximation (LPWA) cross-section with the survival probability given by equation 2.72. In the this approach [19]

$$\frac{d^2\sigma^S(E,E',\Theta)}{dE'd\Omega} \propto P'P''|\psi(\mathbf{p})|^2 \tag{2.73}$$

where P'' is the modulus of the momentum of the break-up fragment, and

$$\psi(\mathbf{p}) = \frac{1}{(2\pi\hbar)^{3/2}}\int \psi(r)\exp[-\frac{i}{\hbar}(\mathbf{p}\cdot\mathbf{r})]d\mathbf{r} \tag{2.74}$$

is the Fourier transform of the wave-function that describe the relative motion of the fragment within the projectile. The fragment internal momentum is given by

$$\mathbf{p} = \mathbf{P'} - (m_f/m_P)\mathbf{P} \tag{2.75}$$

where m_P and m_f are the respective masses of the projectile and the observed fragment, $\mathbf{P}$ is the projectile's momentum during break-up and $\mathbf{P'}$ is the momentum of the observed fragment after break-up, different from the observed momentum due to the Coulomb boost of the fragment after production. The double differential cross-section of the $^{8}\mathrm{Be}_{\mathrm{gs}}$ fragments, considering all possible energy losses, is given by [19]

$$\frac{d^2\sigma}{dE'd\Omega}(E_\circ,E',\Theta) = \sigma_{bu}\frac{\int_{E_{l,min}}^{E_\circ} P(E_l)S(E,E',\Theta)dE_l}{\int_{E_{l,min}}^{E_\circ} P(E_l)dE_l} \tag{2.76}$$

where σ_{bu} is the angle and energy integrated break-up cross-section, and

$$S(E,E',\Theta) = d^2\sigma^S(E,E',\Theta)/dE'd\Omega \tag{2.77}$$

is the cross-section for producing the fragment of energy E' during the break-up of projectile with energy $E = E_o - E_l$. The Fourier transform of equation 2.74 is evaluation using $\psi(r) =$

$F(r)/r$ with the conditions $F(r) = A\sin(Kr)$ for $0 < r \leq R$ and $F(r) = B\exp(-k_1 r)$ for $r > R$. The normalised multiplicity spectrum $d^2N^S(E_C, E, \Theta)/dE'd\Omega$ integrated over the energy and the solid angle for the $^8\mathrm{Be}_{\mathrm{gs}}$ fragments produced when the ^{12}C projectile incident energy, E_o drops to $E_C = E_o - E_l$, is obtained from equation 2.71. The survival probability decreases with increasing energy loss, to a point where the ^{12}C survival becomes nil. The spectra of $^8\mathrm{Be}_{\mathrm{gs}}$ break-up is obtained thus [11]

$$\frac{d^2N}{dE'd\Omega}(E_o, E', \Theta) = \frac{\int_{E_{l,min}}^{E_{l,max}} \exp(-kk'E_l)\frac{d^2N}{dE'd\Omega}(E_C, E', \Theta)dE_l}{\int_{E_{l,min}}^{E_{l,max}} \exp(-kk'E_l)dE_l} \tag{2.78}$$

where $E_{l,min}$ and $E_{l,max}$ are the minimum and the maximum value of the energy losses leading to the ^{12}C breaks-up. The rise of the spectrum to the maximum value depends on $E_{l,max}$ and kk' while the drop from the maximum value depends on $E_{l,min}$ and kk'. The sharp cut-off limit in $E_{l,min}$ appear as a consequence of the assumptions made in the dissipation process. The values of $E_{l,min}$ and kk', are determined from fits to the experimental measurements. A good description of the double differential cross-sections for the break-up α particles, uses a more realistic wave function $\psi(r) = F(r)/r$ with the boundary conditions [3]

$$\begin{aligned} F(r) &= Ar^2, & 0 \leq r \leq b + f \\ F(r) &= B\sin K(r - b), & b + f < r \leq b + R \\ F(r) &= Ce^{-r/R_\circ}, & r > b + R \end{aligned} \tag{2.79}$$

where $K = \sqrt{2\mu(V_0 - B)}/\hbar$, f and V_0 are arbitrary constants, $b = (2\tan Kf - Kf)/k$ and $R = (\arctan(-KR_0))/K$. $A = B(\sin Kf)/(b+f)^2$, $B = \frac{1}{2\sqrt{\pi}}(\frac{b+f}{5}\sin^2 Kf + \frac{1}{2}(R-f) - \frac{1}{4K}(\sin 2KR - \sin 2Kf) + \frac{R_\circ}{2}\sin^2 KR)^{-1}$ and $C = Be^{(b+R)/R_0}\sin KR$, with the corresponding Fourier transform given by

$$\begin{aligned} \psi(\mathbf{p}) = \frac{4\pi B(\hbar c)^2}{(2\pi\hbar)^{3/2}}\frac{1}{pc}\Bigg\{ & \frac{\sin Kf}{pc}\Bigg[\frac{2(\hbar c)^2}{(pc)^2(b+f)^2}\left(\cos\frac{pc(b+f)}{\hbar c} - 1\right) \\ & - \cos\frac{pc(b+f)}{\hbar c} + \frac{2\hbar c}{pc(b+f)}\sin\frac{pc(b+f)}{\hbar c}\Bigg] \\ & + \frac{1}{(\hbar Kc)^2 - (pc)^2}\Bigg[pc\sin KR\cos\frac{pc(b+R)}{\hbar c} - \hbar Kc\cos KR\sin\frac{pc(b+R)}{\hbar c} \end{aligned}$$

$$-pc\sin Kf\cos\frac{pc(b+f)}{\hbar c}+\hbar cK\cos Kf\sin\frac{pc(b+f)}{\hbar c}\Big]$$
$$+\frac{\sin KR}{(\hbar c/R_0)^2+(pc)^2}\Big[pc\cos\frac{pc(R+b)}{\hbar c}+\frac{\hbar c}{R_0}\sin\frac{pc(R+b)}{\hbar c}\Big]\Big\} \tag{2.80}$$

where $\mathbf{p}=\mathbf{p}_S-(M_s/M_p)\mathbf{p}_P$ and $\mathbf{p}_S$, $\mathbf{p}_P$, M_s and M_p are momenta and masses of the spectator fragment and the projectile, respectively. By making some assumptions, the double differential spectrum of the spectator projectile-like fragment is given by [3]

$$\frac{d^2\sigma}{dEd\Omega}\approx p_S\,p_{pt}|\psi(\mathbf{p})|^2 \tag{2.81}$$

where $\mathbf{p}_{pt}$ is the momentum of the participant fragment.

2.6 The Statistical Decay Processes

The theories of the decay chain of a nucleus in a state of statistical equilibrium by sequential evaporation of particles are well established [90]. The probability per unit time for the emission of particle j with kinetic energy about ϵ is given by [91]

$$P_j(\epsilon)d\epsilon=\gamma_j\sigma\epsilon\left[W(f)/W(i)\right]d\epsilon \tag{2.82}$$

where $\gamma=g_jm_j/\pi^2\hbar^3$, g_i is the number of spin states, m_j is the mass of particle j, σ is the cross-section for the inverse reaction and $W(f)$ and $W(i)$ are the level densities of the final and initial nuclei at their respective excitation energies. The three terms given special considerations are σ, $W(f)$ and the limits of integration of the above equation 2.82 [92]. The cross-section for inverse reactions uses the empirical equation given by

$$\sigma_c/\sigma_g=\alpha\,(1+\beta/\epsilon) \tag{2.83}$$

where $\alpha=0.76+2.2A^{-1/3}$ and $\beta=(2.12A^{-2/3}-0.050)/(0.76+2.2A^{-1/3})$ MeV, while σ_c and σ_g are the respective cross-sections for capture and geometry, assuming that $\sigma_g=\pi R^2$. The Coulomb barrier effects for charged particles are accounted for, in the calculation for a given residue mass number Z by

$$\sigma_c/\sigma_g=(1+c_j)\left(1+k_jV_j/\epsilon\right) \tag{2.84}$$

where c_j and k_j are arbitrary constants obtained from the experimental measurements, V_j is the classical barrier potential evaluated for the jth particle using

$$V_j = \frac{zZe^2}{RA^{\frac{1}{3}} + \rho_j} \tag{2.85}$$

where e is the electron charge, z is nuclear mass number and ρ_j is the density of the emitted particle.

The simplest and most widely used formulation for the variation of the nuclear level density $W(E)$ with excitation energy E, for a complete degenerate Fermi gas, is given by

$$W(E) = C \exp\left\{2(aE)^{\frac{1}{2}}\right\} \tag{2.86}$$

since the $W(E)$ depends not only on the total number of nucleons in the nucleus but also on the neutron and proton numbers being either even or odd. This has been corrected for in the equation 2.86 above by assuming that

$$W(E) = C \exp\left\{2\left[a(E-\delta)^{\frac{1}{2}}\right]\right\} \tag{2.87}$$

where $\delta = 0$ for odd-odd nuclei and $\delta \geq 0$ for the rest.

The following equation is obtained for neutron emission by the substitution of equations 2.83, 2.84 and 2.87 into 2.82

$$\begin{aligned} P_\nu(\epsilon)d\epsilon &= g_\nu \frac{m_\nu R^2 A_\nu^{\frac{2}{3}}}{\pi\hbar^3} \exp\left\{-2\left[a_0(E-\delta_0)\right]^{\frac{1}{2}}\right\} \epsilon\alpha\left(1+\frac{\beta}{\epsilon}\right) \\ &\quad \times \exp\left\{2\left[a_\nu(E-Q_\nu-\delta-\epsilon)\right]^{\frac{1}{2}}\right\} d\epsilon \end{aligned} \tag{2.88}$$

where the subscripts 0 and ν stands for the original and the residual nucleus, respectively, while Q_ν is the neutron separation energy. Assuming that the maximum kinetic energy of the emitted neutron is given by

$$(\epsilon_\nu)_{\max} = E - Q_\nu - \delta_\nu \tag{2.89}$$

such that the integration of equation 2.88 gives the total neutron emission width as

$$\begin{aligned} \Gamma_\nu &= g_\nu \frac{m_\nu R^2 A_\nu^{\frac{2}{3}}}{\pi\hbar^2} \exp\left\{-2\left[a_0(E-\delta_0)\right]^{\frac{1}{2}}\right\} \alpha \int_0^{E-Q_\nu-\delta_\nu} (\epsilon+\beta) \\ &\quad \times \exp\left\{2\left[a_\nu(E-Q_\nu-\delta-\epsilon)\right]^{\frac{1}{2}}\right\} d\epsilon \end{aligned} \tag{2.90}$$

which on integration, assuming that $R_\nu = E - Q_\nu - \delta_\nu$, produces

$$\begin{aligned}\Gamma_\nu &= g_\nu \frac{m_\nu R^2 A_\nu^{\frac{2}{3}}}{2\pi\hbar^2} \exp\left\{-2\left[a_0(E-\delta_0)\right]^{\frac{1}{2}}\right\} \\ &\times \frac{\alpha}{a_\nu^2}\left\{a_\nu R_\nu\left[2\exp\left(2(a_\nu R_\nu)^{\frac{1}{2}}\right)+1\right]\right. \\ &-(3-2a_\nu\beta)(a_\nu R_\nu)^{\frac{1}{2}}\exp\left[2(a_\nu R_\nu)^{\frac{1}{2}}\right] \\ &\left.-\frac{1}{2}(3-2a_\nu\beta)\left[1-\exp\left(2(a_\nu R_\nu)^{\frac{1}{2}}\right)\right]\right\} \end{aligned} \tag{2.91}$$

The kinetic energy of a charged particle j cannot be less than the effective Coulomb barrier energy $k_j V_j$, hence the equation for its width is given by the

$$\begin{aligned}\Gamma_j &= g_j \frac{m_j R^2 A_j^{\frac{2}{3}}}{\pi\hbar^2} \exp\left\{-2\left[a_0(E-\delta_0)\right]^{\frac{1}{2}}\right\}(1+c_j)\int_{k_jV_j}^{E-Q_j-\delta_j}\left(\epsilon + k_j V_j\right) \\ &\times \exp\left\{2\left[a_j(E-Q_j-\delta-\epsilon)\right]^{\frac{1}{2}}\right\} d\epsilon \end{aligned} \tag{2.92}$$

on integrating, assuming in this case that $R_j = E - Q_j - k_j V_j - \delta_j$, produces

$$\begin{aligned}\Gamma_j &= g_j \frac{m_j R^2 A_j^{\frac{2}{3}}}{2\pi\hbar^2} \exp\left\{-2\left[a_0(E-\delta_0)\right]^{\frac{1}{2}}\right\}\frac{1+c_j}{a_j^2} \\ &\times\left\{a_j R_j\left[2\exp\left(2(a_\nu R_\nu)^{\frac{1}{2}}\right)+1\right]\right. \\ &-3(a_j R_j)^{\frac{1}{2}}\exp\left[2(a_j R_j)^{\frac{1}{2}}\right] \\ &\left.-\frac{3}{2}\left[1-\exp\left(2(a_j R_j)^{\frac{1}{2}}\right)\right]\right\} \end{aligned} \tag{2.93}$$

Assuming that $\exp\left[2(a_\nu R_\nu)^{\frac{1}{2}}\right] \gg 1$ and also that $\exp\left[2(a_j R_j)^{\frac{1}{2}}\right] \gg 1$ then equations 2.91 and 2.93 reduces to

$$\begin{aligned}\Gamma_\nu &\simeq \frac{m_\nu R^2}{2\pi\hbar^2}\exp\left\{-2\left[a_0(E-\delta_0)\right]^{\frac{1}{2}}\right\}A_\nu^{\frac{2}{3}}\frac{g_\nu\alpha}{a_\nu^2}\exp\left[2(a_\nu R_\nu)^{\frac{1}{2}}\right] \\ &\times\left\{2a_\nu R_\nu - \left(\frac{3}{2}-a_\nu\beta\right)\left[2(a_\nu R_\nu)^{\frac{1}{2}}-1\right]\right\} \end{aligned} \tag{2.94}$$

similarly, for the charged particle emission

$$\begin{aligned}\Gamma_j &\simeq \frac{m_j R^2}{2\pi\hbar^2}\exp\left\{-2\left[a_0(E-\delta_0)\right]^{\frac{1}{2}}\right\}A_j^{\frac{2}{3}}\frac{g_j(1+c_j)}{a_j^2}\exp\left[2(a_j R_j)^{\frac{1}{2}}\right] \\ &\times\left\{2a_j R_j - \frac{3}{2}\left[2(2_j R_j)^{\frac{1}{2}}-1\right]\right\} \end{aligned} \tag{2.95}$$

The positive exponentials are eliminated by multiplying equations 2.94 and 2.95 by $\exp\{-2[(a_jR_j)_{\max}]^{\frac{1}{2}}\}$, such that $(a_jR_j)_{\max}$ is the largest value of aR for all possible particle emissions.

The kinetic energy selection is done following this sequence of events. Assuming that $X = \epsilon - V$, with $V = k_jV_j$ for charged particles and $V = -\beta$ for neutrons, and substituting them in equation 2.88 produces $X_{\max}$ for which $P(X)$ is maximum on differentiation, given by

$$X_{\max} = a_j^{-1}\left[(a_jR_j + 1/4)^{\frac{1}{2}} - 1/2\right] \tag{2.96}$$

$P(X)$ is normalized thus $P(X_{\max}) = 1$, hence

$$P(X) = \frac{X}{X_{\max}} \exp\left\{2\left[a_jX_{\max} - [a_j(R_j - X)]^{\frac{1}{2}}\right]\right\} \tag{2.97}$$

The choice of X involves the consecutive drawing of two random numbers between 0 and 1. The first one say, ξ_1, is used to pick a value of X in the range $0 - R_j$ thus $X = \xi_1R_j$ where R_j is the maximum kinetic energy for the particle j. The second random number, ξ_2, is used to decide whether this values of X is to be accepted (i.e. if $P(X) > \xi_2$) or is rejected (i.e. if $P(X) \leq \xi_2$). The Q-values used in all the above cases can be obtained from experimental data.

In the model developed in Milano, a new set of parameters other than those described in the above equations have been introduced based on the following considerations

- the ratios between the total decay rate for neutron and charged particle emissions,
- the mean energies of the emitted particles obtained above, the optical model inverse cross-sections and the Fermi gas model level density calculations.

The comparison leads to a simple charge-mass dependence of the parameters of equation 2.83 and 2.84, the Coulomb barriers V, and the effective radii $RC^{1/2}$. The effective Coulomb barriers are hence given by $V = (0.107Z + 0.738)$ MeV for protons and $V = (0.107Z + 0.738)$ MeV for alpha particles. The term β in equation 2.83 is retained in the new model.

The emission probabilities of the different particles ν and the probability of exciting residual nucleus states of a given angular momentum J_r, are evaluated by applying the J-

dependent decay widths [77].

$$\Gamma_\nu(E, J, \epsilon_\nu, J_r)d\epsilon_\nu = \frac{1}{2\pi\omega_{CN}}(E, J)\sum_{S'=|\mathbf{J}_r-i_\nu|}^{S'=J_r+i_\nu}\omega_r(U, J_r)\sum_{l'_\nu=|\mathbf{J}-S'|}^{J+S'}T_{l'_\nu}(\epsilon)d\epsilon_\nu \tag{2.98}$$

where $\mathbf{S}' = \mathbf{J}_r - i_\nu$ is the channel spin, i_ν is spin of the emitted particle, $T_{l'_\nu}(\epsilon_\nu)$ is the emitted particle transmission coefficients, $\omega_{CN}(E, J)$ and $\omega_r(U, J_r)$ are the compound and the residual nucleus level densities, respectively. The angular momentum of decaying nucleus $\mathbf{J}$, the channel spin S' and the emitted particle orbital angular momentum l_ν are are all related by $\mathbf{J} = l_\nu + \mathbf{S}'$.

The high values of angular momentum, $\mathbf{J}$, could lead to a deformed nucleus. Assuming that the deformation is axially symmetric and symmetric under rotation about an axis orthogonal to the symmetry axis, then

$$\omega(E, J) = \omega(E)F(J) = \omega(E)\frac{1}{2}\sum_{K=-J}^{K=J}exp\left[-\frac{K^2\hbar^2}{2\ell_\parallel T} - \frac{[J(J+1)-K^2]\hbar^2}{2\ell_\perp T}\right] \tag{2.99}$$

where T is the residual nuclear temperature, K is the projection of $\mathbf{J}$ along the symmetry axis, and $\ell_\parallel$ and $\ell_\perp$ are the moments of inertia for the rotations around the symmetry axis and axis perpendicular to the symmetry axis, respectively. The moment of inertia are evaluated for each A, Z and J along the evaporation chain and as a result, the probability of emission of a given particle ν is given by

$$\Gamma_\nu(E, \epsilon_\nu) = \frac{1}{\omega_{CN}(E)}\frac{(2i_\nu+1)\mu_\nu\epsilon_\nu}{\pi^2\hbar^2}\sigma_{\mathrm{inv},\nu}\epsilon_\nu\omega_r(U) \tag{2.100}$$

assuming that the angular momentum of the residual nucleus are weighted average of $J - \langle l\rangle_{\mathrm{out}} \leq J_r \leq J + \langle l\rangle_{\mathrm{out}}$, and $\langle l\rangle_{\mathrm{out}}$ is the average orbital angular momentum value of the emitted particle without the spin.

Chapter 3

Techniques in Heavy Ion Interaction Measurements

There are a few experimental observables which are widely used to gain insight and information on what happens when two nuclei collide. Of these, a number of them have been investigated by the collaboration. Given in section 3.1, are some of the observables and how to measure them experimentally. These are

- Angular momentum measurements, section 3.1.1;
- Linear momentum transfer measurements, section 3.1.2;
- Recoil angle measurements, section 3.1.3;
- Relative cross section measurements, section 3.1.4;
- Charge measurements, section 3.1.5;
- Reaction times-scale measurements, section 3.1.6.

This investigation is meant to focus on the second and the fourth points, for the near-target residues as other yields have been fully explored for the present system, as presented in section 3.2.1. The technique by which this investigation measures the momentum transfer to the residues and the relative population of given residues is also novel. For this reason, it will be presented in the context of related experimental observables and techniques used to measure them.

A detailed description of each observable is presented in section 3.2. This includes typical experimental results from the work of the collaboration and also various other sources. Section 3.2.1 provide a comprehensive list of experimental measurements done in order to obtain some of these observables, presented in two main categories, the projectile-like fragment (section 3.2.1) and the target-like residue experiments (section 3.2.2). In general, experimental data are an integral or part of all the diverse physical parameters pertaining to the reaction and emission processes. Designing an experiment to discern a particular observable or effect is not easy. Filtering procedures have been developed for data analysis yet the extent of bias introduced in the data and the amount of information lost in the process require careful application [93]. The measuring techniques or equipment may provide high quality data in a given setup for a given observable, or in some aspects, one observable may well serve to tag another. In order to reach a concrete understanding of heavy ion reaction mechanisms, it is necessary to get information of a large set of entrance and exit channel properties. With each measurement made, new ideas are revealed which are essential to solve the difficulties encountered in similar setups and data reduction procedures [94]. The need to widen the scope of investigation and the applications of new scientific techniques is therefore essential and called for. It is no surprise then that the near-target residues of interest in the present study escaped attention over the past decades even though there was overwhelming evidence based on the projectile-like fragment yields. It was only recently that the work of the collaboration pointed out this discrepancy backed-up by a consistent theoretical framework and target-like residue studies [2]. Such yields in the high energy regime had been attributed mainly to the secondary reactions [29] which has been confirmed with GEANT4 simulations.

The emission properties of the highly excited composite nuclear system formed in the collision process are unique (chapter 2) as they evolves in time with the hardest part of the spectrum produced earlier in time and more to the projectile direction. Conversely, the emission properties of the intermediate equilibrated nucleus are much more isotropic with almost no memory effect of the projectile direction. This could lead to event biasing in the detection

process, as they operate on fixed optimum performance limits of measurements. This is why the experimental setup or analysis techniques differ or are used to discriminate between the different emission time-scales during the de-excitation process. In particular, characteristic gamma emissions, give the identity of the residue produced after the statistical decay process of the intermediate equilibrated nucleus and less information in terms of the top-level composite system, figure 3.1. The present technique delivers information below the nucleon binding energy (~ 8 MeV), i.e., that of the residue produced either through a single emission process (independent yield) or via multiple pathways (cumulative yield).

The kinematics observables of the top level highly excited composite nuclear system formed in the fast step are deduced indirectly from the Doppler Effect, a phenomenon attributed to the moving gamma emitter (nucleus) relative to the stationery observer (detector). Exclusive

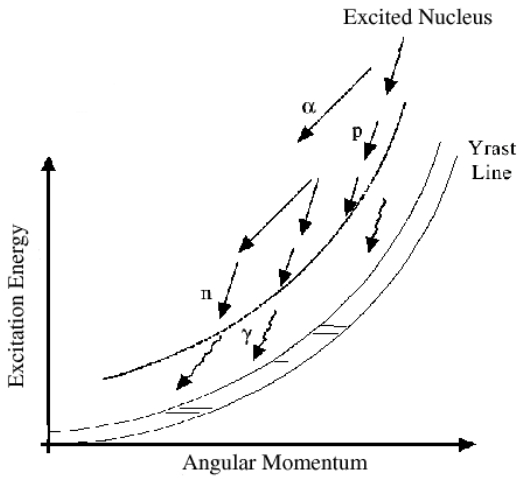


Figure 3.1: A plot of the excitation energy versus angular momentum for the intermediate equilibrated nucleus produced.

measurements such as the *X*-ray, gamma or electron spectroscopy techniques (as used in the present study) or unique exit channels such as the high transverse momentum particle spectra [95] and resonance particle spectra [11] play vital role in nuclear reaction studies as they give tight constraints to the theoretical model applicability.

3.1 Experimental Observables

3.1.1 Angular Momentum Measurements

The studies of residue angular momentum distributions and angular momentum transfer measurements provide useful insight into the nuclear reaction processes [96] addressing the following issues [93]

- The angular momentum transfer (nucleon exchange, collective mode excitations),
- the evolution of angular momentum dissipation mechanism,
- the viscosity of the nuclear matter (tangential friction forces) and,
- their influence on the nuclear de-excitation process. (The relative velocity between the quasi-target and quasi-projectile decrease with the incident projectile energy and the centrality of the collision.)

The initial orbital angular momentum in the interaction between projectile and target nuclei is shared between relative motion and intrinsic spins of quasi-projectile and quasi-target nuclei. For projectile incident energies below 10 A MeV, the angular momentum transfer is obtained from the residues by measuring the multiplicity and angular distributions of electromagnetic emission, angular distributions of light charged particles or fission fragments for heavier nuclei. Large spin values are transferred to the residues in the interaction process (several tens of $\hbar$ units) aligned along the normal to the reaction plane [97] with correlation to both the energy loss and the recoil angle [98]. In the incomplete fusion scenario though, the spectator fragment is expected to carry away a significant fraction of the initial angular momentum of the incident projectile, leading to the reduction of the gamma emission multiplicity yields required to dissipate the rest of it. (This statement does not contradict the fact that the multiplicity of the gamma emissions increased with increasing charge asymmetry or the lighter the spectator fragment in the intermediate energy regime [40], if it refers to the high energy photon emission (figure 3.2) while here it refers to the characteristic gamma emissions). Other techniques

for angular momentum transfer measurement make use of the angular distribution of the light charged particles, projectile-like fragment or gamma emission multiplicities [39, 99, 100, 101].

3.1.2 Linear Momentum Measurements

Both angular and linear momentum transfer to the target-like residue in heavy ion collision are obtained in transverse and longitudinal distribution measurements [96], though much attention has been given to the measurement of the latter because of its relation to the excitation energy of the composite system nucleus [2]. Linear momentum transfer is a convenient and much used observable to experimentally track the time evolution of the composite system, as it provides information about the mass and the velocity of the produced residues [41]. The velocity information could then provide details of the particle emission process. In the mean field dominated interactions, a large fraction of the incident projectile momentum is transferred during the interaction process. In the intermediate energy regime, new channels open up as to cause the deviation from this common concept, such as

- Peripheral direct reaction processes (transfer, pick-up or inelastic).
- Incomplete fusion processes.
- The coalescence effect [81, 78].
- Enhanced nucleon-nucleon interactions (e.g. spallation).
- Projectile pre-break-up (as in spallation).
- Projectile fragment re-emissions [2].
- Pre-equilibrium or dynamic emissions.

The enhancement of two-body nucleon-nucleon collisions leads to a high yield of nucleon emission in the normal plane of the projectile direction, in the laboratory angle, because of close

nucleon mass values (spallation). The fifth and sixth points above have to be coupled to achieve a much smaller magnitude of momentum transfer compared to the projectile input value.

The following experimental techniques have been developed and applied successfully to measure linear momentum transfer from projectile to the target nuclei.

- Simultaneous measurement of the residue time-of-flight and the kinetic energy with detector telescopes [102, 103, 104]. This technique has the limitation that in the case of residues with low velocity, one cannot identify with certainty the mass and the charge of the residues. The measurement is therefore an integral of neighbouring isobars and isotopes, produced through different reaction channels.

- Measurement of the recoil ranges of the radioactive residues on catcher foils using the radiochemical analysis technique [105]. This technique allows one to identify the residues and to measure their recoil range distributions. From that, and the known or predicted range-velocity relationships, the residue linear momentum distributions are inferred. The limitation to the applicability of the technique is in the cumulative recoil range distribution yields, where a residue is populated via many de-excitation pathways [10, 106], if the recoil range measurement is accurately known [2]. The technique works for both linear and transverse momentum distribution measurements for mainly the γ emitting residues, with half-lives of a few tens of minutes to a few years.

- Linear momentum transfer distributions can be deduced for heavier residues by the measurement of the folding angle between the fission fragments emitted in the decay process [79, 107, 108, 109, 110, 111, 112, 113]. This technique allows one to infer the average linear momentum of the intermediate equilibrated nucleus produced, averaged over several precursors of the composite system nucleus. This means that the linear momentum observed differs from that of the composite system nucleus because of the number of particles emitted in the course of the evaporation decay chain which reduces

the initial mass while the mean recoil velocity remain unchanged [2].

The recoil range distribution of the reaction residue yields in a material medium depends on the momentum transferred in the interaction process. This is the basis of the conventional radiochemical technique, which has been extensively applied to investigate linear momentum transfer in all the energy regimes, [114, 2, 33, 34, 22, 23, 115, 116, 117, 21, 118, 20, 119, 120, 121, 122, 24, 26, 123, 46, 124, 28, 29, 30, 125, 126, 127, 10, 128, 77, 105, 129, 130]. The technique provides comprehensive information which includes the residue identities, recoil velocity and angular distributions [77]. It also gives residue energy spectra down to very low energies [118]. The other existing techniques to measure the linear momentum transfer to the residues uses in-beam gamma coincidence spectroscopy or measurements of high energy bremsstrahlung emission done independently or in coincidence with particle detection [45, 50, 39, 43, 42, 44, 51]. The high energy bremsstrahlung gamma emissions produced in first chance nucleon-nucleon collisions in the composite system [15, 131] furnish direct information on the two-body contribution to the energy dissipation and the momentum transfer processes. Figure 3.2 shows high energy photon emission (>35 MeV) measured in coincidence with heavy residues in the interaction of 37 A MeV Ar projectile with ^{98}Mo target nuclei [41]. The linear correlation of the hard photon emission multiplicity with the magnitude of the linear momentum transfer was attributed to the two-body processes governing the momentum transfer process [41]. A number of other high energy photon studies seems to agree on the important role played by the impact parameter in the linear momentum transfer measurements [41, 56] as opposed to the projectile incident energy [112]. In some circumstances, measurements have been done using a combination of the above-mentioned techniques [132, 133, 134, 135, 113, 136, 137, 138, 25, 139] but recently, inverse kinematics in combination with a high resolution mass spectrometer has been favoured over the more established conventional techniques in well resourced facilities [61, 62, 140, 141].

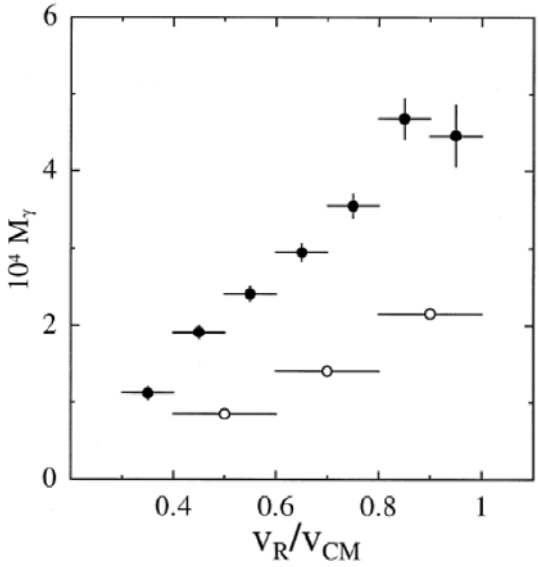


Figure 3.2: The gamma emission multiplicity M_γ, for energy >35 MeV, as function of the residue recoil velocity to the centre of mass value, for the 37 A MeV Ar + Mo (full symbols) and the 27 A MeV Ar + Zr (open symbols) interactions. The y-axis error bars are due to statistical errors while the x-axis error bars represent the bin width (from Ref. [41]).

3.1.3 Recoil Angle Measurements

Only a few measurements of the angular distributions of target-like fragments are available despite the fact that this information provides useful insight into the reaction mechanism [2]. Almost all measurements done on angular distributions relate to projectile-like fragments, section 3.2.1. The measurement of angular distributions of target-like fragments by detector arrays is difficult except for the case of inverse kinematics studies. Alternatively, there are well established techniques based on the conventional radiochemical methods [2, 10, 46, 118], figure 3.3. In the past, the main problems were low energy thresholds and poor energy resolutions of the detectors [61], the former being minimal in asymmetric systems with inverse kinematics collisions. The other common techniques use the energy spectra of the projectile-like fragments and phenomenological model assumptions to deduce the mean values of angular distributions. The recoil direction of the compound nuclei formed in the interaction process is assumed to be along the projectile direction. In that case, only residues which received a transverse momentum

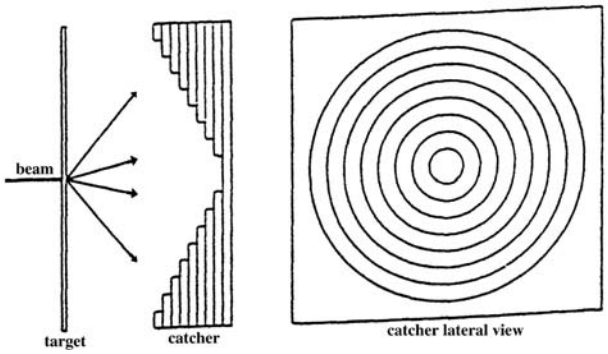


Figure 3.3: The conventional radiochemical-based catcher foils used in the technique for measuring the angular distributions of residues.

by particle emission are expected to deviate from this, i.e. be detected at angles other than the 0°. The more these residue recoil angles deviate from 0°, the larger the transverse momentum the residue received, and the more massive and/or energetic, on average, must be the fragment emitted. Some angular distribution measurements for the present collision system have been done for two residues, ^{66}Ga and ^{70}As, to identify the reaction process leading to their production [46]. The study assumed that ^{70}As residue was produced via complete fusion. The study reported that 36% of ^{66}Ga was produced via a direct process while the rest came from complete fusion followed by emission of two α particles and a neutron, which caused the less forward peaked ^{66}Ga residue angular distribution measurements shown in figure 3.4. The collaboration has done angular distribution measurements for number of residues for the ^{103}Rh(^{12}C system shown in figure 3.5 [2].

3.1.4 Cross Sections Measurements

In classical mechanics, the total reaction cross-section is given by $\sigma_T = \pi(R + \lambda\!\!\!^{-})^2$ where R is the size of the target nucleus and $\lambda\!\!\!^{-}$ is wavelength of the projectile [142]. The total reaction cross-section has seldom been used to decide the nature of reaction mechanisms notwithstanding a lot of measurements for specific exit channels. The determination of the total reaction cross section using the conventional radiochemical techniques was shown to under-estimate it

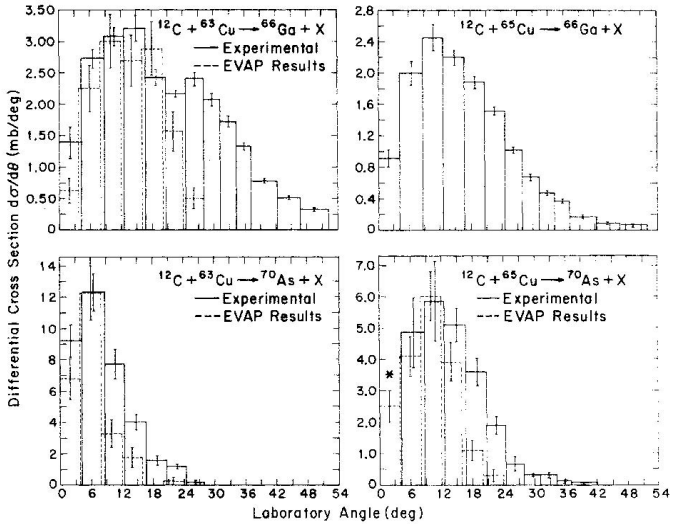


Figure 3.4: The differential production cross section variation with angle of some residues for 6 A MeV incident energy for the present system (from Ref. [46]).

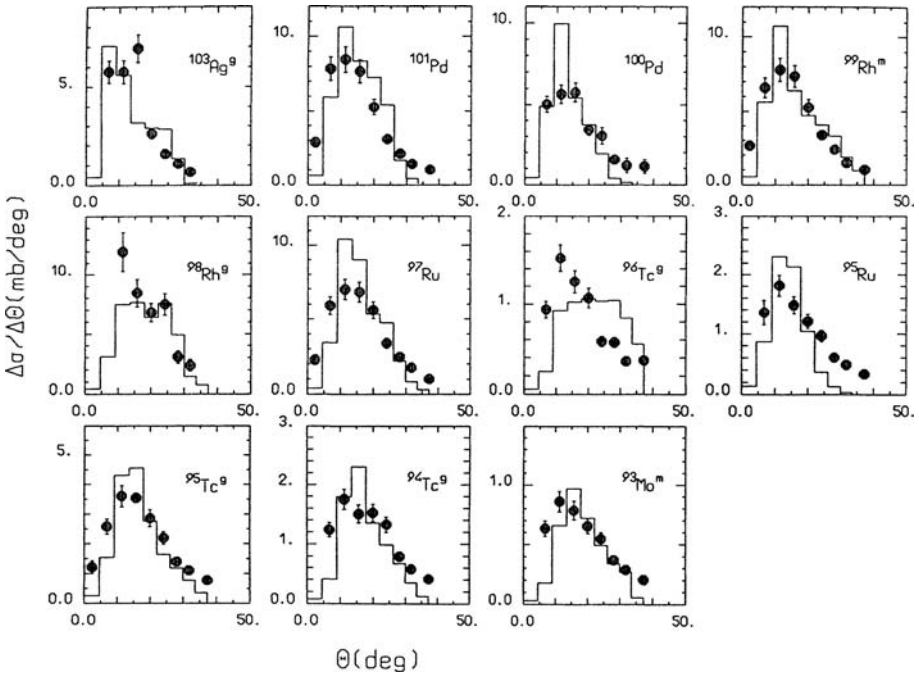


Figure 3.5: Angular distributions of residues produced in the interaction of 19 A MeV ^{12}C with ^{103}Rh target nuclei. The full dots with error bars are experimental values, the full line histograms are theoretical predictions of the model developed in Milano described in chapter 2 (from Ref. [2]).

as discussed in Refs. [2, 20], however, the values obtained for the individual exit channels and

the excitation functions are useful information. The collaboration has done a lot of work on the study of the different exit channel production cross sections using particle detection measurements and [143] and excitation functions studies using conventional techniques [2]. For the present case, the relative cross section for the dominant residues exit channels may be obtained from their gamma emission yield properties.

3.1.5 Charge Measurements

Charge is a conserved quantity in nuclear reactions and the best tag for the 100% charge detection efficiency obtained in the second generation of detector arrays for symmetric type of collisions [144, 145, 146, 147, 148, 149]. For inverse kinematics, the quasi-projectile charge partitions can be isolated with half the efficiency and was the first to be used [150]. The energy thresholds of the detectors, combined with the requirement that the total detected charge equals that of the projectile, are sufficient to discriminate the quasi-projectile in the measurement [151]. This approach was used recently by the collaboration to study the energy dissipation mechanism from the reconstruction of the energy spectra of the quasi-projectile produced from the ^{12}C break-up measurements into ^{8}Be and α fragments. Another demonstration of the effectiveness of this technique is given in figure 3.6, for the multiple break-up of the ^{35}Cl quasi-projectile [151], where contributions due to the low energy particle evaporation from the target were eliminated by the detector energy thresholds. The technique used for charge discrimination is based on the energy loss effect [152]. It is used to identify both the Z and A of the particle if a simultaneous detection of momentum is made, producing an exclusive measurement for the projectile-like fragments, as the case in the present study. If the setup cannot resolve the different isobaric yields, it is inclusive. This setup is often referred to as the telescope and consists of $\Delta E - E$ detector combination for energy loss and total energy detection of the charged particle. In the present study, the Z and A of the residue are obtained with the gamma energy coincidence technique [153, 154].

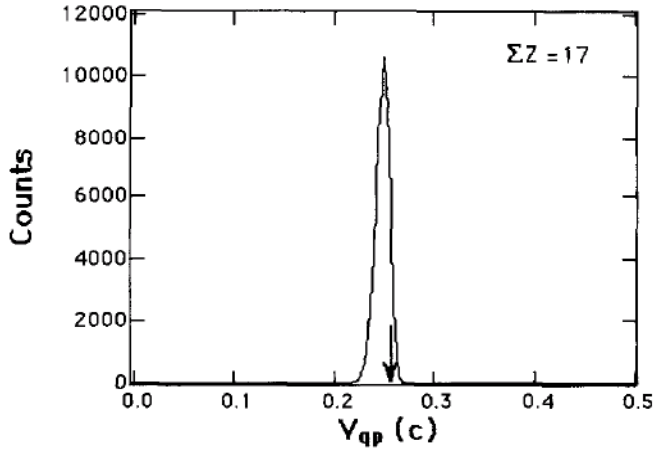


Figure 3.6: The reconstructed velocity V_{qp} of the quasi-projectile break-up with respect to c. The arrow indicates the projectile velocity (from Ref. [151]).

3.1.6 Reaction Time-Scale Measurements

This observable has often been deduced using theoretical calculations (e.g. Heisenberg uncertainty principle) and not by direct measurements. The closest one could discern the composite system, the intermediate equilibrated nucleus and the final residue formed may be provided by the techniques based on the near-perfect crystal lattice target structure, few such attempts are reported [90, 155, 156, 157]. In these crystalline targets, scattered charged particles are "blocked" from travelling along the crystal planes. This fact is utilized in the evaluation of the reaction time-scales measurements, where enhancement in the yield along the axial and planar directions, is measured. This enhancement is directly related to the distance travelled by the composite nucleus before decaying and hence gives the information on its life-time. There have been attempts to use the atomic properties also as discussed in Ref [158]. The gamma emissions used in the present study are produced much later in the de-excitation life-cycle and therefore do not provide significant information on reaction time scales.

3.2 Experimental Techniques

3.2.1 Exclusive and Inclusive Measurements

Exclusive and inclusive measurements involving nuclear interactions induced by light or medium-light projectiles such as ^{12}C, ^{14}N, ^{16}O, ^{20}Ne, ^{24}Mg, ^{32}S, ^{35}Cl, ^{40}Ca on various targets have been done [143, 96, 159, 160, 161, 150, 162, 163, 164, 165, 166, 167, 168, 169, 170, 171, 172, 140, 22, 132, 173]. These measurements were performed using mostly "large" solid-angle multi-detectors for nearly exclusive measurements of the light particle fragments, the intermediate mass fragments, the projectile-like fragments and only rarely done for the target-like fragments (section 3.2.2). These measurements were generally biased to the peripheral reaction processes as they were performed mostly in the forward angles. The break-up of the projectile in the nuclear field was reported to contribute significantly to the total reaction cross section for incident energies of about 10 A MeV [174, 159] whereas compound nucleus formation occurs in more central collisions [175]. In the 10-30 A MeV energy range, the projectile-like fragments are produced with about 90% projectile velocity in the grazing angle direction [176, 177] either promptly [178] or sequentially [179, 180, 181] depending on the level of excitation energy achieved during the reaction process [182]. The role of massive nucleon transfers from projectile to target [183, 184], was one reason which lead to the investigation of the projectile-like fragment [176, 185, 51, 186, 187]. Some of the production mechanisms suggested for the formation of projectile-like fragments are quasi-elastic transfer interactions and deep inelastic collisions processes [187, 188, 189]. Direct multi-step processes with quasi-elastic transfer involving significant mass, energy and angular momentum transfer is also suggested [190]. Others have proposed inelastic binary collision processes, with considerable amount of projectile energy damping [97, 191, 192, 193, 166, 194, 195] or co-existence of two or more processes [175, 196, 192]. Thus, ref. [175] suggests that a clear understanding of the reaction mechanisms leading to the formation of the observed projectile-like fragments is yet to be attained.

The work of the collaboration has shown that in the case of ^{12}C induced reactions, a large

fraction of the α particles observed in inclusive studies originate mainly from the break-up of the ^{12}C projectile into α and ^{8}Be fragments (which decays into two correlated α fragments) [3], as also reported in the exclusive measurement in which coincident γ-rays were used to tag the target-like residues for incident projectile energies up to ~17 A MeV [44]. For the incident projectile energies up to 33 A MeV and for all the target nuclei, mass transfer of α-like cluster fragments from the ^{12}C break-up, and, at higher incident energies, of single nucleons, are, together with incomplete fusion, the dominant reaction mechanisms [77, 72, 96, 105, 197], figure 2.2. The break-up process leads to the production of singles α, two correlated α particles constituting the ^{8}Be fragment and the three α exit channels for the higher incident projectile energies, whereas, the reaction with lower mass target nuclei show significant contribution from other processes [198, 199]. It has been found also that with increasing energy, the projectile^{12}C becomes less efficient in transforming its kinetic energy into the random thermal energy of the composite system nucleus [3]. This has been explained by assuming that not only is incomplete fusion playing an increasingly important role for higher incident energies, but that most of this energy must be rapidly dissipated before significant excitation of the nucleus occur [3]. This implies that a large number of the participant α particles are "re-emitted" with most of their initial momentum, reminiscent of the primary nucleon in the snow-ball coalescence process [82, 83]. A number of other experiments have observed that incomplete fusion processes occur in a wide range of masses and incident projectile energies [128]. In particular, for medium-light systems several investigations have been done to establish the projectile incident energy limits for the incomplete fusion process [197, 200, 146].

The break-up process is normally associated with light ion projectiles in asymmetric heavy ion collisions [201], indistinguishable from the evaporation process because of the Coulomb effects at low energies [202]. It becomes apparent near the Fermi energy and has always been associated with peripheral interactions [24, 61, 112, 163, 173, 203]. Some of the reported types are the far break-up [11] and the Fermi break-up (section 4.2.4). The experimental measurements relating to this phenomenon are reported in Refs. [167, 173, 181, 204]. There are

many suggestions on the origin of this break-up, such as the anomalous alpha clustering excitation states at 7-15 MeV [205]. (The alpha clustering subject is found in Ref. [206]). The break-up process has been an active area of investigation at intermediate energies using different techniques. There are two common fronts to the study, are based on the resonance particle [11, 94, 200] and the halo nuclei measurements [207], the former having been popular within the collaboration's work. The common feature of the two approaches is that both takes advantage of the weakly bound nuclei. The main difference comes from the fact that in the former case, the particles are detected in the exit channel whereas in the latter case, it is introduced in the entrance channel, i.e. it is the projectile. The detection of resonance particles is near-perfect exclusive measurement whilst the halo nuclei have unusual large spatial expansion useful in probing the impact parameter and the break-up process. The resonance particles are too weakly bounded to survive a final state interaction, as explained in the following paragraph. Following from the investigation with the halo nuclei, it has been suggested that the inelastic scattering of the light projectile (Coulomb interaction) with the target could lead to an excitation into an unbound state and the subsequent break-up of the projectile. The break-up effect, due to Coulomb dissociation, is attributed to the high energy photons created in the abrupt changing electric field of the target nucleus relative to the moving projectile. Experimental measurements have shown that this break-up probability is proportional to the square of the target charge Z [208].

To establish a full description of the ^{12}C projectile break-up process, the collaboration has undertaken resonance particle studies using the $^{8}\mathrm{Be}_{gs}$, produced with large cross sections. This particle being unstable is unlikely to survive a final state interaction. Therefore, any significant deviation of $^{8}\mathrm{Be}_{gs}$ spectra from the expectations of a pure break-up process is assumed to be due to the initial state interaction of the projectile with the target nucleus. Given in figure 3.7 is spectra of the $^{8}\mathrm{Be}_{gs}$ fragments emitted at forward angles (7°-20°) in the interaction of ^{12}C with ^{59}Co, ^{93}Nb and ^{197}Au at incident energy range of 10 to 33 A MeV [94]. It is observed that the momentum transfer to ^{59}Co is more than ^{197}Au, easily ascribed to the fact that the projectile break-up impact parameter is greater for ^{197}Au than ^{59}Co because of the large Z, however,

this alone could not explain the observation adequately [94] without introducing some kind of projectile energy damping mechanism (friction) of the ^{59}Co target to adequately explain the ^{8}Be spectrum. The effect of the incident projectile energy variation (impact parameter) on the

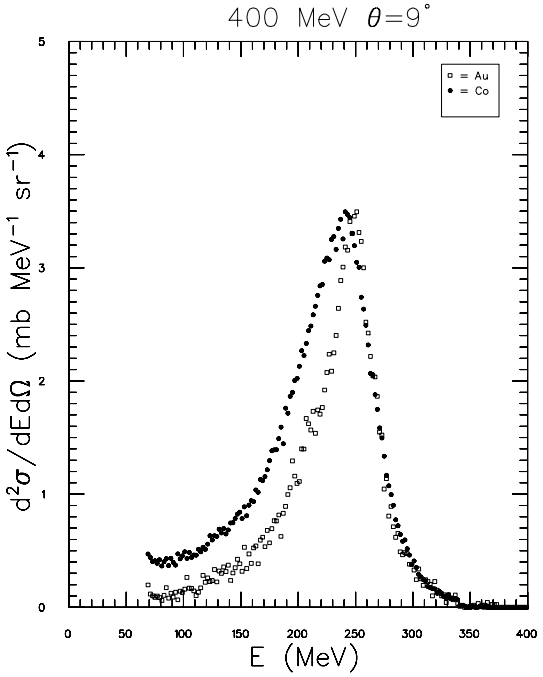


Figure 3.7: The spectra of ^{8}Be emitted at 9° in the interaction of ^{12}C with, respectively, ^{59}Co (full dots) and ^{197}Au (open squares) at incident energy of 33.3 A MeV (from Ref. [94]).

observed spectrum is also given in figure 3.8. When the incident projectile energy for the^{197}Au target nuclei is dropped, the ^{8}Be spectrum, friction followed likewise with almost pure break-up achieved at about 16.7 A MeV. The problem with the resonance particle detection technique, however, is that it cannot discern between the prompt and the sequential^{8}Be$_{gs}$ emission yields.

It is generally accepted that the incomplete fusion process originates from the fusion of only part of the projectile with the target [196], while the rest of the spectator projectile fragment continues in its motion undeterred. The observation of this spectator fragment emission [176] and the measured partial momentum transfer [209] led to the concept of the incomplete fusion process [44, 128, 210, 211]. It was reported that incomplete fusion occurs at just above the Coulomb barrier [127, 129, 212] as recorded in the time-of-flight measurements [213, 214].

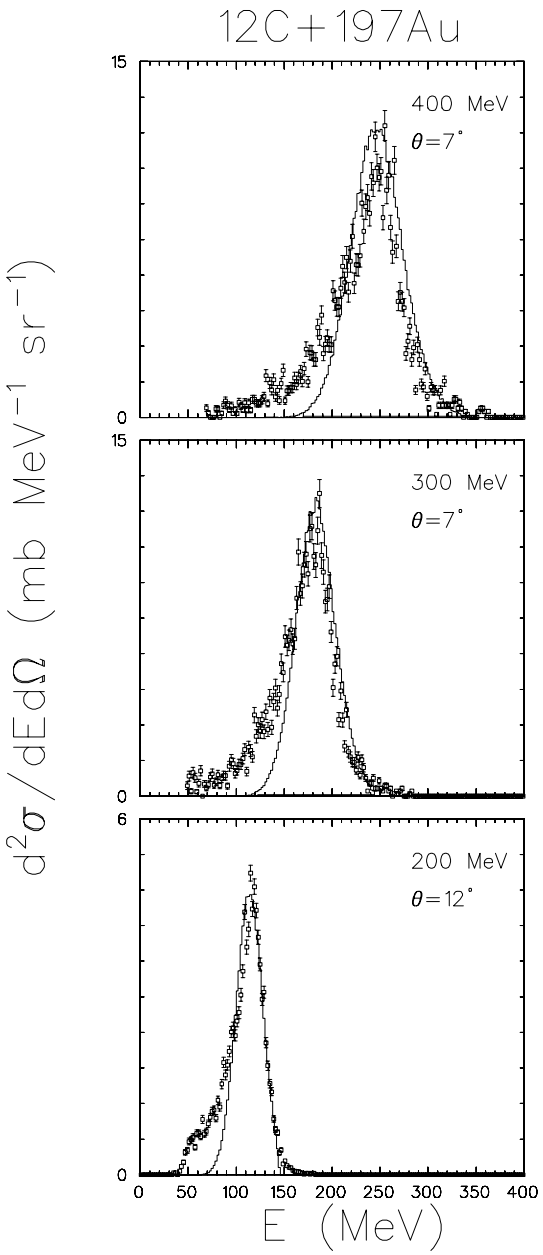


Figure 3.8: The spectra of ^{8}Be fragments observed at the indicated angles in the interaction of ^{12}C with ^{197}Au at incident energy of 33.3 A MeV, 25 A MeV and 16.7 A MeV. The open points are the experimental results, the full line histograms are the predicted break-up spectra based on the description given in section 2.5 (from Ref. [94]).

The process has been reported to depend on the entrance channel mass asymmetry [211, 128] for peripheral collisions [215] but recent studies show what could be collision system symmetrisation at intermediate energies [216]. The original concept of incomplete fusion process was

based on the idea of the disappearance of a pocket in the one-dimensional inter-nuclear potential energy as the angular momentum increases [44, 138, 186, 217]. In order to reduce the effective angular momentum of the composite nucleus and restore a pocket into the inter-nuclear potential energy as the entrance channel angular momentum was increased an increasing fraction of the projectile mass escapes with the excess angular momentum. The reduction of the incomplete fusion process with increasing projectile energy near the Fermi energy is attributed to a saturation of the critical angular momentum, corresponding to the highest order partial wave contributing to the fusion cross section [198]. The gamma multiplicity measurements show that incomplete fusion involves angular momentum values above the critical values [51, 186, 215] except for the case of spherical target nuclei [218], implying a competition with complete fusion even at lower angular momentum contrary to the hypothesis of an angular momentum window in the sum rule model of incomplete fusion [186]. The basic question remains as to whether a separate mechanism operates for these type of interactions or they are described by just a single process [202, 175]. It is the collaboration's objective that through a series of comprehensive systematic measurements, the answer will be found.

It is suggested in Ref. [146] that from the experimental point of view, the distinction between incomplete fusion and inelastic collisions has not often been addressed because the experimental devices are not able to give a general insight of the collision products. For example, the decay properties may be similar for an incomplete fusion nucleus as for a heavy target-like partner resulting from an inelastic process. In both cases, the excited nucleus will recoil in the "forward direction" with a velocity smaller than the centre of mass value in direct kinematics interaction. To distinguish between these two processes, it is necessary to detect also the remaining part of the initial colliding system. In the incomplete fusion case, it would be pre-equilibrium particles escaping from the system; whereas in the case of a deep inelastic process, it would be the light, slowed down quasi-projectile partner. The difficulty in making measurements lies in the fact that the de-excitation step may be complicated further by the opening-up of other extra multiple fragment exit channels. Ref. [146] suggests that in order to gain better

insight of the interaction mechanisms involved, it is necessary to perform experiments in which all the outgoing particles are detected in order to be able to "reconstruct" the products of the fast step [146]. This could be possible with the advent of 4π second generation devices such as INDRA [147, 219, 148, 149]. The INDRA array has large geometrical acceptance (about 90%), good charge resolution (up to Z = 56), ability to identify masses up to Z = 5, and low thresholds (1-1.5 A MeV). Other attempts include inverse kinematics approaches [220], for such systems the interaction products have high longitudinal momentum and more forward focused. These products could then be easily detected with a single-sided 2π array. The CHIMERA array was developed with this in perspective [220]. These extremely complex and expensive detector array systems have their own limitations easily overcome by simpler techniques such as the conventional radiochemical methods described in the next section.

3.2.2 The Conventional Radiochemical Techniques

The application of the conventional radiochemical technique has been the major mode of studying the target-like fragments in heavy ion collisions (indirectly). It is still the most essential and economical tool to that effect to date. The niche advantage offered by the technique far outweighs its pitfalls. The techniques offers the capability to obtain the measurements for isobaric and mass yield distributions, angular distributions and longitudinal momentum transfer information [2]. The exclusive measuring capability leads to a comprehensive information on the reaction mechanisms [77]. Some of the major advantages of these techniques include

- Measurements of cross section and average kinematics properties of individual radioactive residue nuclides [23].
- Superior mass (exclusive), linear and angular resolution measurements.
- Beam axis measurement; offers optimum momentum distribution resolution.
- Potentially no energy detection threshold for the target-like residues.

Nonetheless, the inherent problems of the cumulative yields over many residue production pathways, corrections for the unmeasured residue yields and the high uncertainty in heavy ion stopping powers in recoil range measurements, cannot be ignored. These corrections may causes systematic errors that could lead to wrong interpretations of the experimental measurements [2].

Gamma spectroscopy in coincidence with particle emission measurements, was one of the first techniques to be used in identify the incomplete fusion process in the low energy regime [44, 51]. The multiplicity of the characteristic γ-ray emissions fell-off with the increasing projectile energy [44], because of the decrease in angular momentum transfer with increase in the projectile incident energy [93, 133]. The measurements of the first three moments of the gamma emission multiplicity distribution in coincidence with the out-of-plane gamma emission anisotropy as a function of mass asymmetry for the strongly damped projectile-like fragments of the of 8.4 A MeV ^{20}Ne induced interactions on ^{63}Cu target had shown that the large variance of the multiplicity observed was associated with the anisotropy indicating the existence of a random constituent of the angular momentum comparable to the aligned component induced by the tangential friction [221]. To perform gamma spectroscopy measurements in the present energy regime, there has to be improved detection efficiency for the low energy and multiplicity gamma yields to counter increased level of background contributions.

The following is a list of some of the available data on the application of the techniques to study momentum transfer to residues in the interaction of light heavy projectiles with varied target nuclei. Measurements have been done for projectile energies: 40 A MeV ^{14}N; 35 A MeV ^{16}O; 25 A MeV ^{22}Ne [33]; 90 A MeV ^{6}Li [34]; 135 A MeV ^{12}C [22]; 90 A MeV ^{12}C [23]; energy range 8-46 A MeV ^{20}Ne [116]; 15, 25 and 45 A MeV ^{12}C [21]; 35 A MeV ^{12}C [20]; energy range 22-84,30-84 A MeV ^{12}C [24, 25]; ~83 A MeV ^{12}C [26] and 180-28000 A MeV ^{12}C [28], all with copper target nuclei. Comparisons can be drawn with the ^{4}He data for energy range ~10-21 A MeV [120]; 22.5, 37.5, 50 A MeV [117, 122], 180 A MeV [124] with ^{59}Co target and 10-35 A MeV with ^{93}Nb [121]. These measurements are not limited to the Z $\simeq$ 60 region, heavier targets have also been used in the study: 12-16 A MeV ^{32}S with

^{165}Ho [118]; 12.6, 18, 33.5 A MeV ^{12}C and ~19 A MeV ^{16}O projectiles with ^{103}Rh target [2]; 85 A MeV ^{12}C with ^{238}U [119] and ^{197}Au [222, 137]. In the low energy regime: ~4-~10 A MeV ^{12}C with ^{165}Ho [125], ^{103}Rh [126], ^{89}Y [127], ^{197}Au [10, 77, 105], ^{181}Ta [10], ^{93}Nb [128], ^{169}Tm [130]; ^{16}O with ^{89}Y [128], ^{165}Ho and ^{181}Ta [10] and the effect of particle evaporation on some of the measurements [223, 115]. The recoil range distribution of the target-like fragments, using radiochemical techniques, depends on the momentum transferred in the interaction process. In the incomplete fusion process, the momentum transferred is proportional to the number of nucleons transferred to the target nuclei (equation 2.68) observed 'directly' for evaporation residues, by measurement of their velocity [213, 210]. The measurements of both evaporation residue velocities and fission fragment correlation angles [138], show agreement on the limiting values of linear momentum transfer [25, 44], while the recoil range could be used in distinguishing between the different incomplete fusion processes in light systems where the same product could be formed through multiple pathways [127].

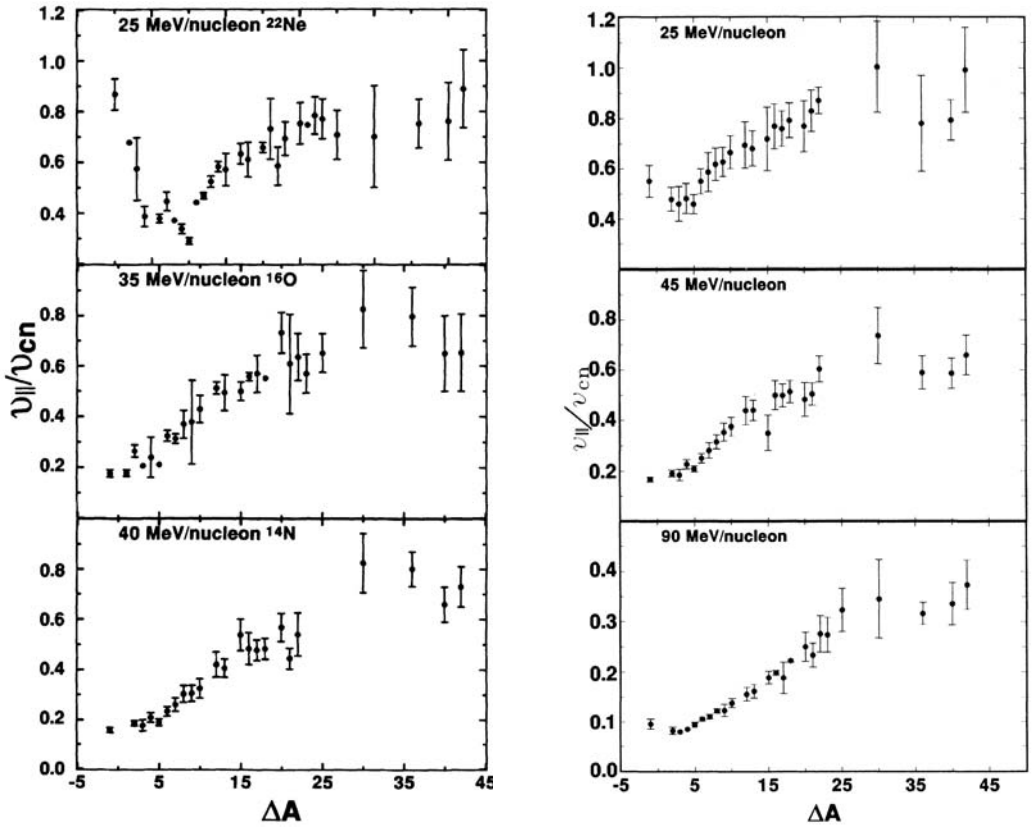
A large number of excitation functions, forward recoil ranges and angular distributions of target-like fragments produced in the interaction of ^{12}C with ^{103}Rh have been measured by the collaboration to investigate various properties of the reaction processes at incident energies up to ~33 A MeV, using the radiochemical technique [2, 9, 8]. The measurements allowed a comprehensive analysis of the major reaction processes in the fast and the slow stages of the de-excitation process. These have shown that the large fraction of α particles which participate in the interaction processes experience a slight reduction of their initial energy due to interaction with a few nucleons of the target, leading to the reduced excitation energy of the final residues. The residues produced evaporate further a relatively few number of particles leading to the formation of mostly near-target products.

The reaction studies of copper with 40 A MeV ^{14}N, 35 A MeV ^{16}O and 25 A MeV ^{22}Ne [33] has shown that the isobaric yields remain essentially unchanged with variation in light projectile mass [23, 34]. The ^{16}O and ^{14}N mass yield distributions give very similar results, with the maximum in the distributions occurring at A $\approx$ 55 and the minimum at A $\approx$ 25-30.

The ^{22}Ne projectile exhibited a greater upturn for the lightest products, indicating that binary fragmentation appears more probable for heavier projectile compared to^{16}O and ^{14}N. The minimum velocity occurred in the near-target residue region, as shown by figure 3.9(a). The shift toward larger masses of the peak in the ^{22}Ne distribution was attributed to the increasing likelihood of mass transfer due to decreased projectile A MeV and the increased role of mean field interactions. The fractional velocity transfer comparisons revealed similar trends for the^{16}O and ^{14}N projectiles, while the ^{22}Ne projectile distribution was quite significantly different for the following reasons; the fractional velocity transfer was larger, on average, for the^{22}Ne projectile compared to ^{16}O and ^{14}N; the distribution also exhibited a V-shape centred about the target mass, with the residue fractional velocity transfer increasing the further away it is from the target nuclear mass, figure 3.9(a).

The above observations made pointed to an increase in mass transfer at low A MeV. When these results were compared with other studies [34, 21], it was apparent that the V-shaped distribution disappears above ~25 A MeV, indicating the increasing importance of nucleon-nucleon collisions in governing the reaction dynamics above this energy [41, 224]. The mean longitudinal momentum transfer measured was shown to increase with projectile mass for constant projectile energy, a trend attributed to the corresponding decrease in A MeV. These observations, with those of the 90 A MeV ^{6}Li [34] missed the near-target residue yield component with the maxima where the minima of the plots given in figure 3.9(a) are, i.e. the target mass. The near-target residue yields reported here with the highest cross sections in mb were^{64}Cu (100±12), ^{65}Zn (48±7) and ^{63}Zn (28±1). The ^{64}Cu residue yield seemed anomalous compared to the rest of the yields even though no suggestion was given [33].

The isobaric yield distribution from the interaction of copper with 90 A MeV ^{12}C projectiles [23] remained unchanged compared to the lower energy measurements [21, 20]. The mass yield distribution, displayed considerable variation with increasing projectile energy, the minimum and maximum of the distribution moved toward lower masses, while the distribution itself flattened out as shown in figure 3.11. This led to a decrease in the slope in the exponential



(a) Projectile energies 25 A MeV ^{22}Ne, 35 A MeV ^{16}O, 40 A MeV ^{14}N.

(b) ^{12}C projectile 25 A MeV, 45 A MeV and 90 A MeV.

Figure 3.9: The fractional velocity transfer for the interaction of copper with the^{12}C projectile at various energies (from Ref. [23, 33]).

region of the distribution with increasing projectile energy. The longitudinal momentum transfer increased to a maximum of ~140 MeV/c at 25 A MeV and then dropped monotonically to the 90 A MeV projectile energy value. There seemed to be a saturation limit to the longitudinal momentum transfer of ~170 MeV/c per incident nucleon, in agreement with Ref. [103]. Similar observations were made in the measurements of linear momentum transfers for^{12}C induced interactions at energies from 30 to 84 A MeV on U, Au and Ni target nuclei [25]. The limitation effect was obtained for projectile incident energy of ~15 A MeV as suggested by earlier studies [25] also shown in figure 3.10. The isobaric yield distribution for the copper interaction with 90 A MeV ^{6}Li projectiles [34] remained essentially unchanged with varying projectile mass and

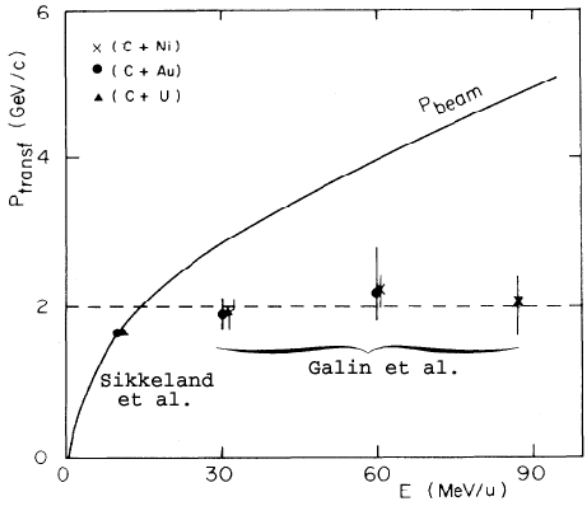


Figure 3.10: The maximum induced linear momentum transfers for ^{12}C-induced interactions between 10 A MeV and 84 A MeV (from Ref. [25]).

energy, up to ^{12}C and incident energy ~100 A MeV. The ^{6}Li projectile mass yield peaked at approximately A ≈ 60, consistent with distributions for lighter projectiles [225] but without the upturn in the low mass yield distribution. The near-target residue yields reported here with the highest cross sections in mb were ^{64}Cu (28±3) and ^{61}Cu (27±1) while the minimum residue velocity is situated in the target nuclei mass. The ^{12}C projectile at comparable kinetic energies yielded a significant upturn, an indication of target fragmentation as mentioned earlier. The analysis of longitudinal momentum transfer data showed that at comparable A MeV energy, the lighter the projectiles the more efficient it is in transferring its momentum to the observed residues [33]. Above the Fermi energy, the amount of longitudinal momentum transfer per incident projectile nucleon appears to scale with total kinetic energy [34], with the limit reached corresponding to ~220 MeV/c per nucleon [20, 21, 23, 26, 116, 124]. The near-target residue yields reported here with the highest cross sections in mb were ^{64}Cu (52±8), ^{62}Zn (8.3±.1) and ^{63}Zn (5±.2). The minimum velocity is situated within these residues while the ^{64}Cu yield seemed anomalously higher.

The isobaric yield distribution of near-target residues from the interaction of copper with 15 A MeV, 25 A MeV, and 45 A MeV ^{12}C projectiles was found to be essentially unchanged

in the energy domain, while the mass yield distribution changed substantially with increasing energy [21]. The mass yield distribution measurements from this study are shown in figure 3.11. The measurement shows that the distribution broadens and the peak moved to lower mass numbers with increasing projectile energies, in agreement with similar studies [33, 34, 20, 21]. The mean mass loss from the target increased from approximately 1 to 10 nucleons within the energy range measured. The mean longitudinal momentum transfer measured reached a maximum value of ~170 MeV/c at 25 A MeV and decreased for higher projectile energies. The fractional longitudinal momentum transfer decreased continuously from ~0.8 to 0.4 for the lowest and the highest projectile energy, respectively. The mean excitation energy deduced both from the mass yield distribution and the longitudinal momentum transfer values seemed to increase with projectile energy but appeared to level-off at 45 A MeV. The excitation functions for selected residues with masses far-removed from the target, intermediate and above the target from the study are given in figure 3.12. For the same system at 35 A MeV, the isobaric yield

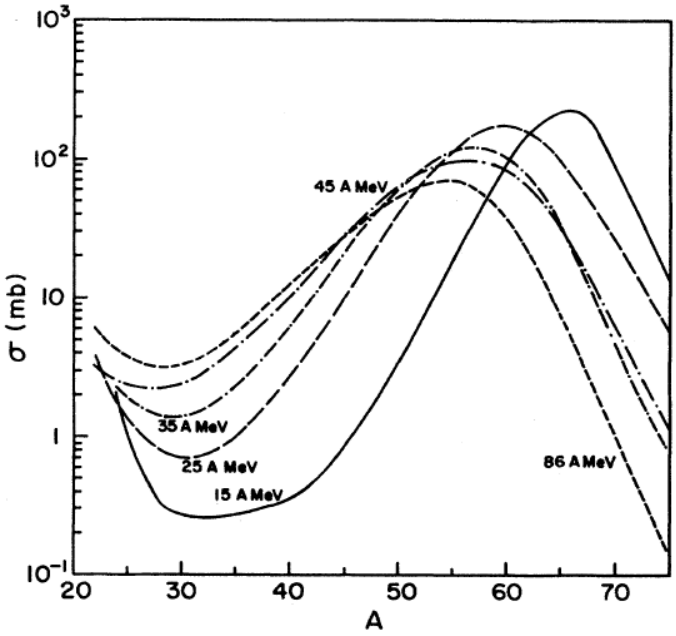


Figure 3.11: The deduced residue yield distributions in the interaction of copper with different energies of the ^{12}C projectiles (from Ref. [21]).

distribution of near-target residues was found to be near-Gaussian [20]. The most probable mass

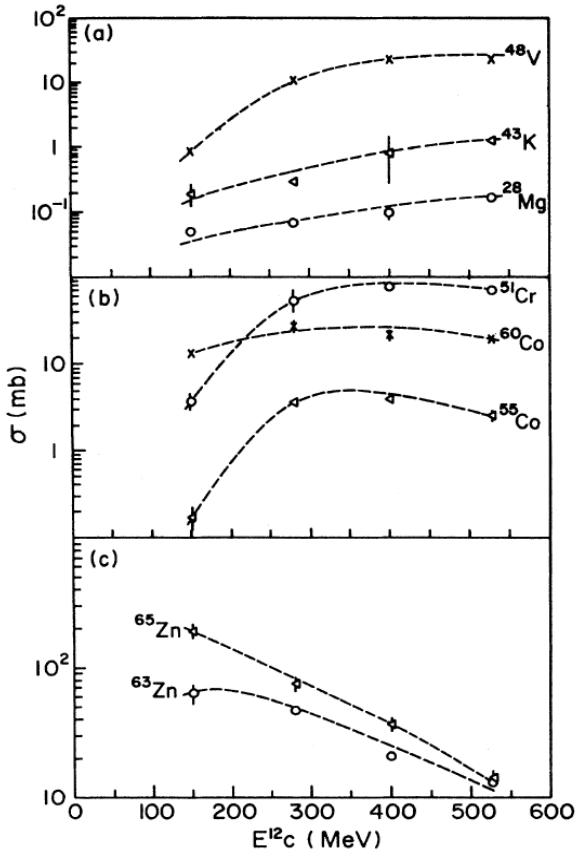


Figure 3.12: The excitation functions for (a) low mass (b) intermediate mass, and (c) high-mass products of the interaction of ^{12}C with copper target nuclei (from Ref. [21]).

yields occurred very close to the stability line for products below A=45, and on the neutron deficient side of stability line for near-target residues. The mass yield distribution peaked at A ~ 58, decreased to a minimum at A ~ 30, and increased again for the lower mass residues. The comparison made with the isobaric yield distribution from other studies [24] showed that the residue yield was independent of the incident projectile energy, while the mass yield distribution shifted to lower masses with increasing projectile energy [20]. The near-target residue yields reported here with the highest cross sections in mb being; for the 15 A MeV energy ^{65}Zn (188±21), ^{67}Ga (129±7), ^{66}Ga (114±10), ^{64}Cu (102±9), ^{63}Zn (63±10); for the 25 A MeV energy, ^{65}Zn (74±7), ^{63}Zn (46±3), ^{66}Ga (35±1), ^{67}Ga (30±1); for the 35 A MeV energy, ^{65}Zn (36±4) and ^{63}Zn (21±1); for the 45 A MeV energy, ^{64}Cu (61±4), ^{65}Zn (14±1), ^{63}Zn (13±1).

The minimum velocity is situated within these residues for the energies measured.

The total reaction cross section obtained for present system within the same incident projectile energy range [20], using integration of mass yield distribution technique, was ≈ 1.7b. This is significantly lower than the calculated value of ≈ 2.4b [108] and ≈ 3.4b [2]. The two possibilities suggested for the anomaly were [21]; interactions in which the target breaks up into fragments none of which have A≥28; or interactions populating very specific final states, e.g., bound excited states of the target nucleus, to a substantially larger extent than predicted by the parameterisation technique used in calculating the cross section. The work of the collaboration has refuted these claims [2], with an alternative view noting that the wrong assumptions were used in the study, which when taken into accounted gave a more realistic value, while the missing cross section is attributed to unobserved abundant near-target residue yields [2], currently being investigated.

The variation of the total reaction cross section with projectile energy is reported to peak at about 25 A MeV, due to the following given reasons [21]; the Coulomb effect reduces the total reaction cross section at low energies; or surface transparency, leading to an increase with energy in the nucleon mean free path, causing reduced reaction cross section at high energies. The measured momentum transfer increased with decreasing residue mass ranging from about 0.3 to 0.8 of the projectile momentum, figure 3.9(a). The measured kinetic energy [20] of one of the detected residues, ^{24}Na, in the moving system was close to the tangent sphere value assuming binary break-up, evidenced the none-spallation origin reported earlier [30, 29]. The upturn in the mass yield distribution observed in the low product mass region was attributed to the target fragmentation. Recent measurements have attributed these products to dynamical break-up of highly excited target-like residue [226, 227, 228]. The first observation of this production is reported in the interaction of 85 A MeV ^{12}C with ^{238}U [119], which found that the heavy fragment complement of the ^{46}Sc distribution was similar in shape to that of ^{146}Gd, and the fact that the fragments with low neutron proton ratio, N/Z, were more anisotropic distributed compared to those of the high N/Z case. The suggestion given was that these fragments were

produced by a new non-equilibrium fast mechanism that leading to very asymmetric fission of the target-like fragments and with varying amounts of excitation energy.

For the case of ^{20}Ne and ^{14}N induced reactions in the 8 to 46 A MeV energy range on natural copper target [116], a saturation of the recoil velocities as a function of the mass is observed for reaction product residues lighter than and far removed from the target nuclei (figure 3.9(a)) mass as also reported in other measurements [229, 230, 25] and interpreted as a manifestation of near-central collisions. The corresponding cross section for heavy ions indicated that the impact parameter of such defined collisions was much larger than that expected for complete overlap collisions. In the case of ^{20}Ne induced reactions, the recoil velocity corresponding to the near-central collisions, corresponded to the compound-nucleus velocity only up to about 11 A MeV incident energies [116]. The saturation of the recoil velocity below that corresponding to the compound nucleus is reported earlier to be due to the emission of fast nucleons having the average projectile velocity in the zero degree angles [123]. The excitation energy inferred from these energetic nucleon spectra was nearly three times higher than that for a fully equilibrated compound nucleus suggesting pre-equilibrium emission source [135]. For the ^{20}Ne induced reactions in the incident energy range 20 to 46 A MeV, the cross section corresponding to the saturation region was found to be about 1.1b, almost corresponding to the range of impact parameter from zero to the target radius, in agreement with suggestion made in Refs. [112, 135]. The reported dominant near-target residue yields about the 29 A MeV energy value were ^{64}Cu (93±10), ^{61}Cu (52±5), ^{65}Zn (37±8), ^{62}Zn (8±6), ^{66}Ga (5±5), ^{67}Ga (3.2±4). The ^{64}Cu yield show no significant variation over the 8 to 46 A MeV while the rest of the residues show some significant energy dependence. The average excitation energy of the composite system deduced both from the kinematics properties of the recoils and from the average mass of the residue yields (reported above to be independent of the target nuclei mass for the ^{12}C, ^{14}N and ^{20}Ne projectiles) is, however, dependant on the assumptions of the fast step process. In addition, the average excitation energy of the highly excited nucleus formed attains its maximum value in the energy range below 100 A MeV, with the peak value not exceeding 3 A MeV [116, 231].

Chapter 4

The GEANT4 Simulation Physics

GEANT4[1] is a free software toolkit composed of tools which can be used to accurately simulate the passage of particles through matter [232]. It comes with a complete functionality for tracking, geometry, physics models and events hits. The capabilities of the toolkit have been summarised as:

- the geometry of the system,
- the materials involved,
- the fundamental particles of interest,
- the generation of primary events,
- the tracking of particles (photons included) through materials and electromagnetic fields,
- the physics processes governing particle interactions,
- the response of sensitive detector components,
- the generation of event data,
- the storage of events and tracks,
- the visualization of the detector and particle trajectories, and

[1] acronym for GEometry ANd Tracking

- the capture and analysis of simulation data at different processing detail depths.

The user constructs a stand-alone application or builds it on top of an existing one based on object-oriented programming framework. At the core of GEANT4 is an abundant set of physics models to handle the interactions of particles with matter across a very wide energy range. The in-built data and expertise are drawn from vast sources making it the largest existing archive of particle interaction software libraries. The toolkit is written in C++ and exploits advanced software engineering techniques and object-oriented technology for maximum transparency.

The projectile ions (beam) in the present study can be tracked using GEANT4, applying the physics models relevant to the interaction process. When the projectile nucleus collides with the target nucleus, the interaction is described using nuclear models detailed in section 4.2 while the emitted photons are tracked using the models given in section 4.1. Tracking of secondary emitted particle ions is ignored in the present investigation. In the tracking of these particles, their energy is the criterion used to select the specific model applicable to the specified projectile and energy range. The ability of the GEANT4 simulation toolkit to track a photon in the germanium detector, had been demonstrated by calculations of the photo-peak detection efficiency at 1332 keV, for several germanium detectors of different shapes and sizes ([233] and references therein). The difference between the simulation and measurements was within 2% over a large set of germanium detector constructions of varying sizes and shapes. Its ability to predict the nuclear interaction processes has not been fully developed for heavy ion reactions at intermediate energies.

4.1 Photon Interaction Physics

The detection physics applicable to the present energy range is the electromagnetic interaction (photon) with matter (detector). The major interaction processes of interest are the photoelectric effect (4.1.1), Compton effect (4.1.3), multiple scattering (4.1.4), gamma conversion to (e^+, e^-) pair (4.1.2) and to a lesser extent the interaction processes of the (e^+, e^-) pairs

i.e. bremsstrahlung (4.1.6), ionisation (4.1.5) and particle annihilation (4.1.7). What constitutes a detector signal is determined by the interaction cross-section of these processes. A plot of the energy dependence of the various photon interaction cross-sections for two common detector materials, silicon and germanium, are plotted in figure (4.1). The low energy physics extensions and the optical properties (for the BGO shielding) were not critical in the current simulations. The GEANT4 physics manual [234] and the references therein provide an extensive coverage of the physics employed, a short review of which is given in the succeeding sections.

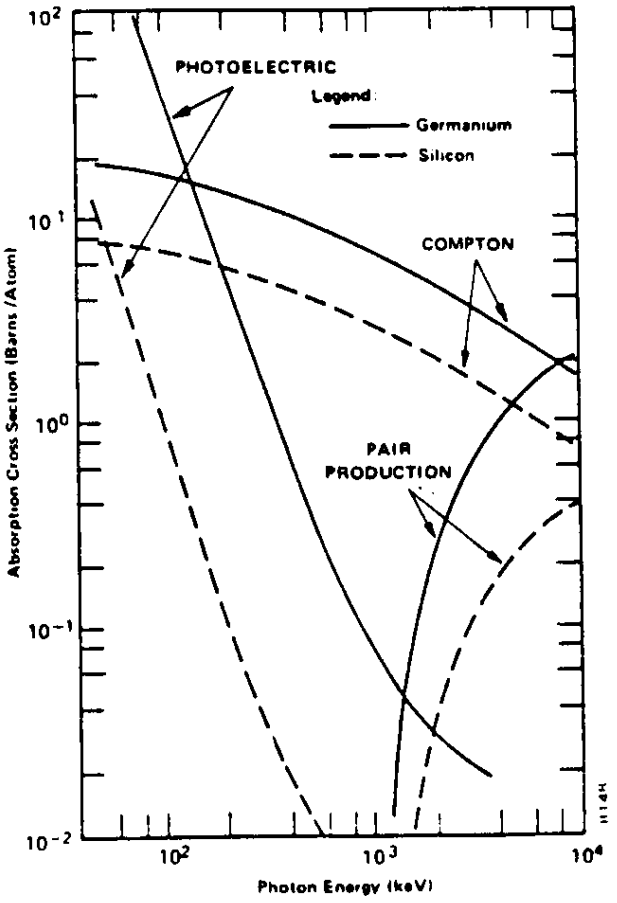


Figure 4.1: The energy dependence of photon interaction processes in Si and Ge materials.

4.1.1 Photoelectric Effect

The process of ejecting an electron from a material via the absorption of a photon quantum is known as the photoelectric effect. In GEANT4, this process is simulated using the solutions to parameterized photon absorption cross section equations to solve for the mean free path, a database of atomic shells is used to decide the energy of the ejected electron and the K-shell angular distribution orientation assigned to the electron. The parameterization equation for the photo-absorption cross section is given by [234]

$$\sigma(Z, E_\gamma) = \frac{a(Z, E_\gamma)}{E_\gamma} + \frac{b(Z, E_\gamma)}{E_\gamma^2} + \frac{c(Z, E_\gamma)}{E_\gamma^3} + \frac{d(Z, E_\gamma)}{E_\gamma^4} \tag{4.1}$$

An experimental database of measurements for several energy range intervals based on the photo-absorption edges, are fitted using the least-squares method to generate the parameters a, b, c and d.

The mean free path, λ, for photoelectric photon interaction in the material is given by:

$$\lambda(E_\gamma) = \frac{1}{\left(\sum_i n_{ati} \cdot \sigma(Z_i, E_\gamma)\right)} \tag{4.2}$$

where n_{ati} is the number of atoms per volume of the i^{th} element of the material. The cross section and mean free path are discontinuous, calculated at run-time using equations 4.1 and 4.2. The binding energy of an electron in the shell of the material nuclei is dependent on the atomic number Z. The probability for the photon to interact with the i^{th} element in compound material is given by [234]

$$P(Z_i, E_\gamma) = \frac{n_{ati}\sigma(Z_i, E_\gamma)}{\sum_i [n_{ati} \cdot \sigma_i(E_\gamma)]}. \tag{4.3}$$

A photon quantum is absorbed only if $E_\gamma > B_{shell}$ where B_{shell} is energy of the shell and the total kinetic energy of the secondary photoelectron produced [234] is given by:

$$T_{photoelectron} = E_\gamma - B_{shell}(Z_i) \tag{4.4}$$

The photoelectron interactions are as given in the relevant sections of this chapter.

4.1.2 Photon Conversion

In the field of the nucleus, a photon quantum above the energy threshold undergoes pair-production conversion. The interaction total cross-section per atom nuclei for the conversion process for a gamma of energy E_γ is given by [234]

$$\sigma(Z, E_\gamma) = Z(Z+1)\left[F_1(X) + F_2(X)\,Z + \frac{F_3(X)}{Z}\right], \tag{4.5}$$

where Z is the atomic number of the nuclei and $X = \ln(E_\gamma/m_e c^2)$. The F_n terms are given by

$$\begin{aligned} F_1(X) &= a_0 + a_1X + a_2X^2 + a_3X^3 + a_4X^4 + a_5X^5 \\ F_2(X) &= b_0 + b_1X + b_2X^2 + b_3X^3 + b_4X^4 + b_5X^5 \\ F_3(X) &= c_0 + c_1X + c_2X^2 + c_3X^3 + c_4X^4 + c_5X^5, \end{aligned} \tag{4.6}$$

the parameters a_i, b_i, c_i are extracted from least-squares fit to the database data. The parameters covers data in the range $1 \leq Z \leq 100$ and $E_\gamma \in [1.5\text{ MeV}, 100\text{ GeV}]$ with fitting accuracy estimated at $\frac{\Delta\sigma}{\sigma} \leq 5\%$ and mean value of $\approx 2.2\%$. For $E_\gamma > 100$ GeV the cross section takes a constant value. For $E_{low} < 1.5$ MeV the following equation for extrapolation is applied

$$\sigma(E) = \sigma(E_{low}) \cdot \left(\frac{E - 2m_e c^2}{E_{low} - 2m_e c^2}\right)^2 \tag{4.7}$$

with the various terms having their usual meaning.

In the material, the photon conversion mean free path, λ, to an (e^+, e^-) pair is given by a similar equation to 4.2. The differential cross section depends on the atomic number Z of the material in which the interaction occurs. In a compound material, the pair production probability with element i is randomly picked using [234]

$$P(Z_i, E_\gamma) = \frac{n_{ati}\sigma(Z_i, E_\gamma)}{\sum_i [n_{ati} \cdot \sigma_i(E_\gamma)]} \tag{4.8}$$

with the various terms having their usual meaning. The electron cloud fields provide an additional contribution to pair production process proportional to Z, which is given by [234]

$$\xi(Z) = \frac{\ln(1440/Z^{2/3})}{\ln(183/Z^{1/3}) - f_c(Z)}. \tag{4.9}$$

where

$$f_c(Z) = (\alpha Z)^2 \left[\frac{1}{1+(\alpha Z)^2} + 0.20206 - 0.0369(\alpha Z)^2 + 0.0083(\alpha Z)^4 - 0.0020(\alpha Z)^6 + \cdots \right]$$

α is the fine-structure constant of the Bethe-Heitler formula [234]. For the e^+ and e^- momentum, they are assumed coplanar with the parent photon. This and energy conservation, is then used to calculate the momentum vectors of the (e^+, e^-) pair and global reference system rotation.

4.1.3 Compton Scattering

In GEANT4, the simulation of the Compton scattering interaction of a photon with an atomic electron is performed by an empirical cross section equation. The technique reproduces the interaction cross section data for $E_\gamma > 10$ keV and is expressed by [234]

$$\sigma(Z, E_\gamma) = \left[P_1(Z) \frac{\log(1+2X)}{X} + \frac{P_2(Z) + P_3(Z)X + P_4(Z)X^2}{1 + aX + bX^2 + cX^3} \right] \tag{4.10}$$

where,

$$\begin{aligned} Z &= \text{atomic number of the medium,} \\ E_\gamma &= \text{energy of the photon} \\ X &= E_\gamma / mc^2 \\ m &= \text{electron mass} \\ P_i(Z) &= Z(d_i + e_i Z + f_i Z^2), \end{aligned}$$

The parameter values are evaluated according to the cross section per atom Z. The parameters are extracted from fits to over 511 data points chosen in the interval range $(1 \leq Z \leq 100)$ and $(E_\gamma \in [10\text{ keV}, 100\text{ GeV}])$ The accuracy of the fit is estimated at

$$\frac{\Delta\sigma}{\sigma} = \begin{cases} \approx 10\% & \text{for} E_\gamma \simeq 10\text{ keV} - 20\text{ keV} \\ \leq 5 - 6\% & \text{for } E_\gamma > 20\text{ keV} \end{cases} \tag{4.11}$$

The Compton Effect mean free path, λ, for a photon in the material is given by [234]

$$\lambda(E_\gamma) = \frac{1}{\left(\sum_i n_{ati} \cdot \sigma_i(E_\gamma)\right)} \tag{4.12}$$

where n_{ati} is the number of atoms per volume of the i^{th} element of the material. The Klein-Nishina quantum mechanical differential cross section per atom is provided by

$$\frac{d\sigma}{d\epsilon} = \pi r_e^2 \frac{m_e c^2}{E_0} Z \left[\frac{1}{\epsilon} + \epsilon\right]\left[1 - \frac{\epsilon \sin^2\theta}{1+\epsilon^2}\right] \tag{4.13}$$

where r_e = classical electron radius $m_e c^2$ = electron mass E_0 = energy of the incident photon E_1 = energy of the scattered photon $\epsilon = E_1/E_0$. Assuming an elastic collision, the Compton scattering angle θ of the photon is expressed as

$$E_1 = E_0 \frac{m_e c^2}{m_e c^2 + E_0(1-\cos\theta)}. \tag{4.14}$$

The differential cross-section is valid for only those collisions in which the energy of the recoil electron is larger than its binding energy, which is negligible overall at very low photon energies because of the small number of recoil electrons produced [234].

4.1.4 Multiple Scattering

The multiple scattering process of particles in matter, is simulated at each step, calculating the path length correction and the lateral displacement using either the "detailed" or the "condensed" model approaches. In the detailed model, all the interactions the particle undergoes are simulated, the result of which are typical of the transport equations. This is done for a low number of interactions, achievable in special geometries such as thin foils or in the case of low particle kinetic energies. For large kinetic energies, the average number of collisions is very large, and the detailed approach becomes inefficient. Therefore for high energy simulation, the condensed algorithm codes are used, with the global effects calculated at the end of a track segment. These effects include; the net displacement, energy loss, and direction change of the particle. The accuracy of the condensed model is set by the multiple scattering theory approximations.

The version of GEANT4 used, has implemented a new kind of multiple scattering simulation based on the Lewis theory and relies on the model functions to determine the angular and spatial distributions for each step [234]. The functions are chosen such that moments of the angular and spatial distributions are the same those of Lewis.

As particle is transported step by step through the detector geometry, the properties of the multiple scattering process is set by the transport mean free path, λ_k, which is a function of the energy in the material. The k^{th} transport mean free path is defined as [234]

$$\frac{1}{\lambda_k} = 2\pi n_a \int_{-1}^{1} [1 - P_k(cos\chi)] \frac{d\sigma(\chi)}{d\Omega} d(cos\chi) \tag{4.15}$$

where $d\sigma(\chi)/d\Omega$ is the differential cross section of the scattering, $P_k(cos\chi)$ is the k^{th} Legendre polynomial, and n_a is the number of atoms per volume.

The majority of the mean properties of multiple scattering simulations depend only on the first and second transport mean free paths. The mean value of the geometrical path length (first moment) corresponding to the given true path length t is represented by [234]

$$\langle z \rangle = \lambda_1 \left(1 - \exp\left[-\frac{t}{\lambda_1} \right] \right) \tag{4.16}$$

where z is the shortest distance between the end points of a given step. Equation 4.16 is an exact result for the mean value of z if the differential cross section has axial symmetry and the energy loss is negligible. At the end of the true step length, t, the scattering angle is θ. The mean value of $\cos\theta$ is

$$\langle cos\theta \rangle = \exp\left[-\frac{t}{\lambda_1} \right]. \tag{4.17}$$

The variance of $\cos\theta$ is

$$\sigma^2 = \langle cos^2\theta \rangle - \langle cos\theta \rangle^2 = \frac{1 + 2e^{-2\kappa\tau}}{3} - e^{-2\tau} \tag{4.18}$$

where $\tau = t/\lambda_1$ and $\kappa = \lambda_1/\lambda_2$. The square of the mean lateral displacement is [234]

$$\langle x^2 + y^2 \rangle = \frac{4\lambda_1^2}{3} \left[\tau - \frac{\kappa + 1}{\kappa} + \frac{\kappa}{\kappa - 1} e^{-\tau} - \frac{1}{\kappa(\kappa - 1)} e^{-\kappa\tau} \right]. \tag{4.19}$$

assuming that the initial particle direction is parallel to the the z axis.

The multiple scattering process calculates the transport mean free path values for electrons and positrons in the kinetic energy range 100 eV - 20 MeV for 15 different materials. It is also possible to linearly interpolate or extrapolate the transport cross section, $\sigma_1 = 1/\lambda_1$, in atomic number Z and in the square of the particle velocity, β^2. The ratio κ takes a constant value of 2.5.

4.1.5 Electron Ionisation

The particle energy loss simulation in GEANT4 treats $(e + /e-)$, $(\mu + \mu-)$ and charged hadrons similarly. The energy loss process considers the continuous and discrete energy loss in the material. The particle energy loss simulation below the threshold energy is continuous whereas above it, it is simulated by the explicit production of secondary particles - gammas, electrons, and positrons. The differential cross-section per atom, for the ejection of a secondary particle with kinetic energy T by an incident particle of total energy E moving in a material of density ρ is represented by $\frac{d\sigma(Z,E,T)}{dT}$ (where Z is the atomic number). The mean rate of energy loss is given by [234]

$$\frac{dE_{soft}(E, T_{\text{cut}})}{dx} = n_{at} \cdot \int_0^{T\text{cut}} \frac{d\sigma(Z, E, T)}{dT} T \, dT \tag{4.20}$$

where n_{at} is the number of atoms per volume in the material and T_{cut} is the kinetic energy cut-off or production threshold. The total cross section per atom for the ejection of a secondary particle of energy $T > T_{\text{cut}}$ is

$$\sigma(Z, E, T_{\text{cut}}) = \int_{T_{\text{cut}}}^{T_{max}} \frac{d\sigma(Z, E, T)}{dT} \, dT \tag{4.21}$$

where T_{max} is the maximum energy of the secondary particle. For the case of particle multiple energy loss processes, the total continuous part of the energy loss is the sum

$$\frac{dE^{\text{tot}}_{soft}(E, T_{\text{cut}})}{dx} = \sum_i \frac{dE_{soft,i}(E, T_{\text{cut}})}{dx}. \tag{4.22}$$

The total cross section per atom for Möller scattering (e^-e^-) and Bhabha scattering (e^+e^-) is obtained from the integration of 4.21. In the simulation T_{cut} is always 1 keV or larger. For delta ray energies much larger than the excitation energy of the material ($T \gg I$), the total cross section is given by the Möller scattering relation,

$$\begin{aligned}\sigma(Z, E, T_{\text{cut}}) &= \frac{2\pi r_e^2 Z}{\beta^2(\gamma-1)} \cdot \\ &\left[\frac{(\gamma-1)^2}{\gamma^2}\left(\frac{1}{2}-x\right)+\frac{1}{x}-\frac{1}{1-x}-\frac{2\gamma-1}{\gamma^2}\ln\frac{1-x}{x}\right]\end{aligned} \tag{4.23}$$

and for Bhabha scattering (e^+e^-),

$$\begin{aligned}\sigma(Z, E, T_{\text{cut}}) &= \frac{2\pi r_e^2 Z}{(\gamma-1)} \cdot \\ &\left[\frac{1}{\beta^2}\left(\frac{1}{x}-1\right)+B_1\ln x+B_2(1-x)-\frac{B_3}{2}(1-x^2)+\frac{B_4}{3}(1-x^3)\right]\end{aligned} \tag{4.24}$$

where

$$\begin{aligned} \gamma &= E/mc^2 & B_1 &= 2-y^2 \\ \beta^2 &= 1-(1/\gamma^2) & B_2 &= (1-2y)(3+y^2) \\ x &= T_{\text{cut}}/(E-mc^2) & B_3 &= (1-2y)^2+(1-2y)^3 \\ y &= 1/(\gamma+1) & B_4 &= (1-2y)^3 \end{aligned}$$

The above formulae give the total cross section for scattering above the threshold energies $T^{\text{thr}}_{\text{Möller}} = 2T_{\text{cut}}$ and $T^{\text{thr}}_{\text{Bhabha}} = T_{\text{cut}}$, whereas the mean free path for a material is obtained from

$$\lambda = (n_{at}\cdot\sigma)^{-1} \quad or \quad \lambda = \left(\textstyle\sum_i n_{ati}\cdot\sigma_i\right)^{-1} \tag{4.25}$$

These values are determined in the initialization stage of the GEANT4 kernel and stored in the dE/dx table. With this table, the ranges of the particle in any materials are calculated and stored in the *Range* table and inverted form *InverseRange* table. During run-time, values of the particle's continuous energy loss and range are retrieved from the tables. For electrons, the default energy interval for these tables extends from 100 eV to 100 TeV in 120 bin numbers.

4.1.6 Electron Bremsstrahlung

In GEANT4, electron and positron bremsstrahlung energy loss via the radiation of photons in the field of a nucleus done as described in section 4.1.5. Above a given energy threshold, the energy loss is simulated by the explicit production of photons whereas below it emission of soft photons is treated as a continuous energy loss. The differential cross section for the production of a photon of energy k by an electron of kinetic energy T in the field of an atom of charge Z is expressed by $d\sigma(Z,T,k)/dk$. If k_c is the energy cut-off below which the soft photons are treated as continuous energy loss, then the average value of the energy lost by the electron is given by [234]

$$E_{Loss}^{brem}(Z,T,k_c) = \int_0^{k_c} k \frac{d\sigma(Z,T,k)}{dk} dk. \tag{4.26}$$

The total cross section for the emission of a photon of energy larger than k_c is expressed by

$$\sigma_{brem}(Z,T,k_c) = \int_{k_c}^{T} \frac{d\sigma(Z,T,k)}{dk} dk. \tag{4.27}$$

A tabulation of the bremsstrahlung cross section $d\sigma/dk$ for electrons with kinetic energies T from 1 keV to 10 GeV was found adequate for normal simulations and whereas above 10 GeV the screened Bethe-Heitler differential cross section combined with the dielectric suppression correction is used [234].

4.1.7 Particle Annihilation

The particle annihilation interaction in GEANT4, simulates the annihilation of moving positron with an atomic electron. The simulation assumes that the atomic electron is unbound and static. It also assumes all other exit channels except the two photon annihilation process $e^+e^- \rightarrow \gamma_a\gamma_b$. The interaction cross section is described by the Heitler formula [234]

$$\sigma(Z,E) = \frac{Z\pi r_e^2}{\gamma+1}\left[\frac{\gamma^2+4\gamma+1}{\gamma^2-1}\ln\left(\gamma+\sqrt{\gamma^2-1}\right) - \frac{\gamma+3}{\sqrt{\gamma^2-1}}\right] \tag{4.28}$$

where

E = total energy of the incident positron

$$\gamma = E/mc^2$$

$$r_e = \text{classical electron radius}$$

The interaction mean free path, λ, for positron annihilation with an electron in the material is given by [234]

$$\lambda(E) = \frac{1}{(\sum_i n_{ati} \cdot \sigma(Z_i, E))} \tag{4.29}$$

where n_{ati} is the number of atoms per volume of the i^{th} element composing the material.

4.2 Nuclear Interaction Models

There are different nuclear interaction models available for particle interaction in GEANT4. For the present energy regime, these include the intra-nuclear cascade models, precompound model and the equilibrium evaporation model among others. The precompound interaction mechanism implemented in the precompound model is based on the semi-classical exciton model and is used to simulate the high energy continuum region of the particle emission in order to fill the missing gap left by the arbitrary cut-off of the Intra-Nuclear Cascade used for simulating high energy collisions and the Equilibrium Evaporation Models used in the low energy regime. The Fermi break-up model for light nuclei and multi-fragmentation for very highly excited nuclei is also implemented. To decide when and where the interactions occur, reaction cross sections are used. For nucleus-nucleus collisions, it is given by $\sigma_R = \sigma_T - \sigma_{el}$ where (σ_T) is the total reaction cross section and (σ_{el}) is the elastic cross section. The total reaction cross section from both theoretical and experimental studies plus several empirical parameterizations is utilised in GEANT4. The four implementations available include the parameterizations formulae from Refs. [235], [236], [237] and [238], selected before the simulation is performed.

4.2.1 The Binary Cascade

The Binary Cascade implementation in GEANT4 is based on the intra-nuclear cascade model for the propagation of primary and secondary particles in the nucleus. The name Binary

Cascade stems from the fact that interactions occur between the primary, secondary and the individual particles of the nucleus. The interaction cross-section σ_i is determined from the stored database values. By solving the equation of motion numerically, the propagation of the nucleons in the in-medium nuclear matter is established. The cascade is terminated when mean and maximum energy of the secondary particles is below the set threshold. The final product is passed on to the precompound and evaporation models covered in sections 4.2.2 and 4.2.3. The impact parameter for the primary particle is selected randomly for a disk at the edge of the nucleus and perpendicular to an axis going through its centre and parallel to the momentum vector direction. The distance of closest approach d_i^{min} to a given target nucleon i and the corresponding time-of-flight t_i^d are evaluated taking a linear trajectory from the disk and with the assumption that the target nucleons are at rest [234].

The projectile primaries are allowed to interact with the target nucleons when distance of closest approach $d_i^{min} < \sqrt{\frac{\sigma_i}{\pi}}$ is satisfied. The potential candidate for interaction forms the collisions, which are stored in order of the time-of-flight t_i^d. A new impact parameter is chosen in the event that no collision occurs. In the course of tracking the primary particle, the time to make the first collision yields the time-step. For the particles that are outside the nucleus given by $3fm$ away from the outermost nucleon radius, particles move in straight lines. Those particles that enter the nucleus will have their energy modified to account for Coulomb effects whereas in the nucleus, particles are propagated in the scalar nuclear field. The equation of motion in the field is evaluated for a given time-step applying the Runge-Kutta integration technique. At the end of each time step, the primary particle and the nucleon interact as determined by the scattering term. The secondary particles produced are checked to ensure that the Pauli Exclusion Principle is obeyed. If any of the two particles has a momentum below Fermi momentum, the interaction is suppressed, and the original primary is tracked to the next collision. When an interaction occurs, the secondary particles created are treated just like the primaries. In certain instances the new primary particles are short-lived intermediaries. These intermediaries are treated like others in the collisions, except that their collision time is tied to the decay of the

particle. All secondary particles which are produced are tracked until they leave the nucleus, or until the cascade is over [234].

In the simulations, the description of the target nucleus, is accomplished by constructing the nucleus from A nucleons and Z protons with nucleon coordinates $\mathbf{r}_i$ and momentum $\mathbf{p}_i$, for $i = 1, 2, ..., A$. The initialization process is obtained by a common Monte Carlo technique often applied in most of the high energy nuclear interaction models. The nucleus is assumed isotropic, with each nucleon placed randomly in space using direction and the predetermined radius r_i. The nuclear radii r_i is randomly selected in the nucleus rest frame and according to the nucleon density $\rho(r_i)$. For nuclei with $A > 16$, the nucleon density is given by

$$\rho(r_i) = \frac{\rho_0}{1 + \exp\left[(r_i - R)/a\right]} \tag{4.30}$$

where $\rho_0 \approx \frac{3}{4\pi R^3}(1 + \frac{a^2\pi^2}{R^2})^{-1}$ for $R = r_0 A^{1/3}$ fm, $r_0 = 1.16(1 - 1.16A^{-2/3})$ fm and $a \approx 0.545$ fm. For $A < 17$ nuclei, nucleon density calculations uses a harmonic oscillator shell model given by

$$\rho(r_i) = (\pi R^2)^{-3/2} \exp\left(-r_i^2/R^2\right) \tag{4.31}$$

where $R^2 = 2/3\langle r^2\rangle = 0.8133A^{2/3}$ fm ^{2}. The nucleon repulsive core is taken handled by assuming the inter-nucleon distance $d > 0.8$ fm. The initially nucleon momentum p_i are obtained by sampling randomly in the range $0 - p_F^{max}(r)$, such that the peak momentum of nucleons, vary according to the nucleon particle density ρ expressed by the equation

$$p_F^{max}(r) = \hbar c(3\pi^2\rho(r))^{1/3} \tag{4.32}$$

with the assumption of isotropic nucleons distribution in momentum space and a static nucleus $\sum_i \mathbf{p_i} = \mathbf{0}$; The energy per nucleon is evaluated using $e = E/A = m_N + B(A,Z)/A$, where m_N is nucleon mass and $B(A,Z)$ the nucleus binding energy in order to get the effective mass of each nucleon $m_i^{eff} = \sqrt{(E/A)^2 - p_i^{2\prime}}$ [234].

The optical and phenomenological potential effect due to collective nuclear elastic interaction of the primary and secondary particles is approximated by the nuclear scalar potential

given for proton and neutron projectiles by the local Fermi momentum $p_F(r)$ equation.

$$V(r) = \frac{p_F^2(r)}{2m} \tag{4.33}$$

where m is the mass of the neutron m_n or the mass of proton m_p. The free particle cross sections used in the simulations are reduced to their effective values in the nucleus because of the Pauli-blocking process. The secondary particles created by the collision are also checked for occupation states allowed by Fermi statistics. The nucleus is assumed to be in its ground state and all the states below Fermi energy are occupied. The momentum p_i of the secondary nucleons is required to satisfy the condition that $p_i > p_F^{max}(r)$ where $p_F(r)$ is the local Fermi momentum. The collision nucleon that fails the condition is Pauli blocked and the secondary products abandoned while keeping the original particle in the cascade process [234].

In the description of the reactive part of scattering term of the scattering amplitude are two particle binary collisions, resonance production and decay. Collisions happen when this condition is satisfied $\frac{\sigma_t}{\pi} > d_t^2$ where d_t is the transverse distance of the projectile target pair and σ_t is the corresponding total cross-section. The final state of the collision is produced through the propagation of all the particles to the time of closest approach. In the calculation of the total inclusive cross-sections for inelastic and elastic processes, experimental data are used wherever available. Individual channel cross-section showing resonance structure and energy dependency are modelled according to the Breit-Wigner function and the actual widths are based on the UrQMD approach [234].

The elastic scattering angular distributions of nucleons are taken from the result of phase-shift experimental analysis. The final states are derived from sampling the tables of the cumulative distribution function of the centre-of-mass scattering angle, tabulated for a discrete set of lab kinetic energies from 10 MeV to 1200 MeV. The Coulomb effects are considered for pp scattering. The angular distributions for final states products are calculated analytically, as inferred from the collision term of the in-medium relativistic Boltzmann-Uehling-Uhlenbeck

equation, nucleon-nucleon elastic scattering cross-sections [234]

$$\sigma_{NN\to NN}(s,t) = \frac{1}{(2\pi)^2 s}\left[D(s,t) + E(s,t) + (s,t \longleftrightarrow u)\right] \tag{4.34}$$

Where s, t, u are the Mandelstamm variables, $D(s,t)$ being the direct term, and $E(s,t)$ the exchange term, given by

$$\begin{aligned} D(s,t) = \quad & \frac{(g^{\sigma}_{NN})^4(t-4m^{*}2)^2}{2(t-m^2_{\sigma})^2} + \frac{(g^{\omega}_{NN})^4(2s^2+2st+t^2-8m^{*2}s+8m^{*4})}{(t-m^2_{\omega})^2} + \\ & \frac{24(g^{\pi}_{NN})^4 m^{*2}t^2}{(t-m^2_{\pi})^2} - \frac{4(g^{\sigma}_{NN}g^{\omega}_{NN})^2(2s+t-4m^{*2})m^{*2}}{(t-m^2_{\sigma})(t-m^2_{\omega})}, \end{aligned} \tag{4.35}$$

and

$$\begin{aligned} E(s,t) = \quad & \frac{(g^{\sigma}_{NN})^4\left(t(t+s)+4m^{*2}(s-t)\right)}{8(t-m^2_{\sigma})(u-m^2_{\sigma})} + \frac{(g^{\omega}_{NN})^4(s-2m^{*2})(s-6m^{*2}))}{2(t-m^2_{\omega})(u-m^2_{\omega})} - \\ & \frac{6(g^{\pi}_{NN})^4(4m^{*2}-s-t)m^{*4}t}{(t-m^2_{\pi})(u=m_p i^2)} + \frac{3(g^{\sigma}_{NN}g^{\pi}_{NN})^2 m^{*2}(4m^{*2}-s-t)(4m^{*2}-t)}{(t-m^2_{\sigma})(u-m^2_{\pi})} + \\ & \frac{3(g^{\sigma}_{NN}g^{\pi}_{NN})^2 t(t+s)m^{*2}}{2(t-m^2_{\pi})(u-m^2_{\sigma})} + \frac{(g^{\sigma}_{NN}g^{\omega}_{NN})^2 t^2-4m^{*2}s-10m^{*2}t+24m^{*4}}{4(t-m^2_{\sigma})(u-m^2_{\omega})} + \\ & \frac{(g^{\sigma}_{NN}g^{\omega}_{NN})^2(t+s)^2-2m^{*2}s+2m^{*2}t}{4(t-m^2_{\omega})(u-m^2_{\sigma})} + \frac{3(g^{\omega}_{NN}g^{\pi}_{NN})^2(t+s-4m^{*2})(t+s-2m^{*2})}{(t-m^2_{\omega})(u-m^2_{\pi})} + \\ & \frac{3(g^{\omega}_{NN}g^{\pi}_{NN})^2 m^{*2}(t^2-2m^{*2}t)}{(t-m^2_{\pi})(u-m^2_{\omega})}. \end{aligned} \tag{4.36}$$

When a particle other than the incident particle leaves the nucleus, the ground state of the system is changed. The outgoing particle energy is disallowed when the total mass of the nucleus produced is below its ground state mass. This is avoided by reducing the energy of the outgoing nucleons by the differences in masses. The calculation of the final excited nucleus momentum using the energy momentum balance may also lead to a mass below its ground state value. This is accomplished by arbitrarily scaling the momentum of the outgoing particles by a factor derived from the nucleus mass and that of the system of outgoing particle [234].

In the simulation of light ion interactions, the initial state of the cascade is prepared in the form of two nuclei, as described in the previous paragraphs. The lighter of the collision partners makes the projectile. The nucleons in it are entered, with position and momentum, into the initial state of the cascade. In the initial interaction of individual nucleons, the projectile nucleon's Fermi-momentum is neglected in the tracking process inside the target nucleus. The nucleon

distribution inside the projectile nucleus is taken to be a representative distribution of its nucleons in configuration space, rather than an initial state in the sense of the Quantum Molecular Dynamics. The Fermi momentum and the local field are taken into account in the calculation of the collision probabilities and final states of the binary collisions. The cascade assumptions eventually break down at low energies, and the right model has to be switched. The transition in the present GEANT4 code has not been studied in depth and some suggestions for further improvements are given. The code uses the following criterion to determine when cascading is turned off and pre-equilibrium decay turned on. If there particles exists whose kinetic energy is above the threshold of 75 MeV, binary cascade is on. The moment the mean kinetic energy of the participants drop below another threshold of 15 MeV, then the cascade is terminated. The final state products of the binary cascade are then used to define the initial state for the precompound model to take up. The initial state is characterized by the number of nucleons in the fragment, the charge of the fragment, the number of holes, the number of all excitons, and the number of charged excitons, and the four momentum of the fragment. The number of holes is provided by the difference of the number of nucleons in the original nucleus and the number of non-excited nucleons left in the product. An exciton is a nucleon captured in the fragment at the end of the cascade. The momentum of the fragment derived from the difference between the momentum of the primary and the outgoing secondary particles is split in two components. These are the momentum acquired by coherent elastic effects and the momentum of the excitons in the nucleus rest frame. The latter is passed to the precompound models. The products arising from the de-excitation models, including the final nucleus, are transformed back to the frame of the moving projectile fragment. The projectile excitation energy is evaluated from the binary collision participants (P) using the statistical approach towards excitation energy calculation in an adiabatic abrasion process described $E_{ex} = \sum_P (E^P_{fermi} - E^P)$. With this excitation energy, the projectile fragment is passed onto the by the evaporation models as in the case of the binary cascade [234].

4.2.2 Precompound Model

The GEANT4 precompound model is the extension of the hadrons kinetic model. As explain in section 4.2.1, the initial state for calculation of the precompound nuclear de-excitation stage is characterised by the atomic mass number A, the charge Z of residual nucleus, its four momentum P_0, the excitation energy U and the number of excitons n from the sum of the number of particles p (with p_Z charged) and number of holes h. The approach is based on the works of Ref. [239], which considers all possible nuclear transitions for the number of excitons n with $\Delta n = +2, -2, 0$, defining the transition probabilities. The emission process of the model take into account only the neutrons, protons, deuterons, tritons and α particles. The precompound stage of nuclear interaction is valid until the nuclear system is in an equilibrium state after which the equilibrium model is switched on for possibly more emission of particles or photons from the quasi-equilibrated nucleus [234]. The statistical equilibrium state is characterized by an equilibrium number of excitons n_{eq}, all three type of transitions are equiprobable. Thus n_{eq} is fixed by $\omega_{+2}(n_{eq}, U) = \omega_{-2}(n_{eq}, U)$. The condition leads to [234]

$$n_{eq} = \sqrt{2gU} \tag{4.37}$$

Equation 4.37 is obtain by assuming an equidistant scheme of single-particle levels with the density $g \approx 0.595aA$, where a is the level density parameter, when the level density of the n -exciton state is

$$\rho_n(U) = \frac{g(gU)^{n-1}}{p!h!(n-1)!}. \tag{4.38}$$

The partial transition probabilities altering the exciton number by Δn is evaluated by the squared matrix element averaged over allowed transitions $\langle|M|^2\rangle$ and the density of final states $\rho_{\Delta n}(n, U)$, which are actually accessible in the transition and defined by

$$\omega_{\Delta n}(n, U) = \frac{2\pi}{h}\langle|M|^2\rangle\rho_{\Delta n}(n, U) \tag{4.39}$$

The density of final states $\rho_{\Delta n}(n, U)$ are derived from the equation 4.38 for the level density of the n -exciton state corrected for the Pauli principle and non-distinguishable identical excitons

to get:

$$\rho_{\Delta n=+2}(n,U) = \frac{1}{2}g\frac{[gU - F(p+1,h+1)]^2}{n+1}[\frac{gU - F(p+1,h+1)}{gU - F(p,h)}]^{n-1} \tag{4.40}$$

$$\rho_{\Delta n=0}(n,U) = \frac{1}{2}g\frac{[gU - F(p,h)]}{n}[p(p-1) + 4ph + h(h-1)] \tag{4.41}$$

and

$$\rho_{\Delta n=-2}(n,U) = \frac{1}{2}gph(n-2) \tag{4.42}$$

with $F(p,h) = (p^2+h^2+p-h)/4-h/2$ equated to zero. The calculation of the averaged squared matrix element $\langle|M|^2\rangle$ is avoided by assuming that transition probability $\omega_{\Delta n=+2}(n,U)$ is equal to the probability for quasi-free scattering of the nucleon-nucleon above the Fermi energy of the target nucleus given by

$$\omega_{\Delta n=+2}(n,U) = \frac{\langle\sigma(v_{\text{rel}})v_{\text{rel}}\rangle}{V_{\text{int}}}. \tag{4.43}$$

In equation 4.43 the interaction volume is estimated as $V_{\text{int}} = \frac{4}{3}\pi(2r_c + \lambda/2\pi)^3$, with the De Broglie wave length $\lambda/2\pi$ which corresponds to the relative velocity $\langle v_{\text{rel}}\rangle = \sqrt{2T_{\text{rel}}/m}$, where m is nucleon mass and $r_c = 0.6$ fm. The averaging in $\langle\sigma(v_{\text{rel}})v_{\text{rel}}\rangle$ is further simplified by

$$\langle\sigma(v_{\text{rel}})v_{\text{rel}}\rangle = \langle\sigma(v_{\text{rel}})\rangle\langle v_{\text{rel}}\rangle \tag{4.44}$$

For $\sigma(v_{\text{rel}})$ the following approximation is used

$$\sigma(v_{\text{rel}}) = 0.5[\sigma_{pp}(v_{\text{rel}}) + \sigma_{pn}(v_{\text{rel}}]P(T_F/T_{\text{rel}}) \tag{4.45}$$

the factor $P(T_F/T_{\text{rel}})$ takes care of the Pauli principle such that

$$P(T_F/T_{\text{rel}}) = 1 - \frac{7}{5}\frac{T_F}{T_{\text{rel}}} \tag{4.46}$$

for $\frac{T_F}{T_{\text{rel}}} \leq 0.5$ and

$$P(T_F/T_{\text{rel}}) = 1 - \frac{7}{5}\frac{T_F}{T_{\text{rel}}} + \frac{2}{5}\frac{T_F}{T_{\text{rel}}}(2 - \frac{T_{\text{rel}}}{T_F})^{5/2} \tag{4.47}$$

for $\frac{T_F}{T_{\text{rel}}} > 0.5$.

The free-particle proton-proton $\sigma_{pp}(v_{\text{rel}})$ and proton-neutron $\sigma_{pn}(v_{\text{rel}})$ interaction cross sections are approximated by the following expressions [234]

$$\sigma_{pp}(v_{\text{rel}}) = \frac{10.63}{v_{\text{rel}}^2} - \frac{29.93}{v_{\text{rel}}} + 42.9 \tag{4.48}$$

and

$$\sigma_{pn}(v_{\text{rel}}) = \frac{34.10}{v_{\text{rel}}^2} - \frac{82.2}{v_{\text{rel}}} + 82.2, \tag{4.49}$$

for cross sections expressed in mb.

The average relative kinetic energy T_{rel} needed to calculate $\langle v_{\text{rel}} \rangle$ and the factor $P(T_F/T_{\text{rel}})$ was computed as $T_{\text{rel}} = T_p + T_n$, with $T_p = T_F + U/n$ representing the average kinetic energies of projectile nucleons and $T_N = 3T_F/5$ for the target nucleons. When equations 4.39 and 4.43 are combined with the assumption that $\langle |M|^2 \rangle$ have the same transitions for $\Delta n = 0$ and $\Delta n = \pm 2$, the other transition probabilities are [234]

$$\begin{gathered} \omega_{\Delta n=0}(n, U) = \\ = \frac{\langle \sigma(v_{\text{rel}}) v_{\text{rel}} \rangle}{V_{\text{int}}} \frac{n+1}{n} \left[\frac{gU - F(p,h)}{gU - F(p+1,h+1)}\right]^{n+1} \frac{p(p-1) + 4ph + h(h-1)}{gU - F(p,h)} \end{gathered} \tag{4.50}$$

and

$$\begin{gathered} \omega_{\Delta n=-2}(n, U) = \\ = \frac{\langle \sigma(v_{\text{rel}}) v_{\text{rel}} \rangle}{V_{\text{int}}} \left[\frac{gU - F(p,h)}{gU - F(p+1,h+1)}\right]^{n+1} \frac{ph(n+1)(n-2)}{[gU - F(p,h)]^2}. \end{gathered} \tag{4.51}$$

The emission probability is selected as done in the classical equilibrium Weisskopf-Ewing model [240]. For nucleon b in the energy interval $(T_b, T_b + dT_b)$ the probability is provided by [234]

$$W_b(n, U, T_b) = \sigma_b(T_b) \frac{(2s_b + 1)\mu_b}{\pi^2 \hbar^3} R_b(p, h) \frac{\rho_{n-b}(E^*)}{\rho_n(U)} T_b \tag{4.52}$$

with $\sigma_b(T_b)$ representing the cross section of the inverse process, s_b the nucleon spin factor, m_b the reduced mass factor, whiles $R_b(p, h)$ takes care of the exciton proton-neutron aspect, $\rho_n(U)$ and $\rho_{n-b}(E^*)$ are level densities of the nucleus before and after nucleon emission as defined in the evaporation model, whiles the $E^* = U - Q_b - T_b$ term represents the excitation energy of nucleus after the emission process [234].

It has been assumed that nucleons inside the excited nucleus are able to "coalescence" to form complex nucleon clusters. The "coalescence probability to produce the cluster consisting of N_b nucleons inside the nucleus of A nucleons is given by [234]

$$\gamma_{N_b} = N_b^3 (V_b/V)^{N_b - 1} = N_b^3 (N_b/A)^{N_b - 1} \tag{4.53}$$

for cluster V_b and and nucleus b volumes. In the pre-equilibrium stage of the interaction process, the complex cluster has a certain probability of being emitted given by [234]

$$W_b(n, U, T_b) = \gamma_{N_b} R_b(p, h) \frac{\rho(N_b, 0, T_b + Q_b)}{g_b(T_b)} \sigma_b(T_b) \frac{(2s_b + 1)\mu_b}{\pi^2 h^3} \frac{\rho_{n-b}(E^*)}{\rho_n(U)} T_b, \tag{4.54}$$

for

$$g_b(T_b) = \frac{V_b(2s_b + 1)(2\mu_b)^{3/2}}{4\pi^2 h^3} (T_b + Q_b)^{1/2} \tag{4.55}$$

representing the single-particle density for the complex cluster b, obtained by assuming that the cluster moves inside the volume V_b of uniform potential and depth of Q_b. The factor $R_b(p, h)$ ensures correct isotopic composition of the cluster b. This total cluster emission probability is defined by

$$W_{\text{tot}}(n, U) = \sum_{\Delta n=+2,0,-2} \omega_{\Delta n}(n, U) + \sum_{b=1}^{6} W_b(n, U) \tag{4.56}$$

to emit cluster b, $W_b(n, U)$ is obtained by integration over T_b equations 4.52 and 4.54 thus

$$W_b(n, U) = \int_{V_b}^{U - Q_b} W_b(n, U, T_b) dT_b \tag{4.57}$$

The kinetic energies of emitted cluster are sampled according to equations 4.52 and 4.54, after which the emitting nucleus parameter are adjusted thus [234]

$$\begin{gathered} A_f = A - A_b; Z_f = Z - Z_b; P_f = P_0 - p_b; \\ E_f^* = \sqrt{E_f^2 - \vec{P}_f^2} - M(A_f, Z_f). \end{gathered} \tag{4.58}$$

where p_b is the emitted cluster four momentum.

4.2.3 Evaporation Model

After the pre-equilibrium stage, the residual nucleus is left in a quasi-equilibrium state, in which the excitation energy E^* of the nucleus is shared by a large number of nucleons. At this stage the nucleus has no memory of its formation. If the excitation energy is higher than some fixed value, it is capable of emitting nucleons and light particles (d, t, ^{3} He, α) that make up the most abundant part of the low energy particle emission in the rest system of the residual

nucleus and comparable to the evaporation of molecules in a liquid drop. The original concept of statistical theory of compound nuclear decay came from Ref. [240]. The approach is based on the application of the detailed balance principle that treats the probabilities of transitions from states i to d or vice-versa via the density of states in the two systems represented by [234]

$$P_{i\to d}\rho(i) = P_{d\to i}\rho(d) \tag{4.59}$$

where $P_{d\to i}$ is the probability per unit of time of a nucleus d to capture a particle j and form a compound nucleus i in proportional to the compound nucleus cross section σ_{inv}. The probability for the parent nucleus i with an excitation energy E^*, to emit a particle j in its ground state with kinetic energy ε is provided by [234]

$$P_j(\varepsilon)\mathrm{d}\varepsilon = g_j\sigma_{\text{inv}}(\varepsilon)\frac{\rho_d(E_{\max}-\varepsilon)}{\rho_i(E^*)}\varepsilon\mathrm{d}\varepsilon \tag{4.60}$$

where $\rho_i(E^*)$ is the level density before emission, $\rho_d(E_{\max}-\varepsilon)$ after emission of a particle j and $E_{\max}$ is the maximum energy of the emitted particle, with spin s_j, mass m_j, g_j and $g_j = (2s_j+1)m_j/\pi^2\hbar^2$. This formula is implemented with a suitable form for the level density and inverse reaction cross section. It relates to the original work given in Ref. [92], representing the first Monte Carlo code for the evaporation process. The advantage of the approach is the fact that it yields a simple expression for equation 4.60 that can be analytically integrated for Monte Carlo sampling.

The inverse reaction cross section is expressed by means of the empirical equation

$$\sigma_{\text{inv}}(\varepsilon) = \sigma_g\alpha\left(1+\frac{\beta}{\varepsilon}\right) \tag{4.61}$$

for geometric cross section $\sigma_g = \pi R^2$. For neutrons, $\alpha = 0.76 + 2.2A^{-\frac{1}{3}}$ and $\beta = (2.12A^{-\frac{2}{3}} - 0.050)/\alpha$ MeV. At lower energies $\sigma_{\text{inv},n}(\varepsilon_{\to 0}) \to \infty$ without causing any problem since only the product $\sigma_{\text{inv},n}(\varepsilon)\varepsilon$ appears in equation 4.60. The inverse cross section used in equation 4.60 is that of a neutron with kinetic energy ε and an excited nucleus state. For the case of charged particles (p, d, t, ^{3}He and α), $\alpha = (1+c_j)$ and $\beta = -V_j$, where c_j is a set of parameters provided for a good fit in the Coulomb barrier potential V_j. The first correction for the Coulomb repulsion

originates from the quantum mechanical barrier penetration phenomenon. The proper uses of quantum mechanical expressions are complex if one wants to keep equation 4.60 in integral form. It is handled by multiplying the electrostatic Coulomb barrier with a coefficient k_j in order to approximately reproduce the barrier penetration.

$$V_j = k_j \frac{Z_j Z_d e^2}{R_c} \tag{4.62}$$

The second correction is for the separation of the nuclei at contact, R_c. This separation is worked out as $R_c = R_j + R_d$ where $R_{j,d} = r_c A_{j,d}^{1/3}$ for r_c given by

$$r_c = 2.173 \frac{1 + 0.006103 Z_j Z_d}{1 + 0.009443 Z_j Z_d} \tag{4.63}$$

The level density used is based on the simplest Fermi gas model of Ref. [91] for a completely degenerate Fermi gas. It is used with the nucleon pairing corrections proposed in Ref. [241] to take into account the displacements of the ground state given by

$$\rho(E) = C \exp\left(2\sqrt{a(E-\delta)}\right) \tag{4.64}$$

where C is a constant requiring only ratios of level densities for equation 4.60. The δ term is the pairing energy correction of the daughter nucleus while the level density parameter is calculated thus

$$a(E, A, Z) = \tilde{a}(A)\left\{1 + \frac{\delta}{E}[1 - \exp(-\gamma E)]\right\}. \tag{4.65}$$

The maximum kinetic energy of the emitted particle is determined by the separation energy $E^* - \delta - Q_j$ of emitted particle j and $Q_j = M_i - M_d - M_j$ for parent mass M_i, daughter mass M_d and the emitted particle mass M_j. The expression, however, does not take into account the recoil energy of the residual nucleus which is given by the expression [234]

$$\varepsilon_j^{\max} = \frac{(M_i + E^* - \delta)^2 + M_j^2 - M_d^2}{2(M_i + E^* - \delta)} - M_j \tag{4.66}$$

The total decay width for the emitted particle j is obtained by integrating equation 4.60 over the available kinetic energy range

$$\Gamma_j = \hbar \int_{V_j}^{\varepsilon_j^{\max}} P(\varepsilon_j) \mathrm{d}\varepsilon_j \tag{4.67}$$

The integration process is done analytically on equation 4.64 for level densities and equation 4.61 for inverse reaction cross section yielding the total width is given by [234]

$$\Gamma_j = \frac{g_j m_j R_d^2}{2\pi\hbar^2}\frac{\alpha}{a_d^2} \times \left\{\left\{\left(\beta a_d - \frac{3}{2}\right) + a_d(\varepsilon_j^{\max} - V_j)\right\}\exp\left\{-\sqrt{a_i(E^* - \delta_i)}\right\} + \left\{(2\beta a_d - 3)\sqrt{a_d(\varepsilon_j^{\max} - V_j)} + 2a_d(\varepsilon_j^{\max} - V_j)\right\}\times \exp\left\{2\left[\sqrt{a_d(\varepsilon_j^{\max} - V_j)} - \sqrt{a_i(E^* - \delta_i)}\right]\right\}\right\} \quad (4.68)$$

where $a_d = a(A_d, Z_d, \varepsilon_j^{\max})$ and $a_i = a(A_i, Z_i, E^*)$.

An alternative model is also available in the GEANT4 code based on the generalized evaporation model of Ref. [242]. The model takes into account the emission of particles heavier than α using a more accurate level density function for total decay width instead of an approximation. It uses the same set of parameters except for the complex cluster. In the Fermi gas model, the level density function is expressed as [234]

$$\rho(E) = \begin{cases} \frac{\sqrt{\pi}}{12}\frac{e^{2\sqrt{a(E-\delta)}}}{a^{1/4}(E-\delta)^{5/4}} & \text{for} \quad \mathrm{E} \geq \mathrm{E_x} \\ \frac{1}{T}e^{(E-E_0)/T} & \text{for} \quad \mathrm{E} < \mathrm{E_x} \end{cases} \quad (4.69)$$

where $E_x = U_x + \delta$ and $U_x = 150/M_d + 2.5$, M_d is the daughter nucleus mass. The temperature of the nucleus T is related as $1/T = \sqrt{a/U_x} - 1.5U_x$, for $E_0 = E_x - T(\log T - \log a/4 - (5/4)\log U_x + 2\sqrt{aU_x})$. Substituting equation 4.69 into equation 4.60 and integrating over the kinetic energy range yields the following expression [234]

$$\Gamma_j = \frac{\sqrt{\pi} g_j \pi R_d^2 \alpha}{12\rho(E^*)} \times \begin{cases} \{I_1(t,t) + (\beta + V)I_0(t)\} & \text{for} \quad \varepsilon_{\mathrm{j}}^{\max} - \mathrm{V_j} < \mathrm{E_x} \\ \{I_1(t,t_x) + I_3(s,s_x)e^s + & \\ (\beta + V)(I_0(t_x) + I_2(s,s_x)e^s)\} & \text{for} \quad \varepsilon_{\mathrm{j}}^{\max} - \mathrm{V_j} \geq \mathrm{E_x}. \end{cases} \quad (4.70)$$

with $I_0(t)$, $I_1(t,t_x)$, $I_2(s,s_x)$, and $I_3(s,s_x)$ expressed as

$$I_0(t) = e^{-E_0/T}(e^t - 1) \quad (4.71)$$

$$I_1(t,t_x) = e^{-E_0/T}T\{(t - t_x + 1)e^{t_x} - t - 1\} \quad (4.72)$$

$$I_2(s,s_x) = 2\sqrt{2}\Big\{s^{-3/2} + 1.5s^{-5/2} + 3.75s^{-7/2} -$$

$$(s_x^{-3/2} + 1.5s_x^{-5/2} + 3.75s_x^{-7/2})\Big\} \tag{4.73}$$

$$\begin{aligned} I_3(s, s_x) = \frac{1}{2\sqrt{2}}\Big[& 2s^{-1/2} + 4s^{-3/2} + 13.5s^{-5/2} + 60.0s^{-7/2} + \\ & 325.125s^{-9/2} - \Big\{(s^2 - s_x^2)s_x^{-3/2} + (1.5s^2 + 0.5s_x^2)s_x^{-5/2} + \\ & (3.75s^2 + 0.25s_x^2)s_x^{-7/2} + (12.875s^2 + 0.625s_x^2)s_x^{-9/2} + \\ & (59.0625s^2 + 0.9375s_x^2)s_x^{-11/2} + \\ & (324.8s^2 + 3.28s_x^2)s_x^{-13/2} + \Big\}\Big] \end{aligned} \tag{4.74}$$

for $t = (\varepsilon_j^{\max} - V_j)/T$, $t_x = E_x/T$, $s = 2\sqrt{a(\varepsilon_j^{\max} - V_j - \delta_j)}$ and $s_x = 2\sqrt{a(E_x - \delta)}$.

Apart from the light particles, 60 nuclide up to ^{28} Mg are taken into account, in their ground states as well as in their exited states. The excited state is assumed to survive if $T_{1/2}/\ln 2 > \hbar/\Gamma_j^*$, where $T_{1/2}$ is the half-live and Γ_j^* is the emission width of the resonance calculated as the ground state particle emission. The total emission width of particle j is found by summing over all states satisfying the condition.

The fission decay channel is open for $A > 65$ nuclei and compete with the particle and photon evaporation channels. The fission probability per unit time W_{fis} is proportional to the level density $\rho_{\text{fis}}(T)$ (equation 4.64) at the saddle point such that [234]

$$\begin{aligned} W_{\text{fis}} = \frac{1}{2\pi\hbar\rho_{\text{fis}}(E^*)} \int_0^{E^* - B_{\text{fis}}} \rho_{\text{fis}}(E^* - B_{\text{fis}} - T)dT = \\ = \frac{1 + (C_f - 1)\exp(C_f)}{4\pi a_{\text{fis}} \exp(2\sqrt{aE^*})}, \end{aligned} \tag{4.75}$$

where B_{fis} is the fission barrier height, $C_f = 2\sqrt{a_{\text{fis}}(E^* - B_{\text{fis}})}$, a is the level density parameter of the compound nucleus and a_{fis} is that of the fission saddle point nucleus. The level density parameter value is larger at the saddle point than in the ground state ($a_{\text{fis}} > a$). The following parameters are used accordingly, $a_{\text{fis}} = 1.08a$ for $Z < 85$, $a_{\text{fis}} = 1.04a$ for $Z \geq 89$ and $a_f = a[1.04 + 0.01(89. - Z)]$ for $85 \leq Z < 89$. The fission barrier $B_{\text{fis}}(A, Z)$ is approximated by $B_{\text{fis}} = B_{\text{fis}}^0 + \Delta_g + \Delta_p$ The fission barrier height $B_{\text{fis}}^0(x)$ varies with the fissility parameter $x = Z^2/A$. $B_{\text{fis}}^0(x)$ given by $B_{\text{fis}}^0(x) = 12.5 + 4.7(33.5 - x)^{0.75}$ for $x \leq 33.5$, $B_{\text{fis}}^0(x) = 12.5 - 2.7(x - 33.5)^{2/3}$ for $x > 33.5$. The $\Delta_g = \Delta M(N) + \Delta M(Z)$, where $\Delta M(N)$ and $\Delta M(Z)$ are shell

corrections and the pairing energy corrections $\Delta_p = 1$ for odd-odd nuclei, $\Delta_p = 0$ for odd-even nuclei, $\Delta_p = 0.5$ for even-odd nuclei and $\Delta_p = -0.5$ for even-even nuclei.

The model assumes as the first approximation that the dipole $E1$-transitions are the major source of γ photons from the highly-excited nucleus. The probability to evaporate the γ in the energy range $(\epsilon_\gamma, \epsilon_\gamma + d\epsilon_\gamma)$ per unit time is given by [234]

$$W_\gamma(\epsilon_\gamma) = \frac{1}{\pi^2(\hbar c)^3}\sigma_\gamma(\epsilon_\gamma)\frac{\rho(E^* - \epsilon_\gamma)}{\rho(E^*)}\epsilon_\gamma^2, \tag{4.76}$$

where $\sigma_\gamma(\epsilon_\gamma)$ is the inverse process cross section and ρ is a nucleus level density as defined in equation 4.64. The expression for the inverse process cross section is

$$\sigma_\gamma(\epsilon_\gamma) = \frac{\sigma_0\epsilon_\gamma^2\Gamma_R^2}{(\epsilon_\gamma^2 - E_{\mathrm{GDP}}^2)^2 + \Gamma_R^2\epsilon_\gamma^2}, \tag{4.77}$$

where $\sigma_0 = 2.5A$ mb, $\Gamma_R = 0.3E_{\mathrm{GDP}}$ and $E_{\mathrm{GDP}} = 40.3A^{-1/5}$ MeV are empirical parameters of the giant dipole resonance. The total radiation probability is given by

$$W_\gamma = \frac{3}{\pi^2(\hbar c)^3}\int_0^{E^*}\sigma_\gamma(\epsilon_\gamma)\frac{\rho(E^* - \epsilon_\gamma)}{\rho(E^*)}\epsilon_\gamma^2 d\epsilon_\gamma. \tag{4.78}$$

which is integrated numerically and the gamma energy distribution sampled from equation 4.76.

The final step of evaporation model consists of evaporation of characteristic photon energies. The competition between photons and particles as well as the giant resonance photons is neglected at this step. The discrete $E1$, $M1$ and $E2$ photon transitions from tabulated isotopes are considered. There are large data set of isotopes with experimental measurements of the excited energies level, spins, parities and relative transitions probabilities for use in the code for atomic number up to $Z = 98$. Internal conversion is a significant competitive process to photon emission channels and a database is available to store the internal conversion coefficients values. In the production of an internal conversion electron, the energy of the transition must be greater or equal to the binding energy of the shell of origin [234].

4.2.4 Fermi Break-up Model

The GEANT4 Fermi break-up model is for simulation of the light nuclei interactions. The model is able to predict the final states produced by the excitation of the nucleus with atomic number $A < 17$ using statistical break-up approach. The values of excitation energy per nucleon for light nuclei are nearly the same as the nucleon binding energy for light nuclei. Consequently, when they become excited, they preferentially undergo break-up to two or more fragments with branching determined by available phase space. Such a process of nuclear disassembling could be described using the Fermi break-up model [243], to explain the multi-fragmentation process in highly excited nucleus [234].

In the model, an exit channel is only allowed, if the final total kinetic energy E_{kin} of all decay fragments produced from the break-up is positive. This energy is calculated from [234]

$$E_{kin} = U + M(A,Z) - E_{\text{Coul}} - \sum_{b=1}^{n}(m_b + \epsilon_b), \tag{4.79}$$

where m_b is the mass and ϵ_b the excitation energies of fragments, E_{Coul} is the Coulomb barrier for the channel approximated by

$$E_{\text{Coul}} = \frac{3}{5}\frac{e^2}{r_0}(1 + \frac{V}{V_0})^{-1/3}(\frac{Z^2}{A^{1/3}} - \sum_{b=1}^{n}\frac{Z^2}{A_b^{1/3}}), \tag{4.80}$$

where V_0 is the volume of the system corresponding to the normal nuclear matter density and $\kappa = \frac{V}{V_0}$ is a parameter set to unit.

The total break-up probability for nucleus to break-up into n fragments in the final state is given by

$$W(E,n) = (V/\Omega)^{n-1}\rho_n(E) \tag{4.81}$$

where $\rho_n(E)$ is the density of the number of final states, V is the volume of the break-up system and $\Omega = (2\pi\hbar)^3$ is the normalization volume. Three factors define the density of states given by [234]

$$\rho_n(E) = M_n(E)S_nG_n \tag{4.82}$$

The first term in equation 4.82 represents the phase space factor defined by

$$M_n = \int_{-\infty}^{+\infty} ... \int_{-\infty}^{+\infty} \delta(\sum_{b=1}^{n} \mathbf{p_b}) \delta(E - \sum_{b=1}^{n} \sqrt{p^2 + m_b^2}) \prod_{b=1}^{n} d^3 p_b, \tag{4.83}$$

where $\mathbf{p_b}$ is fragment b momentum. The second term in the equation (4.82) represents the spin factor $S_n = \prod_{b=1}^{n}(2s_b + 1)$, for the number of states with different spin orientations. The third term the represents the permutation factor $G_n = \prod_{j=1}^{k} \frac{1}{n_j!}$ that takes care of the identity of fragments in final state, for n_j equal to the number of components, j, the particle type and k defined by $n = \sum_{j=1}^{k} n_j$).

Equation 4.82 treated non-relativistically, can be analytically integrated. The probability for a nucleus with energy E break-up into n fragments with masses m_b, where $b = 1, 2, 3, ..., n$ is given by [234]

$$W(E_{kin}, n) = S_n G_n (\frac{V}{\Omega})^{n-1} (\frac{1}{\sum_{b=1}^{n} m_b} \prod_{b=1}^{n} m_b)^{3/2} \frac{(2\pi)^{3(n-1)/2}}{\Gamma(3(n-1)/2)} E_{kin}^{3n/2-5/2}, \tag{4.84}$$

where $\Gamma(x)$ is the gamma function.

The Fermi break-up model has only one free parameter V that is the volume of the decaying system, calculated by $V = 4\pi R^3/3 = 4\pi r_0^3 A/3$, where $r_0 = 1.4$ fm. The fragments characteristics is taken care of by the formation of fragments in their ground and low-lying excited states, stable from nucleon emission decays. The model considers also several unstable fragments with large lifetimes such as ^5He, ^5Li, ^8Be, ^9B and also the fragment characteristics A_b, Z_b, s_b and ϵ_b from different sources [234].

The nucleus break-up in the model is described by the Monte Carlo procedure. The decay channel is selected randomly using equation 4.84 and condition equation 4.79. For each channel, the kinematics quantities of each fragment is calculated using the n-body phase space distribution equation given by[234]

$$M_n = \int_{-\infty}^{+\infty} ... \int_{-\infty}^{+\infty} \delta(\sum_{b=1}^{n} \mathbf{p_b}) \delta(\sum_{b=1}^{n} \frac{p_b^2}{2m_b} - E_{kin}) \prod_{b=1}^{n} d^3 p_b. \tag{4.85}$$

Lastly, Kopylov's sampling procedure is applied assuming an isotropic angular distribution for the emitted fragments [234].

Chapter 5

Experimental Techniques and Data Reduction

This chapter describes the experimental techniques and the data reduction procedures used. The information covers the following aspects of the study:

- The multi-detector gamma-ray spectrometer, section 5.1;
- The experimental setup, section 5.2;
- The Doppler effect measurements, section 5.3;
- The experimental data reduction, section 5.4;
- The GEANT4 and BME simulations, section 5.6;

The concept used is based on the Doppler Effect phenomena, taking advantage of the angle positioning of each gamma detector in the array with respect to the recoiling nucleus after heavy ion interaction. Detailed recoil angles and momentum distribution of the residues produced in the collision process are reconstructed on event by event basis by utilising the information recorded by each detector. The performance of these detectors has been simulated in order to evaluate their response to the gamma energy.

5.1 The Multi-detector Gamma-ray Spectrometer

This study was undertaken at the iThemba Laboratory for Accelerator Based Sciences (LABS)[1] situated at Faure near Cape Town, South Africa. The main accelerator in the facility,

[1] formerly The National Accelerator Centre

for the kind of experiments involved in this study, is the k=200 four sector separated cyclotron accelerator [244]. Light to heavy ion beams can be accelerated to energies of few hundreds of MeV. During the time of the experiment, the upper energy limit was 400 MeV for the $^{12}C^{5+}$ and 790 MeV for the $^{129}Xe^{22+}$ ion beams, the highest possible Z accelerated thus far. Other medium masses can achieve energies within the range of the two nuclei mentioned above. There are two injectors in use. The solid pole cyclotron (SPC2) injector provides the heavy ions needed for a given study. With this injector, any of the two external ion sources can be used. The resulting beam from these ion sources is then axially injected in the accelerator from below. The ECR ion source provides a whole range of heavy ions such as carbon, sodium, argon, krypton, or any other element which needed for acceleration. Initially, the element is ionized using a small oven or through a plasma mediated process.

The AFRODITE [2] gamma detector array [245], which was used for this study, came into operation in the summer of 1998. The initial design specification of the AFRODITE spectrometer was aimed at construction of a cost-effective array of optimal performance for X-ray and γ-ray detection below 200 keV. This gave it capabilities complimentary to other existing gamma arrays. The combined photo-peak efficiency of the array at 100 keV is about 11%, the highest of the operational arrays in this energy regime. Primarily, AFRODITE was designed for studying nuclear phenomena at high spins by measuring X-ray and γ-ray energies, yields and coincidence relationships associated with fusion-evaporation or fission reactions induced by heavy ions [245]. Some parts of the array showing the inner target chamber with kapton windows, some detectors, the beam line and the main frame are shown in figure 5.1.

The AFRODITE consists of 8 Low Energy Photon Spectrometers (LEPS) and 7 escape-suppressed Clover detectors [246] or vice-versa, in a near 4π configuration. Each of these two kinds of detectors has 4-fold segmentation to yield four independent detectors. Some detailed specifications of the array parameters are presented in table 5.1. In total, there are up to 60 detector elements occupying 23.5% of 4π space. The AFRODITE array-frame, has a rhom-

[2] AFRican Omni-purpose Detector for Innovation Techniques and Experiments

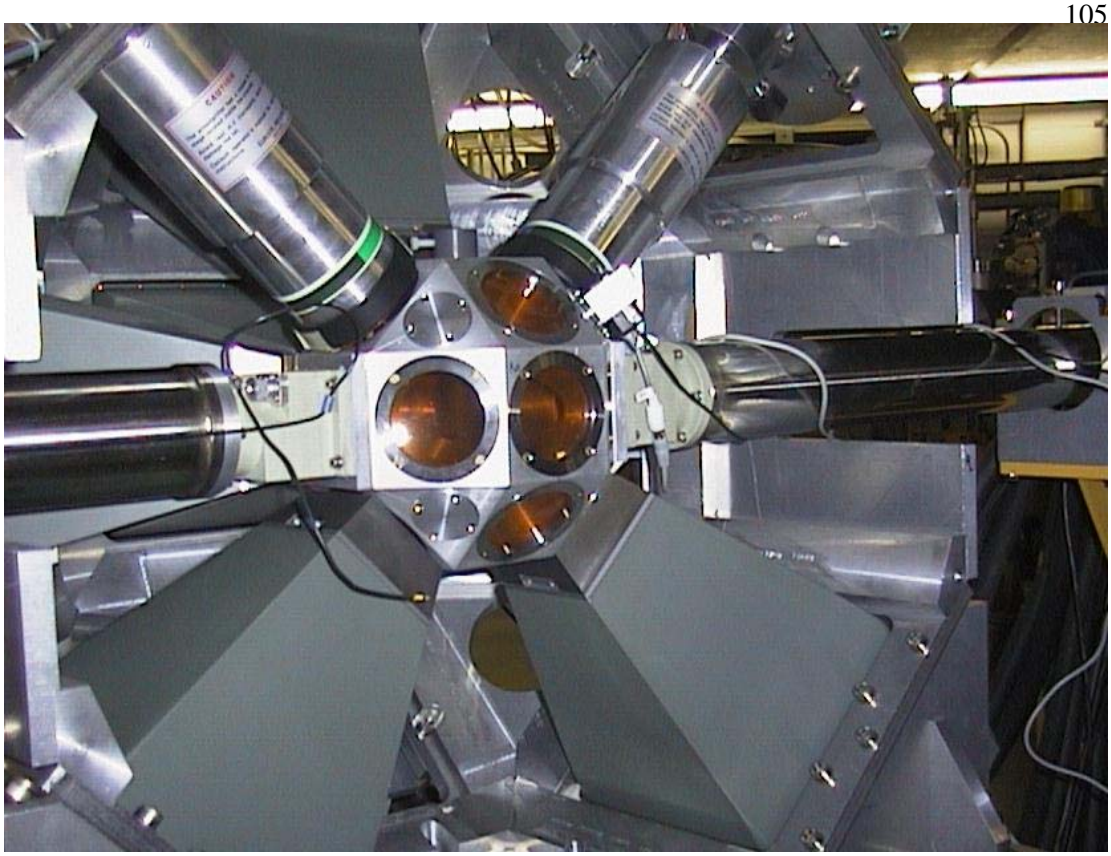


Figure 5.1: The target chamber showing kapton windows, beam line, the closed circuit TV camera, two LEPS (subtended at 45° and135°) and two Clovers (subtended at 45° and135°) are visible on the upper and lower section of the photograph, respectively.

bicuboctahedron shape, which consists of a main-body and an end-cap with a total of eighteen square facets at 45°, 90° and 135° with respect to the beam direction. Of these, fifteen are available for mounting the detectors. One is occupied by the target-ladder placement (figure 5.4).

The increased detection efficiency for gamma-ray detectors is a result of using large-volume high-purity germanium (HPGe) crystal. One cost-effective way of achieving this is by stacking several smaller crystals into one single detector volume. The manufacturer of the Clover detectors, EURISYS, mounts four germanium crystals in one cryostat, side-by-side in a geometry reminiscent of a four-leaf clover [247]. In addition, improved peak-to-total ratio can be achieved by surrounding the germanium detector by the bismuth germinate (BGO) Compton

Table 5.1: Some technical specifications of the AFRODITE spectrometer (Ref. [245]).

specification	Clover	Compton suppressors	LEPS
supplier:	Eurisys	Crismatec	Eurisys
number:	8	8	8
crystal type:	HPGe	BGO	HPGe
length:	71 mm[1]	~26 cm	10 mm
diameter:	51 mm[1]		66 mm[2], 60 mm[3]
thickness:		~(4-20)mm	
taper angle:	7.1°	~8.1°	
L_{ec}[7]:	20 mm		15 mm
entrance window:			119 mm[4]
L_{tc}[8]:			
total opening angle[4]:	23.2°		23.3°
detector solid angle[5]:	1.34%[6]		1.57%

before shaping[1]
external[2]
associated with the active area[3]
for a 4 mm gap between target chamber and end-cap.[4]
percentage of 4π[5]
for a 0.2 mm distance between crystals[6]
L_{ec} the distance from the detector end-cap to crystal surface[7]
L_{tc} the distance from the target centre to the crystal surface[8]

suppression shield, used to detect events where the γ-ray scatters out of the germanium in to the BGO. This design of the Clover detectors was first implemented in the EUROGAM II detector array project [248, 249, 250]. The LEPS detectors, which have a planar configuration, are made out of a single crystal of *p*-type HPGe (10 mm thick, 60 mm diameter) and are electronically segmented into quadrants. The signal from each quadrant is, as in the case of the Clovers, processed individually. More detailed specifications of the detector parameters are given in table 5.1. The complete electronic circuit diagram for the AFRODITE is shown in figure 5.2.

Each Clover crystal segment has its own associated preamplifier. The crystal is housed inside a symmetrically shaped BGO shield. This allows energy deposited in adjacent segment of the detector, as a result of Compton scattering of the incident photon to be summed up, in the add-back mode [233]. A gamma-ray Compton scattered out of the crystals stands a

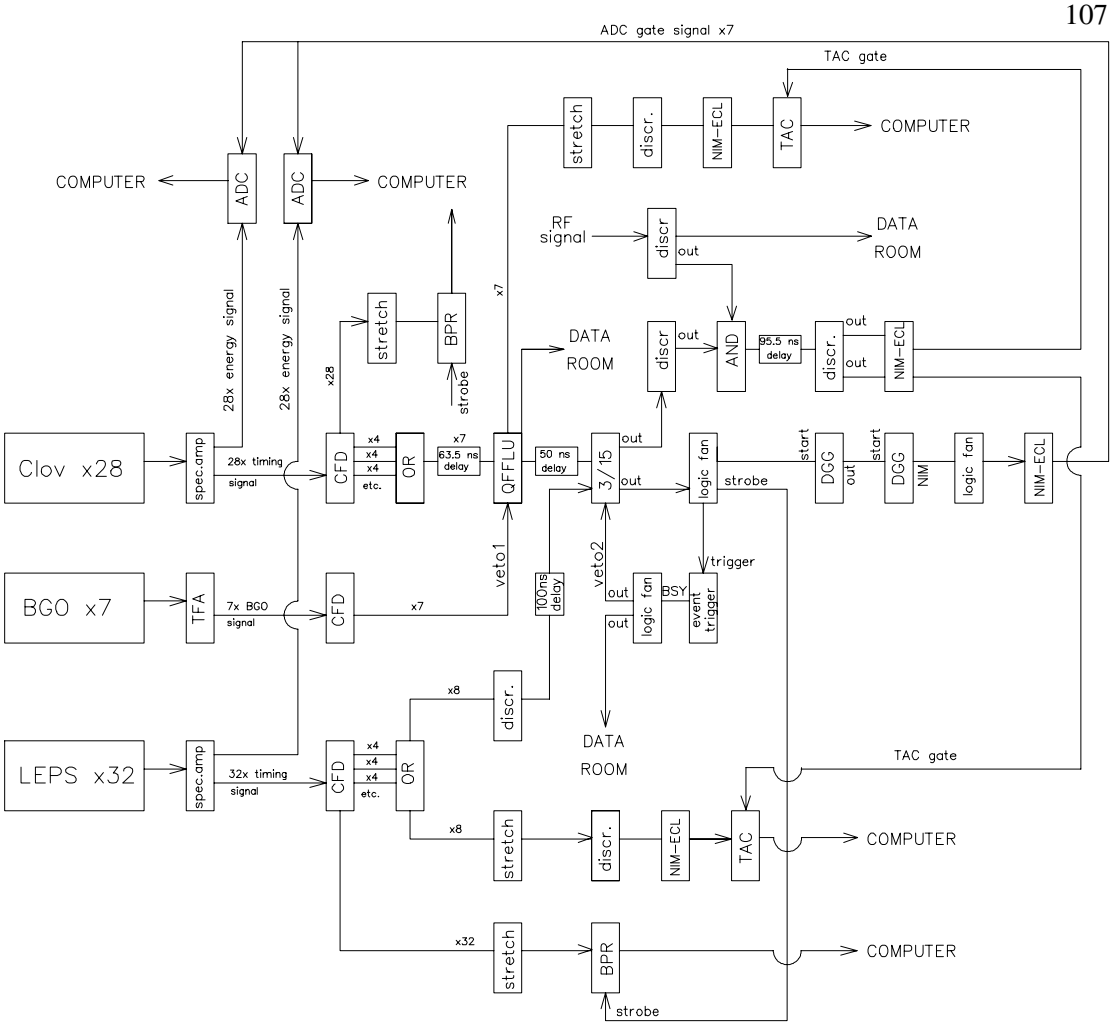


Figure 5.2: Typical electronics of the AFRODITE gamma detector array.

high probability of interacting with the BGO shield because of the geometric design. The shield comprises of sixteen wedge-shaped BGO crystals, each coupled to a photomultiplier tube. The BGO crystals are shielded from direct gamma-rays from the target position via a heavy metal (tungsten alloy) collimator, see section 5.5 for dimension details. Any of the sixteen photomultiplier tubes may generate the signal, which is subsequently used as a veto signal for the corresponding Clover detector. This is done in the electronics setup, the veto works for all the four HPGe crystals, or for just the corresponding HPGe element based on proximity. Detailed description and performance of the Clovers detectors are discussed in Ref. [251].

The LEPS detectors are planar circular shaped disks with the diameter of about 60 mm

and thickness of 10 mm. They are produced from *p*-type semi-conductor HPGe single crystals. The crystal is electrically segmented into four quadrants. The signal from each quadrant is processed separately. Since the thickness of the crystal is small, the optimal performance of the detector is limited to low energies. The detector comes with a thin beryllium window and a protective cover typical of SiLi detectors for *X*-ray detection. The range of performance is typically 20-600 keV with the lower energy range determined by the noise and low *X*-ray intensity level. The energy resolution of the LEPS is about 30% better than the Clover detector even at much higher count rates. Its solid angle is also larger than the Clover because of its proximity to the target position i.e. smaller radius.

The fifteen AFRODITE detectors require 60 channels of spectroscopic amplifiers, ADCs, TDCs and CFDs. The Clover requires an extra 7 or 8 channels of TFAs and CFDs for the BGO shields. There is also the need for readout hardware and control, see figure 5.2. The electronics can be divided into two categories for handling the fast and slow signal processing. The fast processing involves mainly logic time signals while the slow processing involves the energy signal information. The energy detection processing starts in the preamplifier close to the detector crystal for minimal signal interference with the total charge directly proportional to the energy deposited in the detector crystal. Typically, the magnitude of the preamplifier output voltage signal (amplitude) is directly proportional to the total charge contained in the input pulse, making it an integrator and an amplifier of the order of 1 Volt per Pico coulomb of charge [252]. In the experiment, this was performed by the CAEN 568 NIM 16 channel spectroscopy amplifiers. The output of the amplifiers (1-10 Volts) is then digitised, the slowest stage of the signal processing. The amplifier fast output is fed into the CFD to get the best timing precision signal. The digitalisation process was performed by the zero-suppressed 4096 channels (12-bit) Silena 4418 ADCs, for all the Clover and LEPS detectors. The only difference in the signal processing of the Clover detector compared to the LEPS is the logic pulse veto of the Compton suppression shield. The shield has got 16 outputs which are combined in the simplest circuit configuration to get the final veto signal for the corresponding Clover detector. The complete

processing of the various signals is shown on the diagram 5.2.

For event triggering, the time signals from all detectors (15) are fed into the MLU module, a coincidence unit. The four crystal outputs of each detector are logically ORed to produce only one time logic signal. The MLU module works on concept of thresholds, where one defines the minimum number of detectors needed to get a valid event trigger. The corresponding detector energy signals constitute the coincidence hit of the measurement. This setup sometimes uses the coincidence between the valid event trigger and the RF start signal, after the first beam burst, to initiate the start signal of the TDC. The stop logic pulse is generated by the first detector signal to arrive after 200ns of delay applied to the start signal.

The ADC data readout was performed by the front panel ECL data bus and transferred to a LeCroy VME-based fast memory unit. During the readout, the event trigger module sends a busy signal to the MLU to inhibit further processing of any in-coming valid events during this busy time. The resulting dead-time depends on the speed of ADC conversion as well as the number of data words written per valid event. This time loss limits the data acquisition rate achievable in this kind of setup.

The data acquisition front-end module produces event buffers which are sent to the control work station via an Ethernet connection. The **XSYS** data acquisition and analysis software [253] performs the on-line sorting of the received buffers and stores the raw event files on tape. Each event file is written as a block of words and contained energy and time information for each coincident measurements and the bit pattern for the detector elements which fired based on the pre-assigned settings. The actual pattern of the data words written to the tape for off-line analysis is user dependent. This pattern must be satisfied in all subsequent replays of the stored data tapes.

5.1.1 The Target Ladder

The target ladder frame used is manually operated, with three locations for holding the samples A, B and C, as shown in figure 5.3. By sliding the ladder frame within the target

chamber, the needed sample is put in position with respect to the beam axis. The ruby material produces visible florescence at the spot stroked by the beam in the dark. The material, in conjunction with the closed circuit camera placed on the target chamber wall with good view of ruby, provides the necessary information for the beam alignment. The empty position serves as a check for the presence of a halo in the beam. A halo free beam should not register significant count rates on the detectors when the empty slot is in the beam path position.

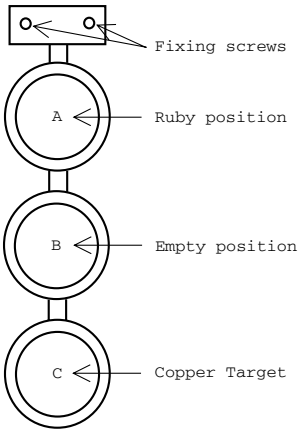


Figure 5.3: The target ladder.

5.2 The Experimental Setup

The 400 MeV $^{12}C^{5+}$ beam of 5nA used during the beam time was delivered by the separated sector cyclotron accelerator. The trigger logic for data acceptance was on the condition that ≥2/15 of the detectors record a signal. The detectors were distributed as follows, 2 Clovers and 2 LEPS at both 45° and 135°, 3 Clovers and 4 LEPS at 90°, as shown in figure 5.4. The amplifier gains for the gamma energy detection were set to produce half a keV/channel for the Clover and quarter keV/channel for the LEPS, with a valid range of 10-820 keV and 30-2048 keV, respectively. The pile-up events use the upper energy channels making them unusable in the present setup. Aluminium disks of 0.9 mm and 1.55 mm thickness were also put in front of the Clover and LEPS detectors, respectively, for low energy photon attenuation, in addition to the electronic signal thresholds.

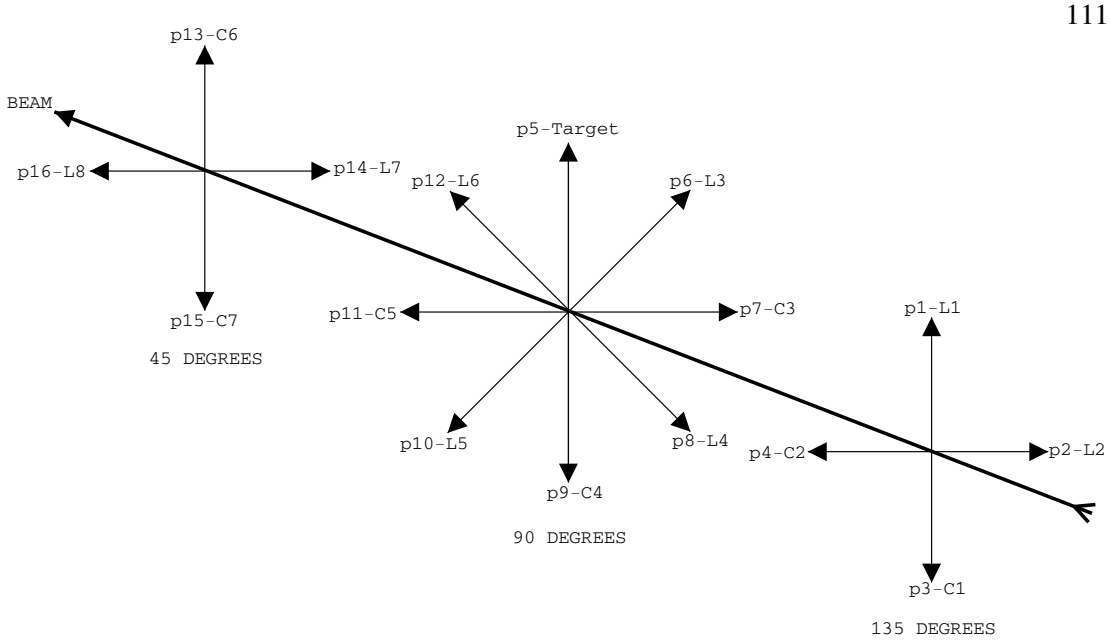


Figure 5.4: The position (p) and detector number in the array during the experiment, L and C represents LEPS and Clover, respectively.

The ^{63}Cu target material used were 150-200 μgcm^{-2} ($\approx$17 nm) thick, mounted in the centre of the target chamber of the AFRODITE gamma detector array. The target element was enriched to more than 99.9% of ^{63}Cu. In the trial phase, up to three foils were used resulting in poor energy dissipation and subsequent melting on the target beam-spot. The thicknesses were measured by the supplier using a radioactive α source attenuation technique to within 5% error. During in-beam measurement, the data collected were recorded event by event on magnetic DLT tape for off-line analysis. A total of about 10^9 events were recorded. The highest detector multiplicities were the counts recorded for LEPS-Clover coincidences, followed by the LEPS-LEPS combinations, as shown in figure 5.5.

5.2.1 Detector Energy Calibration

Calibration of each detector element was performed using the ^{133}Ba and ^{152}Eu Standard point sources placed at the target position of the AFRODITE target chamber. This was done in three stages in the following order:

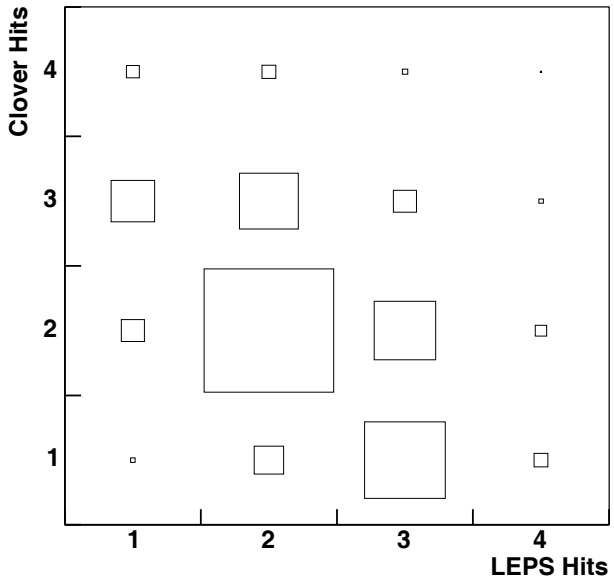


Figure 5.5: The Clover detector versus the LEPS detector coincidence hits.

- The gain settings were performed for all the detector amplifiers. This is accomplished by tagging a specific gamma line of the Standard sources and ensuring that its centroid was in a predetermined channel through adjusting the amplifier gain accordingly. The low limit of detection (LLD) in the amplifiers were initially adjusted by observing Standard source emitting low energy photons (^{152}Eu X-rays), and with the aid of a scope, ensured that the cut-off thresholds were set just above the electronic noise level and below the source signal. This was verified in the collected spectrum to ensure that the low energy threshold was not set too low to allow excess electronic noise into the channel or too high to cut out useful information.

- The second stage of calibration was performed within the data acquisition software. The digitalised raw-pulse-height (RPH) signal of the Standard sources generates the 12 bit spectra, in which the adopted gamma lines are clearly identifiable. The centroid of these gamma lines in the spectra are fitted onto the known energies, and a mathematical relationship established. The simplest case involves a linear fit of two terms, gain and

zero offset. By using fitting procedures, it was found that a 5-parameter function gave the best fit, figure 5.6. The residual for both the 5-parameter and linear functions fits are shown by the dashed and solid lines, respectively. The residual for the linear function exceeded 1 keV for two of detector elements at the very low gamma energies. The residual of the 5-parameter function adopted in the study lies within 0.2 keV throughout the energy scale for all the detectors used. The 5-parameter function is represented by

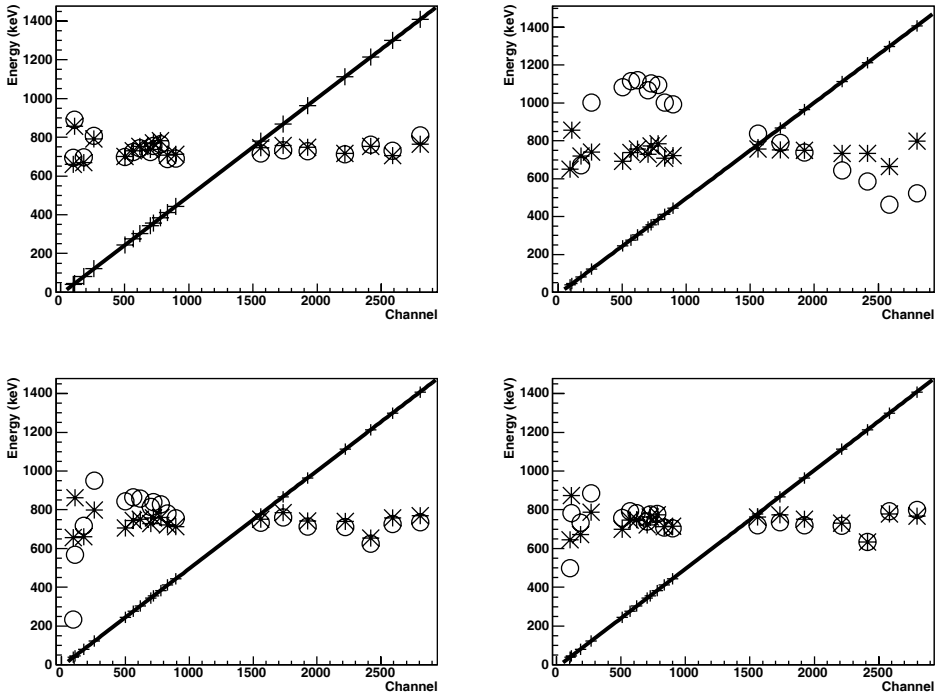


Figure 5.6: The calibration fits for the Clover detector (C3) elements, the open circles and asterisks are the residuals multiplied by 500 and centred along the Y-axis for 2-parameter and 5-parameter fits, respectively.

the following equation 5.1

$$E = A + Bc + Cc^2 + D\sqrt{c} + \frac{G}{c} \tag{5.1}$$

where A, B, C, D, G are the fit parameters, E is energy and c is the channel number. The same function was used to calibrate each of the detectors used, and their corresponding parameters derived. These fitting parameters kept varying for some

detectors during in-beam use. The variations were applied at the appropriate time intervals during the process of off-line sorting in order to correct for it. The following lines were used for in-beam measurements 42.35,67.40,77.10,111.60,197.14, 511.00,596.10,835.60,1015.55,1040.85,1370.10,1608.58 keV lines.

- The third step of calibration involves the time dependent detector parameter corrections. This is the most crucial stage also referred to as "gain-matching procedure as errors here are propagated to the final results. To tackle this problem, source data for calibration is collected just before and immediately after in-beam detector use. By overlapping the two energy spectra for each detector before and after the run, gain drifts can be identified if the γ lines are not perfectly overlapping or when they fail to give the same fit parameters (peak centroid). This is not entirely true for cases of intermittent gain drifts, which affected less than 10% of the detectors. The problem of gain drifts affected about 35% of the detectors. These detectors had to undergo gain matching using the corresponding stable detector spectral lines. Energy calibration is performed with the Standard source data for the 'ideal' detectors, these then acted as the reference to the unknown gamma lines of the experiment data. This can only be done per given detector angle because of the Doppler Effect. The in-beam raw data, saved into files at two hourly intervals, are each gain matched and the independent detector parameters generated. In severe cases up to 10 keV energy drifts were measured. An in-beam effect typical of the detector charge collection problem was associated with this phenomenon. The GEANT4 simulations show a similar effect due the delta electron processes, i.e. bremsstrahlung X-rays from the interaction with the metallic materials in the target chamber. This problem crops-up two hours into the beam time, and persists until about two hours after, after-which it disappears. (This might also be associated with the activation of the detector elements.) It affected mainly the low energy part of the spectrum of the forward detectors in a way that the linear response,

charge collection and the resolution of the detectors were adversely affected (see figure 5.8). The G term in equation 5.1 handles this effect, as shown by the residual of the third element in figure 5.6. The gamma energy calibrated spectrum was supposed to be accurate to within 0.2 keV overall within the measured energy ranges.

The energy efficiency calibration of the detectors was achieved using γ line intensities from the Standard sources relative to the measured values. A dedicated package is available in the RadWare gamma analysis suite [254, 255] known as "**effit**" to accomplish this. The program generates up to a maximum of 5-order polynomial parameter fit to the source data for a set of detectors, which can then be used to correct for energy detection efficiency during off-line sorting of the data. A typical energy efficiency curve is shown in figure 5.7.

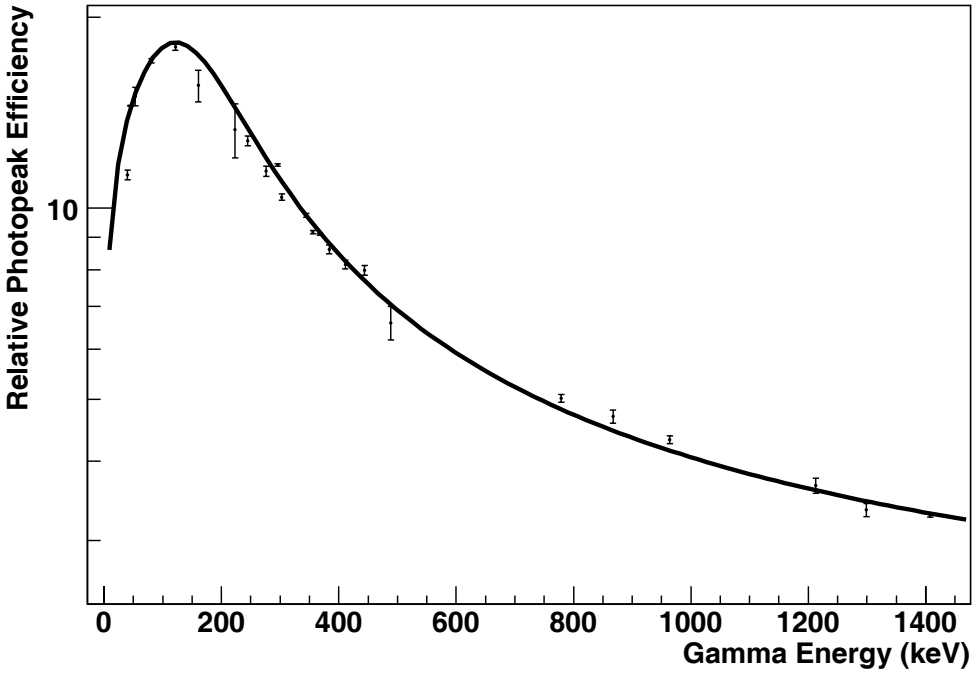


Figure 5.7: The typical energy efficiency curve for the combined 90º detectors

5.2.2 Detector FWHM Calibration

The Full Width-at-Half-Maximum (FWHM) calibration was performed for the combined Clover detector spectra of the Standard sources. The calibration curve is shown in figure 5.8. The polynomial fit shown on the plot is of the form:

$$FWHM_{E_0} \approx p_0 + p_1 \cdot E_0 + p_2 \cdot E_0^2 + p_3 \cdot E_0^3 \tag{5.2}$$

where p_0=1.96424, p_1=-1.16654 $\times 10^{-3}$, p_2=2.40490$\times 10^{-6}$ and p_3=-8.63761$\times 10^{-10}$; where $FWHM_{E_0}$ is the full width-at-half-maximum for the detected gamma energy E_0. This expression seems to deviate from the usual square root relation to energy, which is washed away by the process of summing together many detectors. The deviation contribution, from the mean energy of each of the detector, constituted the overall FWHM of the summed spectra. The in beam

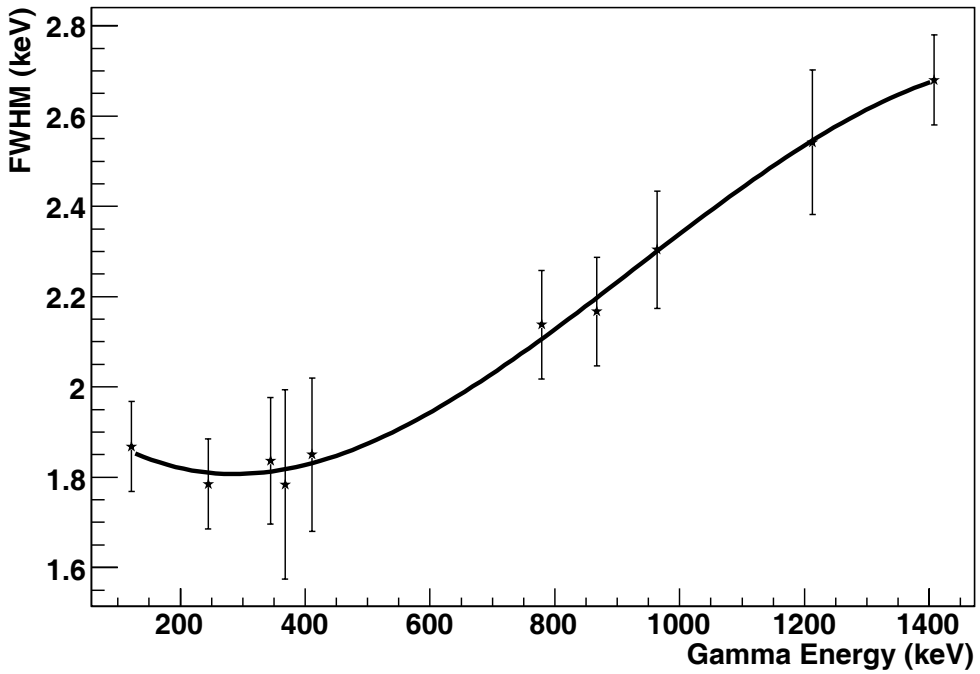


Figure 5.8: The FWHM calibration curve for the combined Clover detectors.

values are even more difficult to obtain due to run-time issues such as the long-term stability of electronic and the beam current (detector count rates). The process of getting the true intrinsic

resolution of the combined detectors for the various detector angles is almost impossible due to many factors. In many cases, the resolution of in-beam measurements deviates from those of the Standard calibration sources due to many factors such as event count rate, gain drifts corrections etc. In order to approximate the true values, detector artefacts could be used, such as the known gamma lines mostly from the activation of the Aluminium target frame. These gamma lines are not affected by the problem of Doppler Effect because of the target frame thickness. A universal Doppler broadening calibration curve is derived by fitting the resolution of at least five gamma lines produced by gating on each of their respectively coincident pairs in an inclusive matrix (generated using all the Clovers, irrespective of their angle position). The target residues produced with masses farther away from the target mass and not from the target frame have significant Doppler broadening especially as the gamma energy rises. The other option is to resort to the residues with at least two coincident gamma lines in the in-beam measurements, as this implies constant mean angle and mean recoil velocity. Both options failed to produce consistent results and the calibration source method was found to be consistent enough for in-beam use and simulation purpose (equation 5.2). To achieve more realistic values, a correction factor for each detector angle set using the near-target residue with least Doppler effect and maximum number of gamma-ray emissions is used (e.g. ^{64}Cu).

The measured Doppler broadening of a given residue gamma lines has two major contributions, the intrinsic resolution of the detector σ_{int} and the Doppler broadening σ_{DB}. The latter components are contributions from the detector opening angle, recoil angle distributions and the velocity distributions. The following Doppler broadening expression may be used assuming Gaussian distributions (note that for many detectors summed together, this is not the case (equation 5.2)) for the 90° degree detectors:

$$\sigma_{E_0} \approx \sqrt{\sigma_{int}^2 + \sigma_{DB}^2} \tag{5.3}$$

where $\sigma_{int} \approx (k/E_0)^{\frac{1}{2}}$ and $\sigma_{DB} \approx 2E_0\beta_r\theta$. A simulation of the combined effect of the σ_{int} and the σ_{DB} is performed as follows. Firstly, a Gaussian random deviate G_1 representing a Doppler

broaden gamma line is generated, with a mean gamma line of energy 212.1 (keV) and standard deviation width of σ_{DB}=1.65 keV. This deviate G_1 in then considered as the mean value to generate a new Gaussian deviate with a distribution standard deviation width of σ_{int}=0.77 keV, for the intrinsic detector resolution. This is represented by the dash-line histogram in figure 5.9. It is observed that the Doppler broadening effect is not a perfect Gaussian distribution. The values used in the simulation are the nearest experimental values for the ^{54}Mn nucleus.

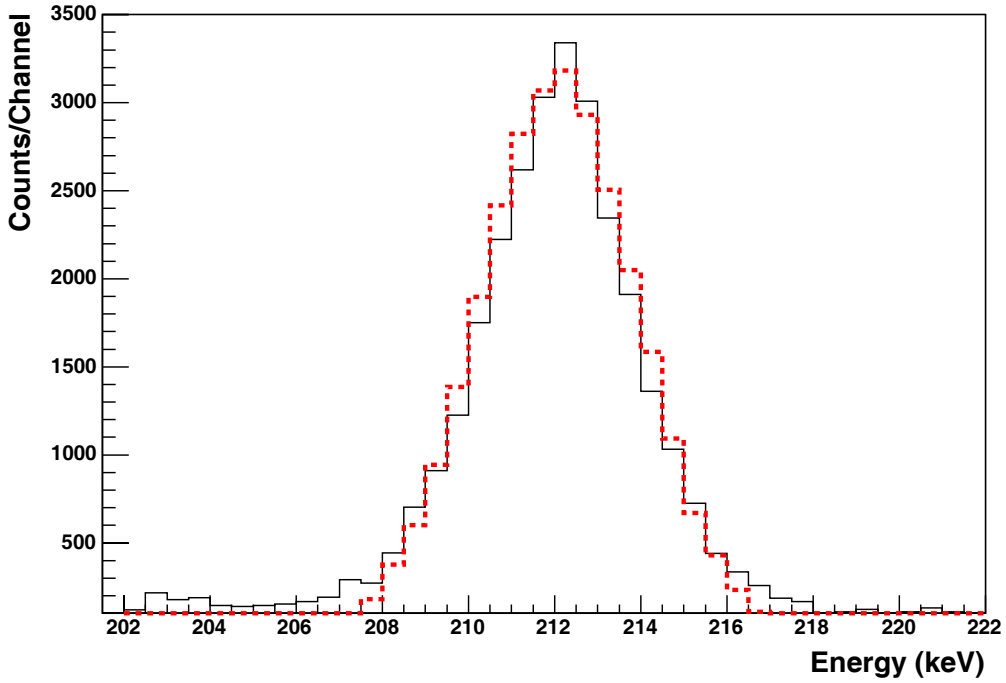


Figure 5.9: Simulation of the Doppler broadening of the gamma line detected in the Clover detector, full histogram represents the experimental spectrum.

5.3 The Doppler Effect

5.3.1 Gamma Coincidence Measurements

The concept of gamma coincidence detection technique is based on the fact that the nucleus, in the de-excitation process, sometimes produces photons in a cascade. The time duration between two gammas is mostly within a few picoseconds of each other, which is by far smaller

than the time resolution of typical modern electronic timing circuits. The gamma emissions from the cascade are detected in coincident with the electronics operating with some nanoseconds time gates. These gammas have unique energies and emission time-scale depending upon the A, Z and N of the nucleus, making it the ideal fingerprint tool in nuclear identification studies, section 5.3.3. Assuming that the cascade is made of two gamma lines of energy E^1 and

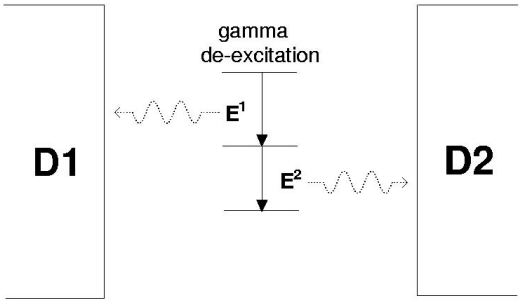


Figure 5.10: The coincidence measurements of two gamma lines, E^1 and E^2, produced in a cascade during the de-excitation of a nucleus.

E^2, the spectrum of E^2 can be generated by putting a restriction that each time E^1 is detected, the signal in detector D2 is accepted on condition that D1 detection, assuming a Gaussian distribution of the E^1 energy, lies within 3σ widths about the mean value. If the number of the de-exciting nuclei were more than 30, typical of some nuclear interaction measurements, each emitting up to about 10 gammas in the cascades, the spectrum required would have to be obtained by gating on each nucleus and performing the experiment repeatedly. This is avoided by storing each coincident measurement event by event. To simplify the above task, the stored data can then be replayed, and stored in a matrix. Assuming only three nuclei a, b and c emitting the gammas γ_a^1, γ_b^1, γ_c^1 in coincidence with γ_a^2, γ_b^2, γ_c^2, respectively, the events can be sorted into a 2-D matrix so that the 1's gammas are on the x-axis and the 2's gammas are on the y-axis, with the corresponding bin incremented. This produces an asymmetric matrix. If the energies of the two detectors correspond (calibrated), then gammas can be swapped such that the 1's gammas are on the y-axis and the 2's gammas are on the x-axis with the corresponding bin incremented

to create a symmetric matrix widely used in gamma spectroscopy. The 3-D matrices are used for higher order gamma coincidences.

5.3.2 Residue Gamma Doppler Effect

A residue produced in heavy ion interactions could recoil with velocity β_r in the direction given by (θ_r, ϕ_r) where θ_r and ϕ_r are the respective polar and the azimuthal angles with respect to the vertex point of interaction and the projectile momentum direction. This residue could then emit a cascade of gamma emissions, E^1 and E^2 in the respective directions (θ_{D1}, ϕ_{D1}) and (θ_{D2}, ϕ_{D2}), where $D1$ and $D2$ are the detector locations. The apparent recoil angle θ_A is evaluated from the difference in the two angles. The observed experimental Doppler Effect arises from the variation in these parameters. It is common practice to introduce some assumptions when dealing with the Doppler Effect to make the interpretation of observed experimental data much easier. The common approaches use the following assumptions:

- the production of the residues occur at the vertex point produced by the axis joining all the detectors in the array,
- the recoil angle has a mean value about zero and insignificant distribution σ_{θ_r}.

The above assumptions are not always true. If the residues are produced with relatively large β_r and if the gamma transition energy states have long half-lives, the emission process will occur on-flight and by then the vertex position will have changed significantly (section 5.4.4). The residues produced may also come in angles other than zero, making the second assumption also untrue.

When the geometry of the detector array (AFRODITE) relative to the recoiling nucleus is known accurately, it is utilised in the detailed interpretation of the experimental measurements. The residues produced recoil from vertex point in the target material with typical fractional velocities of $\leq$5% that of the speed of light. The gamma photon emitted, has a Doppler shift associated with the detected energy of the photon, which is dependent on the detector angle θ_i

with respect to the recoil angle θ_r, given by

$$E_s(\theta_A) = E_0 \frac{\sqrt{1-\beta_r^2}}{1-\beta_r \cos\theta_A} \approx E_0\,(1+\beta_r \cos\theta_A) \tag{5.4}$$

where $\beta_r = v/c$, v is the residue recoil velocity, c is the speed of light, E_s is the observed Doppler shifted and broadened gamma energy, E_0 is the gamma transition energy, θ_A is the angle the detector makes with the recoil direction of the emitting nucleus and $\lim_{\theta_r \to 0} E_s(\theta_A) = E_s(\theta_d)$. By utilising 45° and 135° detector angles of AFRODITE, equation 5.4 reduces to this form for residue recoil angle $\theta_r \approx 0$

$$\langle\beta\rangle = \frac{1}{\sqrt{2}E_0}(E_{45} - E_{135}) \tag{5.5}$$

where $\langle\beta\rangle$ is the mean value of β_r, E_{45} and E_{135} are the mean gamma energies of the 45° and 135° detector angles, respectively. The 90° detector can be useful for setting the residue gamma energy gates, to extract the E_{45} and E_{135} values.

According to equation 5.4, the shift in energy is greatest at angles aligned with the recoil direction (0° or 180°, i.e. in the forward or backward angles). The granularity of the LEPS and Clovers is beneficial this way for the size of the opening angle of each detector crystal to be kept relatively small, so the angle θ_d is known more accurately. This is seen by differentiating equation 5.4 with respect to θ_d and β_r, which yields

$$\Delta E_s \approx E_0 \cos\theta_d \Delta\beta_r - E_0\beta_r \sin\theta_d \Delta\theta_d \tag{5.6}$$

whereby the cos factor relation of the velocity distribution, $\Delta\beta_r$, means its effect is pronounced as the detector angle tends to the projectile direction. The converse is true for the recoil angular distribution or opening angle, $\Delta\theta_d$, with its maximum peaking for detector angles positioned normal to the recoil axis as shown by the following reduced expressions of equation 5.6:

at 90°;

$$\Delta E_{90} \approx |E_0\beta_r\Delta\theta_d| \tag{5.7}$$

at 135/45°;

$$\Delta E_{45} \approx \frac{E_0}{\sqrt{2}}(\Delta\beta_r - \beta_r \Delta\theta_d) \tag{5.8}$$

at 0°;

$$\Delta E_0 \approx E_0 \Delta\beta_r \tag{5.9}$$

The velocity distribution term $\Delta\beta_r$ of the residual nucleus has these main experimental contributions:

- From conservation of momentum law, the nucleus recoil velocity is proportional to the magnitude of the momentum transferred from the projectile to the target nuclei in the interaction process, equation 2.68. (This technique of measuring β or momentum transfer, has an advantage over other existing techniques that rely on direct momentum measurement, because of their mass-energy dependence.)

- The energy loss in the target would be different if the interaction occurs at the front of the target than if it occurred at the back of it or elsewhere in the bulk. Effort was made to minimise this effect in this study by using as thin targets as possible while remaining self-supporting.

- The large recoil angles mean more energy loss or full stopping of the nucleus in the target material. This may culminate in the gamma line asymmetry between the forward and backward angles.

The angular distribution $\Delta\theta_r$ term of the residual nucleus originates from these experimental contributions:

- The distributions of the recoil angles of the residues depends on the interaction process that lead to their formation and is of much interest in the present study.

- The detector opening angle, a γ-ray interacting at one edge of the crystal will be Doppler shifted by a slightly different amount than an event in the other side. Consequently, the two events will deposit different amounts of energy, and so there will be

a spread in the corresponding peak. Since it is a fixed detector quantity, its magnitude could be accounted for in the experimental measurements if the detection efficiency of the various hit positions were known.

- Multiple scattering in the target foil proportional to the thickness.

The geometry of the AFRODITE detectors may not be optimised to evaluate the β_r distribution accurately for small recoil angles because none of the detectors covers the angles near or in the direction of the beam axis. This is not the case with large recoil angles. The θ_r distribution, however, can be evaluated with high accuracy at 90° if the detector opening angle contribution is significantly smaller.

Another manifestation of Doppler Effect is in the broadening of the gamma lines. This effect is caused by

- The finite size of the angle subtended by the crystal face to the target ($\Delta\theta_d$).
- The inherent residue recoil angle distributions ($\Delta\theta_r$) brought about by the transverse component of velocity contributions.
- The inherent residue recoil velocity distributions ($\Delta\beta_r$).

The broadening can be minimised by having as large detector granularity as can be affordable, thus reducing the detector opening angle and making the equation 5.4 above realistic. This forms the basis of residue tracking device which is essential to the present study. The detector opening angle could limit the accuracy of the Doppler broadening measurements of the recoil residues. This quantity was evaluated to establish its magnitude. The detector opening angles for the Clover and the LEPS detectors were found to be 0.26 and 0.25 rads, respectively. Using equation 5.7, the calculated Doppler broadening for the detected gamma energies in the normal plane of the projectile momentum axis, for both the Clover and LEPS detectors, yields the following equations for the Clover:

$$\Delta E_{90} \approx |0.26 E_0 \langle\beta\rangle| \tag{5.10}$$

and for the LEPS:

$$\Delta E_{90} \approx |0.25 E_0 \langle\beta\rangle| \tag{5.11}$$

The two calculated constants are approximation to the actual experimental values. To get the experimental values, one would have to measure the Doppler broadening of a known gamma line E_0 corrected for intrinsic resolution to get the detector opening component ΔE_{90} then substitute this back into equation 5.7 using a known $\langle\beta\rangle$ and extract $\Delta\theta_l$. This calculation assumes $\theta_r \approx 0$, otherwise this quantity would couple with the effects of the Doppler broadening. If the energy of the gamma emitted is assumed to be 212 keV and the recoil velocity β_r is 0.019, equations 5.10 and 5.11 are expected to introduce an uncertainty of more than 1 keV and 2 keV for the Clovers and LEPS, respectively. These values are about 50% and 60% of the two respective detectors FWHM at this energy. One factor which could minimise the opening angle even further, for the case of the LEPS, is the strict filtering condition employed in the off-line sorting of event by event process (section 5.3.5). The opening angle gives the lower limit of the residue recoil angle. The simulation to investigate the opening angle effect is described in section 5.4.8.

The measurement of the gamma energy is given by the distribution determined by the properties of the detector and the electronics in use, also known as the intrinsic energy resolution of the detection (section 5.2.2). This effect has been simulated to investigate its impact on the observed velocity distribution β, σ_β measurements. The mean gamma energies of 45° (E_{45}) detector and the 135° (E_{135}) with their corresponding standard deviation widths from the experiment measurements (^{54}Mn residue, 212.1 keV line) are substituted with two Gaussian random generators $G1_{45}$ and $G1_{135}$. For a total of 50000 events, Gaussian deviates are selected from both $G1_{45}$ and $G1_{135}$, each time, the value of β_r is evaluated using equation 5.5 and stored in the appropriate bin in a histogram. This is shown in figure 5.11 by the full-line histogram. The process is repeated with the standard deviation widths corrected using equation 5.3. The Gaussian deviates generated are then considered the mean values to generated new Gaussian

deviates with widths σ_{int}, from which the value of β_r is again evaluated and stored in the appropriate bin of a second histogram. This is shown in figure 5.11 by the dotted line histogram. The effect of the intrinsic detector resolution is insignificant at this (<5%) or higher energies but not for very low gamma energies (>10%) for the ^{47}V 87.5 keV line).

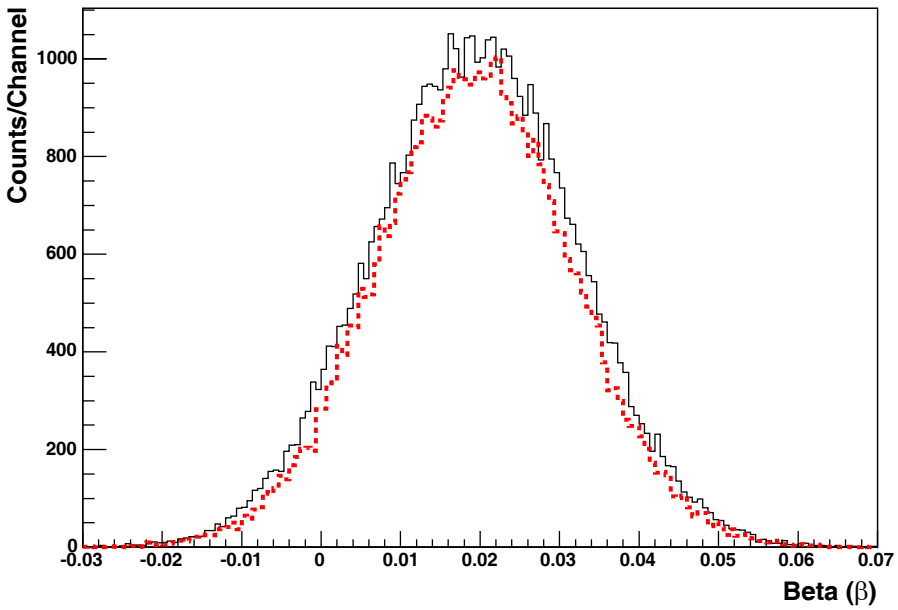


Figure 5.11: The effect of intrinsic detector resolution on the velocity distribution, with (full-line) and without the correction.

The other issue to consider is that of the residue recoil angle. Unless this is de-convoluted from the experimental measurements, there is very little chance of getting the true recoil angles other than just the mean recoil value from equation 5.7. The residues with small velocity values and large recoil angles have the same gamma emission properties as those of larger velocity values and smaller recoil angles as measured by the 90° detector. This is demonstrated in figure 5.12 where a simulation of the two contrasting velocities has been performed using (I) velocity β_r=0.05945 and uniform recoil angle distribution in the range 0-8° (solid line) and, (II) velocity β_r=0.0114 and uniform recoil angle distribution in the range 0-45°. Though the above effect could be counteracted by the fact that (I) has more than five-times the Doppler shift magnitude

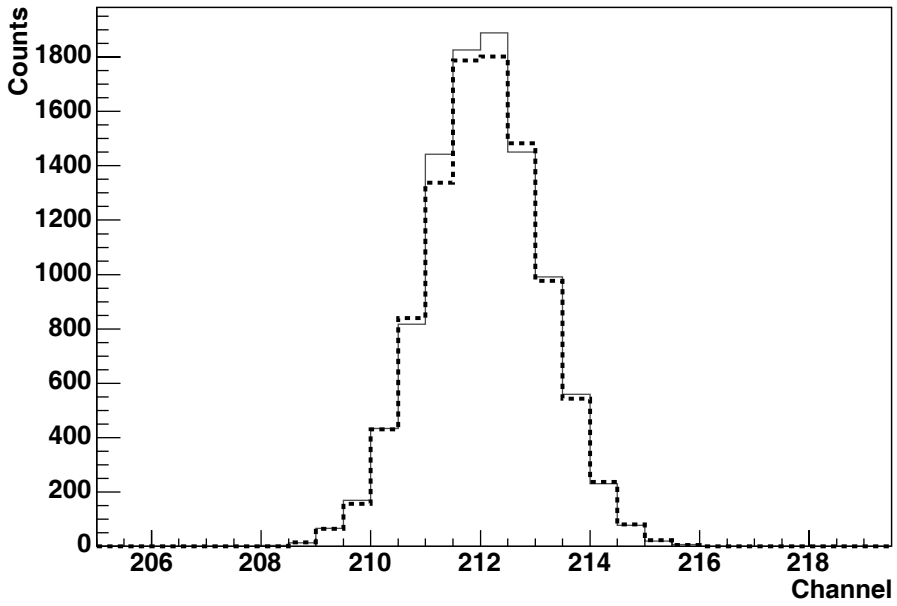


Figure 5.12: Recoil velocity (full-line) versus recoil angle ambiguity.

of (II) between the 45° and 135° detector angles, it is a problem to deal with. This is treated in more detail in the velocity and angle reconstruction procedures (section 5.4.8).

5.3.3 Residue Identification

The identification of the residues produced in the interaction process is achieved through γ-γ coincidence, with the **escl8r** of RadWare [254, 255] and the associated web interface γ database 'coincident finder' facility at **http://radware.phy.ornl.gov/cf.html**. The 90º detectors are useful in this respect for identification of residues recoiling mainly in the beam axis direction. The residues formed with large transverse velocities require a matrix made up of all the Clover detectors, so as to maximise the solid angle and improve the identification of weakly populated channels. The coincident gamma lines produced by these residues when gated in the matrix are characterised by their large Doppler broadening. This is due to the fact that a nucleus recoiling at a given angle (θ_r, ϕ_r), has a certain probability of emitting a gamma detected in a plane normal to the trajectory axis. The recoil angle distributions are symmetric about the beam

axis and coincident lines produced by residues deviating from this have their energies counter shifted such that their combined average energy distribution remain the same. However, this leads to Doppler broadening and shifting of coincident gamma lines of the gated gamma line, in the residue spectrum of the γ-γ energy matrix, corresponding to the magnitude of the velocity and the recoil angle with respect to the beam direction. Gates may be most easily set in the 90° spectra, as the Doppler shifting is less and the lines are more easily identified. However, if one could set gates on the 135° and 145° degree spectra as well, one could generate additional statistics in the produced spectrum. This is illustrated in figure 5.13, where the coincident gamma lines of ^{55}Fe are reproduced in three cases: using a matrix made up of 90° Clover detectors only (top spectrum), using all the Clover detectors in the matrix (middle spectrum) and using the 90° Clover detector for display but gating more broadly using the technique described in section 5.3.5 (bottom spectrum). The number of possible detector combinations for each of these three procedures is 3, 21 and 105, respectively. This affects the statistics of the particular method adopted in the analysis. The gamma energy distribution widths (ΔE) for the 1223 keV gamma are 16.7±0.1 keV and 10.8±0.1 keV, respectively, measured from the last two techniques, as expected. The two situations give the same values for β when analysed appropriately. The gate in the all clover matrix has been optimised by increasing the gate width gradually, to take into account the Doppler broadened events in the gated gamma line, and until the maximum peak area of the coincident line is achieved. Extra caution is required to avoid line interference from other residues whose coincident gamma lines fall within the range of the appropriate residue line spread. This is observed when one extra channel width in the gate produces a sudden increase for the coincident gated residue of interest. The all-Clover matrix was subsequently utilised for supplementary identification of residues due to the much improved statistics, which for this purpose give the number of detector combinations $k \approx 21$ for 7 Clover detectors, and a much lower limit of detection for all the residues. With the all-Clover kind of matrix, it is possible to extract the value of mean Doppler shifts by measuring the magnitude of the Doppler broadening ΔE of the coincident gamma line(s) of the gated nucleus. This is done by substituting the $(E_{45} - E_{135})$

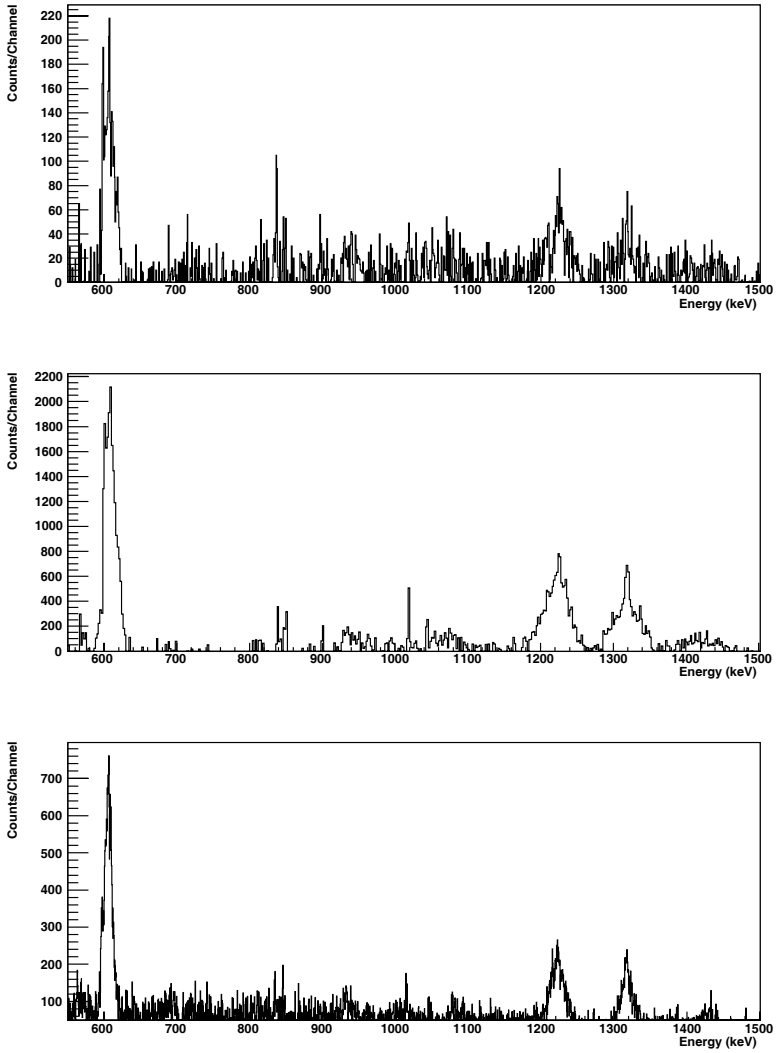


Figure 5.13: The spectrum of the coincident gamma lines of ^{55}Fe gated at 274 keV, the lines are of energies 605 keV, 1223 keV and 1317 keV produced from three 90° matrix (top), all the seven Clovers matrix and the 90° Clovers gated on any other coincident detector in the array.

in equation 5.5 with ΔE. This procedure applies to even the weakly populated residues of the reaction. This was crucial especially for the near-target residue observables which could not be identified or measured using the procedure given in section 5.3.5. A number of other residues identified and reported in appendix B were obtained by applying the all-Clover matrix approach.

5.3.4 Doppler Effect Extraction using the γ-γ Matrix Techniques

The technique introduced in section 5.3.1 could be extended further to any given number of detectors, n, assuming that there are r gamma emissions detected from the nuclear de-excitation cascade. The number of detector combinations, k, used to generate a 2-fold coincidence spectrum is related to the number of detectors (n) through the combination expression $k = {}_nC_2 \cdot {}_rC_2$. The lowest number of detector combinations for the coincidences measurements in an experimental setup is for r=2 gamma detections, such that $k = {}_nC_2$. The setup used in this study had five detector parameters affecting the spectrum generation constituting of the following:

- The detector types; Clover or LEPS.
- The detector angles; 45°, 90° or 135°.

The experimental setup consisted of two Clovers placed at both 45° and 135° and three at 90° positions (figure 5.4). The Clover detector's four elements are summed up to get one gamma energy signal (section 5.4.5). The corresponding detector combinations are $k = {}_2C_2 = 1$ (for the 45° and 135° matrices) and $k = {}_3C_2 = 3$ (for the 90° matrix), which are relatively small. In order to extract the Doppler Effect information from this kind of setup, alternative approaches are sought, the matrix way being in the forefront. In the low energy nuclear structure studies, the nuclei produced are normally assumed to be produced with nearly the same velocities (β), corrected appropriately in the software, for the different detector angles during the construction of the matrices. This route cannot be taken in the present case as each residue comes with its own velocity value (β_r). The gamma spectroscopy techniques using γ-γ coincidence matrices and cubes are well established [254, 255, 256]. The matrices, which are built from coincident gammas of one detector on one axis against the other detector on another axis, are analysed using dedicated software programs from the RadWare suite of packages[3] . The **escl8r** and **slice** packages are used for the symmetric and the asymmetric matrices, respectively. The identity of

[3] http://radware.phy.ornl.gov/download.html

the residue is obtained from the 90° versus 90° γ-γ matrix because the Doppler shift effect is minimal for small recoil angles of residue. By utilising the 90°-135° matrix generated, the 135° detector gamma energy spectra is obtained by setting a gate on the x-axis (90° angle), getting the slice so produced and projecting it onto the y-axis (135° angle), S^{γ}_{135}. This is repeated with a gate set on the broad background spectrum, lower in energy to the actual gate and the produced spectra S^{bg}_{135} subtracted from S^{γ}_{135} (using the **gf3** application of RadWare) to obtain the 135° coincident and background subtracted gamma spectrum of the initial gated line. The exercise is repeated for all possible combinations of matrices corresponding to the detector angles. In the case of the Clover detectors, using the symmetric matrix, three matrices are created corresponding to the number of angle placements. The coincidence combinations for the 135° Clover detector angles consists of $2C_{135}$, $3C_{90} + 2C_{135}$, $2C_{45} + 2C_{135}$, $2L_{135} + 2C_{135}$, $4L_{90} + 2C_{135}$, $2L_{45} + 2C_{135}$, where L and C denotes the LEPS and Clover detectors, respectively, 45, 90 and 135 denotes the angle placement. The pure LEPS combination (figure 5.5) is not useful because the Clover and LEPS spectra are not compatible. In each case, the spectra obtained are added to make up for each angle placement of the detectors (using **gf3**). This is repeated for all distinct angle positions to achieve the total coincident spectrum of the array. The Doppler shift is given by the difference in energy of the gamma line in any two spectra produced from the different detector spectra.

5.3.5 Doppler Effect Extraction using Offline Sorting Technique

The attempts made using the above techniques proved tedious because of the large number of combinations required to accomplish the task. A more efficient technique of extracting the Doppler Effect information from the data was therefore developed. In the new technique, off-line sorting with an algorithm implemented in the **XSYS** code [253], was applied. In the algorithm, all the possible detector and angle placement combinations were utilised achieving for the number of detector combinations $k = {}_{15}\mathrm{C}_2 = 105$ in the spectra produced. The extraction of Doppler shifted and broadened gamma spectra gated for particular residues from the data set

is obtained in the **XSYS** sorting code, operating on the calibrated and timing filtered event by event data files. The technique works thus, two gates G_n^{γ} and G_n^{bg} are set, where G_n^{γ} is the known gamma line gate, G_n^{bg} is the corresponding background gate and n is the number of the detector. A loop is performed through all the measured coincident events. If a gamma falls within gate G_n^{γ} among the coincident events, the rest of the gammas (from other detectors) are incremented into their corresponding histograms to produce a spectra. On the contrary, if the gamma energy falls within the gate G_n^{bg}, the corresponding coincident gammas are decremented from the spectra. The gate of the residue gamma line is set to correspond to the energy shift and broadening ascertained by inspection of the total projection spectrum for all the runs. This allows non-90° spectra to be used in the gating procedure with good knowledge of all the spectra components. The detectors that were not performing well during in-beam use (e.g. bad resolution) are used in logic decisions in the code but their spectra are not incremented into the generated histograms. All possible combinations of detector angle spectra are obtained, for a given gamma line identifying the nucleus, in one single off-line sorting of the event by event data from the experiment. This ensures that the highest possible statistics is obtained.

The off-line sorting code implemented based on the **XSYS** data acquisition and analysis system for the μVAX computers operated on the following set of decisions, deduced from systematic investigation of the Doppler effect extraction and background subtraction trial tests:

- Only the lowest gamma energy transitions were gated on. This minimise losses into the background of the coincident gammas of higher energies. (The lower the energy gate, the lower the Doppler effect, equation 5.4.)

- Only single events (one out of the four detector element recorded an event) were considered valid for the LEPS detector because they are prone to a relatively high background level, mostly from the low energy Compton back-scattering within the target chamber and from one LEPS detector to another.

- Add-back was applied to all the Clovers detectors (section 5.4.5). Coincident tests

showed that most of the double events within the detector elements, were as a result of Compton scattering from one crystal element to the other, see figures 5.18 and 5.19.

- The two gates mentioned above G_n^{bg} and G_n^{γ} have the same width set in each of the detectors. Gate G_n^{γ} belongs to a residue gamma line and G_n^{bg} to the broad background spectra, on the lower energy side of G_n^{γ}.

- If gate G_n^{γ} in detector n was satisfied, the coincident gamma lines in the other detectors are incremented to their respective histograms. If G_n^{bg} is satisfied, a decrement takes place accordingly. (Any existence of contaminant gamma lines within the broad background gate G_n^{bg}, is reveal by a negative peak elsewhere in the produced spectrum, corresponding to the coincident gamma line in the G_n^{bg} gate.

The code sorts through the stored event by event data files performing the above set of decisions and incrementing the histograms as appropriate. The sorting technique is effective in minimising and normalising the background spectrum, at the same time extracting the needed information for each detector. The major problem of this kind of study is the enormous level of background (section 3.2.2). The additional background reduction provided by cyclotron RF timing signal was not possible because of a fault in the transmission during in-beam time. The approach combines the parameters of two detector types, three detector angles and two independent gate widths indicated initially. The disadvantage though is that each of the residue nuclei identified need an independent off-line sorting of the stored data set for the whole experiment. It is time consuming but the advantage is a high statistics spectra.

5.3.6 Recoil Angle Versus Residue Velocity Simulation

A simulation has been performed to test the biasing effect introduced by the detector array to the observed recoil angle distributions $(\theta_r, \sigma_{\theta_r})$ and velocity distributions (β, σ_β) of the residues using the technique explained in the section 5.4.8. If one were to have performed the analysis simply based only on equation 5.5 with its concomitant assumption that $\theta_r \approx 0$.

Known spectra (but artificial) are simulated for comparison with the output information using the procedure described in section 5.4.8. The artificial data is assumed to be based on Gaussian distributions represented by β, σ_β, θ_r and σ_{θ_r} for the mean velocity, its standard deviation width, the mean recoil angle and its standard deviation width, respectively. The simulation is achieved by using Gaussian random deviates with angle of mean value given by θ_r and width of $30\%\theta_r$ and velocity of mean value β_r and width of $30\%\beta_r$. Shown in figure 5.14(a) are the re-extracted distributions (using the method of section 5.4.8) for each of the artificial data sets at simulated angles of θ_r = 15°, 30°, 45° and 60°. In figure 5.14(b), the effect of the residue recoil angle on both β_r and σ_β is plotted. It is observed that if the width of β_r is greater than the mean β_r, a region of indeterminacy is obtained. The upper limit of which is set by the gamma energy distribution in the detector, which for a $\sigma_\beta = 30\%\ \beta_r$ the value is 56°. The lower limit is set by the intrinsic resolution of the detector and the gamma energy. The calculated mean velocity of the distribution β_{exp} is found to be shifted to the lower energy such that the apparent velocity measured is

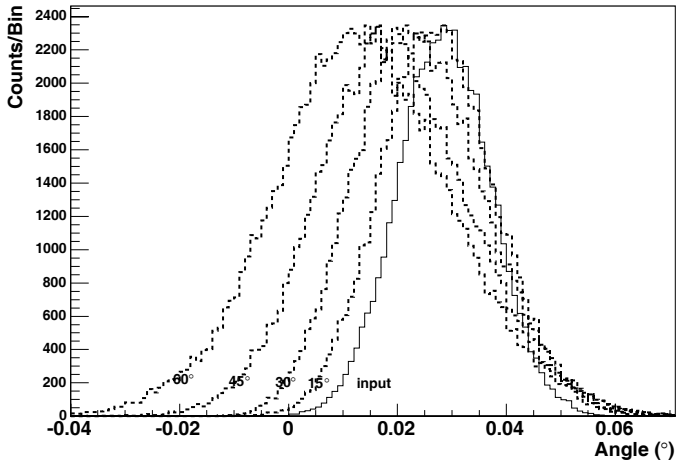
$$\beta_{exp} = \frac{\beta_r}{cos\theta_r} \tag{5.12}$$

This suggests that the experiment values are in fact the resolved components of the actual event by event residue velocity distributions in the beam direction. This indicates that the experimental value β deduced using the expression given in equation 5.5 is under-estimated by the reciprocal of the cosine angle of the recoil angle θ_r. In order to accurately determine β_r, one needs to accurately know θ_r or vice-versa. The mean value of θ_r obtained from equation 5.7 is not valid in this aspect.

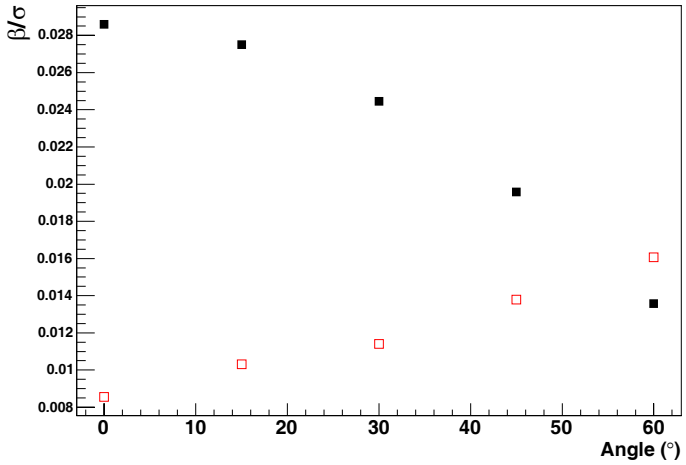
5.4 Experimental Data Reduction

5.4.1 Relative Residue Production Cross Section

The determination of independent and cumulative population of individual energy levels and exit channels, in compound nucleus reactions using gamma coincidence measurement tech-



(a) Residue recoil angle effect on the observed velocity distribution.



(b) Residue recoil angle effect on the observed velocity (solid boxes) and σ_β (open boxes).

Figure 5.14: The effect of residue recoil angles θ_r assuming a constant velocity value.

niques, is a well established field in nuclear structure studies [257]. To obtain the total reaction cross-section from the experimental measurements for a given projectile energy, all the residues produced need to be measured to cover the decay emissions from the time of formation $t = 0$ to $t = \infty$ for stable nuclei. This is on the assumption that all the nuclei produced undergo gamma

emission at one stage of their de-excitation process. This also ensures that all the residue decay life-times are taken into account to give the integrated yield for all the produced residue nuclei. In practice e.g. in conventional radiochemical techniques, this is not realised, only limited time window measurement is achieved. To get the total reaction cross section directly from these measurements is impossible except in systematic set of measurements covering all the time windows, which include both in-beam and off-line studies [35, 36]. During in-beam time, the accelerator beam pulse width sets the limit of the longest possible nucleus life-time measurements. The beam pulse time gate is applied to discern the in-beam prompt gamma emission production from the off-beam delayed gamma events (for the relatively short life-time nuclei). These emissions include both particles and photons, of which the present study is dedicated to measure the characteristic gamma-rays. (If the measurements proceed for up-to 3 days after the beam on target stops, the information of short-lived and medium-lived (1 hour $< T_{1/2} <$70 days) nuclei is obtained. The final time window would last from 70 days, for up to 6 months, for accurate identification of the long-lived products ($T_{1/2} >$ 10 days) typical of the conventional radiochemical techniques, which is not the focus of present study. For complete coverage of all the residue nuclei, other exit channels, not detected with the present setup might have to be considered.)

For the purposes of analysis, gamma-gamma correlation matrices were generated using the 90° Clover detectors and all the Clover detectors in the array. The in-beam matrix produced contained all prompt coincident gamma emissions occurring within 100 ns of the main beam burst. Though the timing cyclotron RF signal is not used in the present study, the residues are produced on flight because of the very thin target used and consequently any delayed emissions are emitted far away for the current setup to detect. The coincident gamma-rays were examined by specifying coincidence gamma line energy gates on one axes of the matrix and projecting a one-dimensional spectrum onto the second axis. The production yields of the residue nuclei populated were deduced from the quantitative in-beam gamma-gamma coincidence analyses, where the intensities were corrected for efficiency and internal conversion (section 6.2.8). The

residue production yields were extracted using the following procedures:

- The yields of even-even nuclei were derived from in-beam gamma-gamma coincidence intensities of transitions from low-lying states. Typically, the intensities of $4^+ \rightarrow 2^+$ transitions in coincidence with $2^+ \rightarrow 0^+$ transitions were measured. The assumption made being that the populated nuclei de-excite mostly through the 4^+ state.

- The yields of other nuclei were obtained by measuring the coincident gamma emission for the intense transitions of the nucleus. For the specific decay branches, in-beam gamma-gamma coincidence intensities of transitions between low-lying states were measured and values were normalised to a 100% decay branching ratio and the intensity ratio of the energy state. In some cases this could be done for more than one branch, so several independent yield values were extracted and a weighted mean of consistent yield values was then taken.

The analysis was completed by examining practically the full distribution of reaction products. The plots for each isotope were made and extrapolation was done to establish the supposed yields of the unobserved from which a search was conducted through the experimental data. For each residue, the production yield value for a specific nucleus was obtained by gating on the low-lying transitions in the coincidence matrix. The gamma line corresponding to the next transition up in the level scheme of the nucleus was then integrated and corrected for the double gamma emission coincidence efficiency and the internal conversion. In all cases, the gamma intensity ratios used for comparison were those given in the Evaluated Nuclear Structure Data File (ENSDF), Experimental Unevaluated Nuclear Data List (XUNDL) and Heavy Ion Data (HI,XNG) obtained from the these databases: **ftp://radware.phy.ornl.gov/pub/nd/** or **http://www.nndc.bnl.gov/ensdf/za_form.jsp**. The variation in the gamma gate energy, which normally leads to the largest deviation [36], was avoided in the present study in order to obtain uncertainty of less than 10%. This was achieved through the simulation of the observed coincident gamma pairs using the same setup of detector arrays as in the real experiment. According

to Ref. [35], the determination of residue yields from the in-beam gamma-gamma coincidence analysis is difficult for the following reasons. The interpretation of in-beam results require a good knowledge of the population of various states in a given residue nuclei. Meaning that it is necessary to estimate how much of the total production yield, is represented by the coincidence intensity of two specific transitions, for each of the observed nucleus. This is crucial for nuclei produced in the peripheral interactions, where quasi-elastic processes populate mainly the non-yrast energy states. The coincidence condition put in the electronic hardware inhibits detection of single photon transitions to the ground states energy level, deduced from the branching ratios of the energy level. The values obtained for some of residues are given in section 6.2.8.

5.4.2 Residue Recoil Asymmetry and Tracking

If two gamma emissions in coincidence E^1 and E^2 from a cascade are detected in two detectors opposite each other at 90° then the events may be plotted as a 2-dimensional distribution. This distribution is characterised by two axes either a positive (+) 45° slope or negative (-) 45° slope, figure 5.15. The sets of Doppler equations map the Doppler parameters onto the axes as follows

$$E^2_{90} + E^1_{90} = 2E_0 + \sqrt{2}E_0\beta_r\Delta\theta_A + \sqrt{2}\delta \tag{5.13}$$

This expression indicates the (+) slope axis measures $\sqrt{2}E_0\beta_r\Delta\theta_A$.

$$E^2_{90} - E^1_{90} = 2E_0\beta_r\cos\theta_A + \sqrt{2}E_0\beta_r\Delta\theta_A + \sqrt{2}\delta \tag{5.14}$$

This indicates the (-) slope axis measures $2E_0\beta_r\cos\theta_A + \sqrt{2}E_0\beta_r\Delta\theta_A$. The above expressions are based on equations 5.4 and 5.6, assuming that the distribution of hits on the detector faces as well as the energy residual, are expressed as Gaussian distributions characterised by $\Delta\theta_A$ and δ, respectively. The second expression (measured on the (-) slope) has an extra term in it given by $\Phi = |2E_0\beta_r\cos\theta_A|$ which is the residue recoil asymmetry, with an added advantage of the improved intrinsic detector resolution of $\sqrt{2}$. The additional information available in this 2-dimensional plot as compared to the 1-dimensional plot could be used to discern the

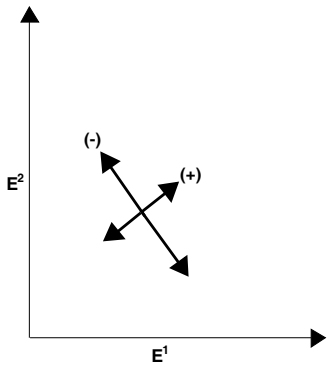


Figure 5.15: Two dimensional plot of opposite detectors oriented perpendicularly to the beam axis.

two contributions of the Doppler shift, i.e. the recoil velocity component and the recoil angle component. If for example, any of the two terms in Φ tends to zero, then no asymmetry is observed in the distribution obtained above. To observe this phenomena, two opposite detectors (Clover) both at 90° with respect the beam axis were utilised, see figure 5.16. The line energy E observed in detector D1 is plotted in 2-dimensional with the coincident energy E on the opposite detector D2. As shown in the figure, when the residue recoils towards detector D1 at some angle θ_r°, then the gamma recorded in detector D2 will be shifted to the lower energy side whereas the gamma recorded in the detector D1 will be shifted to the higher energy side and vice versa. Plotting these data in the parameter space of energy D1 versus energy D2 should consequently give a negative gradient locus, proportional to the magnitude of Φ. When the residues recoil out of plane, its relative gamma energy is resolved onto the plane of the two detectors and the longer the spread of the measured locus, the larger is the Φ. The projection of the spectrum along the locus axis provides information on the intrinsic resolution of the detector. Since the mean value of β_r is known (from section 5.3.2), the mean width of the recoil angle σ_{θ_r} distribution, assuming a Gaussian distributions about the beam axis, can be deduced. Residue recoil tracking could be realised through the knowledge $(\beta_r, \theta_r, \phi_r)$. Any three detectors

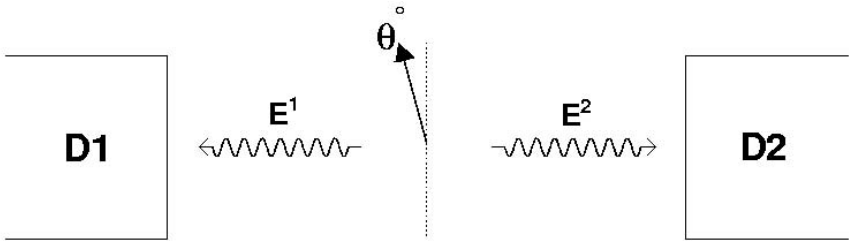


Figure 5.16: Two opposite detectors on one plane detecting two coincident gamma rays of energies E^1 and E^2, Doppler broadening causes $E^1 > E_0^1$ and $E^2 < E_0^2$ and for $\theta_r = 0°$ or $\beta_r = 0$, $E^1 = E_0^1$ and $E^2 = E_0^2$.

in the array are potentially capable of giving a panoramic view of the recoiling gamma emitting nucleus. Full description is beyond the scope of the present study but for this to be realised the nucleus must have at least three gamma energies in the emission cascade. Because of the higher level of coincidence it demands, few events could be obtained in the process. The results obtained from this work are given in section 6.2.7.

5.4.3 Velocity Distribution Reproducibility

The reproducibility of the velocity distribution was investigated using nuclei with more than one gamma energy emission in the cascade. An example are the ^{54}Mn and ^{55}Fe residues. The raw velocity distribution of the nuclei were generated using the prominent gamma line using reconstruction technique explained in section 5.4.7. These are shown in figures 5.17. The ^{55}Fe 605 keV line generated velocity distribution has larger $\beta(\sigma_\beta)$ values compared to the other lines. (There could be some interferences from the ^{74}Ge(n,n$'\gamma$) and ^{73}Ge(n,γ) 596 keV and 597 keV gamma lines, respectively, due to the activation of the detector material elements, (see figure 5.13).) The generated respective Gaussian fitted velocity distribution $\beta(\sigma_\beta)$ for the ^{55}Fe

605 keV, 1223 keV and 1317 keV were 0.020±0.011, 0.017±0.008 and 0.017±0.008. It was clearly evident from the fits that the high energy gamma lines leads to under-estimation of the high energy component of the velocity distribution during the reconstruction routine (either due to poor statistics or some cut-off problems) whereas the low energy gamma lines over-estimates (due to the intrinsic detector resolution). The respective values for the ^{54}Mn 212 keV and 705 keV were 0.0190±0.012 and 0.0190±0.011, having no significant difference in this case.

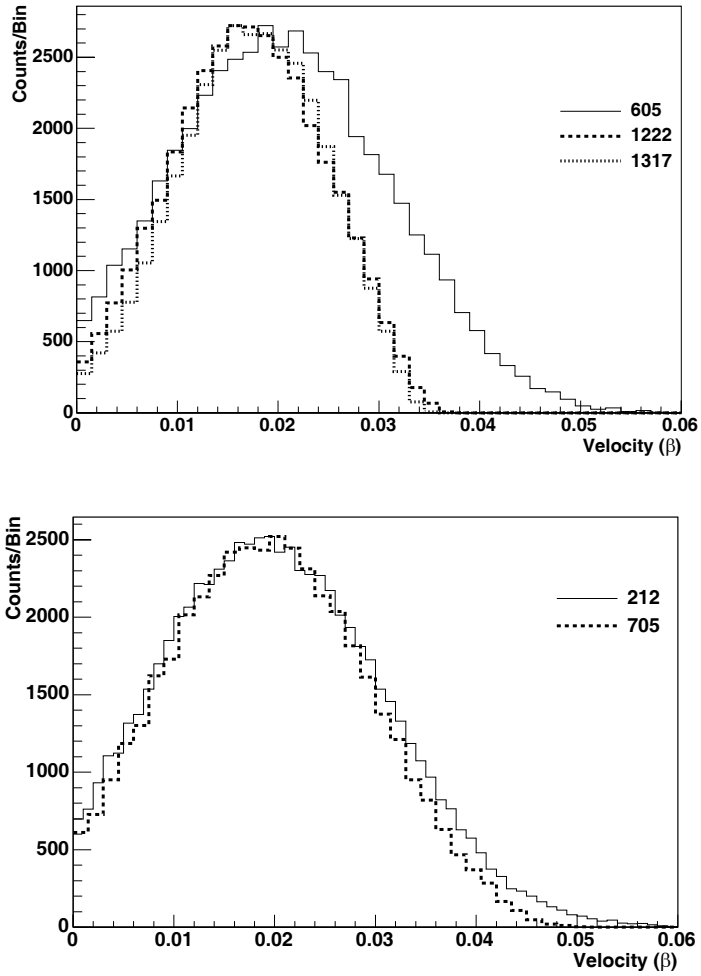


Figure 5.17: The comparison of raw velocity distributions for the different gamma transition energies of ^{55}Fe (top) and ^{54}Mn nuclei.

5.4.4 Residue Half-Lives ($T_{1/2}$)

A problem arises, if the gamma emission is delayed or has a long life-time. This is due to the fact that the nucleus decays on flight and by that time the vertex position of the gamma emission will have been shifted with respect to the detector positions. This could be avoided by using pulsed beam from the cyclotron RF or a thicker target material. In the case of thin target, one has to compute the mean distance travelled by the nucleus before it decays through gamma emission process based on the known life-times. Taking the case of the ^{57}Fe nucleus with relatively high velocity and long half-life of 8.7 ns, the mean distance covered before decay is about 7 cm from the vertex position assuming a velocity of $0.026c$ or nearly 35% of the Clover distance from the target (vertex) point. This causes a negative off-set to the detected gamma line. For the ^{57}Fe nucleus, the magnitude of the shift for the 90° detector is about 2.5%, or more than 6 keV reduction for the gamma transition energy of 256 keV. This could easily lead to misidentification of the nucleus. (The Clover collimator minimised this effect as orientation in space is partially confined.)

5.4.5 Evidence of High Energy Photons

An investigation was conducted to identify the contribution of multiple hits in the Clover detectors. A two-dimensional matrix of the coincidence hits of the four detector elements, whose total projection is given in figure 5.18 for all the well-performing Clover detectors in the array ($k = {}_{26}C_2 = 325$), was constructed. It was evident from the matrix that most of these multiple hits were caused by Compton scattering of 511 keV photons across the detector elements. The structure of the spectrum is typical of the photo-peak energy efficiency curve of the Clover detector given in figure 5.7. A gamma energy gate G_1 set at any point below the 511 keV energy line produces the coincident gamma line whose energy G_2 satisfy the condition $G_1+G_2 = 511$ as shown in figure 5.19. Since there is no 1022 keV line in the Clover sum spectra, this implies that the Compton scattered 511 keV is the product of an annihilation process of

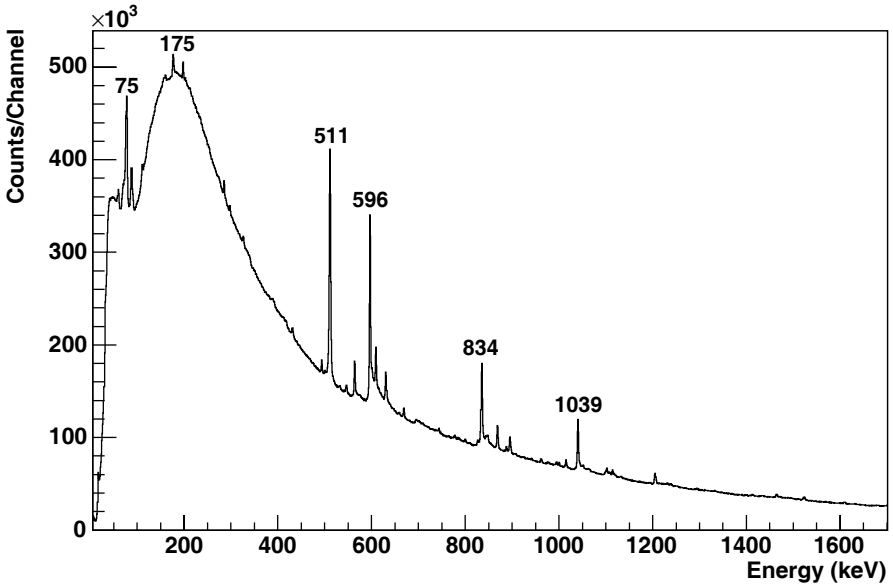


Figure 5.18: The total projection spectrum of coincidence hits within the Clover detectors. The characteristic gamma lines and *X*-rays observed in the spectrum are due to the excitation of the detector and surrounding elements.

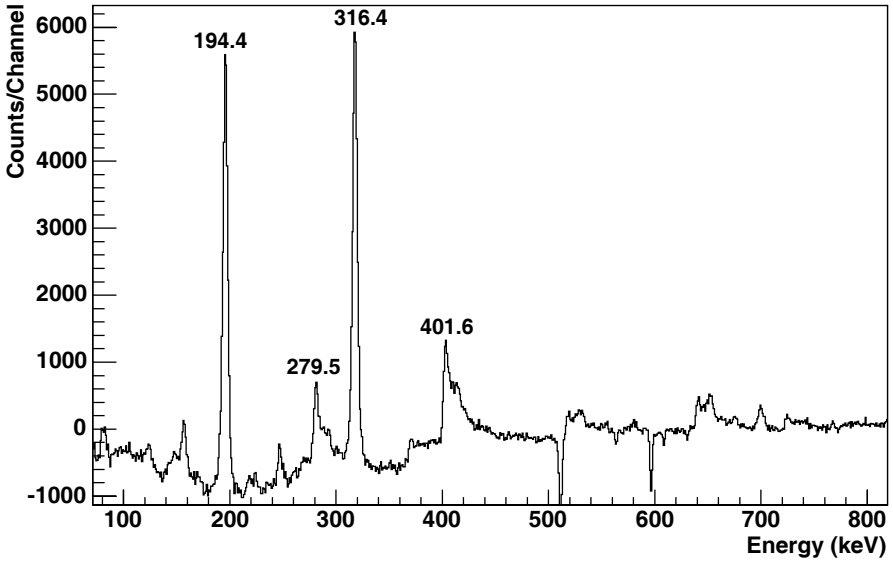


Figure 5.19: The spectrum of the coincident energy gates of 194.4 keV and 316.4 keV logically ORed. The total energy is 511 keV reflecting the Compton scattered event across the adjacent detector crystal elements.

the pair produced positrons from a high energy gamma photon. This suggests that the add-back process could potentially reveal energies of high energy gamma rays, since the detector amplifier gain settings for each of the four element was set for a maximum of 2 MeV, the setup could then be able to provide energies of up to 8 MeV. The reason for doing this was mainly to search for the evidence of the gamma emission decay from the excited projectile-like fragments produced through inelastic interaction process with target nuclei, e.g. the 4.4 MeV ^{12}C gamma line. The simulations done for 100000 events using GEANT4 show that the Clover detector can detect a full photo-peak for gamma energies of up to about 10 MeV.

5.4.6 Residue Cross-Coincidence

Any excited two or more fragments produced in the interaction process, decaying via gamma emissions (see section 5.4.5) have a certain probability of coming in coincidence if the emission time scale corresponds. This is utilised in cross-coincidence studies [6]. The minimum number of photons is two from each of the de-exciting nucleus, making a total of four-fold coincidence or four minimum detectors for absolute identification of the respective nuclei. The probability for single gamma coincidence could be more dominant but their identification could be a problem except in the case of transfer reactions. Since the two fragments have totally different velocities (β_r) when using a thin target material, their coincident gamma lines will not have a consistent Doppler effect. The target-like fragments will have much less Doppler broadening compared to their partner projectile-like fragment. The situation is worsened by the high velocity - large angle combination which leads to the significant reduction of the observed gamma energy (section 5.3.6). The lowest energy transitions are more like to coincide, especially for the even-even nuclei because of their high gamma emission intensities.

5.4.7 Residue Velocity Reconstruction

This section assumes that two detectors D1 and D2, randomly selected in the array, detects coincident gammas emitted by a recoiling nucleus moving with some velocity β_r and

angle θ_r, figure 5.20. By utilising Monte Carlo techniques and the actual experimental data extracted as explained in sections 5.3.5 and 5.3.4, attempts are made to reconstruct event by event properties of the detected residue utilising the Von Neumann Rejection (VNR) technique. The simplest case is the extraction of velocity distribution (β,σ_β) from the experimental data.

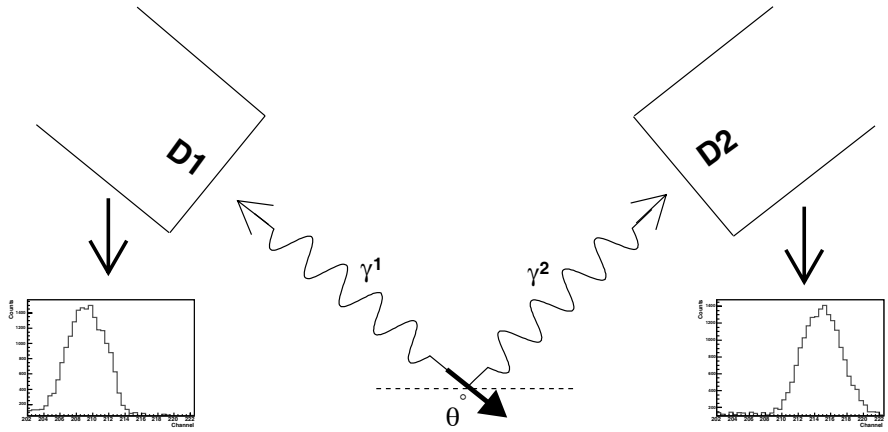


Figure 5.20: The reconstruction technique showing coincident gamma detection measurements and the obtained spectra used in the selection criteria.

Assuming that detector D2 is at 45° and D1 is at 135°, the following steps are applied

- Set up the gates G_{D2} and G_{D1} corresponding to the gamma line widths in the actual measured spectra (figure 5.20) for the D2 and D1 detector angles, respectively;
- Select (uniform) randomly any bins (using the random number generator) in the gate to get B_{D1} and B_{D2} for the corresponding gates.
- Read the contents of the selected bins, subtract the background counts and divide by the maximum value within the corresponding gates, to get P_{D2} and P_{D1}, the bin relative probabilities.
- Evaluate the corresponding energy values for each of the selected bins, E_{D1} and E_{D2};

- Select another set of two uniform random numbers, R_{D1} and R_{D2};
- Evaluated the recoil velocity β using equation 5.5 and the energies E_{D1} and E_{D2};
- If $R_{D2} < P_{D2}$ and $R_{D1} < P_{D1}$ are both true, β the value of the event selected conforms to the actual distribution of the experimental data and is stored in a histogram.

The spectrum shown in figure 5.11 was produced using the above procedure. The problem with it stems from the fact that the recoil angle is unknown and explains why there are negative velocities in the β distribution plot. This is here referred to as the raw velocity distribution as the most appropriate approach could have been to use the experimental event by event data in the reconstruction routine above.

5.4.8 Residue Velocity and Angle Reconstruction

The simulation to reconstruct the detailed event by event properties of the residue nucleus follow similar steps as described in section 5.4.7. The steps used in the reconstruction process of the residue velocity β_r and angle θ_r uses the following procedures

- Select a random β_r, θ_r and ϕ_r for the residue;
- Select two sets of random ϕ_d and θ_d corresponding to the two detectors D1 and D2, at the experimental θ_d, (Apply the detector opening angle correction to the quantities selected here, using uniform deviates with the width of the detector opening angle.);
- Evaluate the angles θ_{A1} and θ_{A2} between the quantities obtained in point one and two, using vector geometry;
- Use the Doppler effect equation to get the respective gamma energies E'_{D1} and E'_{D2} detected at D1 and D2, (Gaussian deviates with mean values of E'_{D1} and E'_{D2} and respective standard deviation widths taken from the corresponding intrinsic detectors resolutions, could be used to simulate detector resolution and establish the actual detected energies E_{D1} and E_{D2}.);

- Read the bin content corresponding to the two energies of the event in the actual experimental spectra (point four), subtract the background counts and divide by the maximum value within the corresponding gates, to get P_{D2} and P_{D1}, the bin relative probabilities (experimentally).

- Select two random numbers, R_{D1} and R_{D2};

- If $R_{D2} < P_{D2}$ and $R_{D1} < P_{D1}$ are both true then β_r and θ_r of the event selected randomly conforms to the distribution of the data and are stored. Repeat this process to establish event by event data of β_r and θ_r values.

The maximum possible longitudinal velocity β_{max} set may be given by the condition that assumes 100% pre-equilibrium nucleon loss, say ^{54}Mn.

$$\beta_{max} \approx \frac{A_P}{A_r}\sqrt{\frac{2E_P}{A_P 931.5}} \tag{5.15}$$

where A_r is the mass of the nucleus and A_P is the projectile mass in atomic mass units, E_P is the projectile energy in MeV. This gives $\beta_{max} \approx 0.05945$. The cut-off limits may be set by the range of values $0 - \beta_{max}$ for β_r, 0-180° for θ_r and 0-360° for ϕ_r. The correct angle manipulation is performed using G4ThreeVector in GEANT4, or TVector3 classes in **root** and energy using the Doppler Effect. This process effectively corrects for the opening angle of the detectors if a random number generator is used to sample the various hit points on the volume detector. The ambiguity arising in section 5.12 may be difficult to eliminate. The spectra of the three detector angles of ^{54}Mn, for instance, could also be ascribed to a biased contribution of almost a uniform velocity distribution, the maximum value defined by the compound nucleus, and a fixed recoil angle close to 20°. The technique, however, could serve well as an event filtering mechanism, providing the most optimal conditions necessary to reproduce the experimental observables. The alternative way is to utilise 3-fold gamma coincidence events.

5.5 GEANT4 Simulations

The GEANT4 simulations in this work covered two aspects, namely the photon and nuclear interaction processes described in sections 4.1 and 4.2, respectively. The latter case is done directly and indirectly. In the direct approach, a complete simulation has been done by tracking the incoming projectile ions impinging on the target material as in the real experiment, utilising the relevant interaction processes. The problem with this approach was found to be the delta electrons produced with significant cross-section, which GEANT4 has to track. The other problem being the fact that a thin target requires tens of thousands of primary incident projectiles to initiate a single nuclear interaction. The first problem is minimised by setting the nuclear physics processes energy cuts small whereas the energy cut-off of the other processes are set to large values or simply stopped by disabling the electromagnetic interaction processes for ions. The second problem is solved by using either event biasing technique [232] or increasing the target thickness while ensuring that secondary interactions are kept at minimum. The problem of the complete simulation is that the different interaction processes are cascaded, in the nuclear interaction stage, and in the detection part. This implies that an error at any level of the calculation is propagated to the final outcome leading to systematic errors. This may be avoided by doing each simulation independently.

In the indirect approach, two different methods have been investigated in the study:

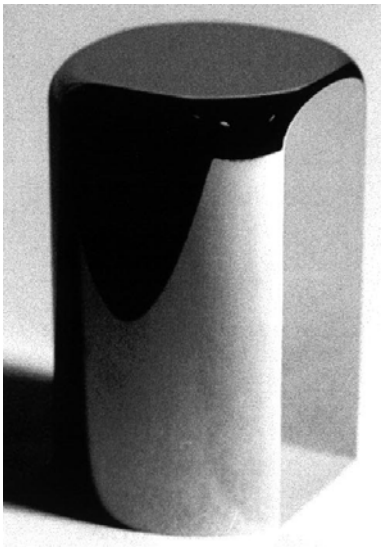
- Data output from other theoretical calculations has been used as the input to the GEANT4 code. This is done at different levels of complexity. In the simplest case, the gamma line shapes are generated by setting the residue production vertex recoil conditions (β_r,θ_r,ϕ) using the output values obtained from other independent model calculations. The relative angle of the detector position with respect to recoil direction of the nucleus is then calculated and using the Doppler effect formula, the final energy detected is evaluated, or

- using kinematics event reconstruction algorithm based on the experimental spectra of

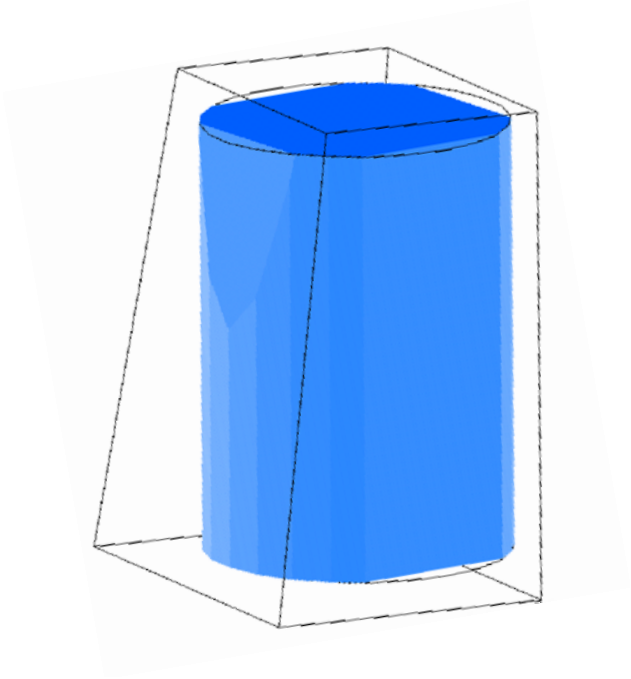
the residues for the various detector angle positions, as explained in section 5.4.8. This is easily implemented using the ROOT analysis package.

5.5.1 Detector Simulation

The performance of the Clover detector constructed for the simulation exercise is an attempt to reproduce the real detector, by ensuring that the entire physical parameters of the detectors used in the experiment are matched. The physics for simulating the gamma detection processes takes into account all the relevant interaction cross-sections such that the actual experimental conditions are reproduced (section 4.1). This could then be used for quantitative and qualitative analysis of the experimental data, leading to possible predictions of the experimental parameters. The construction of the basic units of the Clover detector was achieved in a series of steps in GEANT4 code. The germanium crystals were derived from a Boolean union operation of double-axes rotation of a trapezium and an un-rotated cylindrical solid, see figure 5.21(b). This resulted in a solid with quasi-squared front section obtained by the bevelled two adjacent faces with and angle of 7.1° starting at almost half of the crystal length and cutting the other two faces parallel to the cylindrical axis along its whole length. Close packing of 0.2 mm germanium-germanium distance is achieved with this shape. The total active germanium volume element is about 470 cm^3, which corresponds to 89% of the complete solid cylinder. The distance between the bevelled edges of the crystals and the internal surface of the end-cap is 3.5 mm. The thickness of the surrounding and the end-cap Aluminium is 1.5 mm, similar to those used in Ref. [233]. The construction of the BGO shield was modified slightly from the actual shape and setup to simplify and shorten the code used. Two trapezium solid objects, one slightly rotated about the smaller axis and Boolean subtraction performed on the two objects resulting in “L” shape solid just enough to shield each crystal independently. This meant that only four BGO were required compared to the actual number of 16. The critical dimensions were maintained such that the length of each BGO crystal remained as 242 mm while its thickness varied from 19.5 mm at the back to about 3 mm at the front of the shield. The front faces



(a) Photograph taken of a Clover crystal.



(b) Matching Clover crystal constructed for use in the simulation.

Figure 5.21: The HPGe crystal element in the Clover detector.

of the germanium crystals were positioned 6 cm behind the front edge of the BGO shield for good suppression of back scattered events [233]. A Tungsten collimator was placed just in front of the BGO shield. The dimension of the collimator was 36 mm long and 18.5 mm thick. To build it, two trapezium solid objects, of different dimensions and same thickness were used. The smaller one of the two was then used to perform the Boolean subtraction on the larger object to make the collimator hollow. The complete construction of the Clover detector with the BGO shielding and the tungsten collimator for the simulation purpose is shown in figure 5.22 The photo-peak efficiency ϵ_p of the detector in both the experiment and in the simulation is given by

$$\epsilon_p = \frac{N_p}{N_s \frac{\Delta\Omega}{4\pi}} \tag{5.16}$$

where N_s is the number of gamma photons generated at the vertex, N_p is the number of counts constituting the photo-peak in the spectrum and Ω is the solid angle. Equation 5.16 is simplified

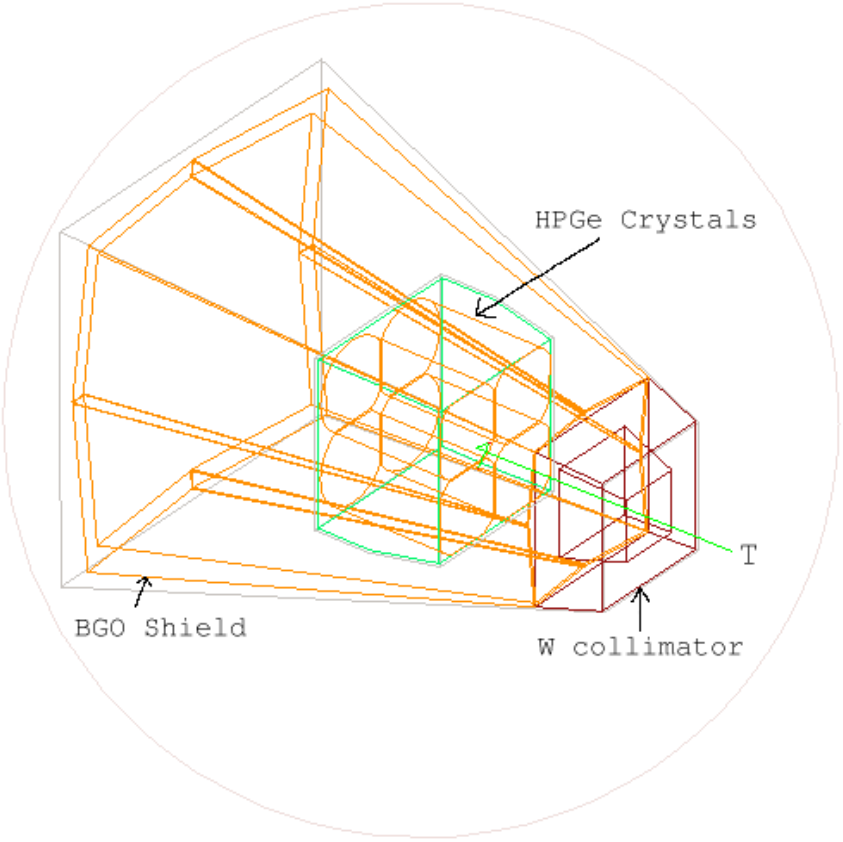


Figure 5.22: The geometry of simulated Clover detector, the gamma-rays are produced at the target position (T) and directed randomly to the front face of the Clover detector.

further by putting $\omega = \frac{\Delta\Omega}{4\pi}$ and taking it to the right hand side of the equation (table 6.1). To get the coincidence efficiency for the experimental data, two gamma energy lines observed in the experiment are simulated using the setup as the experiment. The number of gamma used in the simulation and the final intensities of the two lines from the simulation provide the correction factor for the experiment. The result are shown in section 6.1.

5.6 The BME - GEANT4 Simulations

The simulations below were performed using the output data sent from Milano. For the interaction of the 33 A MeV ^{12}C projectile with the ^{63}Cu target nuclei. The different sets of output data files generated from the model developed in Milano which contained the following information for each residue nuclei observed experimentally, in the first row.

- The number of the emitted neutrons (n_n).
- The number of the emitted protons (n_p).
- The N of the residue ($6 + 34 - n_n$).
- The Z of the residue ($6 + 29 - n_p$).
- The number of subsequent rows.

The rest of the rows, corresponding to each column were the following information

- The mean emission angle (θ_r) in 2° steps,
- The momentum p in (A MeV)$^{\frac{1}{2}}$ (The conversion to GeV/c factor is 0.03052.)
- The residue production cross section σ_i given in arbitrary units.

The data were used as input to the GEANT4 simulations. The residue recoil ϕ_r angle distribution is assumed to be a uniform distribution and that the angles for weakly populated exit channels are assumed to be naught. The following algorithm based on the Von Neumann Rejection (VNR) method was applied in the GEANT4 simulations using the above source of information as the input

- The largest cross section σ_m is selected from the σ_R column,
- The number of rows is determined n_r,
- A random number generator is sampled, $0 \leq n_1 \leq 1$,

- The $n_1 \times n_r$ provide the possible values of θ_r, p, and σ_i (row-wise),
- A random number generator is sampled again, $0 \leq n_2 \leq 1$,
- If $n_2 < \sigma_i/\sigma_m$ then θ_r, p, and σ_i are accepted,

When the possible values of θ_r and p are obtain, the value of ϕ_r is obtained by sampling the uniform random number deviate for the third time, $0 \leq n_3 \leq 1$ and multiplying it by 360°. For the p values, $p = (p' \times 0.03052)$GeV/c. The residue velocity β_r is then obtained by dividing pc (p') by mc^2 or $(A \times 0.9315)$, where A is the residue mass in atomic mass units. The θ_r, ϕ_r and β_r values selected constitutes the vertex point properties of the residue product for the inputs in the simulate of the Doppler effect gamma energy distribution described in section 5.4.8. This constitute a single Doppler shifted event for the residue under consideration. The procedure is repeated for a number of times to obtain the gamma distribution spectrum of the residue recoiling with the appropriate properties set by the theoretical expectation values. The Doppler shifted and broadened gamma line shape produced is compared with the experimental measurements in section 6.2.9.

Chapter 6

Results and Discussion

This chapter reports on the results of the measured observables in the study and theoretical calculations performed for comparison. This is covered in two parts covering

- Photon interactions, section 6.1,
- Nuclear interactions, section 6.2.

The physics of photon interaction is well established. The comparison between the theory and the simulation done are in agreement. The nuclear interaction, on the one hand, is on the process of achieving the same status. The present study of the latter is dependent on the reliability of the photon interaction, gamma spectroscopy and the Doppler Effect phenomena measurements. The following observables were then deduced:

- The residue formed;
- Their relative production cross-sections to gain insight information on the excitation energy, the equilibration and particle emission processes;
- The average Doppler shifts for information on the longitudinal momentum transfer processes;
- Doppler broadening from which the recoil angle distributions mean value and width information relating to the impact parameter of the interaction could be investigated.

Comparison have been done between the theory and the experimental measurements based on the model developed in Milano[1] and some specific GEANT4 model calculations, presented in chapters 2 and 4, respectively. The approach used in both models is based on the similar theoretical concepts, except in cases which will become apparent in the course of the discussion. The two theories assume the macroscopic properties of the nucleus in the interaction process. A brief comparison of the residue production based on the theory of quantum molecular dynamics, an alternative approach which treat macroscopic properties explicitly in the calculation, is presented in the appendix 4, (chapter E).

6.1 Photon Interaction Processes

The performance of the Clover detector constructed for the simulation purpose, subjected to the same experimental conditions, is useful in the validation of the theory of photon interaction processes implemented in the GEANT4 code as well as in verifying development of the implemented model. The comparison obtained from the simulations, experimental values and the reported values of Ref [233], for the performance of the Clover detector are shown in table 6.1. The energy gamma used in the study is 1332 keV. The comparison between the relative photo-peak efficiency of the Clover detector simulation and the experimental measurements is shown in figure 6.1. It is observed from the comparison that the simulated germanium detector (see section 5.5.1) performs very well, and is consistent with the measurements taken with the actual detector, within the experimental error limits. There are minor deviations observed originating mainly from the geometry of the actual Clover detector whose exact shape and dimensions are not provided in detail by the manufacturers. The simulation thus offers additional information which makes it possible to optimise the experimental setup for gamma detection. It is observed, for example, that the add-back mode enhances the $(P/T)_b$ ratio compared to singles mode. Using a selective BGO veto over the logic OR of all the BGOs, improves the performance ($(P/T)_c$) significantly. The coincidence within the crystal segments did not, however,

[1] All calculations relating to this model presented here is the work of E. Gadioli and the Milano group

Table 6.1: The calculation and measurement characteristics of Clover detector obtained at 1332 keV; absolute photo-peak efficiency, peak-to-total ratio (P/T) in (a) singles, total detection mode (b) any fired BGO veto and (c) adjacent BGO veto only, add-back factor F and distribution of the number of firing germanium crystal for full gamma photon energy absorption events.

Characteristic	Calculated	Measured[1]
$\epsilon_p\omega(\times 10^{-4})$	15.9(5)	16.1(5)*
$(P/T)_a$	0.16	0.16(1)*
$(P/T)_b$	0.28	0.30(1)*
$(P/T)_c$	0.36	-
F	1.47	1.53(1)*
Single hits(%)	75.72	75.76
Double hits(%)	22.03	20.44
Triple hits(%)	2.15	3.41
Quad hits(%)	0.10	0.39

* Values referenced in the text[1]

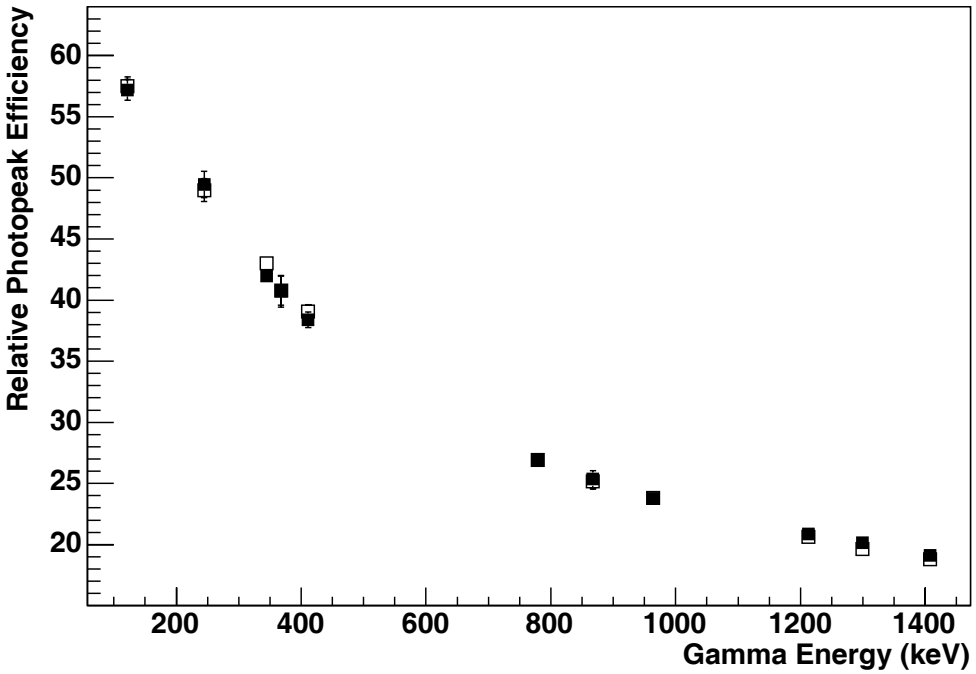


Figure 6.1: The relative gamma energy photo-peak efficiency curves obtained from GEANT4 calculations compared to the experimental values (open boxes).

show good agreement with experimental measurements [233], as it deviates with the number of the registered coincidence hits. It may not be a good parameter for characterising a detector because of its energy dependency and from the fact that most gamma emitting nuclei are not mono-chromatic. The relative gamma energy photo-peak efficiency values from the simulations were found to agree with the experimental measurements within the experimental error limits. The presence of the heavy metal (tungsten alloy) Clover collimator was observed to reduce the gamma-rays reaching the detector appreciably if the vertex is off-centred. This feature is important in minimising scattered radiation within the target-chamber and also from one detector to the other in the 4π array configuration. The scattered radiation was quite pronounced within the LEPS detector spectra during the in-beam use because of their lack of the Compton scattering shields.

The relative gamma energy intensity measurements have been compared with the reported values for the ^{64}Cu and ^{54}Mn nuclei [258, 259, 260]. The error estimates based on the values evaluated from the experiment with respect to these values are displayed in figure 6.2. The coincident efficiency correction terms were obtained from the simulations, as explained in section 5.4.1. The lines of the ^{64}Cu nucleus have positive relative intensity errors in most instances while the ^{54}Mn nucleus values are negative. This could be attributed to the fact that the Doppler broadening effect causes the distribution of the gamma line energy over extra channels proportional to the energy, leading to the reduction of the ^{54}Mn gamma line intensities. The gamma intensity ratios of the present study compared favourably with the existing data for the nuclei which have been measured in the study, with at least three gamma lines in the cascade.

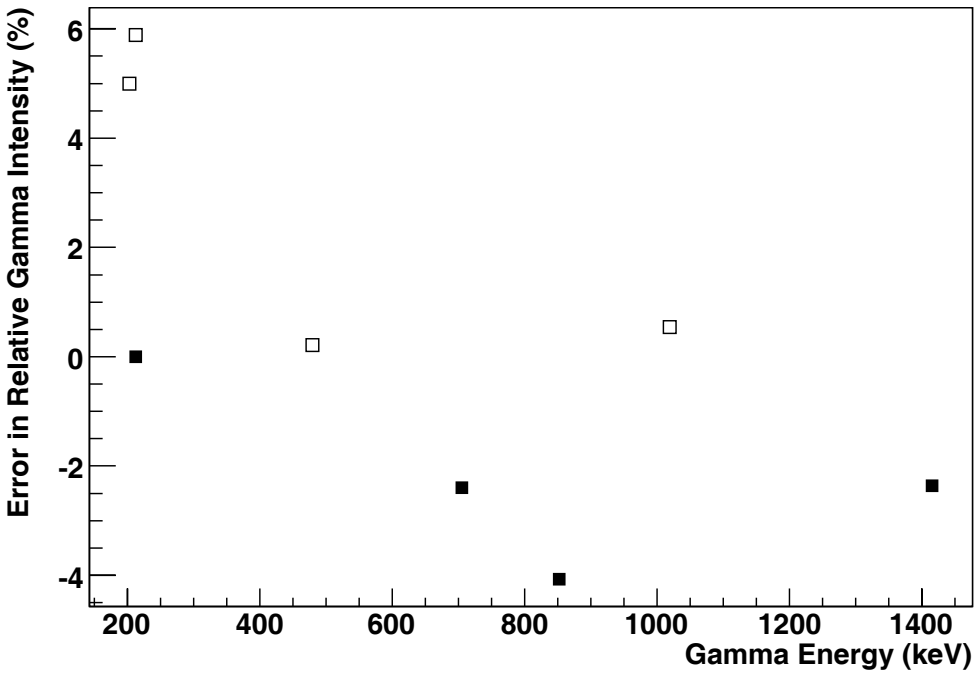


Figure 6.2: The percentage error estimates in the evaluation of the relative gamma intensity ratios of 212 keV, 705 keV 852 keV and 1416 keV lines for the ^{54}Mn nucleus gated on the 156 keV gamma line, and those of the 203 keV, 212 keV, 479 keV and 1019 keV lines for ^{64}Cu nucleus gated on the 159 keV line represented by the closed and open boxes, respectively.

6.2 Nuclear Interaction Processes

6.2.1 Relative Residue Yields

The total projection spectrum obtained during in-beam time is shown in figure 6.3 for the 90° Clover detector. The spectrum has been corrected for gamma energy photo-peak detection efficiency (section 5.5.1). The lines are assigned the identity of each gamma emitting nucleus on the all inclusive spectrum. The line intensities in the spectrum reveal the observed relative population of each of the identified nucleus. For instance, ^{54}Mn and ^{55}Fe lines are apparently the most prominent in the spectrum. The details of the gamma emission information of the observed residue gamma lines are given in appendix B. In general, the observed gamma emission lines provide information about the population of the various exit channels, the momentum transfer processes and the nuclear shapes. The most populated channels reported from the conventional radiochemical measurements for the present system were ^{64}Cu, ^{56,57,58,60}Co, ^{52,54}Mn, ^{51}Cr, ^{48}V, ^{44,46,47,48}Sc, ^{42}K [20, 21, 23, 33, 34, 116]. The highest cross sections in mb were reported for ^{58}Co, ^{57}Co, ^{51}Cr, and ^{54}Mn, as 94±8, 86±7, 78±8 and 69±7, respectively, have not been confirmed in the present study. Some of the abundantly produced residues observed in the present study but not reported in previous studies include ^{63,64,65}Zn, ^{62,63,64}Cu, ^{59,60,61,62}Ni, ^{55,56,57}Fe and ^{55}Mn, which clearly shows that the conventional radiochemical technique does not provide a complete set of residue identities.

The proton-neutron ratio of most of the residues lies within the valley of stability. The intense 511 keV line has been excluded in the plot (positron annihilation peak). It may be assumed to be the signature of significant residue production in the neutron deficient (β^+ unstable) mass region reported in other techniques [20, 61] but further investigation revealed that it is in coincidence mainly with the projectile-like fragments, indicating that its origin is in the high energy gamma emission which accompany their decay. These were some of the identified channels, when the total projection spectrum is gated on the 511 keV gamma line: ^{11}C due to the knock-out of one neutron from the projectile, ^{13}C due to the pick-up of one neutron from the

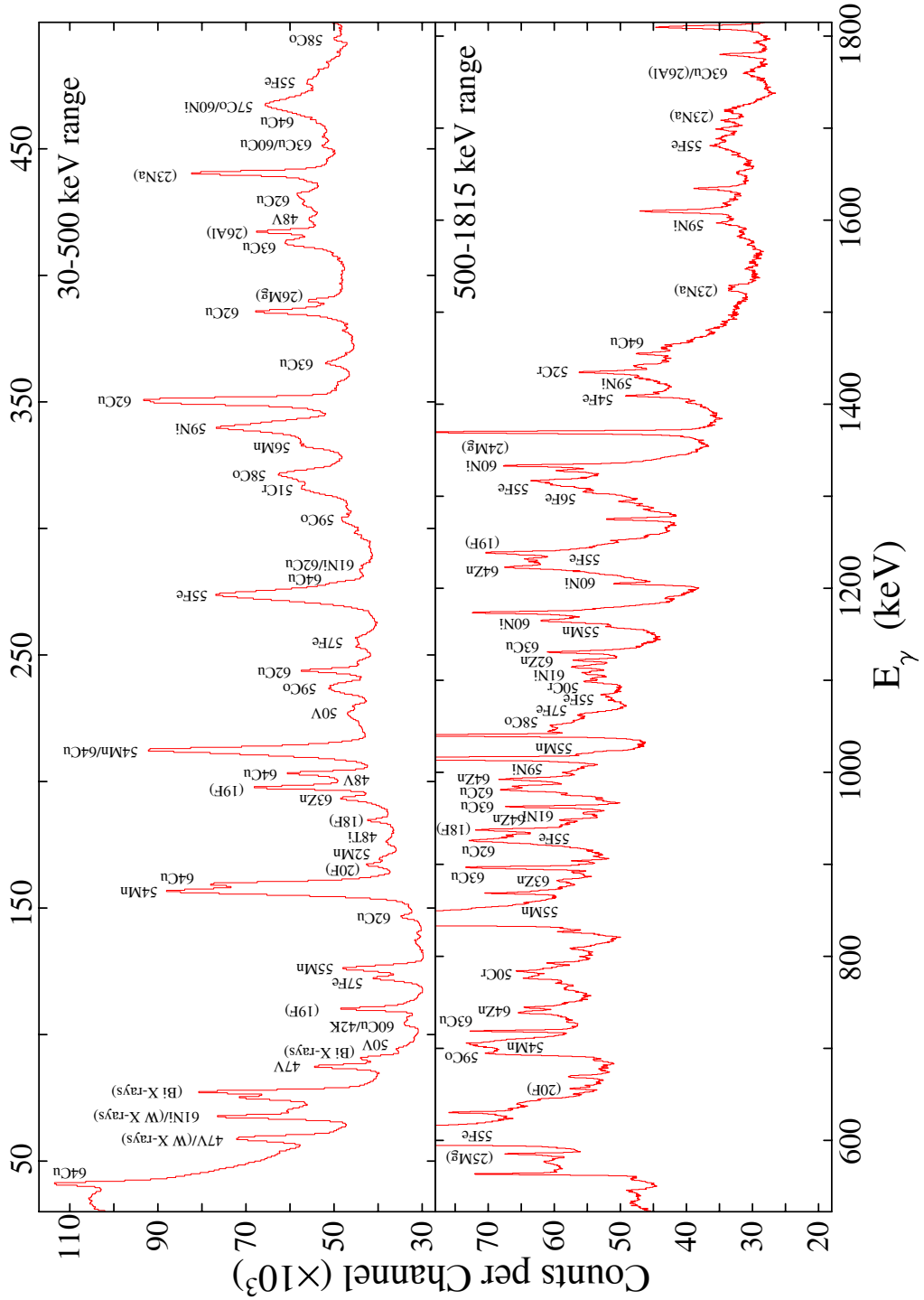
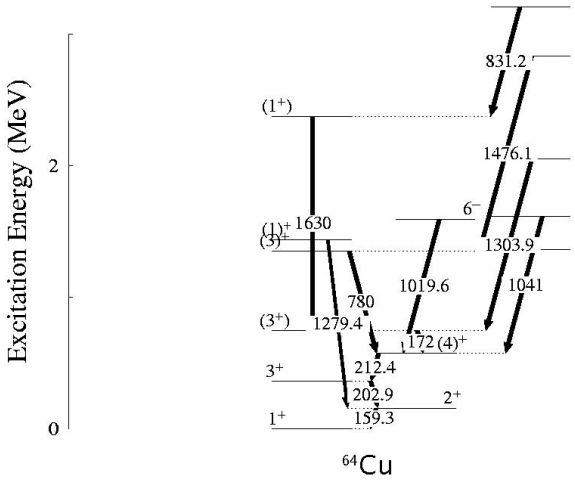


Figure 6.3: The total projection spectrum corrected for photo-peak efficiency. Gamma lines are assigned to their respective emitters based on gamma-gamma coincidence identification.

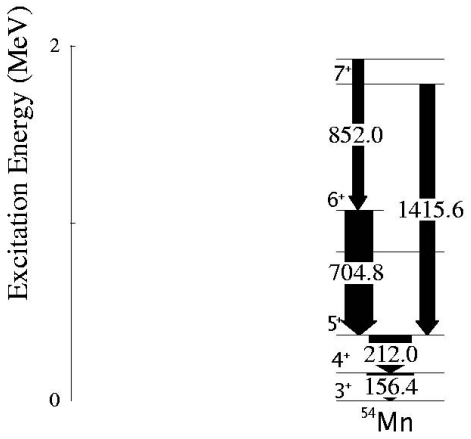
target by the projectile, ^{13}N due to the pick-up of one proton from the target by the projectile and ^{14}N due to the pick-up of one deuteron from the target by the projectile. The target frame also contributes significantly by virtue of its thickness. Among the intermediate mass fragment residues observed, the half-life of the ^{24}Na nucleus of 20 ms, suggests that it is a target frame (aluminium) product contrary to earlier claims [20, 33]. If it was a target product, the long life-time of the decay compared to the time of flight, could have made it impossible to detect it due to the distance covered before gamma emission occurs. If the beam was striking the target frame, which is a thick target, this product could be stopped and the gamma emission would occur at rest with no significant Doppler effect measured. This is also true for the other nuclei observed ^{27,26}Al, ^{26,25,24}Mg and ^{20,19,18}F. Some projectile-like fragment residues stopped in the target frame were also identified.

6.2.2 Angular Momentum Transfer

The magnitude of the angular momentum transfer to the residue product measurements in the present setup is difficult to obtain because of the reduction in the peak to total ratios as a function of the gamma energy due to the Doppler broadening effect. It has also been found in previous studies that the characteristic gamma multiplicity spectra reduces with increasing projectile energy, due to the reduction in angular momentum transfer [44, 261], or the preferable excitation, of the low-lying yrast transitions that produce the low gamma emission multiplicity of which the coincident intensities of the lowest lying yrast transitions represent the bulk of the gamma production yields [35]. Typical level schemes obtained from the identified nuclei for ^{64}Cu and ^{54}Mn residues are shown in figure 6.4. Unlike in the low energy regime, no evidences of population of high-spin states are observed. A detailed analysis of the level schemes and band structures of the identified nucleus is beyond the scope of the present study, and further work is suggested especially as few unidentified gamma lines have been observed in this investigation.



(a) The gamma energy level scheme of ^{64}Cu nucleus



(b) The gamma energy level scheme of ^{54}Mn nucleus

Figure 6.4: Typical level schemes for some nuclei.

6.2.3 The Doppler Broadening of Gamma Energy

The Doppler broadening values $|\beta\sigma_{\theta_r}|$ for the prominent gamma lines of the three nuclei, ^{64}Cu, ^{55}Fe and ^{54}Mn, corrected for the intrinsic resolution of the detector (equation 5.2) as a

function of the gamma energy are shown in figure 6.5 for the 90° detectors. The slope $|\beta\Delta\theta|$ of the graphs vary as ^{64}Cu < ^{55}Fe < ^{54}Mn or 0.001, 0.009 and 0.011, respectively. The relationship between the two terms in the equation are unknown, hence only the mean values may be evaluated.

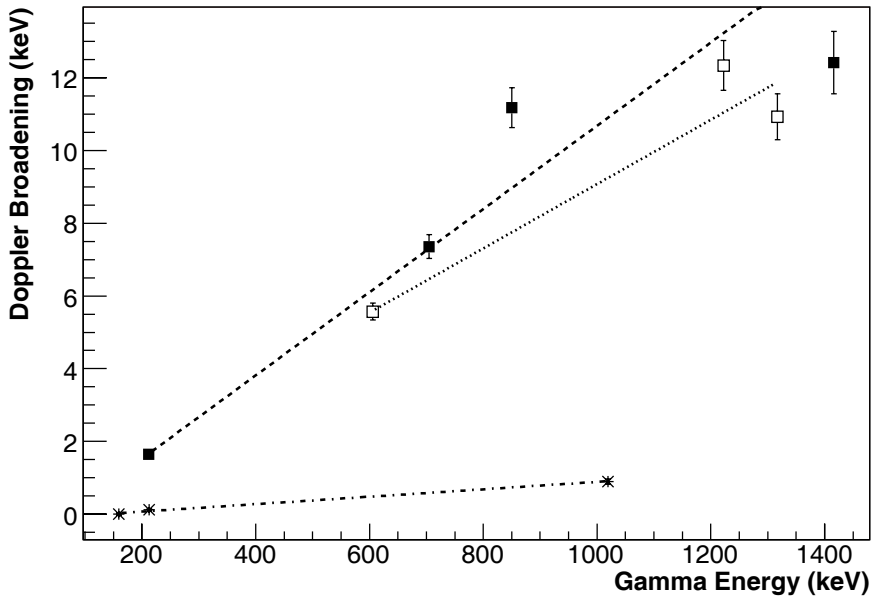


Figure 6.5: The Doppler broadening effect versus gamma energy for the three nuclei, ^{64}Cu (astericks), ^{55}Fe (open boxes) and ^{54}Mn (closed boxes)

A list of the observed Doppler broadened gamma lines for some of the observed nuclei evaluated is presented in table 6.2. In column one is the nuclear identity and the corresponding gamma line energy used is given in column two. In column three is the full-width at half-maximum for detectors at the 90°. The measured average longitudinal momentum transfer β, using equation 5.5, is given in column four. The fifth column is the residue longitudinal momentum transferred expressed as a fraction of the projectile momentum. The sixth column is the approximate mean recoil angle obtained using the technique described in section 5.4.8 The gated gamma spectra typical of the intermediate mass fragments for the^{24}Mg nucleus is shown in figure 6.6. The absence of the Doppler broadening effect observed in the gamma lines sug-

Table 6.2: The observed prominent residues and their corresponding observables.

TLF	γ energy (keV)	$E_0\sigma_{90}$ (keV)	β (c)	$\frac{\beta}{\beta_{cn}}$	θ (°)
^{64}Cu	212.4	0.12(0.03)	0.001	0.03	-
^{62}Cu	385.3	0.69(0.04)	0.001	0.03	-
^{61}Ni	947.6	2.4(0.1)	0.007	0.16	22
^{60}Cu	453.8	2.2(0.1)	0.008	0.19	37
^{59}Ni	998.5	8.3(0.4)	0.014	0.32	39
^{59}Co	302.4	1.6(0.08)	0.015	0.35	21
^{57}Fe	256.0	2.8(0.1)	0.013	0.31	-
^{55}Fe	605.2	5.7(0.2)	0.020	0.47	28
^{55}Mn	307.9	3.7(0.2)	0.017	0.40	44
^{54}Mn	212.0	1.63(0.07)	0.019	0.45	24
^{47}V	87.5	1.1(0.06)	0.019	0.45	39
^{42}K	151.4	5.5(0.2)	0.019	0.44	-

gest that these are target frame residues. Typical gated gamma spectra obtained for some of the prominent nuclei, are shown in figures 6.14 to figure 6.16. The gated gamma spectrum of the ^{64}Cu nucleus, given in figure 6.14(a), does not show any significant Doppler effect. Similarly, the spectrum of the ^{62}Cu nucleus, figure 6.14(b), show a slight Doppler broadening which produces the asymmetry of the gamma line shapes of the 45° detector with respect to the 135° detector. The asymmetry of the line shapes get more enhanced for the^{61}Ni nucleus, as shown in figure 6.7. The energy loss of the nucleus in the target material was found to be insignificant for small recoil angles and cannot be attributed to this effect, (section 6.2.9). The minimum recoil angle for 50% transmission of ^{61}Ni ions of mean energy 2 MeV is about 89.35° as calculated using the SRIM-2003.20 code [262] for half the target thickness. This translates to 176 MeV in longitudinal momentum, more than 2 orders larger than the magnitude of the actual value. The life-time of the nucleus could also be causing the effect but simulations conducted using the Clover detectors, without the collimation effect (section 5.5.1), showed that the consequence of the nucleus decay life-time is to off-set the true gamma transition energy to the low energy scale. That leaves the nuclear interaction effect as the only cause. The spectrum of^{55}Fe, ^{54}Mn

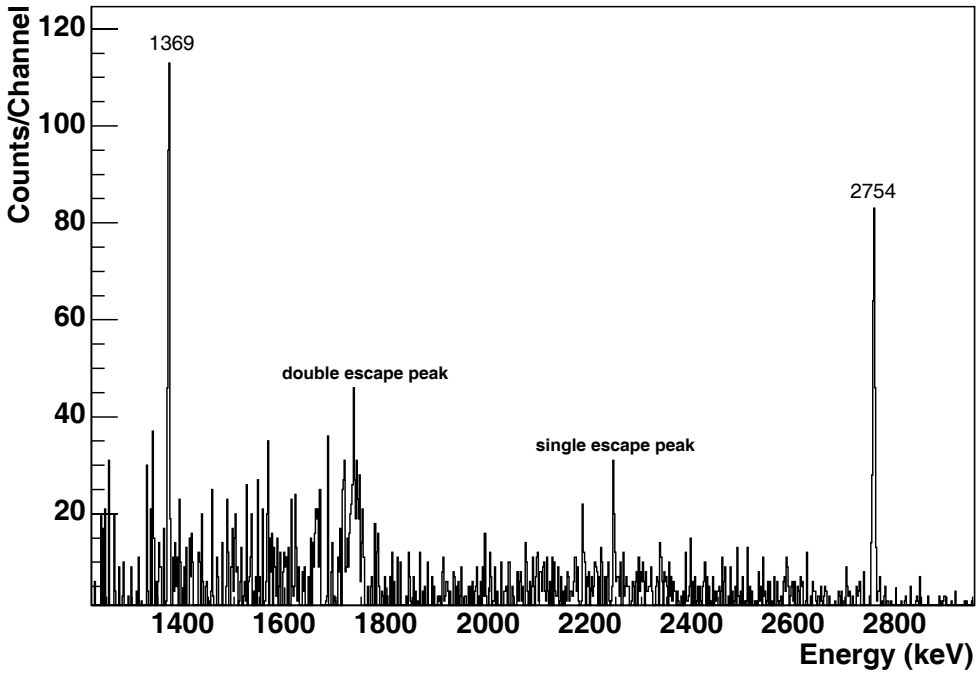


Figure 6.6: The intermediate mass fragments extracted using the extended energy inclusive Clover matrix (section 5.4.5). The spectrum is a potential target frame ^{24}Mg residue product with the two coincident line gates ORed.

and ^{47}V, in the respective figures of 6.16(a), 6.16(b) and 6.16(c), provide clear evidence of the Doppler effect, shown by the simulations to be a consequence of the residue velocity (β, σ_β) distributions and recoil angle asymmetry $(\theta_r, \sigma_{\theta_r})$ distributions (section 5.3.6). The dotted line histograms are the predictions based on the model developed in Milano. The GEANT4 model prediction was found to be largely over-estimated, except for the inelastic component which gives good agreement with the experimental data for near-target residues.

6.2.4 Gamma Residue Cross Coincidence

The spectrum of the ^{62}Cu nucleus gated on the 351 keV gamma line is shown in figure 6.8. The significant Doppler broadening of the 1121 keV gamma line gives the velocity of the source as 0.026, which is typical of the projectile-like fragment, and may be assumed to be^{13}N from ^{13}C decay. The 1397 keV gamma line gives the velocity of the source as 0.024, which

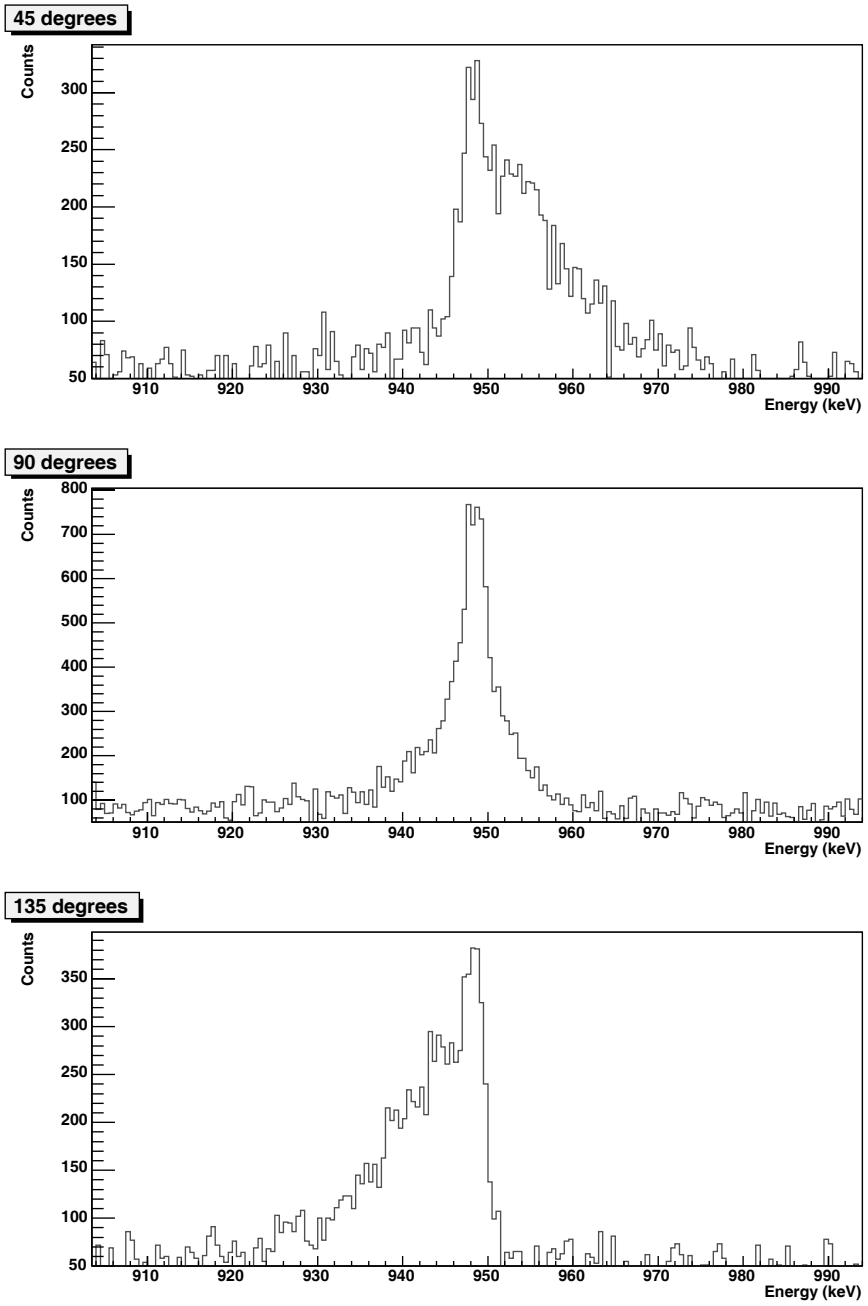


Figure 6.7: The Doppler broadening asymmetry due to detector angle position of the 948 keV ^{61}Ni gamma line.

may be assumed to be the ^{10}B. This may mean that the projectile picked up a low and high energy neutron from the target nuclei, which led to the two de-excitation channels. It was found to be rather difficult to detect the projectile-like fragments in coincidence with the target-like

fragments in the present system, probably because the interaction leads mainly to their break-up, just like the projectile ^{12}C nucleus.

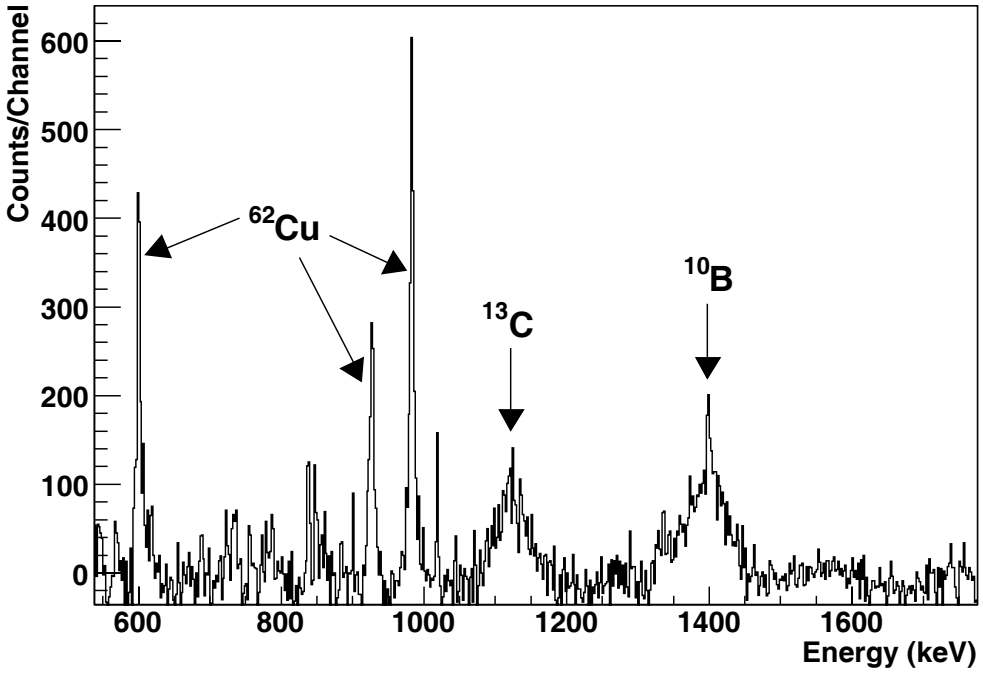


Figure 6.8: The spectrum gated on 351 keV shows the sharp ^{62}Cu lines and the two Doppler broadened potential target-like fragments gamma lines.

6.2.5 Mean Residue Energy and Loss in the Target Foil

The first two columns in table 6.3 represents the residue identity and the gamma line energy. The third column is the average recoil velocity of the residues. The fourth column is the average kinetic energy of the residues in the longitudinal direction. The calculated average energy loss in the target is given in the fifth column. The energy loss of the residues have been evaluated using the SRIM-2003.20 code [262] based on the values of the mean velocity β, as given in table 6.2 and equation 2.69. The calculations show that the effect of the energy loss in the target even for the lowest velocity residues has a negligible effect on the gamma line shapes.

Table 6.3: The residue energy and the corresponding energy loss in the target foil

TLF	γ (keV)	$\langle\beta\rangle$ (c)	Energy (MeV)	Loss (MeV)
^{64}Cu	212.4	0.001	0.3	0.03
^{62}Cu	385.3	0.001	0.3	0.02
^{61}Ni	947.6	0.007	1.4	0.03
^{60}Cu	453.8	0.008	1.8	0.04
^{59}Ni	998.5	0.014	5.4	0.05
^{59}Co	302.4	0.015	6.2	0.09
^{57}Fe	256.0	0.017	7.7	0.13
^{55}Fe	605.2	0.018	8.3	0.13
^{55}Mn	307.9	0.017	7.4	0.13
^{54}Mn	212.0	0.019	9.1	0.13
^{47}V	87.5	0.019	7.9	0.13
^{42}K	151.4	0.019	7.1	0.13

6.2.6 Average Momentum Transfer Versus the Projectile Energy

The variation of the projectile energy with mean fractional longitudinal momentum transfer ($\beta/\beta_{\mathrm{cn}}$) for the ^{55}Fe nucleus is shown in figure 6.9. The peak-maximum seems to feature close to 23 A MeV, which is in agreement with what other measurements had found [20, 21, 23, 26, 116, 124], see figure 2.5(b). There have been questions as to why this peak arises. This may be explained by the model developed in Milano by the re-emission process, a situation where most of the projectile energy is carried away by the re-emitted projectile fragment [2]. In this kind of scenario, one could expect the cross-section of most produced residue to remain relatively constant at some point as the incident projectile energy is increased, since the excitation energy of the composite nucleus remains relatively constant (figure 2.4). The observation could also be explained using the recoil angle distribution assuming the peripheral nature of the interaction as demonstrated in figure 5.14. As the projectile energy increases, the impact parameter for the production of the residue increases. This consequently leads to larger residue recoil angles and less momentum transfer to the residues in the longitudinal direction. It

has also been associated to the incompressibility of the nucleus, a macroscopic property, which measurements have shown to be about 25±4 A MeV [263, 264, 265, 266]. On the lower energy side of the peak-maximum, the projectile velocity is below the incompressibility energy needed by the nucleus, so there is almost no participant zone in the peripheral collisions, but dominantly inelastic interactions. The shape of the cross-section of ^{55}Co nucleus given in figure 3.12 seems

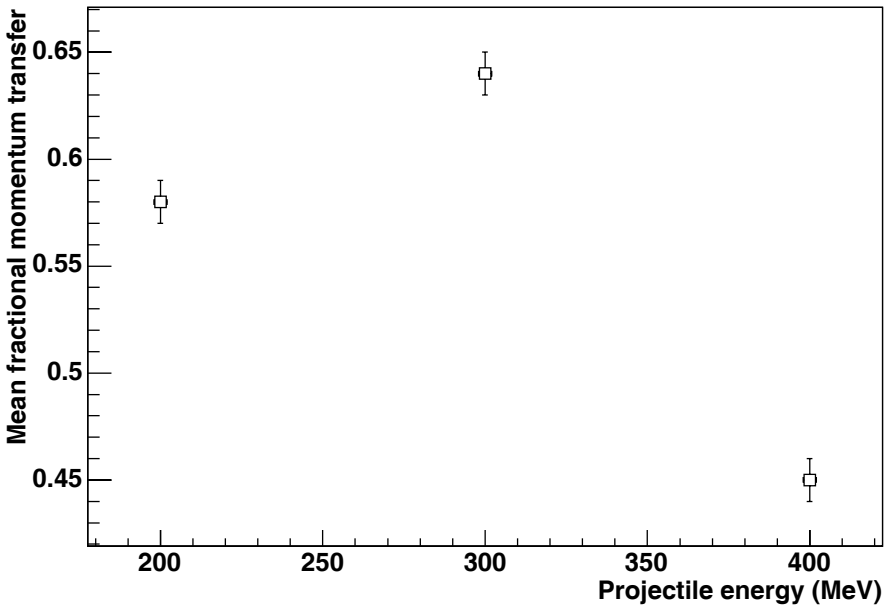


Figure 6.9: The mean fractional momentum transfer (β/β_{cn}) versus the ^{12}C projectile energy for the ^{55}Fe nucleus.

to follow the same trend as that of figure 6.9. This residue is populated by the fusion process in the low energy regime, the fact that it continuously decreasing above the peak maximum clearly suggest that the fusion channel is diminishing or a new channel is opening up. On the higher energy side of the peak-maximum, the projectile energy exceeds the incompressibility energy of the nucleus causing the scaling of the participant zone with the projectile energy, in a "pure participant-spectator" scenario. Consequently, the nuclei produced far-removed from the target tend to have less and less momentum as the incident energy goes up, figure 2.5(b). The near-target residues have almost zero momentum since the interaction mechanisms are basically

inelastic reactions as observed in the case of ^{64}Cu nuclei. At 33 A MeV and 25 A MeV incident energies, the nucleus has insignificant Doppler Effect observed, whereas at 17 A MeV incident energies the converse is true.

6.2.7 Residue Recoil Asymmetry

From the correlation of the coincident gamma emissions using the 90° opposite Clover detectors, the recoil asymmetry of two nucleus, ^{54}Mn and ^{64}Cu, was studied. This was made possible by the fact that the two nuclei have coincident gamma lines very close in energy. The generated 2-dimensional histogram described in section 5.4.2 is plotted in figure 6.10. This

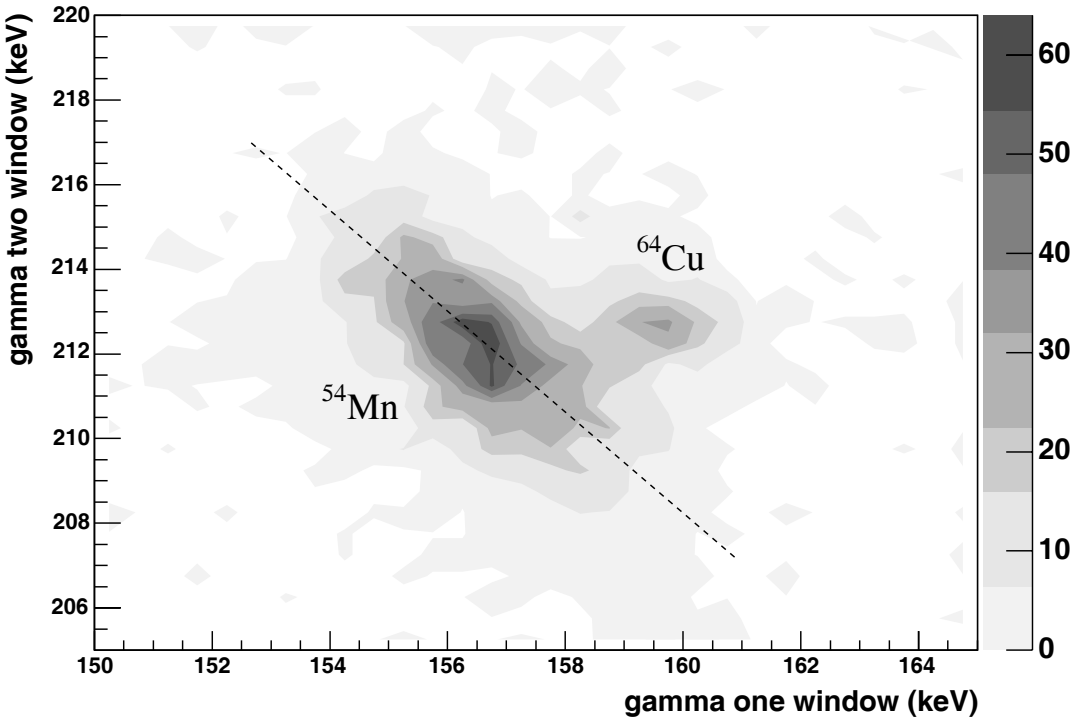


Figure 6.10: Gamma-gamma coincident gates showing the recoil asymmetry of ^{54}Mn and ^{64}Cu nuclei, line drawn on the ^{54}Mn locus. The transitions are 156 and 212 keV lines $5^+ \rightarrow 4^+ \rightarrow 3^+$ for ^{54}Mn; 159 and 212 keV lines $4^+ \rightarrow 3^+$, $2^+ \rightarrow 1^+$ for ^{64}Cu.

is a 15 keV by 15 keV 2D-window set for the coincidence gamma energy gates 150-165 keV on the x-axis and 205-220 keV on the y-axis of the detectors. In the x-axis are the 156.3 keV

and the 159 keV gamma lines, in the y-axis are the 212 keV and the 212.4 keV corresponding coincident gamma lines for ^{54}Mn and ^{64}Cu nuclei, respectively.

6.2.8 Relative Residue Yields

The relative residue formation described here is a probe to estimate the accuracy of the various interaction models incorporated in the calculations and their contributions. The measurements are based on the relative gamma intensity yields with the appropriate corrections done. In all cases, ^{64}Cu was chosen as the most appropriate standard near-target residues, with a relative production weight of unity. The relative residue production cross section is the best probe of the accuracy of any model, as errors associated with measurements cancel out. The relative residue yields also provide an extremely high resolution measurement of residue production cross section of unprecedented quality and proportion. The comparison of the relative yields from the model developed in Milano and the GEANT4 calculations with respect to the experimental value are presented in figure 6.11. The plot shows that the GEANT4 model overestimates the relative production of some residues by as much as five times the experimental values. The model developed in Milano shows a very good agreement with the experimental data after scaling up only the relative production of the standard nuclei (^{64}Cu) by almost 2 orders of magnitude (80 times) the calculated value. This is consistent with more recent review of the model where the inelastic cross section is now treated leading to a better estimate of this nucleus. The plots are presented in figure 6.11. The errors given in the figure are due to the statistics of the gamma line intensities. In comparison with the measurements made using the radiochemical technique [20], it is clearly evident that a lot of the near-target and other residue yields were not observed.

6.2.9 Residue Velocity Distribution

The measured residue velocity distributions from the raw velocity distribution data (section 5.4.8) are shown in figure 6.12. In the plot, a comparison is made with the predictions of

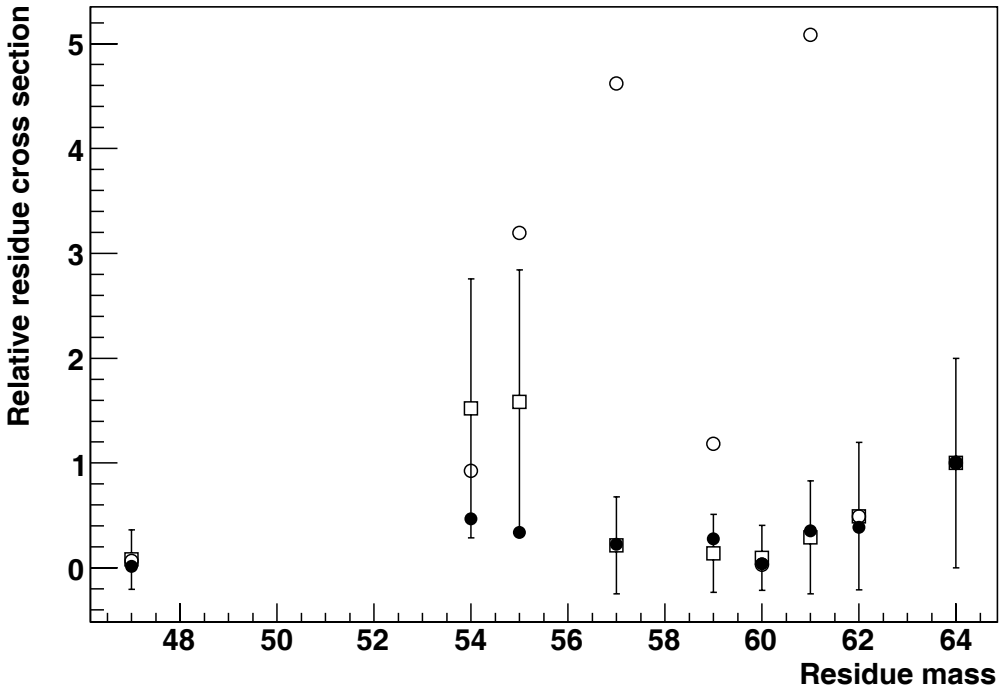


Figure 6.11: The relative residue yields based on the predictions of the various theoretical calculations reported, with respect to the experimental measurement. The closed circles are the predictions of the model developed in Milano and the open circles are GEANT4 values.

the model developed in Milano and the GEANT4 codes in the longitudinal directions. For the near-target residues, a single component of velocity distribution has been observed. Both models predict two components, one due to the various inelastic collisions with small mean velocity and another component due to various contributions of incomplete fusion processes. The two component structure, is apparent in the experimental velocity distribution measurements of the ^{61}Ni nucleus. The model developed in Milano prediction initially assumes that most of the near-target residue yields (^{62,63,64}Cu) are produced by the incomplete fusion process of a single break-up alpha with the target whereas GEANT4 attribute it to mostly complete fusion with a small contribution of the inelastic collision processes. (This is also evident in the Doppler effect from the spectrum shown in figures 6.14(a) and 6.14(b)). The experimental measurements indicate that the most significant contribution to the near-target residue production is the

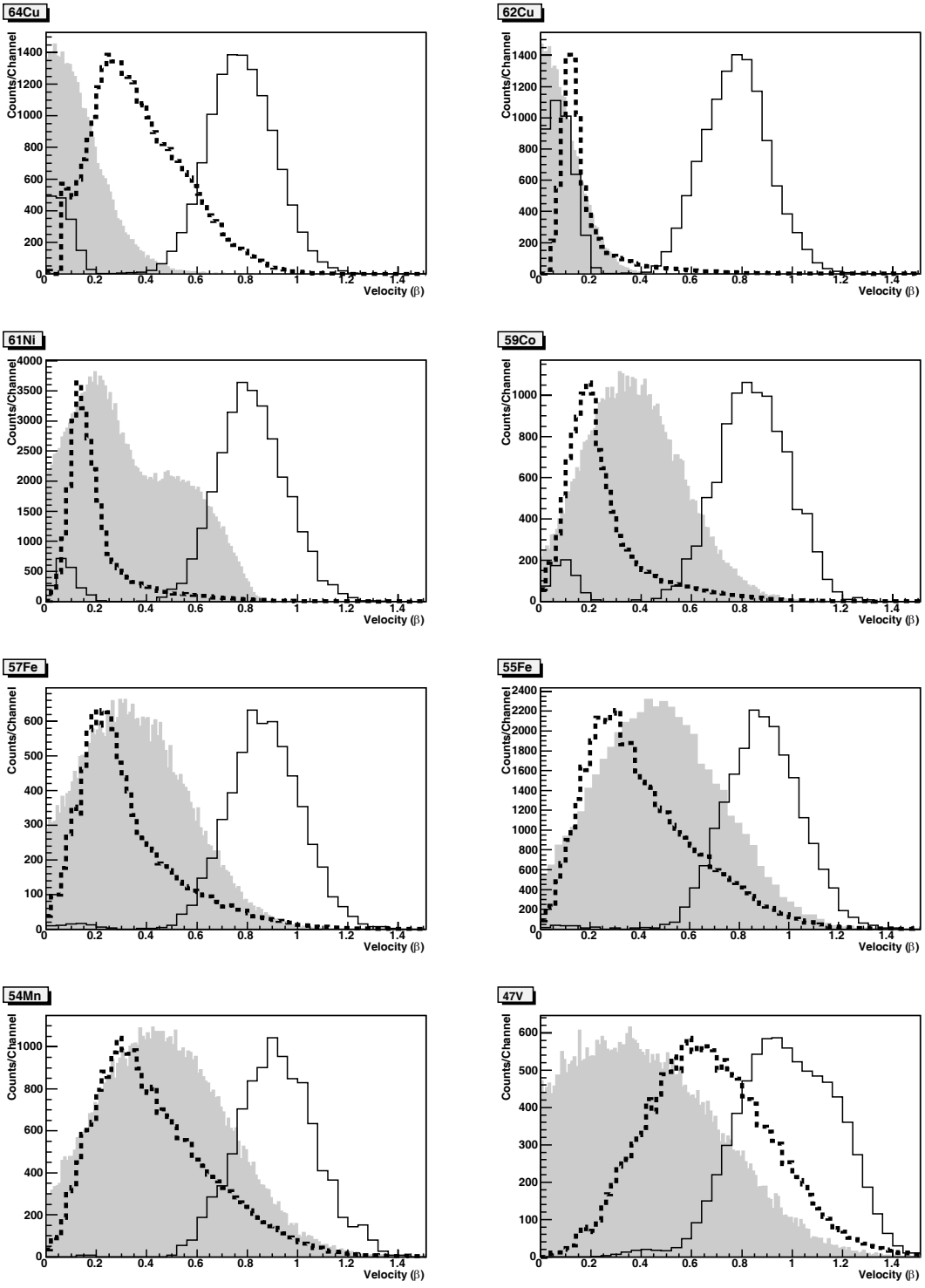


Figure 6.12: The experiment residue velocity distribution (shaded) comparison with the model developed in Milano (dotted) and GEANT4 (line) model calculations. The experimental values have not been corrected for the intrinsic detector resolution.

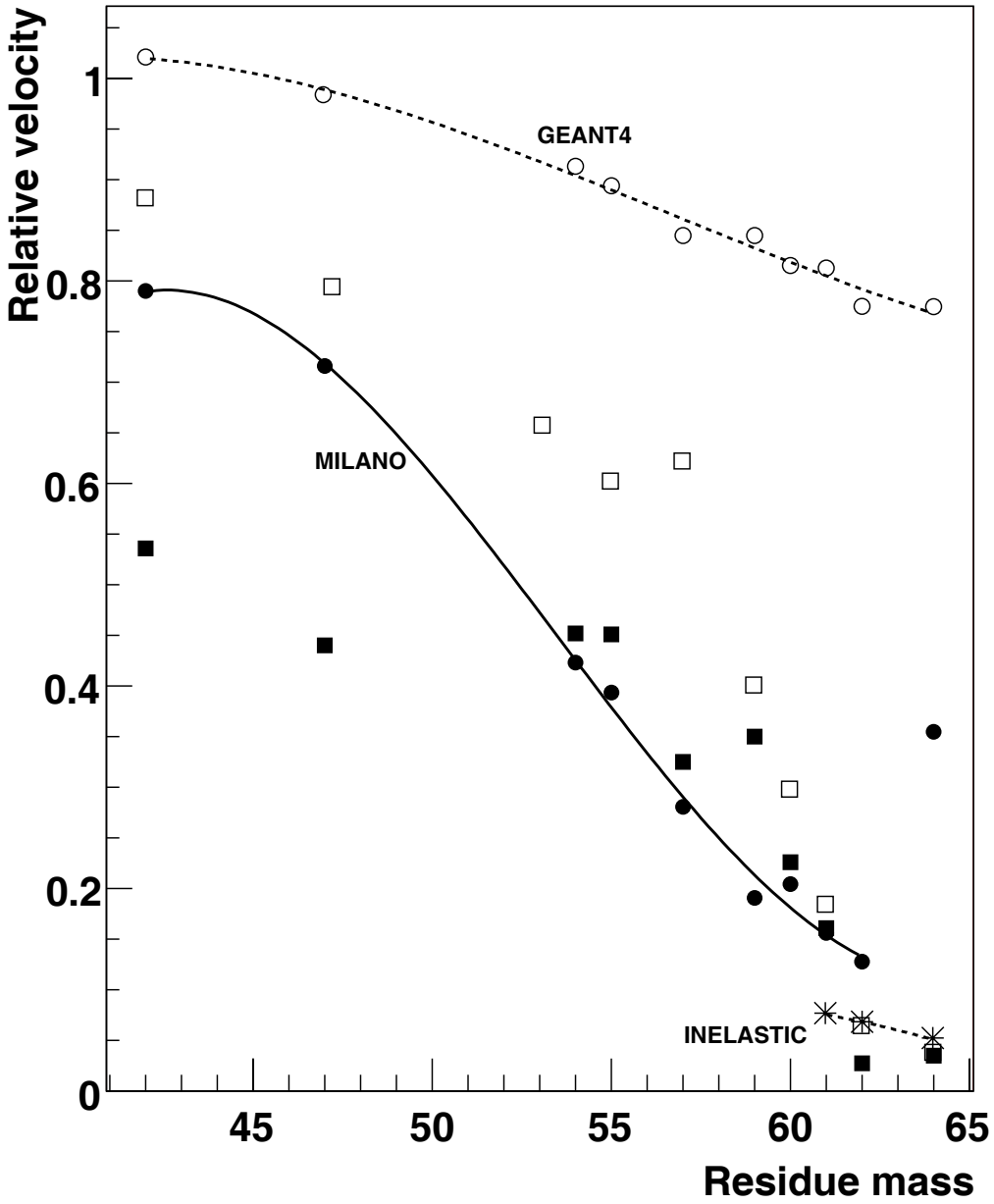


Figure 6.13: The residue mean relative velocity (β/β_{cn}) as predicted by the various theoretical calculations compared to the experimental values. These are the experimental values with (open boxes) and without angle correction (closed boxes), model developed in Milano (closed circles), GEANT4 pre-compound (open circles) and GEANT4 inelastic (asterisks).

inelastic collision process, figure 6.12. Recent studies has lead to the reviewing of the model developed in Milano to account for this fact [1]. In inelastic collisions, the near-target residues are produced mainly through the excitation of the target nucleus as reported in the coincidence measurement of 60 A MeV ^{209}Bi(α, $\alpha'\gamma$) reaction [267]. In the inelastic scattered (48-60) A MeV α' energy window, the observed gamma lines were mainly those of the Bi isotopes. Since the projectile loses very little energy, the produced near-target residues have little or no velocity distribution (Doppler Effect), the case with copper isotopes measurements in the present study. The highest momentum is achieved for complete fusion followed by the isotropic emission of particles, whereas the least is achieved for the case of incomplete fusion since the rest of the projectile momentum is carried by the spectator fragment [268, 261] or by the quasi-projectile in the case of the inelastic collisions. The mean velocity distribution prediction of the various models in comparison to the experimental values are shown in figure 6.13. The observed saturation of the measured mean fractional longitudinal momentum transfer, which occurs at half the value of the compound nucleus in the raw velocity distribution data, vanishes when the recoil angles of the residues are taken into account. This may explain the contradiction with the measurements previously reported, which showed the saturation of the longitudinal momentum transfer per incident nucleon (section 3.2.2). The comparison of the theory to the data is performed as described in section 5.6. The saturation of the longitudinal momentum transfer may also be explained by a simple assumption of a uniform distribution of residue velocities as explained in section 5.4.8, a consequence of the interplay of the one and two-body collision processes [229].

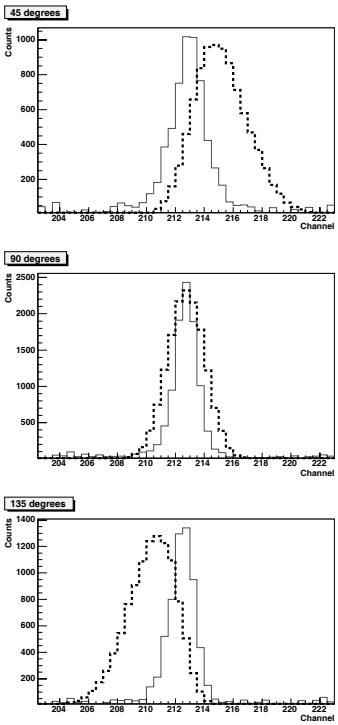
For the residues with mass far-removed from the target nucleus, which are expected to be produced with comparatively larger energy and momentum transfer processes, the average velocity is just about half of the complete momentum transfer. The model developed in Milano, makes the assumption that at the present energy, the break-up of^{12}C followed by the interaction of one of the fragments with the target nuclei, is the dominant interaction process. The output of the calculation, which are given in figures 6.14-6.16, show that the prediction reproduces

the Doppler Effect phenomena reasonably well for most of the observed residue gamma lines. The predicted angles also compares well with the experimental measurements. There are few deviations such as the over-estimation of the average velocities of the target isotopes (^{62}Cu and ^{64}Cu). These residues which are produced via inelastic processes were not considered explicitly in the model developed in Milano prior to the new changes as it was assumed to constitute only a very small part of the total reaction cross-section. This is not the case in the present model calculations, figure 2.2. The direct production of ^{64}Cu residue, whose experimental mean relative fractional velocity value of β/β_{cn} is 0.093 compared to the theoretical estimate of 0.161 can be attributed to the pick-up of a very low energy ^{12}C neutron by the target. Though this process is dynamically unfavourable at high incident energies, it could be spectroscopically favoured in comparison to the transfer of a higher energy neutron. The very small value of the Doppler shift for the ^{62}Cu γ lines is attributed to the inelastic scattering of ^{12}C and the emission of a neutron by the excited target nucleus. The processes which the model developed in Milano code considers include these exit channels, though their contribution to the overall cross-section were initially under-estimated [269]. The momentum transfer to the two residues with masses far-removed from the target (^{47}V and ^{42}K) are within the experimental limits, showing that the pre-equilibrium emissions and the incorporation of the various incomplete and complete fusion contributing processes are adequately treated in the model developed in Milano.

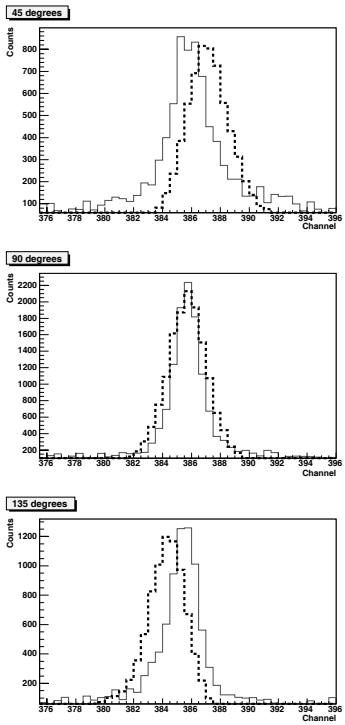
The inelastic component of the GEANT4 predictions agree favourably with the experimental results except for the residue recoil angles which GEANT4 predicts it to have a mean value of 80° for the ^{64}Cu nucleus and which could not be directly verified in the experimental measurements. Large residue recoil angles increases the chance of the residue stopping in the target, which could lead to recoil velocity distribution asymmetry between the 45 and 135 degree detectors, similar to the observation made in the case of the ^{61}Ni spectrum (figure 6.7), but this was not the case (section 6.2.5). The GEANT4 prediction shows that the inelastic component is under-estimated or the composite system formation is largely over-estimated. The pre-equilibrium emission is also over-estimated for the composite system leading to the

population of mainly the A=59 mass region and under-estimation of the A=47 mass region. When the projectile break-up is incorporated into GEANT4 calculations, the agreement with the experimental measurements is drastically improved both, for the Doppler shifts and the recoil angles, which are over-estimated and under-estimated, respectively. The calculation assuming alpha projectiles instead, for example gave a good agreement with the experimental values than those obtained using the ^{12}C projectile, giving convincing evidence of the break-up mechanism assumed in the model developed in Milano. The conservation of linear momentum demands that the mean recoil velocity of ^{64}Cu nucleus $\beta = 0.0042c$, assuming a pick-up process of the energetic neutron from the projectile. The measured value of $0.004c$ (table 6.2) is in perfect agreement. The ^{62}Cu nucleus is produced in the grazing angle collisions through evaporation of the neutron after the inelastic excitation of the target nucleus and from nucleon transfers of a maximum of 2 nucleon from the projectile to the target, based on the measured mean recoil velocity $\beta = 0.006c$. As the mass of the residue moves further away from that of the target, the number of nucleons involved in the interaction rises. The model developed in Milano calculations give much better predictions than the GEANT4 model calculations having undergone rigorous testing and comparison with a lot of other experimental measurements [7], in addition to critical interaction processes which seems to be ignored in other model calculations. The GEANT4 output for the present system is among the first application of the model as the physics implemented was done a few months ago at the time of writing and is currently undergoing the tests and improvement.

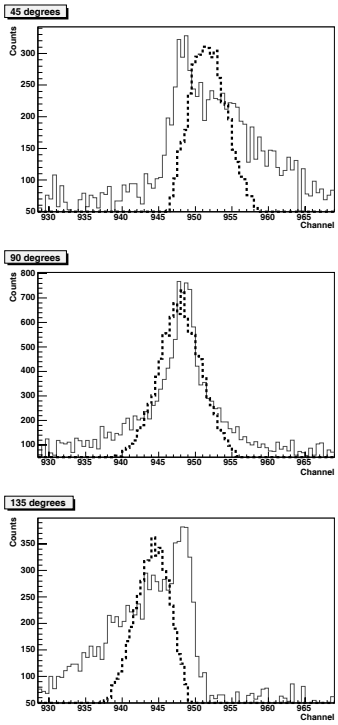
The model developed in Milano as it was implemented computationally at the time introduces a bias into the theoretical calculations of certain properties of the residues far from the target. This is the case for the Monte Carlo simulation of pre-equilibrium emissions from the composite systems created in the incomplete fusion process. It is difficult to include sufficient emission of the intermediate mass fragments produced by nucleon coalescence during the thermalisation process. This affects the prediction of the cross-sections for production of the residues far-removed from the target nuclear mass, such as the K and V isotopes in the



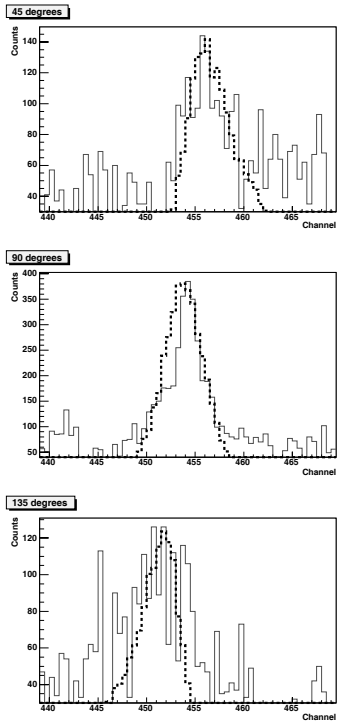
(a) ^{64}Cu 212.4 keV line



(b) ^{62}Cu 385.3 keV line

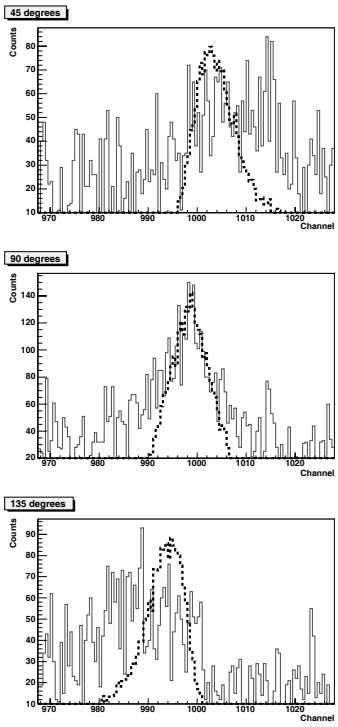


(c) ^{61}Ni 947.9 keV line

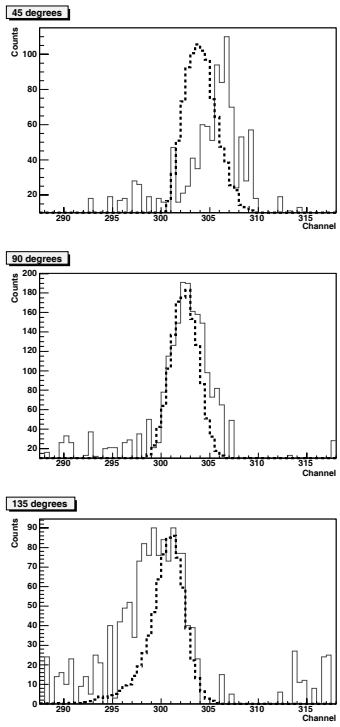


(d) ^{60}Cu keV 453.8 line

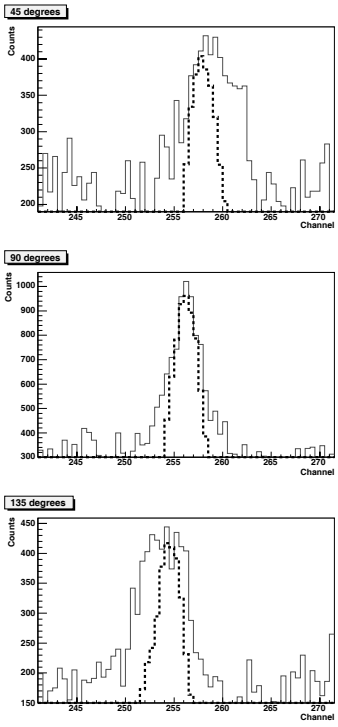
Figure 6.14: The model developed in Milano predictions versus experiment measurements (histogram)



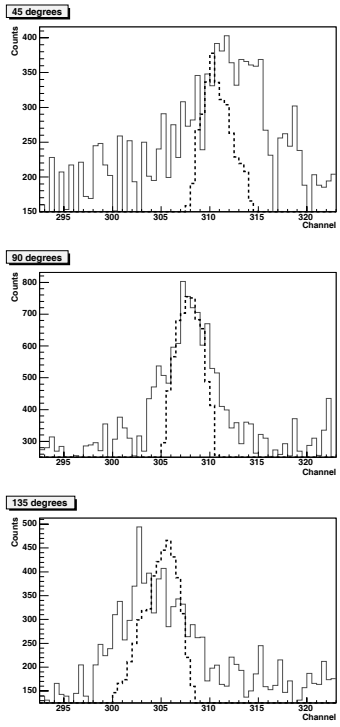
(a) ^{59}Ni 998.5 keV line



(b) ^{59}Co 302.4 keV line

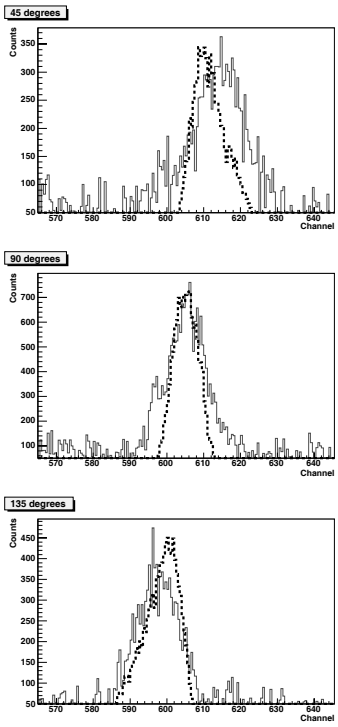


(c) ^{57}Fe 256.0 keV line

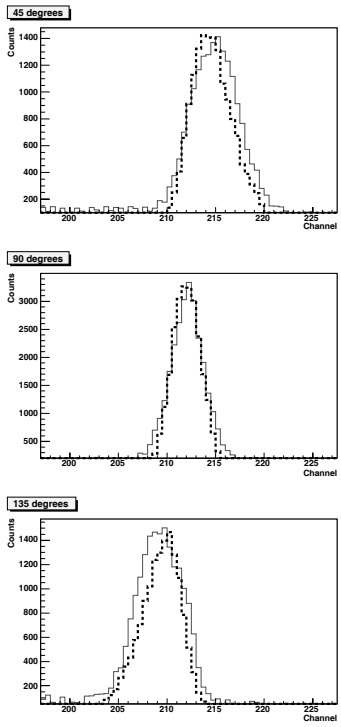


(d) ^{55}Mn 308.1 keV line

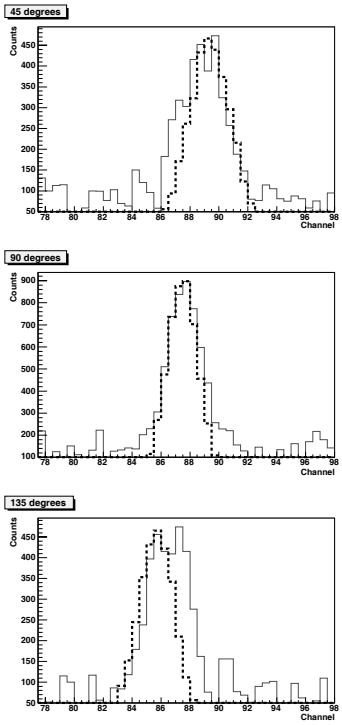
Figure 6.15: The model developed in Milano predictions versus experiment measurements (histogram)



(a) ^{55}Fe 605.2 keV line



(b) ^{54}Mn 212.0 keV line



(c) ^{47}V 87.5 keV line

Figure 6.16: The model developed in Milano predictions versus experiment measurements (histogram)

present study. For these nuclei, the calculated production threshold is typically higher than the experimental value leading to the under-estimation of cross-section. This, however, is not an indication of the deficiency of the theoretical approach, but it is a consequence of the neglecting of the emission of the intermediate mass fragments in the Monte Carlo simulation during the thermalisation process. The emission of a cluster particle instead of all the independent constituent nucleons requires less energy and is relatively more significant especially at the low incident energies. The production of the intermediate mass fragments from break-up of the projectile nuclei is explicitly treated in the calculation. However it is not so easy to take into account their pre-equilibrium emission by nucleon coalescence, which experimental and theoretical predictions, shows it to be quite significant even at low incident energies of the projectile [74]. If the emission of coalescence fragments increases with increasing energy, their impact on the predicted yield of residues diminishes progressively above the threshold energy as a consequence of the opening of new exit channels which are treated in the theory. More work is currently in progress to address these shortcomings.

Chapter 7

Summary and Outlook

In chapter 1, a brief background of the research work and the motivation of the present study, based on the investigations of the collaborating scientist is presented. In the proposal, the need to carry out an exhaustive study of the momentum transfer to near-target residues in heavy ion collisions was indicated. The Doppler Effect phenomenon was the technique of choice in conjunction with a gamma detector array. In the investigation of mechanisms of heavy ion reactions and de-excitation in processes induced by 33 A MeV ^{12}C projectile incident on ^{63}Cu target nuclei, the AFRODITE gamma detector array was utilised to detect the Doppler effect experienced by the characteristic gamma emissions from the various de-excitation states of the nucleus. Coincidence of these emissions is used to assign the identity of the nucleus. In the study, many residues produced from the nuclear interaction process were identified. The Doppler shifted and broadened gamma lines were extracted utilising the different detector angles of the array, for selected characteristic gamma transitions. Subsequently, the Doppler shift distribution measurements were obtained which provided information on the momentum transfer from the projectile to the residue nuclei during the interaction process. The Doppler broadening of the gamma lines give insights on the residue recoil angle distributions.

In chapter 2, an extensive description of the model which has been developed in Milano is presented. This is a comprehensive model for use in explaining the various physical observables obtained from heavy ion nuclear collision measurements, which is unlike the typical models, which have limited scope of applicability mostly to the study of specific observables.

A number of these observables are presented in chapter 3, following it is a brief description of the various experimental techniques used to measure each one of them. In addition, the application of some of the techniques in real experimental measurements typical of the present system, with their subsequent findings for collision systems similar to the present study, is also mentioned. In chapter 4, the description of the GEANT4 models relevant to the current investigation is presented. These are mainly the photon interaction and heavy ion interaction models, for comparison and application in the present measurements.

The techniques used to carry out the investigation are described in chapter 5. A number of the experimental techniques for extraction of the relevant information have been developed in the course of the study. The Doppler shift extraction process using off-line sorting of coincident event by event data gated on a specific nucleus, produces the appropriate Doppler shifted gamma line spectrum, from which the velocity distribution of the residue nucleus may be reconstructed. This is done using uniform random deviates for the velocity distributions and double von Neumann rejection techniques using the experimental distributions of say two detector angles 45/135 to establish the optimal event by event conditions of the experimental observables. This was extended further to include the recoil angles so as to reconstruct the full kinematics of the collision process. This information shows the momentum transfer in the interaction process leading to the production of the specific residue nucleus. The Doppler broadening is a useful observable in the determination of the recoil angle distribution assuming that other potential effects plays an insignificant role. The recoil angle or recoil asymmetry, deduced from the correlation the observed residue gamma emissions is related to the impact parameter of the two colliding nuclei and the magnitude of the spectator fragment momentum in the incomplete fusion process. The relative residue production cross section is a unique probe for the accuracy of the theoretical nuclear interaction models, as errors associated with absolute cross section measurements cancels out. These relative residue cross sections also provide extremely high resolution measurements of residue mass and charge production processes of unprecedented proportion and quality.

The results of the study are presented in chapter 6. These include residue yields, Doppler shifts and the Doppler broadening measurements, relative production cross sections and the comparison with the predictions of the two model calculations, the model developed in Milano and GEANT4. Based on the Doppler shift measurements of near-target residues (^{62,63,64}Cu), there is no evidence observed of yields from other mechanisms apart from the inelastic contribution processes. The revised form of the model developed in Milano suggests good agreement with the observation. GEANT4 predicts a two component structure which has not been observed in the data. In the A=61(Ni) mass region there is clear evidence of transition with a two velocity component structure in the observed residue momentum distribution. The two components are made up of the inelastic part, with almost no Doppler shift, and another mechanism of which the Doppler shift measurement corresponds to a α interaction process. This second component in the model developed in Milano has been attributed to the projectile break-up followed by the interaction of one of these α fragments with the target nucleus, through either complete or incomplete fusion process, while the rest of the projectile fragments escapes as the spectator fragments.

The comparison of the experimental measurements with the predictions of the model developed in Milano and GEANT4 calculations, shows that projectile break-up and the emission of some of the fragments, incorporated in the former model, leads to a much better agreement between the calculations and the experimental measurements. The model developed in Milano model therefore treats the nuclear interaction processes in a much better approach than the current implementation of the GEANT4 models. This is expected as the model developed in Milano has undergone rigorous development and testing such that it can reproduce the observables of a large set of experiment data performed on target nuclei within the $A \sim 100$ mass region using a unique calculation. The model has shown that the cross sections of the reaction residues are weakly dependent on the mass and charge of the target nucleus. The calculations of the model have consistent predictability for reactions induced by the ^{12}C projectile on the target nuclei of other mass regions, important for the inter-disciplinary applications of the model

in heavy ion nuclear interactions. The model is incorporated in the current version FLUKA, a fully integrated particle physics Monte Carlo simulation package with a wide applications in high energy experimental physics and engineering, shielding, detector and telescope design, cosmic ray studies, dosimetry, medical physics and radio-biology.

The projectile break-up process has been shown to play an important role in the interaction process of two heavy ion nuclei and further investigation is suggested, to get a detailed insight information into the mechanism ([270]). One such study could take advantage of the fact that ^{8}Be fragment does not survive the final state interactions, based on the work of the collaboration. If one considers odd and even alpha-like cluster projectiles, preferably ^{12}C and ^{16}O projectile nuclei and that for ^{12}C, the production of the unstable ^{8}Be is mainly produced by the peripheral interaction processes (^{12}C,^{8}Be) while in the case of (^{16}O,^{8}Be) reaction, a much reduced impact parameter is required, which effectively closes this specific channel in the most forward angles. The same channel may subsequently be fed weakly and almost entirely by sequential decay of the projectile-like fragments of ^{16}O, mainly from the ^{12}C break-up process. The properties of ^{12}C in the (^{16}O,^{12}C) reaction is similar to those of ^{8}Be in the (^{12}C,^{8}Be) case. Through this simple test, one could estimate the contribution of direct peripheral interaction break-up process of the projectile from the sequential decay of the projectile-like fragments. The above investigation may be extended by studying the $\phi - \theta$ asymmetry of the correlated ^{8}Be α pairs, to discern the statistical contribution to the break-up process as opposed to the dynamical break-up contribution. The $\phi - \theta$ cut, may provide a clue based on the nuclear potential distortion of the two alpha pair trajectories in the reaction plane with respect to the normal plane. This direct approach is relatively simpler than the isospin techniques [271, 272].

Bibliography

[1] E. Z. Buthelezi *et al.* Nucl. Phys. A, 753:29, 2005.

[2] E. Gadioli *et al.* Nucl. Phys. A, 641:271, 1998.

[3] E. Gadioli *et al.* Nucl. Phys. A, 654:523, 1999.

[4] E. Gadioli *et al.* Prompt Doppler Shift Measurement of Momentum Transfer to Residues after Heavy Ion Collisions. PAC proposal, 1999.

[5] E. Gadioli *et al.* Z. Phys. A, 299:1, 1981.

[6] R. Broda *et al.* Phys. Rev. C, 49:R575, 1994.

[7] M. Cavinato *et al.* Nucl. Phys. A, 679:753, 2001.

[8] E. Gadioli *et al.* Phys. Lett. B, 394:29, 1997.

[9] C. Birattari *et al.* Phys. Rev. C, 54:3051, 1996.

[10] M. Cavinato *et al.* Phys. Rev. C, 52:2577, 1995.

[11] E. Gadioli *et al.* Eur. Phys. J. A, 8:373, 2000.

[12] M. Cavinato *et al.* Nucl. Phys. A, 643:15, 1998.

[13] I. Cervesato *et al.* Phys. Rev. C, 45:2369, 1992.

[14] E. Fabrici *et al.* Phys. Rev. C, 40:2548, 1989.

[15] E. Fabrici *et al.* Phys. Rev. C, 42:2163, 1990.

[16] V. Andersen *et al.* The FLUKA Code for Space Applications: Recent Developments. Manuscript, CERN, Geneva, Jan. 2005.

[17] E. Gadioli. FIZIKA B, 12:1, 2003.

[18] M. Cavinato *et al.* Phys. Lett. B, 382:1, 1996.

[19] E. Gadioli *et al.* Nucl. Phys. A, 708:391, 2002.

[20] S. Y. Cho *et al.* Phys. Rev. C, 36:2349, 1987.

[21] S. Y. Cho *et al.* Phys. Rev. C, 39:2227, 1989.

[22] Y. K. Kim *et al.* Nucl. Phys. A, 578:621, 1994.

[23] J. P. Whitfield and N. T. Porile. Phys. Rev. C, 47:1636, 1993.

[24] L. Kowalski *et al.* Phys. Rev. Lett., 51:642, 1983.

[25] J. Galin *et al.* Phys. Rev. Lett., 48:1787, 1982.

[26] T. Lund *et al.* Phys. Lett. B., 102:239, 1981.

[27] T. Lund *et al.* Z. Phys. A, 306:43, 1982.

[28] J. B. Cumming *et al.* Phys. Rev. C, 24:2162, 1981.

[29] J. B. Cumming *et al.* Phys. Rev. C, 18:1372, 1978.

[30] J. B. Cumming *et al.* Phys. Rev. C, 14:1554, 1976.

[31] S. Ben-Hao *et al.* Phys. Rev. C, 40:2680, 1989.

[32] C. Ta-Hai *et al.* Phys. Rev. C, 42:2187, 1990.

[33] J. P. Whitfield and N. T. Porile. Phys. Rev. C, 50:2047, 1994.

[34] J. P. Whitfield and N. T. Porile. Phys. Rev. C, 49:304, 1994.

[35] W. Królas *et al.* Nucl. Phys. A, 724:289, 2003.

[36] J. F. C. Cocks *et al.* J. Phys. G: Nucl. Part. Phys., 26:23, 2000.

[37] B. Fornal *et al.* Phys. Rev. C, 49:2413, 1994.

[38] H. O. U. Fynbo. Nucl. Inst. and Methods B, 207:275, 2003.

[39] M. N. Namboodiri *et al.* Phys. Rev. C, 35:149, 1987.

[40] R. A. Dayras *et al.* Phys. Rev. C, 22:1485, 1980.

[41] P. Piattelli *et al.* Phys. Lett. B, 442:48, 1998.

[42] R. L. Robinson *et al.* Phys. Rev. C, 24:2084, 1981.

[43] D'Onofrio *et al.* Phys. Rev. C, 35:1167, 1987.

[44] K. Siwek-Wilczyńska *et al.* Nucl. Phys. A, 330:150, 1979.

[45] S. Mandal *et al.* PRAMANA - Journ. of Phys., 57:161, 2001.

[46] R. A. Williams and Jr A. A. Caretto. Phys. Rev. C, 10:601, 1974.

[47] R. Broda *et al.* Phys. Lett. B, 251:245, 1990.

[48] C. T. Zhang *et al.* Nucl. Phys. A, 628:386, 1998.

[49] R. Broda *et al.* Phys. Lett. B, 74:868, 1995.

[50] J. G. del Campo *et al.* Phys. Rev. C, 43:2689, 1991.

[51] T. Inamura *et al.* Phys. Lett. B, 68:51, 1977.

[52] J. H. Lee *et al.* Phys. Rev. C., 41:1562, 1990.

[53] R. Alba *et al.* Nucl. Phys. A, 681:339, 2001.

[54] R. Alba *et al.* Nucl. Phys. A, 654:761, 1999.

[55] J. H. G. van Pol *et al.* Phys. Rev. Lett., 76:1425, 1996.

[56] T. Suomijarvi *et al.* Phys. Rev. C, 53:2258, 1996.

[57] S. Riess *et al.* Phys. Rev. Lett., 69:1504, 1992.

[58] C. Cavata *et al.* Phys. Rev. C, 42:1760, 1990.

[59] D. G. d'Enterria *et al.* Phys. Rev. Lett., 87:022701, 2001.

[60] M. J. van Goethem *et al.* Phys. Rev. Lett., 88:122302, 2002.

[61] G. A. Souliotis *et al.* Phys. Rev. C, 57:327, 1998.

[62] G. A. Souliotis *et al.* Phys. Rev. C, 46:1383, 1992.

[63] R. Nebauer and J. Aichelin. Nucl. Phys. A, 681:353, 2001.

[64] R. Nebauer and J. Aichelin. Nucl. Phys. A, 683:605, 2001.

[65] R. Serber. Phys. Rev., 72:1114, 1947.

[66] G. D. Harp *et al.* Phys. Rev. C, 165:1166, 1968.

[67] G. D. Harp and J. M. Miller. Phys. Rev. C, 3:1847, 1971.

[68] T. C. Sangster *et al.* Phys. Rev. C, 46:1404, 1992.

[69] K. Niita *et al.* Phys. Rev. C, 52:2620, 1995.

[70] Y. Tosaka *et al.* Phys. Rev. C, 60:064613, 1999.

[71] M. Blann. Phys. Rev. C, 23:205, 1983.

[72] E. Gadioli *et al.* Eur. Phys. J. A, 11:161, 2001.

[73] W. W. Wilcke *et al.* At. Data Nucl. Data Tables, 25:389, 1980.

[74] B. Becker *et al.* Eur. Phys. J. A, 18:639, 2003.

[75] S. Kox *et al.* Phys. Rev. C, 35:1678, 1987.

[76] E. Gadioli *et al.* In Proc. of the 8th Int. Conf. on Nuclear Reaction Mechanisms, page 271. Ricerca Scientifica ed Educazione Permanente, 1997.

[77] P. Vergani *et al.* Phys. Rev. C, 48:1815, 1993.

[78] D. H. Boal. Phys. Rev. C, 25:3068, 1982.

[79] T. C. Awes *et al.* Phys. Rev. C, 24:89, 1981.

[80] H. H. Gutbrod *et al.* Phys. Rev. Lett., 37:667, 1976.

[81] J. I. Kapusta. Phys. Rev. C, 21:1301, 1980.

[82] S. T. Butler and C. A. Pearson. Phys. Rev., 129:836, 1963.

[83] A. Schwarzschild and C. Zupancic. Phys. Rev., 129:854, 1963.

[84] T. C. Awes *et al.* Phys. Rev. C, 25:2361, 1982.

[85] D. Glas and U. Mosel. Nucl. Phys. A, 237:429, 1975.

[86] K. Siwek-Wilczyńska *et al.* Phys. Rev. C, 42:1599, 1979.

[87] J. Wilczyński. Nucl. Phys. A, 216:386, 1973.

[88] D. Glas and U. Mosel. Phys. Rev. C, 10:2620, 1974.

[89] E. Gadioli *et al.* Z. Phys. A, 321:107, 1985.

[90] E. Gadioli and P. E. Hodgson. Pre-equilibrium Nuclear Reactions. Clarendon Press, Oxford, 1992.

[91] V. Weisskopf. Phys. Rev., 52:295, 1937.

[92] I. Dostrovsky *et al.* Phys. Rev., 116:683, 1959.

[93] J. C. Steckmeyer *et al.* Nucl. Phys. A, 686:537, 2001.

[94] E. Gadioli *et al.* In Proc. of the 9th Int. Conf. on Nuclear Reaction Mechanisms, page 487. Ricerca Scientifica ed Educazione Permanente, 2000.

[95] M. Germain *et al.* Phys. Lett. B, 437:19, 1998.

[96] R. Bimbot *et al.* Nucl. Phys. A, 189:193, 1972.

[97] M. Lefort and Ch. Ngo. Ann. Phys. (NY), 3:5, 1978.

[98] A. Lazzarini *et al.* Phys. Rev. Lett., 46:988, 1981.

[99] J. Colin *et al.* Nucl. Phys. A, 593:48, 1995.

[100] R. Reif and G. Saupe. Sov. Jou. of Part. and Nucl., 14:377, 1983.

[101] M. N. Namboodiri *et al.* Phys. Rev. C, 20:982, 1979.

[102] S. B. Kaufman *et al.* Phys. Rev. C, 26:2694, 1982.

[103] S. Leray. Journ. Phys. C (Paris), 4:275, 1986.

[104] R. Wada *et al.* Phys. Rev. C, 39:497, 1989.

[105] D. J. Parker *et al.* Phys. Rev. C, 44:1528, 1991.

[106] R. D. Evans. In The Atomic Nucleus. McGraw-Hill, New York, 1986.

[107] W. J. Nicholson *et al.* Phys. Rev., 116:175, 1959.

[108] T. Sikkeland *et al.* Phys. Rev., 125:1350, 1961.

[109] V. E. Viola *et al.* Nucl. Phys. A, 174:321, 1971.

[110] H. Freiesleben *et al.* Phys. Rev. C, 12:42, 1975.

[111] B. B. Back *et al.* Phys. Rev. C, 22:1927, 1980.

[112] V. E. Viola *et al.* Phys. Rev. C, 26:178, 1982.

[113] M. Fatyga *et al.* Phys. Rev. Lett., 55:1376, 1985.

[114] W. Loveland *et al.* Phys. Rev. C, 59:1472, 1993.

[115] J. P. Whitfield and N. T. Porile. Nucl. Phys. A, 550:553, 1992.

[116] L. Pieńkowski *et al.* Phys. Rev. C, 43:1331, 1991.

[117] W. Skulki *et al.* Phys. Rev. C, 41:2605, 1990.

[118] C. Casey *et al.* Phys. Rev. C, 40:1244, 1989.

[119] K. Aleklett *et al.* Phys. Rev. C, 33:885, 1986.

[120] E. Gadioli *et al.* Phys. Rev. C, 32:1214, 1985.

[121] E. Gadioli *et al.* Phys. Rev. C, 29:76, 1984.

[122] J. Jastrzebski *et al.* Phys. Lett. B, 136:153, 1984.

[123] G. Mantzouranis *et al.* Z. Phys. A, 276:145, 1976.

[124] P. J. Karol. Phys. Rev. C, 10:150, 1974.

[125] S. Gupta *et al.* Phys. Rev. C, 61:064613, 2000.

[126] B. B. Kumar *et al.* Phys. Rev. C, 59:2923, 1999.

[127] B. B. Kumar *et al.* Phys. Rev. C, 57:743, 1998.

[128] B. S. Tomar *et al.* Phys. Rev. C, 49:941, 1994.

[129] D. J. Parker *et al.* Phys. Rev. C, 39:2256, 1989.

[130] S. Chakrabarty *et al.* Nucl. Phys. A, 678:355, 2001.

[131] W. Bauer *et al.* Phys. Rev. C, 34:2127, 1986.

[132] H. Wu *et al.* Nucl. Phys. A, 617:385, 1997.

[133] A. A. Sonzogni *et al.* Phys. Rev. C, 53:243, 1996.

[134] A. Wieloch *et al.* Nucl. Phys. A, 584:573, 1995.

[135] M. Fatyga *et al.* Phys. Rev. C, 35:568, 1987.

[136] R. H. Kraus *et al.* Nucl. Phys. A, 432:525, 1985.

[137] H. Kudo *et al.* Phys. Rev. C, 30:1561, 1984.

[138] J. R. Huizenga *et al.* Phys. Rev. C, 28:1853, 1983.

[139] W. G. Meyer *et al.* Phys. Rev. C, 20:1716, 1979.

[140] Y. Futami *et al.* Nucl. Phys. A, 607:72, 1996.

[141] D. Rentsch *et al.* Phys. Rev. C, 48:2789, 1993.

[142] D. Morrissey W. Loveland and G. Seaborg. Modern Nuclear Chemistry, chapter 10. Wiley Inc., 2000.

[143] E. Gadioli *et al.* In The Nucleus; New Physics for the New Millennium. Kluwer Academic/Plenum Publishers, New York, 2000.

[144] E. Vient *et al.* Nucl. Phys. A, 700:555, 2002.

[145] J. D. Frankland *et al.* Nucl. Phys. A, 689:905, 2001.

[146] V. Métivier *et al.* Nucl. Phys. A, 672:357, 2000.

[147] J. Pouthas *et al.* Nucl. Instr. and Meth A, 357:418, 1995.

[148] I. Tilquin *et al.* Nucl. Instr. and Meth A, 361:472, 1995.

[149] S. Aiello *et al.* Nucl. Instr. and Meth A, 369:222, 1996.

[150] P. Désesquelles *et al.* Phys. Rev. C, 48:1828, 1993.

[151] L. Beaulieu *et al.* Nucl. Phys. A, 580:81, 1994.

[152] R. M. Barnett *et al.* Phys. Rev. D, 54:1, 1996.

[153] J. P. Martin *et al.* Nucl. Inst. Meth. A, 257:301, 1987.

[154] D. C. Radford *et al.* Nucl. Phys. A, 545:665, 1992.

[155] Z. Y. He *et al.* Nucl. Phys. A, 620:214, 1997.

[156] J. G. del Campo *et al.* Phys. Rev. C, 41:139, 1990.

[157] E. Fuschini *et al.* Phys. Rev. C, 50:1964, 1994.

[158] U. Heinz. Rep. Prog. Phys., 50:145, 1987.

[159] C. Pruneau *et al.* Nucl. Phys. A, 500:168, 1989.

[160] D. Dore *et al.* Nucl. Phys. A, 545:363, 1992.

[161] A. Lleres *et al.* Phys. Rev. C, 48:2753, 1993.

[162] J. Pouliot *et al.* Phys. Rev. C, 43:735, 1991.

[163] P. L. Gonthier *et al.* Phys. Rev. C, 43:1504, 1991.

[164] A. Badalà *et al.* Phys. Rev. C, 48:633, 1993.

[165] L. Bealieu *et al.* Nucl. Phys. A, 580:81, 1994.

[166] V. Lips *et al.* Phys. Rev. C, 49:1214, 1994.

[167] R. J. Charity *et al.* Phys. Rev. C, 52:3126, 1995.

[168] R. Laforest *et al.* Nucl. Phys. A, 568:350, 1994.

[169] M. Samri *et al.* Nucl. Phys. A, 583:427, 1995.

[170] L. Beaulieu *et al.* Nucl. Phys. A, 583:427, 1995.

[171] M. Bini *et al.* Phys. Rev. C, 22:1945, 1980.

[172] J. P. Bondorf *et al.* Phys. Rev. C, 46:374, 1992.

[173] M. Samri *et al.* Nucl. Phys. A, 609:108, 1996.

[174] S. B. Gazes *et al.* Phys. Rev. C, 38:712, 1988.

[175] B. S. Tomar *et al.* Phys. Rev. C, 58:3478, 1998.

[176] H. C. Britt and A. R. Quinton. Phys. Rev., 124:877, 1961.

[177] R. H. Siemssen *et al.* Nucl. Phys. A, 400:245, 1983.

[178] A. C. Schotter *et al.* Phys. Rev. Lett., 46:12, 1981.

[179] A. Magiera *et al.* Phys. Rev. C, 57:749, 1998.

[180] B. G. Harvey. Phys. Lett. B, 252:536, 1990.

[181] B. A. Harmon *et al.* Phys. Lett. B, 235:234, 1990.

[182] D. Durand *et al.* Phys. Lett. B, 345:397, 1995.

[183] R. Kaufmann and R. Wolfgang. Phys. Rev., 121:192, 1961.

[184] R. Bimbot *et al.* Nucl. Phys. A, 228:85, 1974.

[185] J. Galin *et al.* Nucl. Phys. A, 159:161, 1970.

[186] J. Wilczyński *et al.* Nucl. Phys. A, 373:109, 1982.

[187] C. K. Gelbke *et al.* Phys. Lett. B, 70:415, 1977.

[188] M. C. Mermaz *et al.* Nucl. Phys. A, 441:129, 1985.

[189] G. J. Balster *et al.* Nucl. Phys. A, 468:131, 1987.

[190] V. Zagrebaev and Yu. Penionzhkevich. Prog. Part. Nucl. Phys., 35:575, 1995.

[191] Y. D. Kim *et al.* Phys. Rev. C, 45:338, 1992.

[192] F. Terrasi *et al.* Phys. Rev. C, 40:742, 1989.

[193] S. Cavallaro *et al.* Phys. Rev. C, 40:98, 1989.

[194] G. J. Wozniak *et al.* Phys. Rev. Lett., 45:1081, 1980.

[195] R. Ritzka *et al.* Phys. Rev. C, 31:133, 1984.

[196] A. Brondi *et al.* Phys. Rev. C, 54:1749, 1996.

[197] D. J. Parker *et al.* Phys. Rev. C, 30:143, 1984.

[198] S. Pirrone *et al.* Phys. Rev. C, 64:024610, 2001.

[199] B. Borderie *et al.* Nucl. Phys. A, 402:57, 1983.

[200] L. F. Canto *et al.* J. Phys. G: Nucl. Part. Phys., 23:1465, 1997.

[201] N. Aissaoui *et al.* Phys. Rev. C, 55:516, 1997.

[202] G. D. Dracoulis *et al.* J. Phys. G: Nucl. Part. Phys., 23:1192, 1997.

[203] M. Westenius *et al.* Nucl. Phys. A, 509:630, 1990.

[204] R. J. Charity *et al.* Phys. Rev. C, 46:1951, 1992.

[205] H. Takemoto *et al.* Phys. Rev. C, 57:811, 1998.

[206] P. Hodgson and E. Bétăk. Phys. Rep., 374:1, 2003.

[207] T. Baumann. Longitudinal Momentum Distributions of ^{8}B and ^{19}C. Phd thesis, Darmstadt, 1999.

[208] C. A. Bertulani and G. Baur. Phys. Rep., 163:299, 1988.

[209] J. M. Alexander and L. Winsberg. Phys. Rev., 121:529, 1961.

[210] Y. Chan *et al.* Phys. Rev. C, 27:447, 1983.

[211] H. Morgenstern *et al.* Phys. Rev. Lett., 52:1104, 1984.

[212] H. Morgenstern *et al.* Z. Phys. A, 324:443, 1986.

[213] H. Morgenstern *et al.* Phys. Lett. B, 113:463, 1982.

[214] I. Tserruya *et al.* Phys. Rev. Lett., 60:14, 1988.

[215] W. Trautmann *et al.* Phys. Rev. Lett., 53:1630, 1984.

[216] Y. Larochelle *et al.* Phys. Rev. C, 57:1027, 1998.

[217] J. Wilczyński *et al.* Phys. Rev. Lett., 45:606, 1980.

[218] H. Tricoire *et al.* Z. Phys. A, 306:127, 1982.

[219] J. Pouthas *et al.* Nucl. Instr. and Meth A, 369:222, 1995.

[220] A. Pagano *et al.* Nucl. Phys. A, 681:331, 2001.

[221] R. A. Dayras *et al.* Phys. Rev. Lett, 42:697, 1979.

[222] K. Aleklett *et al.* Nucl. Phys. A, 499:591, 1989.

[223] T. Batsch *et al.* Phys. Lett. B, 189:287, 1987.

[224] P. Sapienza *et al.* Nucl. Phys. A, 630:215, 1998.

[225] E. Hagebø *et al.* Radiochim. Acta, 35:133, 1984.

[226] F. Bocage *et al.* Nucl. Phys. A, 676:391, 2000.

[227] J. Lukasik *et al.* Phys. Rev. C, 55:1906, 1997.

[228] G. Casini *et al.* Phys. Rev. Lett., 71:2567, 1993.

[229] S. Bhattacharya *et al.* Phys. Rev. Lett., 62:2589, 1989.

[230] J. Jastrzebski *et al.* Phys. Rev. C, 34:60, 1986.

[231] K. Hagel *et al.* Phys. Rev. C, 62:034607, 2000.

[232] S. Agostinelli *et al.* Nucl. Inst. and Methods A, 506:250, 2003.

[233] G. Duchêne *et al.* Nucl. Instr. and Meth A, 432:90, 1999.

[234] D. H. Wright. Physics Reference Manual. Technical Report Version: Geant4.6.0, CERN, Dec. 2003.

[235] L. Sihver *et al.* Phys. Rev. C, 47:1225, 1993.

[236] S. Kox *et al.* Phys. Rev. C, 35:1678, 1987.

[237] S. Wen qing *et al.* Nucl. Phys. A, 491:130, 1989.

[238] R. K. Tripathi *et al.* NASA Technical Paper, 3621:1, 1997.

[239] K. K. Gudima *et al.* Nucl. Phys. A, 401:329, 1983.

[240] V. F. Weisskopf and D. H. Ewing. Phys. Rev., 57:472, 1940.

[241] H. Hurwitz and H. A. Bethe. Phys. Rev., 81:898, 1951.

[242] S. Furihata. Nucl. Inst. and Methods B, 171:251, 2000.

[243] E. Fermi. Prog. Theo. Phys., 5:570, 1950.

[244] J. V. Pilcher *et al.* Phys. Rev. C, 40:1937, 1989.

[245] R. T. Newman *et al.* Balkan Phys. Lett., Special Issue:182, 1998.

[246] F. A. Beck. Prog. Part. Nucl. Phys., 28:443, 1992.

[247] B. T. Turko *et al.* A High Resolution 14-bit ADC for Gammasphere Project. Laboratory Report LBL-32246, Lawrence Berkeley, October 1992.

[248] I. Y. Lee *et al.* Rep. Prog. Phys., 66:1095, 2003.

[249] C. W. Beausang *et al.* Nucl. Inst. and Methods A, 313:37, 1992.

[250] P. J. Nolan *et al.* Nucl. Phys. A, 520:657, 1990.

[251] P. M. Jones *et al.* Nucl. Inst. and Methods A, 362:556, 1995.

[252] W. R. Leo. Techniques for Nuclear and Particle Physics Experiments, chapter 14. Springer-Verlag, 2nd ed., 1994.

[253] R. Setze *et al.* XSYS Reference Manual. Technical Report Seventh Edition, Triangle Universities Nuclear Laboratory, June 1995.

[254] D. C. Radford. Nucl. Inst. Meth. A, 361:297, 1995.

[255] C. Radford. Nucl. Inst. Meth. A, 361:306, 1995.

[256] R. E. Doebler *et al.* Phys. Rev. C, 20:1112, 1978.

[257] J. H. Barker and D. G. Sarantities. Phys. Rev. C, 9:607, 1974.

[258] T. U. Chan *et al.* Nucl. Phys. A, 257:413, 1976.

[259] R. L. Kozub *et al.* Phys. Rev. C, 30:1324, 1984.

[260] A. R. Poletti *et al.* Phys. Rev. C, 10:2329, 1974.

[261] D. R. Zolnowski *et al.* Phys. Rev. Lett., 41:92, 1978.

[262] J. F. Ziegler and J. P. Biersack. SRIM-2003 program (www.srim.com). Technical Report 20, Annapolis, Dec. 2003.

[263] H. Kouno *et al.* Phys. Rev. C, 53:2542, 1996.

[264] H. Kouno *et al.* Phys. Rev. C, 52:135, 1995.

[265] H. Kouno *et al.* Phys. Rev. C, 51:1754, 1995.

[266] M. V. Stoitsov *et al.* Phys. Rev. C, 50:1445, 1994.

[267] D. Fabris *et al.* In Proc. of the 8th Int. Conf. on Nuclear Reaction Mechanisms, page 96. Ricerca Scientifica ed Educazione Permanente, 1997.

[268] J. Galin *et al.* Phys. Rev. C, 9:1126, 1974.

[269] S. H. Connell and R. Tegen. In Proc. of the Int. Conf. on Fundamental and Applied Aspects of Modern Phys., Luderitz, Namibia, page 535. World Scientific, 2001.

[270] R. Moustabchir *et al.* Nucl. Phys. A, 739:15, 2004.

[271] H. Y. Wu *et al.* Phys. Lett. B, 538:39, 2002.

[272] R. Laforest *et al.* Phys. Rev. C, 59:2567, 1999.

[273] A. Pop *et al.* Nucl. Phys. A, 679:793, 2001.

[274] S. P. Baldwin *et al.* Phys. Rev. Lett., 74:1299, 1995.

[275] R. Bougault *et al.* Nucl. Phys. A, 587:499, 1995.

[276] J. Péter *et al.* Nucl. Phys. A, 593,:95, 1995.

[277] X. Qian *et al.* Phys. Rev. C, 59:269, 1999.

[278] L. Beaulieu *et al.* Phys. Rev. Lett., 77:462, 1996.

[279] J. F. Lecolley *et al.* Phys. Lett. B, 354:202, 1995.

[280] Y. Larochelle *et al.* Phys. Lett. B, 352:8, 1995.

[281] A. Sokolov *et al.* Nucl. Phys. A, 562:273, 1993.

[282] B. Lott *et al.* Phys. Rev. Lett., 68:3141, 1992.

[283] B. S. Kumar *et al.* Phys. Rev. C, 46:1946, 1992.

[284] S. Cavallaro *et al.* Phys. Rev. C, 41:1606, 1990.

[285] W. K. Wilson *et al.* Phys. Rev. C., 41:1881, 1990.

[286] S. J. Sanders *et al.* Phys. Rev. C, 40:2091, 1989.

[287] B. Grabez *et al.* Phys. Rev. C., 34:170, 1986.

[288] S. Wald *et al.* Phys. Rev. C, 25:1118, 1982.

[289] D. v. Harrach *et al.* Phys. Rev. Lett., 42:1728, 1979.

[290] R. Wada *et al.* Nucl. Phys. A, 548:471, 1992.

[291] C. P. Montoya *et al.* Phys. Rev. Lett., 73:3070, 1994.

[292] J. Tõke *et al.* Nucl. Phys. A, 583:519, 1995.

[293] W. Lynch. Nucl. Phys. A, 583:471, 1995.

[294] J. E. Sauvestre *et al.* Nucl. Phys. A, 335:300, 1994.

[295] J. F. Dempsey *et al.* Phys. Rev. C, 54:1710, 1996.

[296] J. Tõke *et al.* Phys. Rev. Lett., 77:3514, 1996.

[297] L. G. Sobotka. Phys. Rev. C, 50:1272, 1994.

[298] Y. Larochelle *et al.* Phys. Rev. C, 55:1869, 1997.

[299] P. Pawłowski *et al.* Phys. Rev. C, 57:1771, 1998.

[300] E. Plagnol *et al.* Phys. Rev. C, 61:014606, 2000.

[301] R. Wada *et al.* Phys. Rev. C, 62:034601, 2000.

[302] Y. Larochelle *et al.* Phys. Rev. C, 62:051602, 2000.

[303] G. Casini *et al.* Phys. Rev. Lett., 83:2537, 1999.

[304] H. Müller and B. D. Serot. Phys. Rev. C, 52:2072, 1995.

[305] M. Colonna *et al.* Phys. Rev. C, 57:1410, 1998.

[306] S. Bishop. Measurement of the ^{21}Na(p,γ)^{22}Mg Reaction Rate in Nova Nucleosynthesis. Phd thesis, Simon Fraser University, 2003.

[307] W. Cassing *et al.* Phys. Rep., 188:361, 1990.

[308] T. Lefort *et al.* Nucl. Phys. A, 662:397, 2000.

[309] A. Ono and H. Horiuchi. Phys. Rev. C, 51:299, 1995.

[310] P. Eudes *et al.* Phys. Rev. C, 56:2003, 1997.

[311] L. Stuttgé *et al.* Nucl. Phys. A, 539:511, 1992.

[312] Y. Larochelle *et al.* Phys. Rev. C, 59:565, 1999.

[313] S. L. Chen *et al.* Phys. Rev. C, 54:2114, 1996.

[314] M. Colonna *et al.* Nucl. Phys. A, 589:2671, 1995.

[315] M. Colonna *et al.* Nucl. Phys. A, 583:525, 1995.

[316] W. Scheid *et al.* Phys. Rev. Lett., 32:741, 1974.

[317] W. Bauer. Phys. Rev. Lett., 69:1888, 1992.

[318] C. B. Das *et al.* Phys. Rev. C, 56:1444, 1997.

[319] J. D. Frankland *et al.* Nucl. Phys. A, 689:940, 2001.

[320] P. Désesquelles *et al.* Phys. Rev. C, 62:024614, 2000.

[321] J. F. Lecolley *et al.* Phys. Lett. B, 387:460, 1996.

[322] M. D'Agostino *et al.* Phys. Lett. B, 368:259, 1996.

[323] N. Marie *et al.* Phys. Lett. B, 391:15, 1997.

[324] A. Szanto de Toledo *et al.* Phys. Rev. Lett., 70:2070, 1993.

[325] D. H. E. Gross *et al.* Phys. Rev. Lett., 56:1544, 1986.

[326] J. P. Bondorf *et al.* Nucl. Phys. A, 443:321, 1985.

[327] B. Borderie *et al.* Phys. Rev. Lett., 86:3252, 2001.

[328] K. Grotowski. Act. Phys. Pol. B, 31:253, 2000.

[329] G. Bertsch and P. J. Siemens. Phys. Lett. B, 126:9, 1983.

[330] M. Colonna and P. Chomaz. Phys. Rev. C, 49:1908, 1994.

[331] M. F. Rivet *et al.* Phys. Lett. B, 430:215, 1992.

[332] M. F. Rivet *et al.* Phys. Lett. B, 388:219, 1996.

[333] B. Jouault *et al.* Nucl. Phys. A, 615:82, 1997.

[334] J. F. Lecolley *et al.* Nucl. Inst. Meth. Phys. Res. A, 441:517, 2000.

[335] J. Wilczyński *et al.* Phys. Lett. B, 47:484, 1973.

[336] M. D'Agostino *et al.* Nucl. Phys. A, 650:329, 1999.

[337] H. Jaqaman *et al.* Phys. Rev. C, 27:2782, 1983.

[338] H. Jaqaman *et al.* Phys. Rev. C, 29:2067, 1984.

[339] J. Pochodzalla *et al.* Phys. Rev. Lett., 75:1040, 1995.

[340] M. L. Gilkes *et al.* Phys. Rev. Lett., 73:1590, 1994.

[341] J. B. Elliott *et al.* Phys. Rev. C, 49:3185, 1994.

[342] J. A. Hauger *et al.* Phys. Rev. C, 57:764, 1998.

[343] J. A. Hauger *et al.* Phys. Rev. Lett., 77:235, 1996.

[344] P. F. Mastinu *et al.* Phys. Rev. Lett., 76:2646, 1996.

[345] J. P. Bondorf *et al.* Nucl. Phys. A, 444:460, 1986.

[346] M. D'Agostino *et al.* Phys. Lett. B, 473:219, 2000.

[347] J. B. Natowitz *et al.* Phys. Rev. C, 52:2325, 1995.

[348] S. Albergo *et al.* Nuovo Cim. A, 89:1, 1985.

[349] F. Gulminelli and D. Durand. Nucl. Phys. A, 615:117, 1997.

[350] A. Siwek *et al.* Phys. Rev. C, 57:2507, 1998.

[351] K. Turzó. Study of the $^{12}C + ^{197}Au$ at Relativistic Energies with the INDRA 4π Multidetector. Phd thesis, L'university Lyon, 2002.

[352] Y. G. Ma *et al.* Phys. Lett. B, 390:41, 1997.

[353] P. Chomaz and F. Gulminelli. Nucl. Phys. A, 647:153, 1999.

[354] J. C. Steckmeyer *et al.* Phys. Rev. Lett., 76:4895, 1996.

[355] J. B. Natowitz *et al.* Phys. Rev. C, 65:034618, 2002.

[356] F. R. Lecolley *et al.* Nucl. Phys. A, 620:327, 1997.

[357] X. Campi *et al.* Phys. Rev. C, 50:2680, 1994.

[358] A. Gökmen *et al.* Phys. Rev. C, 29:1595, 1984.

[359] P. M. Milazzo *et al.* Phys. Lett. B, 509:204, 2001.

[360] P. M. Milazzo *et al.* Nucl. Phys. A, 703:466, 2002.

[361] H. Xi *et al.* Nucl. Phys. A, 630:160, 1998.

[362] H. Xi *et al.* Phys. Lett. B, 431:8, 1998.

[363] M. J. Huang *et al.* Phys. Rev. Lett., 78:1648, 1997.

[364] P. M. Milazzo *et al.* Phys. Rev. C, 60:044606, 1999.

[365] G. Lanzanò *et al.* Phys. Rev. C, 58:281, 1998.

[366] B. V. Jacak *et al.* Phys. Rev. C, 35:1751, 1987.

[367] E. Vient *et al.* Nucl. Phys. A, 571:588, 1994.

[368] A. Badalà *et al.* Phys. Rev. C, 45:1730, 1992.

[369] K. A. Griffioen *et al.* Phys. Rev. C, 40:1647, 1989.

[370] W. Bohne *et al.* Phys. Rev. C, 41:R5, 1990.

[371] A. Badalà *et al.* Phys. Lett. B, 299:11, 1993.

[372] J. Aichelin. Phys. Rep., 202:233, 1991.

[373] K. Hagel *et al.* Phys. Rev. C, 50:2017, 1994.

[374] R. Wada *et al.* Phys. Rev. C, 55:227, 1997.

[375] J. Cibor *et al.* Phys. Rev. C, 55:264, 1997.

[376] T. Maruyama *et al.* Phys. Rev. C, 53:297, 1996.

[377] N. Wang *et al.* Phys. Rev. C, 69:034608, 2004.

[378] H. Horiuchi and Y. Kanada-En'yo. Nucl. Phys. A, 588:121, 1995.

[379] A. Ono and H. Horiuchi. Phys. Rev. C, 53:2958, 1996.

[380] A. Ono and H. Horiuchi. Phys. Rev. C, 53:2341, 1996.

[381] A. Ono and H. Horiuchi. Phys. Rev. C, 53:845, 1996.

[382] J. Aichelin and H. Stoker. Phys. Lett. B, 176:14, 1986.

[383] J. Aichelin *et al.* Phys. Rev. C, 37:2451, 1988.

[384] G. Peilert *et al.* Phys. Rev. C, 39:1402, 1989.

[385] T. Maruyama *et al.* Prog. Theo. Phys., 98:87, 1997.

[386] S. Chiba *et al.* Phys. Rev. C, 54:285, 1996.

[387] S. Chiba *et al.* Phys. Rev. C, 53:1824, 1996.

[388] T. Maruyama *et al.* Phys. Lett. B, 358:34, 1995.

[389] A. E. Glassgold and P. J. Kellogg. Phys. Rev., 107:1372, 1957.

[390] J. O. Newton *et al.* Phys. Rev. C, 70:024605, 2004.

Appendix A

Some Residue Observables

Table A.1: A number of the measured observables for the prominent residue gamma lines are given in table A.1. These are residue identity (A, Z) in column one, the half-life of the gamma transition energy state for the gated line and the corresponding coincident gamma cascade energies used in the identification of the residue nucleus is given in column three.

Residue identity	$T_{\frac{1}{2}}$ (ps)	Coincident γ-lines (keV)
^{64}Zn	1.80	340.8/991.6
^{64}Cu	<4	159.1/202.9/212.4
^{63}Zn	530	193/870,872,875/1242/1245
^{63}Cu	0.61	365.0/962.2/899.1
^{62}Cu	4570	40.8/349.6/385.3/512
^{61}Ni	5340	67.4/947.6/1114.1
^{60}Cu	-	103.7/453.8
^{60}Ni	0.91	1165.5/1332.5;1164.5/1173.2
^{59}Ni	68	339.4/998.5/1428.0
^{59}Co	-	235.72/302.4
^{58}Co	0.6	320.8/504.4
^{57}Co	0.24	465.7/1224.0
^{57}Fe	8700	122.06/256.0
^{56}Fe	6.07	846.8/1238.3
^{55}Fe	37.9	274.8/605.20
^{55}Mn	259	125.9/307.9
^{54}Mn	186	156.2/212.0
^{53}Mn	-	472/1228
^{52}Cr	41.4	744.2/935.5/1434.1
^{51}Cr	0.55	316.0/1165.0
^{50}V	56	94.0/226.2
^{48}V	75	427.9/199.3
^{47}Ti	210	159.4/1092.7
^{47}V	680	58.2/87.5
^{42}K	280	106.8/151.4

Appendix B

Gamma Emission Properties

Coincident Gamma-rays extracted from the gamma-gamma energy matrix and the corresponding nuclear gamma emitters. These data are derived from the array matrix made up of the all clover detectors and only those at 90° for confirmation. The former produces a much more enhanced gamma coincidences spectra compared to the 90° detector matrix. In a few cases, there were some ambiguities in residue assignment either as a result of low statistical counts, or when only two coincident gamma-rays coincide for a number of nuclei. Some suspected contaminations from the thick aluminium target frame nuclear products were clearly distinct when the full-width at half-maximum of the gamma lines is considered.

$E_{\gamma 1}$	$I_{\gamma 1}$	J_i	E_i	$E_{\gamma 2}$	$I_{\gamma 2}$	J_i	E_i	Branch(%)
^{65}Ga[1]								
349.90	0.06	23/2	6293.4	1397.40	0.49	21/2	5943.4	100.00
^{65}Zn								
201.30	6.30	9/2+	1065.5	864.20	10.00	7/2-	864.2	86.95
201.30	6.30	9/2+	1065.5	870.00	0.00	13/2	2923.1	88.80
202.00	10.00	9/2+	1066.0	785.00	0.00		2924.0	100.00
201.30	10.00	9/2+	1065.5	988.20	10.00	13/2+	2053.8	91.05
1011.00	0.30	(21/2+)	4236.5	826.80	0.26	21/2+	5063.4	100.00
1012.70	0.10	33/2+	7996.0	826.80	0.26	21/2+	5063.4	6.31
^{64}Zn								
340.80	1.10	(4+)	3077.8	991.56	10.00	2+	991.5	80.01
340.80	1.10	(4+)	3077.8	993.00	10.10	(10+)	7118.2	0.55
744.80	10.00	(6)	4669.7	937.16	10.00	4+	2736.5	10.58
746.90	0.00		4824.3	937.16	10.00	4+	2736.5	54.45
746.00	0.40	(6)	4669.5	937.15	1.52	4+	2736.1	10.75
743.50	0.09	7-	4979.6	937.15	1.52	4+	2736.1	90.52
743.50	0.70	(7)-	4981.2	937.16	10.00	4+	2736.5	86.65
743.50	0.09	7-	4979.6	1435.00	0.39		13838.5	1.20*
937.15	1.52	4+	2736.1	807.70	1.20	2+	1798.9	83.11
937.16	10.00	4+	2736.5	1435.00	10.00		13840.6	21.04
^{63}Zn								
192.90	10.00	5/2-	192.9	1498.60	0.60	5/2-	1691.3	100.00
192.90	10.00	5/2-	192.9	1497.20	10.00	13/2-	2934.5	100.00
193.00	100.00	5/2-	193.2	1244.00	30.10	9/2-	1437.1	100.00
192.90	10.00	5/2-	192.9	1013.40	4.58	7/2-	1206.4	100.00
192.90	10.00	5/2-	192.9	1013.00	0.00	19/2-	5916.4	20.91
192.90	10.00	5/2-	192.9	870.80	1.04	7/2-	1063.8	100.00
192.90	10.00	5/2-	192.9	875.00	0.66	(15/2)-	4355.3	20.91
192.90	10.00	5/2-	192.9	639.50	8.20	9/2+	1703.7	12.78
389.40	9.58	3/2-	637.2	510.00	2.30	19/2-	5916.4	0.86
413.20	2.80	7/2-	1063.3	650.14	10.00	5/2-	650.1	86.20
881.30	10.00	13/2+	2584.2	639.50	10.00	9/2+	1702.9	84.74

$E_{\gamma 1}$	$I_{\gamma 1}$	J_i	E_i	$E_{\gamma 2}$	$I_{\gamma 2}$	J_i	E_i	Branch(%)
^{64}Cu								
159.10	10.00	2+	159.1	202.90	9.50	3+	362.0	100.00
159.10	10.00	2+	159.1	212.40	7.30	(4)+	574.4	98.45
159.10	10.00	2+	159.1	1019.00	5.50	6-	1593.4	98.54
159.28	10.00	2+	159.3	1279.41	7.10	(1)+	1438.7	100.00
159.28	10.00	2+	159.3	1303.90	10.00		2050.0	21.33
467.99	10.00	(3+)	746.2	831.18	10.00		3207.6	35.14
278.24	10.00	2+	278.3	467.99	10.00	(3+)	746.2	100.00
159.28	10.00	2+	159.3	1241.50	10.00		3596.0	76.71
159.10	10.00	2+	159.1	321.10	0.10	(3)+	895.7	98.54
202.90	9.50	3+	362.0	784.10	2.70	(7-)	2377.4	92.76
202.00	0.21	2+	243.0	432.00	0.37	3+	674.8	14.62
202.00	0.21	2+	243.0	427.00	0.33	5+	1676.8	5.21
202.90	9.50	3+	362.0	479.00	1.20		2072.4	92.76
202.95	10.00	3+	362.2	1041.10	10.00		1615.7	92.16
184.61	0.40	1+	343.9	937.01	10.00		3191.1	3.88*
779.65	3.40	(3)+	1354.2	1476.10	10.00		2830.5	18.79
278.24	10.00	2+	278.3	467.99	10.00	(3+)	746.2	100.00
119.00	0.00	2+	278.3	157.40	0.00	(3)+	895.7	0.00
202.95	10.00	3+	362.2	625.35	10.00	(1+)	2892.4	48.83
202.90	9.50	3+	362.0	608.80	0.80	9+	3798.8	92.76
159.28	10.00	2+	159.3	1287.40	2.00		2726.2	51.26
159.28	10.00	2+	159.3	1293.92	10.00		3033.8	97.79
1127.84	10.00	(1+)	2896.8	1407.08	10.00	1769.0	100.00	

$E_{\gamma 1}$	$I_{\gamma 1}$	J_i	E_i	$E_{\gamma 2}$	$I_{\gamma 2}$	J_i	E_i	Branch(%)
159.28	10.00	2+	159.3	1303.90	10.00		2050.0	21.33
159.10	10.00	2+	159.1	813.00	0.00	(8-)	3190.0	98.54
1128.40	10.00		1288.6	159.28	10.00	2+	159.3	100.00
1131.20	0.00		1290.6	159.28	10.00	2+	159.3	100.00
1127.84	10.00	(1+)	2896.8	159.28	10.00	2+	159.3	97.66
^{63}Cu								
365.00	1.68	7/2-	1327.0	962.20	10.00	5/2-	962.0	100.00
962.20	10.00	5/2-	962.0	899.10	4.12	7/2-	1861.0	100.00
340.90	10.00	17/2+	4496.2	414.30	3.30	9/2+	2505.7	33.01
413.00	0.00	9/2+	2505.0	1130.00	0.00	7/2-	2092.0	50.00
414.00	71.80	7/2-	1064.0	1411.00	15.50	(23/2)+	6489.8	25.17
413.10	2.80	9/2+	2505.6	1649.80	7.60	13/2+	4155.5	28.01
413.00	0.00	9/2+	2505.0	342.00	0.00	17/2+	4497.0	50.01
413.00	0.00	9/2+	2505.0	765.00	0.00	7/2-	2092.0	50.00
1130.70	10.00	7/2-	2092.6	962.06	10.00	5/2-	962.1	100.00
1129.00	10.00		2678.7	962.06	10.00	5/2-	962.1	21.52
^{63}Ni*								
155.60	10.00	3/2-	155.6	845.50	10.00	1/2-	1001.1	100.00
^{62}Zn								
630.00	10.00	7-	4648.7	1172.90	10.00	2+	1172.9	100.00
1232.00	0.00	4+	2186.0	370.00	0.00	7-	4904.0	100.00
1119.80	6.40	(14+)	11756.0	1604.20	10.00	(6+)	4347.8	23.85
^{62}Cu								
40.84	10.00	2+	40.8	924.80	10.00	(6-)	2295.3	96.16
40.84	10.00	2+	40.8	349.25	10.00	4+	390.1	100.00
40.84	10.00	2+	40.8	349.60	0.17	1+	637.5	100.00
40.84	10.00	2+	40.8	351.60	2.42	(9)	3979.2	96.16
40.84	0.00	2+	40.8	385.00	3.52	3+	426.5	100.00

$E_{\gamma 1}$	$I_{\gamma 1}$	J_i	E_i	$E_{\gamma 2}$	$I_{\gamma 2}$	J_i	E_i	Branch(%)
40.80	0.00	2+	40.8	586.80	0.00		1286.0	50.00
40.70	0.00	2+	40.9	596.70	38.30	(7-)	2892.6	91.77
40.70	0.00	2+	40.9	924.80	92.70	6-	2295.7	91.78
40.70	0.00	2+	40.9	980.30	95.00	5+	1370.8	90.98
40.70	0.00	2+	40.9	1012.80	3.30	(9-)	4447.6	89.10
272.00	0.28	3+	698.3	385.00	3.52	3+	426.5	100.00
597.00	2.42	7-	2891.8	350.00	10.00	4+	390.1	75.17
597.00	2.42	7-	2891.8	351.00	0.20	9(-)	3978.6	21.97
600.00	0.15	8-	3627.5	350.00	10.00	4+	390.1	75.54
600.00	0.15	8-	3627.5	351.00	0.20	9(-)	3978.6	5.25
600.00	0.15	(10-)	5047.0	350.00	10.00	4+	390.1	74.86
600.00	0.15	(10-)	5047.0	351.00	0.20	9(-)	3978.6	2.68
243.50	3.05	2+	243.3	147.00	8.70	4+	390.4	100.00
243.50	3.05	2+	243.5	431.60	1.60	3+	675.2	100.00
243.50	3.05	2+	243.5	429.00	7.60	5+	1678.1	48.43
243.50	19.10	(8-)	3435.3	429.00	7.60	5+	1678.1	17.44
243.40	0.00	2+	243.4	454.90	0.00		698.3	100.00
243.40	0.00	2+	243.4	484.40	0.00	2+	727.8	100.00
202.67	0.04	2+	243.4	1040.00	5.00	5+	1677.6	0.03
202.67	0.04	2+	243.4	1046.70	0.00		1745.0	0.15
202.00	0.21	2+	243.0	427.00	0.33	5+	1676.8	5.21
439.00	4.80		1354.3	627.80	0.49	2+	915.3	2.13
349.50	100.00	4+	390.6	1332.20	35.30	(8-)	3628.0	83.04
351.60	3.85	(9)	3979.7	1332.20	35.30	(8-)	3628.0	72.78
147.00	0.34	4+	390.1	1135.00	0.24	9-	4165.0	2.93
285.00	0.50	3+	675.0	349.30	0.00	4+	390.2	100.00
349.50	100.00	4+	390.6	1119.00	22.20	(9+)	4746.9	83.04
349.50	100.00	4+	390.6	1135.30	4.80	(9-)	4165.4	83.04

$E_{\gamma 1}$	$I_{\gamma 1}$	J_i	E_i	$E_{\gamma 2}$	$I_{\gamma 2}$	J_i	E_i	Branch(%)
349.50	100.00	4+	390.6	1287.70	4.60	5+	1678.1	90.98
351.60	3.85	(9)	3979.7	1287.70	4.60	5+	1678.1	0.00
349.50	100.00	4+	390.6	1332.20	35.30	(8-)	3628.0	83.04
351.60	3.85	(9)	3979.7	1332.20	35.30	(8-)	3628.0	72.78
349.50	100.00	4+	390.6	1372.30	6.40	(9-)	5000.4	83.04
349.25	10.00	4+	390.1	1390.00	0.00		2067.5	17.79
349.50	100.00	4+	390.6	1417.80	0.90	(9-)	4447.8	83.04
349.50	100.00	4+	390.6	1757.80	8.70	6+	2148.4	90.98
350.00	10.00	4+	390.1	512.00	0.33	(11-)	5618.2	74.86
351.00	0.20	9(-)	3978.6	512.00	0.33	(11-)	5618.2	2.68
1135.30	4.80	(9-)	4165.4	349.50	100.00	4+	390.6	83.04
^{61}Ni								
67.40	10.00	5/2-	67.4	947.60	7.50	7/2-	1015.0	100.00
67.40	10.00	5/2-	67.4	1109.80	1.00	7/2-	2018.0	21.00
67.40	10.00	5/2-	67.4	1106.20	10.00	9/2+	2121.4	75.00
67.40	10.00	5/2-	67.4	1113.60	10.00	11/2-	2128.6	75.00
283.40	10.00	1/2-	283.3	372.50	1.70	1/2-	655.9	100.00
283.40	10.00	1/2-	283.3	816.70	5.10	3/2-	1099.6	100.00
^{60}Cu								
61.4	0.00	1+	62.2	224.9	0.00	2+	287.3	100.00
103.70	5.30	(4+)	557.5	453.80	10.00	(3+)	453.8	98.99
237.00	0.00		571.0	272.00	0.00		334.0	100.00
103.00	0.00	(4+)	557.0	1640.00	0.00	(6+)	2197.0	25.84
103.00	0.00	(4+)	557.0	1640.00	0.00		3837.0	12.92
669.00	8.70	1+	669.0	338.00	0.00		1007.0	87.01
237.00	0.00		571.0	273.40	10.00		335.8	100.00

$E_{\gamma 1}$	$I_{\gamma 1}$	J_i	E_i	$E_{\gamma 2}$	$I_{\gamma 2}$	J_i	E_i	Branch(%)
^{60}Ni								
1164.50	0.00	4+	3670.2	1173.20	10.00	4+	2505.7	100.00
1165.50	0.67	4+	3671.4	1332.48	10.00	2+	1332.5	100.00
467.00	0.80	3+	2626.0	1332.00	10.00	2+	1332.0	100.00
467.00	0.00	3+	2626.0	827.00	0.00	2+	2159.0	100.00
605.00	0.00		3730.7	1332.50	10.00	2+	1332.5	90.55
1787.20	10.00	4+	3119.7	1332.50	10.00	2+	1332.5	100.00
1791.60	10.00	2+	3124.0	1332.50	10.00	2+	1332.5	100.00
826.06	10.00	2+	2158.6	1332.50	10.00	2+	1332.5	100.00
1130.00	0.00		4399.4	346.93	0.00	4+	2505.8	0.00
^{59}Ni								
339.41	10.00	5/2-	339.4	998.52	10.00	7/2-	1337.9	100.00
339.40	10.00	5/2-	339.4	1428.02	9.30	9/2-	1767.5	100.00
339.41	10.00	5/2-	339.4	429.58	1.01	(9/2)-	1767.4	71.28
339.41	10.00	5/2-	339.4	427.00	1.60	9/2+	3054.3	42.86
339.41	10.00	5/2-	339.4	426.50	12.80	(19/2-)	6502.5	83.87
339.40	10.00	5/2-	339.4	1367.00	3.50	11/2	2704.9	72.73
339.41	10.00	5/2-	339.4	1608.31	6.40	7/2-	1947.9	100.00
339.41	10.00	5/2-	339.4	1609.50	10.00	(11/2)-	3376.9	97.36
339.41	10.00	5/2-	339.4	1611.30	2.60	(11/2)-	3559.4	35.99
339.41	10.00	5/2-	339.4	1615.20	2.50		5754.8	6.22
465.10	0.76	1/2-	465.0	836.40	0.00	1/2-	1301.4	100.00
339.40	10.00	5/2-	339.4	1609.50	1.60		1949.1	100.00
339.40	10.00	5/2-	339.4	1609.50	1.60		3376.8	96.97
^{59}Co								
235.72	6.80	(15/2)	4412.7	302.35	10.00	(17/2)	4715.1	68.00
235.72	10.00	(15/2)	4412.7	333.90	10.00	(13/2)	4176.7	43.10
302.35	10.00	(17/2)	4714.8	653.00	10.00	(19/2)	5368.0	100.00

$E_{\gamma 1}$	$I_{\gamma 1}$	J_i	E_i	$E_{\gamma 2}$	$I_{\gamma 2}$	J_i	E_i	Branch(%)
235.72	10.00	(15/2)	4412.7	992.88	10.00	(11/2)	2183.5	27.06
235.72	10.00	(15/2)	4412.7	994.10	10.00	(21/2)	6362.2	68.03
693.94	10.00	(13/2)	2153.5	1459.62	9.50	11/2-	1459.6	94.98
^{58}Co								
320.76	9.90	5+	373.9	504.43	2.08		1929.0	86.63
320.76	10.00	5+	373.9	1050.81	10.00	(6)	1424.6	94.25
320.76	9.90	5+	373.9	701.70	1.16	6+	1075.5	96.68
504.43	2.08		1554.7	1049.40	1.51	1+	1050.1	60.88
504.43	2.08		1929.0	1050.81	7.50	(6)	1424.6	89.61
504.43	2.08		1929.0	320.76	9.90	5+	373.9	86.63
320.76	9.90	5+	373.9	332.50	0.50	1+	1377.0	0.01
^{57}Co								
465.70	10.00	11/2-	1689.6	1224.00	10.00	9/2-	1224.0	100.00
465.70	10.00	11/2-	1689.6	834.20	10.00	(13/2)-	2524.1	54.08
466.10	0.00	11/2-	1690.1	596.10	0.00		6442.3	50.02
^{57}Fe								
122.06	10.00	5/2-	136.5	256.03	10.00	(15/2)-	3134.8	88.10
122.10	10.00	5/2-	136.4	870.60	3.90	7/2-	1007.0	87.20
122.10	10.00	5/2-	136.4	1061.40	9.10	9/2-	1197.8	87.20
122.10	10.00	5/2-	136.4	1680.70	5.80	(13/2)-	2878.5	87.20
352.36	10.00	3/2-	366.8	1705.00	3.80	(3/2)-	4209.6	44.06
352.36	10.00	3/2-	366.8	1722.40	10.00		2987.9	73.29
136.47	0.00	5/2-	136.5	256.03	10.00	(15/2)-	3134.5	53.02

$E_{\gamma 1}$	$I_{\gamma 1}$	J_i	E_i	$E_{\gamma 2}$	$I_{\gamma 2}$	J_i	E_i	Branch(%)
^{56}Fe								
846.80	10.00	2+	846.8	1238.30	10.00	4+	2085.1	100.00
846.80	10.00	2+	846.8	1303.70	9.80	6+	3388.8	100.00
^{55}Fe								
274.80	10.00	13/2-	2813.8	605.20	10.00	15/2-	3419.0	100.00
273.60	10.00	13/2-	2813.2	1222.80	9.40	11/2-	2539.6	93.98
273.60	10.00	13/2-	2813.2	1316.80	9.30	7/2-	1316.8	87.39
273.60	10.00	13/2-	2813.2	1680.60	10.00	(19/2-)	5099.4	100.00
931.00	8.70	5/2-	931.0	477.10	3.10	7/2-	1408.2	100.00
1078.00	10.00	23/2	7605.6	605.60	10.00	15/2(-)	3418.8	100.00
^{55}Mn								
125.94	10.00	7/2-	125.9	307.86	2.50	(11/2-)	1292.1	96.00
125.87	0.00	7/2-	125.9	112.00	0.00		2312.0	93.12
125.94	10.00	7/2-	125.9	858.31	9.60	(9/2)-	984.3	100.00
125.94	10.00	7/2-	125.9	1019.50	9.00	(13/2-)	2311.6	99.00
125.87	0.00	7/2-	125.9	1164.00	1.00	11/2-	1290.0	100.00
^{54}Mn								
156.27	10.00	4+	156.3	212.00	10.00	5+	368.3	100.00
156.27	8.10		156.3	704.93	1.90		1073.2	100.00
156.27	10.00	4+	156.3	851.98	10.00	7+	1925.2	100.00
156.40	87.50		156.4	1415.60	29.00		1784.0	100.00

$E_{\gamma 1}$	$I_{\gamma 1}$	J_i	E_i	$E_{\gamma 2}$	$I_{\gamma 2}$	J_i	E_i	Branch(%)
^{52}Cr								
744.20	3.96	6+	3113.9	1434.20	10.00	2+	1434.2	100.00
600.10	0.75	5+	4015.6	1333.70	2.34	4+	2767.9	98.28
^{51}Cr								
316.00	0.00	11/2-	1481.0	775.00	0.00	15/2-	2256.0	50.04
315.60	9.27	11/2-	1480.1	510.80	6.20	3/2-	2890.2	9.06
316.00	0.00	11/2-	1481.0	636.00	0.00	19/2-	3817.0	50.04
316.00	0.00	11/2-	1481.0	925.00	0.00	17/2-	3181.0	50.04
316.00	0.00	11/2-	1481.0	1165.00	0.00	9/2-	1165.0	100.00
^{50}Cr								
783.00	0.00	2+	783.0	1098.00	0.00	4+	1881.0	100.00
783.20	10.00	2+	783.2	1282.50	8.50	6+	3163.6	100.00
1097.90	9.70	4+	1881.1	1581.40	8.20	8+	4745.1	100.00
^{50}V								
94.00	5.20	4+	320.1	226.20	6.50	5+	226.2	100.00
^{49}V								
463.90	0.30	15/2-	2727.6	597.10	0.80	(17/2-)	3325.5	42.87
464.00	1.40	(17/2-)	3325.5	599.00	0.80	13/2-	2861.8	64.00
^{48}V								
427.90	10.00	5+	428.0	199.30	4.50	6+	627.4	100.00

$E_{\gamma 1}$	$I_{\gamma 1}$	J_i	E_i	$E_{\gamma 2}$	$I_{\gamma 2}$	J_i	E_i	Branch(%)
^{47}V								
58.20	9.94	7/2-	145.8	87.50	10.00	5/2-	87.5	100.00
^{42}K								
106.85	0.00	3-	106.8	151.24	6.50	4-	258.1	100.00
106.82	10.00	3-	106.8	289.21	3.80		1400.0	6.10
106.82	10.00	3-	106.8	283.78	1.10		2766.0	18.87
106.78	11.00	3-	106.8	440.68	8.50	5-	698.8	100.00
106.78	11.00	3-	106.8	444.40	0.51	4+	1143.2	100.00
106.82	10.00	3-	106.8	454.01	0.80	2-	1861.9	13.94
106.82	10.00	3-	106.8	450.97	1.70	3+	2388.8	4.79
106.82	10.00	3-	106.8	676.87	10.00	6+	1376.0	99.62
106.82	10.00	3-	106.8	671.15	10.00		1513.1	13.79
440.85	10.00	5-	699.1	632.68	6.50		2991.5	80.48
106.82	10.00	3-	106.8	676.87	10.00	6+	1376.0	99.62
106.82	10.00	3-	106.8	671.15	10.00		1513.1	13.79

Target frame contaminant and probable IMF products

^{20}F								
$E_{\gamma 1}$	$I_{\gamma 1}$	J_i	E_i	$E_{\gamma 2}$	$I_{\gamma 2}$	J_i	E_i	Branch(%)
166.78	6.68	4+	822.7	656.00	10.00	3+	656.0	100.00
^{19}F								
109.90	10.00	1/2-	109.9	1235.80	9.68	5/2-	1345.7	100.00
^{18}F								
184.00	10.00	5+	1121.4	937.00	10.00	3+	937.2	100.00
^{27}Al								
1014.42	10.00	3/2+	1014.5	1720.30	10.00	5/2+	2734.9	97.09
^{26}Al								
416.85	10.00	3+	416.9	1651.95	10.00	4+	2068.9	100.00
416.85	10.00	3+	416.9	1652.56	2.84	2+	2069.5	100.00
416.85	10.00	3+	416.9	1654.73	1.19	1+	2071.6	100.00
^{26}Mg								
411.40	10.00	6+	2949.3	145.90	10.00	10+	6526.9	100.00
411.40				965				
145.90	2.70	10+	6526.2	1129.60	9.80	4+	2537.4	100.00
145.90	2.70	10+	6526.2	1407.80	10.00	2+	1407.8	100.00
^{25}Mg								
389.70	9.60	3/2+	974.9	585.03	10.00	1/2+	585.1	100.00
^{24}Mg								
1368.63	10.00	2+	1368.7	2754.03	10.00	4+	4122.9	100.00
^{23}Na								
439.99	10.00	5/2+	440.0	627.48	5.41	9/2+	2703.5	103.03
439.99	10.00	5/2+	440.0	1635.96	10.00	7/2+	2076.0	100.00
^{21}Ne								
350.72	10.00	5/2+	350.7	1396.00	10.00	7/2+	1745.9	100.00
350.72	10.00	5/2+	350.7	1121.00	10.00	9/2+	2866.8	94.98

Appendix C

Studies based on the 4π Particle Detector Arrays

The advent of large acceptance detectors has produced a wide spectrum of data on the heavy ion collisions showing the deviation from the purely binary picture [146]. Several studies [273, 274, 275, 276, 277, 278, 279, 280, 141, 281, 228, 282, 283, 284, 285, 286, 118, 192, 193, 287, 288, 289] have shown that sequential fission events for medium size systems points to a fast process where the fission products are often aligned along the deflection axis and are not isotropically distributed as they should be if long fission lifetimes were assumed [228, 283, 162, 285, 118]. The characteristics of quasi-projectiles reconstructed from their decay products revealed several features reminiscent of damped interactions at low and intermediate projectile energies [277].

The INDRA data [146] have shown that, between 25 and 74 A MeV, heavy ion collisions are mostly binary whatever the system mass and the bombarding energy. From the slowing-down of the partners, it was possible to establish the continuous evolution from quasi-elastic to complete damping of the projectile momentum. The observations were independent of the total system mass if energies involved were expressed in A MeV. It was also found that dynamical effects play a sizable role and that many intermediate mass fragments and light charged particles could be attributed to the neck emission or to the intermediate velocity source based on the nearly symmetrical systems ^{36}Ar + KCl and ^{129}Xe + ^{nat}Sn were used in the study, in the 32-74 A MeV and 25-50 A MeV projectile energy ranges, respectively. This established the link between the low energy pure binary process and the participant-spectator picture of the high

energy limit in the sense that neck-emission is created by the overlap region between both partners during the collision process. The neck emission did not necessarily produce a third participant zone but revealed the formation of highly deformed final binary products.

Measurements taken from the INDRA array and published recently [146] are shown in figure C.1. In the figure, one can single out three partitions: events located in zone A and B correspond to peripheral collisions for which both the projectile-like and target-like fragments have not been detected because of the forward hole 2° off the beam axis and energy threshold effects, respectively. For events located in zone B, the projectile-like fragment has been detected but the target-like fragment was not. For events located in zone C, a quasi "complete detection" was achieved. Most of the central or violent collision events were located in this zone and most of peripheral ones in either zone A or B. In order to establish more clearly such a feature, the events are sorted according to the impact parameter, using the total charged particle multiplicity in each event. In figure C.2, particle multiplicity was plotted for the Xe + Sn system at

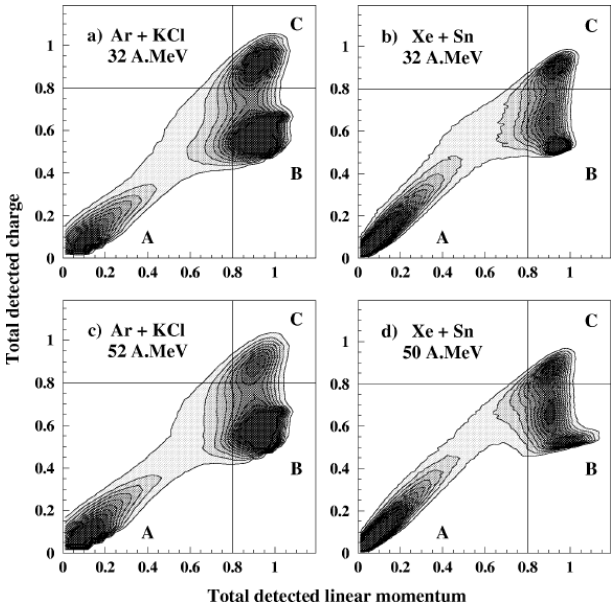


Figure C.1: The contour plots "total pseudo linear momentum versus total charge" for the events detected in Ar + KCl and Xe + Sn systems at two bombarding energies. The measured quantities have been normalized to their expected values (from Ref. [146]).

39 A MeV, the full curve corresponds to all registered events. The dashed one is associated

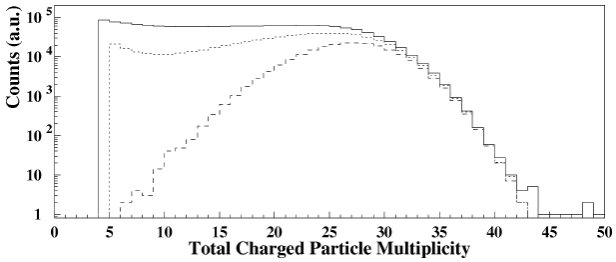


Figure C.2: The charged particle total multiplicity distributions for the Xe + Sn system at 39 A MeV. Full curve: all events; dashed curve: “complete events”, dotted curve: “completed events” (from Ref. [146]).

with “complete events” (zone C in figure C.1). The dotted line corresponds to zone B + C. For events in zone B, it was assumed that only one large fragment (target-like fragment) was missed and the event multiplicity was the measured value corrected for the undetected fragment. The atomic number and momentum of the fragment was obtained from conservation laws. The most central collision events (multiplicities larger than 35) were “completely detected”, whereas the “incomplete detection” occurred mainly for peripheral ones, for which the thresholds and forward hole effects were more pronounced (figure C.2). The three partitions of the interaction processes identified are the peripheral, central and the neck zones in the figure.

Other heavy ion collision measurements (Pb+Au, Pb+Ag, Pb+Al,Gd+C, Gd+U, Xe+Sn), conducted with the INDRA and NAUTILUS 4π arrays [226], have also shown the dominant binary and highly dissipative character of the nuclear interaction process. The large excited binary fragments produced in the first stage of the interaction can decay into various exit channels ranging from evaporation to multi-fragmentation including fission. However, deviations from this simple picture is reported by analysing the angular and velocity distributions of light charged particles and fragments. There is a certain amount of matter in excess emitted between the two primary sources suggesting either the existence of a mid-rapidity source similar to the one observed in the relativistic regime (participants) or a strong deformation induced by the dynamics of the collision (neck instability). The latter was proposed from detailed analysis of the angular distributions of the fragments.

A number of other related studies [290, 279, 291, 292, 293, 294, 295, 296, 297, 298, 227, 299, 300, 301, 302, 226] have also shown that, for peripheral interactions, some fraction of the intermediate mass fragments comes from the region in velocity space that could imply the emission of fast dynamical particles and fragments and the formation of a neck-like structure. According to Ref. [302], the neck favours the transfer of nucleons from the heavier partner to the lighter one in mass-asymmetric systems [216, 303]. That way, a neutron enrichment in the mid-rapidity zone would occur before a fast neck rupture, attributed to the longer time scales involved in overcoming the Coulomb barrier for the protons. Isospin asymmetry term in nuclear potential also favours the neutron enrichment of the low density region (neck)[304, 305]. (Other known mechanism of neutron enhancement arises from the weak nucleon interaction falling out of equilibrium as expressed by the Saha equation [306]).

A number of effects could explain the presence of particles with velocities intermediate between the apparent quasi-projectile and quasi-target velocities [93]. The contact region between the two interacting nuclei is the source of prompt dynamic emissions [224] and production of new particles at higher incident energies of the projectile[307]. The promptly emitted particles are those that suffered elastic first-chance nucleon-nucleon target-projectile collisions knocking them out of the attractive potential of the bulk. There are dedicated experiments on this subject e.g. from nucleon-nucleon bremsstrahlung studies [53, 54, 55, 56, 57, 58, 131, 15]. In symmetric systems, the mean velocities of these particles coincide with the total center-of-mass velocity. These particles are essentially protons and neutrons. According to Ref. [226] it is not yet understood to what extent more complex fragments, e.g. α particles, is emitted in this manner. More collectively and depending on whether the interacting nuclei make contact for sufficient time, a neck of matter may join them and, unless fusion follows, the size and breaking of this neck will depend on the impact parameter as well as on the relative velocity of the two [93]. It was noted that although a neck of matter may be defined, it does not follow that complete stopping of the two nuclei is achieved. On the contrary, the existence of a neck has been seen as the nucleons which participates in the collision process whereas the rest of the

nucleons are the spectators. In that aspect, the neck is viewed as the hot spot, whose apparent temperature could be significantly different from the spectator fragment. When the projectile and the target nuclei interact, some of the nucleons that undergo nucleon-nucleon collisions in the overlap region acquire sufficiently high energy to escape from the attractive potential of the bulk and get emitted around the mid-rapidity [308]. Other nucleons may undergo energy dissipation by bremsstrahlung emission of high energy photons leading to coalescence. This prompt dynamic emission concerns mostly nucleons and light clusters (^{2}H, ^{3}H, ^{3}He, ^{4}He, ^{5}Li, ...). The cluster emissions are attributed to the collisions of the nucleons with the pre-formed clusters. It could also be explained by the coalescence of the promptly emitted nucleons as predicted by AMD or BME calculations [309, 13]. There after, other intermediate products could come from the de-excitation of the overlap region. Their decay can occur during the sticking of the quasi-projectile and the quasi-target and/or after their separation [310]. The two scenarios proposed to explain the cision mechanism of the overlap region with the two fragment partners are: the formation of a neck of matter between the quasi-projectile and quasi-target, and the sharp and geometrical cision between the two and the overlap region, forming the third intermediate velocity source. The competition between the two mechanisms is governed by the interaction time [308]. If the di-nuclear system has sufficient time to reach a deformed shape, a neck of matter can be formed between the two interacting nuclei. Then, the rupture and/or the emission from the neck leads to the formation of products around mid-rapidity as reported in the following studies [299, 300, 301, 302, 297, 227, 311, 279, 298, 312, 295, 292, 313, 291] and predicted in some theoretical calculation [227, 297, 314, 315] for the peripheral to semi-central collisions below 50 A MeV. The shearing-off may occur later on, from one of the two outgoing nuclei. In that case, quasi-projectile and/or quasi-target are deformed along the axis which connects them and their decays are anisotropic. One observes a preferential emission in the backward region of the quasi-projectile frame and/or in the forward zone of the quasi-target frame. This emission enhances the product yields around mid-rapidity. This effect has been observed from peripheral to semi-central collisions [227, 228] and has been called fast emission or dynamic fission of the

two outgoing nuclei. That meant one could observe in the same events both processes: dynamic fission and neck rupture. If the system has not enough time to deform itself, then the interaction mechanism corresponds to the participant-spectator scenario with three sources: two spectators and the participant region [316]. The participant zone comes from the stopping of nuclear matter in the overlap region between the two colliding nuclei. The intermediate velocity products come from the decay of this participant zone created at mid-rapidity. The spectators correspond to the remaining matter of the initial projectile and the target, which conserve a large part of their initial momenta. Above 50 A MeV, the transition from the neck or dynamic fission processes to the participant-spectator scenario is expected. The properties of this transition could probably depend on the viscosity of hot and probably compressed nuclear matter in the interaction zone with useful information on the viscosity of the nuclear matter and the in-medium nucleon-nucleon cross section [308].

The processes leading to the formation of neck-like structures cannot be described on the basis of statistical approaches but the dynamics of the collision [297, 298, 227, 299, 300, 301, 302]. The central issues concerning the multi-fragmentation process is the interplay between the attainment of the thermal and chemical equilibrium of the excited nuclear matter prior the production of fragments and the dynamics involved in their emission. In this respect, the study of the characteristics of the formation and decay of the neck-like structures is of great importance. With the advent of radioactive beam facilities and of high resolution experimental apparatus, the interest has been addressed toward the influence of the isospin degree of freedom, which could certainly be an important probe of the dynamical aspects of the formation and decay of the hot nuclear matter in heavy ion collisions. In fact, the non-equilibrium dynamical behaviour of nuclear systems, such as the neck-like structures, may be strongly influenced by the isospin effects. In that perspective, the mechanism leading to the rupture or to the re-absorption by the collision partners of the neck-like structures has important theoretical implications [317, 314, 315] i.e. the isospin dependence and the viscosity term of the equation of state play a fundamental role in the formation and the decay of such intermediate mass fragment sources.

The advent of heavy-ion collisions have also opened up new vistas for the production of nuclear matter away from a saturation density which had been hitherto impossible in the laboratory. Of the two scenarios; namely, nuclear matter with higher and lower densities relative to the saturation one, the former has drawn much attention because of the prospect of creating a quark-gluon plasma, a new form of matter. The latter, although not that exotic and epoch-making in nature, has great bearing on our understanding of the stellar evolution, the phenomena in which nature deals profusely with nuclear matter of widely varying densities largely lower than the saturation density. This opened a new dimension of nuclear physics with the ever increasing challenges to describe the wide varieties of astrophysical phenomena. The multi-fragmentation phenomena observed in high-energy light and intermediate energy heavy ion induced interactions, in which the low dense nuclear matter is characteristically produced, provides a unique opportunity for the study of its properties. The key issues such as whether multi-fragmentation is a new mode of decay or a series of sequential binary decays such as fission, and the possibility of a liquid-gas phase transition or the spinodal effect in the nuclear system, are intriguing. Understanding these occurrences in terms of standard concepts such as energy deposition, thermalization, isospin, the hot spot and the geometry of the collision etc., is presently inadequate and continues to be sought after [318]. Faced with such a highly complex situation for most of the heavy ion nuclear collisions, the so-called "single-source" or "fusion-like" events observed for a small part of the cross section [319, 320, 321, 322, 323, 324, 325, 326] are of great interest. In these events, all of the emitted fragments and particles, apart from a small prompt dynamic component of light particles, seem to originate in the multi-fragmentation of a single nuclear system containing almost all of the available mass and energy of the entrance channel, which simplifies enormously the analysis. Such events provide a unique opportunity to study the decay of well-defined and heavy pieces of excited nuclear matter, for which one expects that bulk effects, if present (for example the mechanical instability associated with spinodal decomposition [327, 328, 329, 330, 331, 332]), to play a dominant role. In its study [145], the concept of fusion was extended to this single nuclear system formed after full stopping. Semi-classical transport

calculations [333, 319] predict the interactions to occur for central collisions of heavy nuclei for small impact parameters ($b < 0.3\ b_{\mathrm{max}}$). The initial system formed is expected to suffer large amounts of compression and heating, and may subsequently expand into the low-density coexistence region, the freeze-out volume mentioned earlier.

The charge distributions of the multi-fragmentation events has been observed to be independent of the total mass of the incident nuclei [331], while fragment multiplicities scales according to their total charge. These were the first indication of a bulk property in the production of the fragments. How could one isolate the sample of events that corresponds to the formation and multi-fragmentation of a single source? Some suggestions include using the impact parameter. The 'fusion-like' events looked for in the low-energy domain, is characterised by high angular momentum transfer whereas in the high-energy domain it is the maximising of the participant zone. As observed in the low energy heavy systems [334], a dog-legged correlation appears in the 'Wilczyński plot' [319] with a crest running from forward-peaked, slightly dissipative collisions (large TKE, equation C.1) to highly-damped interactions with little or no memory of the entrance channel (large θ_f), as shown in figure C.3. TKE refers to total measured centre of mass kinetic energy of detected charged particles products and θ_f is the principal direction of fragment flow.

$$TKE = E_{\mathrm{c.m.}} + Q + \sum E_{\mathrm{neutron}} + \sum E_{\gamma}, \tag{C.1}$$

where $E_{\mathrm{c.m.}}$, Q, $\sum E_{\mathrm{neutron}}$ and $\sum E_{\gamma}$ are, respectively, the available centre of mass energy, the mass balance of the interaction, and the total neutron and gamma emission kinetic energies. In summary, the single source events are characterised by [145],

- no memory of the entrance channel remains;
- no projectile or target-like fragments are observed;
- mean event shapes are the most compact of all the very dissipative collisions;
- fragment kinematics are consistent with rapid emission from a single source;

- must contain a very large proportion of the available mass and energy, i.e. prompt dynamic emission is limited (otherwise for an asymmetric system in direct kinematics one would expect the 'fused' system to recoil with a velocity less than that of the system centre of mass.)

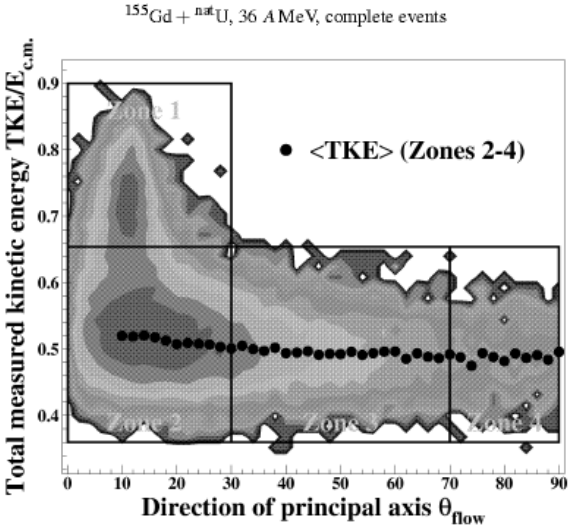


Figure C.3: The 'Wilczyński diagram' for complete events: The logarithmic intensity scale representing measured cross section as a function of total measured centre of mass kinetic energy (as a fraction of the available centre of mass energy) and 'flow' angle θ_f or direction of the event principal axis flow. The four zones indicated classify the complete events. For events in Zones 2 to 4 the mean value of TKE is indicated (points) for each flow bin (from Ref. [145]).

The 'Wilczyński diagram' permits the isolation of a sample of single-source events for $\theta_f \geq 70°$ [335]. For these single-source events, the flow angle takes all values, therefore they are present for $\theta_f < 70°$. However, events with small θ_f flow are dominated by a 'binary' fragment emission topology, with a strong memory of the entrance channel. Only at large flow angles do single-source events become dominant and separable using a flow cut. This selection criterion functions only if the flow angle retains a memory of the direction of the projectile-like and target-like fragments coming from highly dissipative binary interactions, and this direction must remain close to the beam axis. It is possible that this may only occur for heavy systems, for which binary highly dissipative collisions are strongly focused around the grazing angle due

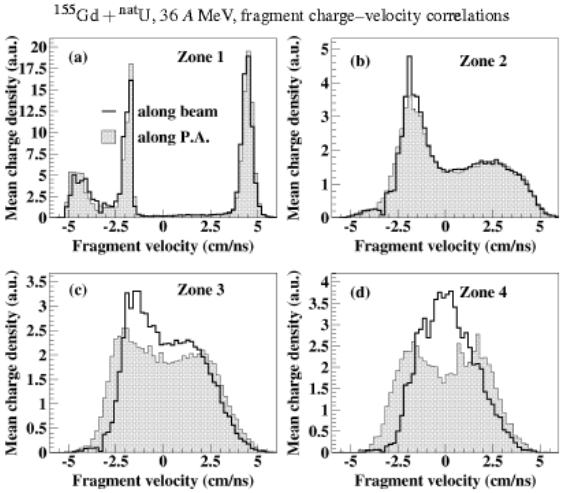


Figure C.4: The fragment charge-velocity correlations for the four classes of events corresponding to the zones defined in the Wilczyński diagram (Fig C.3). The mean charge density is plotted as a function of the velocity parallel to the beam axis (thick lines) or the principal axis of each event derived from the tensor (shaded histograms) (from Ref. [145]).

to Coulomb effects [321, 323]. If binary collisions of light systems lead to large flow angles even with low cross sections then single-source events, may not be revealed by a $\theta\!\!\!/$ cut as more refined selection methods need to be applied [320].

The nuclear multi-fragmentation associated to "single-source" events and its possible connection with the occurrence of a phase transition of the liquid-gas type has been the subject of intensive theoretical and experimental investigations [336]. Theoretical studies indicate that a finite nuclear matter has an equation of state similar to that of a Van der Waal's gas, which is characterized by the existence of a liquid-gas phase transition [337, 338]. Experimental measurements [339, 340, 341, 342, 343, 344] seem to indicate the existence of signatures related to a possible liquid-gas phase transition. While some of the measurements [340, 341, 344] suggest critical behaviour of some observables, other studies [339, 342, 343] rely on the measurement of the apparent nuclear temperature and on the particular shape of the caloric curve. These observations agree with the predictions of the statistical multi-fragmentation models [345] and suggest that multi-fragmentation may originate from a phase transition near the critical point [346]. The calorific curve obtained for the ^{197}Au + ^{197}Au system at 600 A MeV, together with

the ^{12}C, ^{18}O + ^{nat}Ag, ^{197}Au at 30-84 A MeV, and ^{22}Ne + ^{181}Ta at 8 A MeV is shown in figure C.5 [328, 339, 347]. The He-Li isotope ratio thermometer of Ref. [348] was used in the study. Three regions are noticeable in the caloric curve, figure C.5. The fusion/evaporation region,

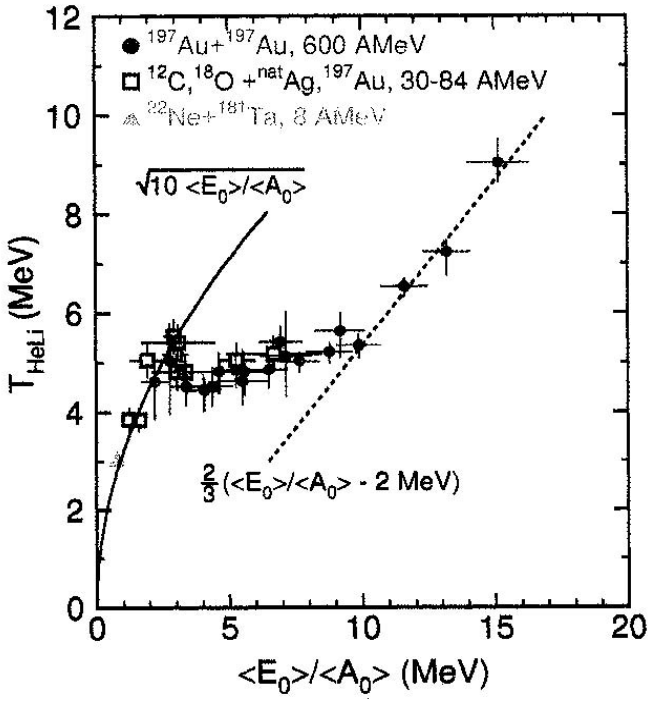


Figure C.5: Typical calorific curve of the nucleus (from Ref. [339]).

where excitation energies of about 2 A MeV or less are observed. The intermediate region of the curve, between 2 and 10 A MeV of near-constant apparent temperature of 5 MeV, and the "vaporisation" region. There have been reported signatures of the spinodal instabilities in finite nuclear matter, in agreement with this observations [327]. These apparent temperature measurements are applicable to the single source events, which constitute a small cross-section overall. In peripheral interactions, it applies only to the participant zone or the intermediate velocity source, but its measurement is not easy because of the large background of spectator events.

Appendix D

Nuclear Excitation Energy and the Apparent Temperature

The nuclear excitation energy is determined by the total energy balance, i.e. one sums the kinetic energies of all the products in the reference frame of the excited nuclear system taking into account the mass balance. At high excitation energies the measurement of the apparent nuclear temperature is a difficult task but there are several different techniques to do it [349, 350]. The dependence of the apparent nuclear temperature on the excitation energy, the so-called calorific curve, has been measured [339] and is still the subject of heated discussions. The main difficulty when comparing calorific curves obtained from different incident energies is the determination of the excitation energy. This is obtained by summing up the kinetic energies of all particles after equilibration has been achieved. A significant number of particles, whose number and energy have to be accounted for, are emitted prior to equilibration. Detailed knowledge of the energy emission spectra is essential [351]. To extract from experiments a calorific curve of nuclear matter, there has to be a capability to isolate and characterise hot nuclei. This in turn, requires good knowledge and understanding of their formation and decay mechanisms, which is a complex experimental task. The studies which concerns equation of state of nuclear matter (calorific curves [326, 339, 352] or calorific capacities [353, 336]) requires the calorimetry of the hot nuclei. To be unassailable scientifically, real control of the measurement of the excitation energy and of experimental error is needed [352, 354, 144]. An example of this is the methodological study using the classical characterisation technique of hot nuclei measured by a 4π detection array. The experimental set-up on one hand, introduces various biases, which

have to be perfectly understood to interpret these data correctly [93].

The following techniques have been developed and used for determining the apparent temperature of the excited nucleus. More recent studies are given in [355] and reference therein.

- the neutron multiplicity measurement obtained with neutron balls [327, 356, 274],
- detailed balance (masses, charge and kinetic energies) of the detected charged products of the hot nucleus or calorimetry [144, 93, 231, 336, 173, 276, 347, 151, 357, 161, 150, 164, 162, 173, 358],
- the double ratios of isotope yields [359, 360, 231, 361, 362, 350, 363, 347].

The first and the second technique have some drawbacks, which are that not all emitted products can be detected and that not all detected particles originate from the decay of the hot nucleus [231, 364, 155]. The detailed balance techniques used to deduce the excitation energy consist of measuring related parameters like the residue velocity. The techniques rely on the results of phenomenological models which give an approximate description of the hot nucleus production process [350, 365, 132, 104, 203]. The other option could be to measure the apparent temperature of the excited nuclei through the energy spectra of the evaporated particles. This requires that one has to separate the various sources of emission. This is done easily for neutrons compared to charged particles [356]. The nuclear excitation information relative to the light particle emission spectra, or to the properties of the sources emitting them, is extracted from the shape of energy spectra, angular distributions, their multiplicity and their relative abundances [276, 84, 366]. The average excitation energy for heavy ion collision event may thus be determined using the total energy balance [357]:

$$< E_0 >= \left(\left\langle \sum_i m_i \right\rangle + \left\langle \sum_i K_i \right\rangle \right) - (< m_0 > + (< K_0 >) \qquad \text{(D.1)}$$

the sum runs over all decay products i within an event where m_i is the mass and K_i the kinetic energy. The m_0 and K_0 denote the mass and kinetic energy of the decaying fragments with mass number $A_0 = \sum_i A_i$ and $Z_0 = \sum_i Z_i$.

The quasi-projectiles from the ion collisions offer the possibility of studying the formation and de-excitation properties of nuclei over a large range of excitation energy. Several methods have been proposed in the past to reconstruct the characteristics of quasi-projectiles (charge, mass and excitation energy). They all suffer from the same drawbacks. It is impossible to separate unambiguously particles sequentially emitted by the quasi-projectiles and particles originating in the fast processes such as prompt dynamic emission or emission from the neck of nuclear matter located between the projectile and target. However, the sequential and non-sequential particles are emitted with time scales not very different from one another. There is no reason to believe that the different processes occur in a well-defined time scale as there is no sharp time cut-off and the processes could overlap. Another drawback is that the hierarchy of the emission times of the particles is unknown. The question is, how can one reconstruct the nucleus while the sequence of its disintegration has not been observed by the experiment? This is one reason why the recoil effect is an important observable [367]. The various attempts to extract mean values of the quasi-projectile excitation energy have been made [368]. Comparison of the data with those taken at different lower bombarding energies [339, 104, 162, 369, 370] confirmed that the saturation of the excitation energy of a quasi-projectile nucleus at around 3 A MeV. This value was shown to be independent of the target over a wide range of nuclear masses [371], indicating that the observed saturation is related mainly to the internal structure of the nucleus. It was further observed that the energy sharing process is very fast and very far from a thermally equilibrated system picture [164].

Appendix E

The Quantum Molecular Dynamics Model

In order to establish the entrance channel dynamics, other microscopic models such as the Quantum Molecular Dynamics (QMD) [372, 373, 374, 375] can also be used. There have been different approaches to this theory and the comparison with the experimental data seems promising. The Extended QMD model (EQMD) is proposed in Ref. [376], in which the Pauli potential was introduced to make definite the initial ground states of the projectile and target nuclei as the minimum energy states. The parameters of the Pauli potential were adjusted to reproduce the ground state properties of the nuclei. The initial ground state nucleus of ^{40}Ca, generated by solving a damping equation of motion, was stable for at least 104 fm/c and 99.9% of the nucleon-nucleon collisions were Pauli blocked. The widths of the wave packets were also treated as time dependent parameters to introduce more freedom in the dynamics of the wave packet. This variation of the widths significantly improved the fusion cross section of the (^{16}O,^{16}O) system in the low energy region, showing that the Pauli blocking and nucleon-nucleon interactions were properly treated in the model [376]. More recently, an improved version of quantum molecular dynamics (ImQMD) model has been applied at just above the Coulomb barrier [377].

The incorporation of antisymmetrisation of the wavefunctions into the QMD theory leads to the antisymmetrized Molecular Dynamics (AMD) model. The model has been successfully used to study the static nature of light nuclei [378]. In recent studies, the AMD-V model has been suggested [379], in which the stochastic branching process of the wave packet diffusion

is incorporated. In the model, the widths of the wave packets in each stochastic branch are kept constant and the dynamics of the widths of the wave packets are calculated by the Vlasov equation incorporated as a stochastic diffusion process of the wave packets centroids. The diffusion process improved the treatment of the particle emission from the excited nucleus. It was shown that, in a model based on the usual QMD approach, the particle emission from a hot nucleus obeys classical statistics [380]. The incorporation of the diffusion process in AMD-V removed this problem and the particle emission obeyed quantum statistics [381].

The original Quantum Molecular Dynamics Model (QMD) approach [382, 383, 384], incorporates the important quantum features of the Vlasov-Uehling-Uhlenbeck (VUU) theory, namely, the Pauli principle, stochastic scattering, and particle production, into the N-body phase space dynamics of the classical molecular dynamics method [68]. The nucleons are represented by Gaussians of the form

$$f_i(r,p,t) \quad = \quad \frac{1}{(\pi\hbar)^3} exp\Big\{ - \frac{[r - r_{i0}(t)]^2}{2L} - [p - p_{i0}(t)]^2 \frac{2L}{\hbar^2} \Big\} \tag{E.1}$$

where r_{i0} and p_{i0} are the centroid in i coordinate and momentum space. $2L$ is the characteristic width of the wave packet. Note the compatibility of the width in momentum space $\hbar^2/2L$ with the uncertainty principle; $2L(\hbar^2/2L) = \hbar^2$. The interactions used here are a local Skyrme two and three particle interaction, a Coulomb and a Yukawa interaction. With these Gaussian nucleons, the interactions lead to the following Hamiltonian:

$$\begin{aligned} \mathrm{H} \quad = \quad & \sum_{i=1}^{N} \frac{p_i^2}{2m} + \frac{1}{2} \sum_{i,j=1}^{N}{}' \frac{V^0_{Yuk}}{2|r_{i0} - r_{j0}|} (e^L/\gamma^2_{Yuk}) \Big\{ e^{-|r_{i0}-r_{j0}|/\gamma_{Yuk}} \Big[1 - \mathrm{erf}\Big[\frac{2L/\gamma_{Yuk} - |r_{i0} - r_{j0}|}{\sqrt{4L}} \Big] \Big] \\ & - e^{+|r_{i0}-r_{j0}|\gamma_{Yuk}} \Big[1 - \mathrm{erf}\Big[\frac{(2L/\gamma_{Yuk}) + |r_{i0} - r_{j0}|}{\sqrt{4L}} \Big] \Big] \Big\} + \Big(\frac{Z}{A}\Big)^2 \frac{1}{2} \sum_{i,j=1}^{N}{}' \frac{e^2}{|r_{i0} - r_{j0}|} \mathrm{erf}\Big[\frac{|r_{i0} - r_{j0}|}{\sqrt{4L}} \Big] \\ & + \sum_{i=1}^{N} \Big[\frac{\alpha}{2} \frac{1}{(4\pi L)^{3/2}\rho_0} \sum_{j=1}^{N}{}' e^{-(r_{i0}-r_{j0})^2/4L} + \frac{\beta}{\gamma+1} \Big[\frac{1}{(4\pi L)^{3/2}\rho_0} \sum_{j=1}^{N}{}' e^{-(r_{i0}-r_{j0})^2/4L} \Big]^{\gamma} \Big] \end{aligned} \tag{E.2}$$

The primes on the sums indicate that the self-interaction terms are omitted. The first term is the kinetic energy and the second one is the Yukawa interaction of Gaussian distributed nucleons characterised by its strength V^0_{Yuk}. The third term describes the Coulomb interaction of the

Gaussian distributed nucleons and the last term denotes the Skyrme interaction, characterised by the parameters α and β. The three-body part of the Skyrme interaction is approximated to be proportional to ρ^{γ}, in order to allow for the compressibility of nuclear matter.

The calculation made using JQMD[1] for the present system is shown in figure E.1. The model has been described in Refs [69, 385, 386, 387, 388]. The parameters used were corrected appropriately for the two nuclei e.g. using best values given in Refs [377, 389, 390]. The increased near-target residue yield was attributed to be produced mainly by the inelastic processes. The general agreement between the predictions of the model and the experimental

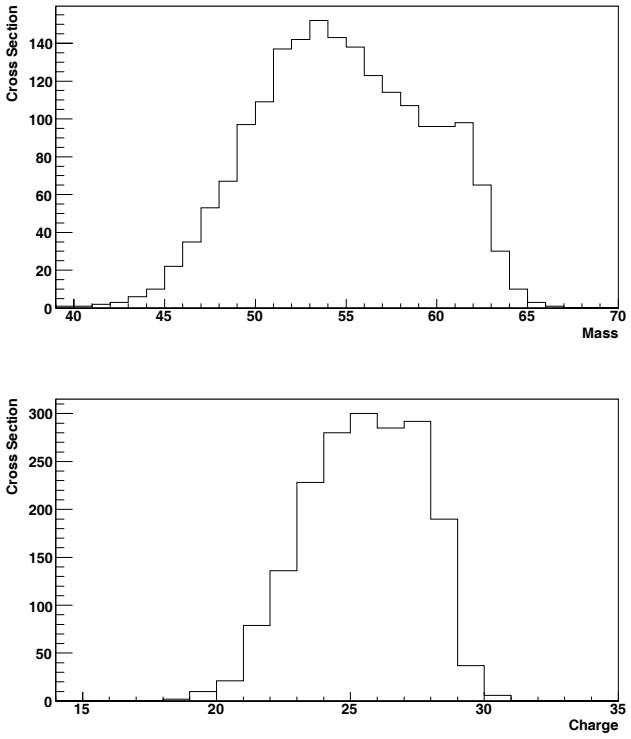


Figure E.1: The mass and charge distribution of residues produced using the QMD calculation for the ^{12} and ^{63} collision system.

observables was not good except for the residue mass distribution.

[1] http://hadron31.tokai.jaeri.go.jp/jqmd/